

<sup>1</sup> Observation of the Higgs boson in the  $WW^*$   
<sup>2</sup> channel and search for Higgs boson pair  
<sup>3</sup> production in the  $b\bar{b}b\bar{b}$  channel with the  
<sup>4</sup> ATLAS detector

<sup>5</sup> A DISSERTATION PRESENTED  
<sup>6</sup> BY  
<sup>7</sup> TOMO LAZOVICH  
<sup>8</sup> TO  
<sup>9</sup> THE DEPARTMENT OF PHYSICS

<sup>10</sup> IN PARTIAL FULFILLMENT OF THE REQUIREMENTS  
<sup>11</sup> FOR THE DEGREE OF  
<sup>12</sup> DOCTOR OF PHILOSOPHY  
<sup>13</sup> IN THE SUBJECT OF  
<sup>14</sup> PHYSICS

<sup>15</sup> HARVARD UNIVERSITY  
<sup>16</sup> CAMBRIDGE, MASSACHUSETTS  
<sup>17</sup> MAY 2016

<sup>18</sup> ©2016 – TOMO LAZOVICH

<sup>19</sup> ALL RIGHTS RESERVED.

<sup>20</sup> **Observation of the Higgs boson in the  $WW^*$  channel and search  
<sup>21</sup> for Higgs boson pair production in the  $b\bar{b}b\bar{b}$  channel with the  
<sup>22</sup> ATLAS detector**

<sup>23</sup> ABSTRACT

<sup>24</sup> This dissertation presents the observation and measurement of the Higgs boson in the  $H \rightarrow WW^* \rightarrow$   
<sup>25</sup>  $\ell\nu\ell\nu$  channel at  $\sqrt{s} = 7$  TeV and  $\sqrt{s} = 8$  TeV and a search for Higgs pair production in the  $HH \rightarrow$   
<sup>26</sup>  $b\bar{b}b\bar{b}$  channel at  $\sqrt{s} = 13$  TeV with the ATLAS detector in  $pp$  collisions at the Large Hadron Collider.

<sup>27</sup> First, the discovery of a particle consistent with the Higgs boson in  $4.8 \text{ fb}^{-1}$  at  $\sqrt{s} = 7$  TeV and  
<sup>28</sup>  $5.8 \text{ fb}^{-1}$  at  $\sqrt{s} = 8$  TeV is discussed. Then, the measurement of the Higgs boson signal strength  
<sup>29</sup> and cross section in both the gluon fusion and vector boson fusion (VBF) production modes using  
<sup>30</sup>  $20.3 \text{ fb}^{-1}$  of  $\sqrt{s} = 8$  TeV data combined with  $4.8 \text{ fb}^{-1}$  of 7 TeV data is shown. The combined signal  
<sup>31</sup> strength is measured to be  $\mu = 1.09^{+0.23}_{-0.21}$ . The total observed significance of the  $H \rightarrow WW^*$  process  
<sup>32</sup> is observed to be  $6.1\sigma$  (with  $5.8\sigma$  expected). Advanced methods for background reduction and estima-  
<sup>33</sup> tion, particularly in same-flavor lepton final states, are shown. The VBF signal strength is measured to  
<sup>34</sup> be  $\mu_{\text{VBF}} = 1.27^{+0.53}_{-0.45}$  with an observed significance of  $3.2\sigma$  (with  $2.7\sigma$  expected). In the VBF chan-  
<sup>35</sup> nel, a selection requirement based method, the precursor to the final multivariate technique used for the  
<sup>36</sup> result, is detailed.

<sup>37</sup> Finally, a search for Higgs pair production in the  $b\bar{b}b\bar{b}$  final state with  $3.2 \text{ fb}^{-1}$  at  $\sqrt{s} = 13$  TeV is  
<sup>38</sup> presented. A particular focus is placed on a tailored signal region for resonant production of Higgs pairs  
<sup>39</sup> at high masses. No significant excesses are observed, and upper limits on cross sections are placed for  
<sup>40</sup> spin-2 Randall Sundrum gravitons (RSG) and narrow spin-0 resonances. The cross section of  $\sigma(pp \rightarrow$   
<sup>41</sup>  $G_{\text{KK}}^* \rightarrow hh \rightarrow b\bar{b}b\bar{b})$  with  $k/\bar{M}_{\text{Pl}} = 1$  is constrained to be less than 70 fb for masses in the range  
<sup>42</sup>  $600 < m_{G_{\text{KK}}^*} < 3000$  GeV. The cross section upper limits for  $\sigma(pp \rightarrow H \rightarrow hh \rightarrow b\bar{b}b\bar{b})$  ranges  
<sup>43</sup> from 30 to 300 fb in the mass range of  $500 < m_H < 3000$  GeV.

# Contents

44

45	o INTRODUCTION	I
46	I Theoretical and Experimental Background	5
47	I THE PHYSICS OF THE HIGGS BOSON	6
48	1.1 The Standard Model of Particle Physics	6
49	1.2 Electroweak Symmetry Breaking and the Higgs	8
50	1.3 Higgs Boson Production and Decay	II
51	1.4 Higgs Pair Production in the Standard Model	16
52	1.5 Higgs Pair Production in Theories Beyond the Standard Model	17
53	1.6 Conclusion	22
54	2 THE ATLAS DETECTOR AND THE LARGE HADRON COLLIDER	23
55	2.1 The Large Hadron Collider	24
56	2.2 The ATLAS Detector	26
57	2.3 The ATLAS Muon New Small Wheel Upgrade	37
58	2.4 Object Reconstruction in ATLAS	42
59	II Observation and measurement of Higgs boson decays to $WW^*$ in LHC	
60	Run 1 at $\sqrt{s} = 7$ and 8 TeV	52
61	3 $H \rightarrow WW^* \rightarrow \ell\nu\ell\nu$ ANALYSIS STRATEGY	53
62	3.1 Introduction	53
63	3.2 The $H \rightarrow WW^* \rightarrow \ell\nu\ell\nu$ signal in ATLAS	54
64	3.3 Background processes	55
65	3.4 Shared signal region selection requirements	59
66	3.5 Background reduction in same-flavor final states	61
67	3.6 Parameters of interest and statistical treatment	67
68	4 THE DISCOVERY OF THE HIGGS BOSON AND THE ROLE OF THE $H \rightarrow WW^* \rightarrow \ell\nu\ell\nu$ CHANNEL	
69	4.1 Introduction	72

71	4.2	Data and simulation samples . . . . .	73
72	4.3	$H \rightarrow WW \rightarrow e\nu\mu\nu$ search . . . . .	73
73	4.4	$H \rightarrow \gamma\gamma$ search . . . . .	78
74	4.5	$H \rightarrow ZZ \rightarrow 4\ell$ search . . . . .	79
75	4.6	Combined results . . . . .	81
76	4.7	Conclusion . . . . .	83
77	5	EVIDENCE FOR VECTOR BOSON FUSION PRODUCTION OF $H \rightarrow WW^* \rightarrow \ell\nu\ell\nu$	85
78	5.1	Introduction . . . . .	85
79	5.2	Data and simulation samples . . . . .	86
80	5.3	Object selection . . . . .	90
81	5.4	Analysis selection . . . . .	94
82	5.5	Background estimation . . . . .	101
83	5.6	Systematic uncertainties . . . . .	112
84	5.7	Results . . . . .	116
85	6	COMBINED RUN I $H \rightarrow WW^* \rightarrow \ell\nu\ell\nu$ RESULTS	120
86	6.1	Introduction . . . . .	120
87	6.2	Results of dedicated gluon fusion $H \rightarrow WW^* \rightarrow \ell\nu\ell\nu$ analysis . . . . .	121
88	6.3	Signal strength measurements in ggF and VBF production . . . . .	123
89	6.4	Measurement of Higgs couplings to vector bosons and fermions . . . . .	128
90	6.5	Higgs production cross section measurement . . . . .	128
91	6.6	Conclusion . . . . .	130
92	III	Search for Higgs pair production in the $HH \rightarrow b\bar{b}b\bar{b}$ channel in LHC	
93		Run 2 at $\sqrt{s} = 13$ TeV	132
94	7	SEARCH FOR HIGGS PAIR PRODUCTION IN BOOSTED $b\bar{b}b\bar{b}$ FINAL STATES	133
95	7.1	Introduction . . . . .	133
96	7.2	Motivation . . . . .	134
97	7.3	Data and simulation samples . . . . .	136
98	7.4	Event reconstruction and object selection . . . . .	138
99	7.5	Event selection . . . . .	141
100	7.6	Data-driven background estimation . . . . .	146
101	7.7	Systematic uncertainties . . . . .	152
102	7.8	Results . . . . .	155

103	<b>8 COMBINED LIMITS FROM BOOSTED AND RESOLVED SEARCHES</b>	157
104	8.1 Introduction . . . . .	157
105	8.2 Resolved results . . . . .	158
106	8.3 Search technique and results . . . . .	158
107	8.4 Limit setting . . . . .	159
108	<b>IV Looking ahead</b>	163
109	<b>9 CONCLUSION</b>	164
110	<b>APPENDIX A <i>b</i>-TAGGING PERFORMANCE AT HIGH <math>p_T</math></b>	168
111	A.1 Changes in MV2 score at high $p_T$ . . . . .	168
112	A.2 Effect of multiple <i>b</i> -quarks inside one jet . . . . .	170
113	A.3 Changes in track quality at high $p_T$ . . . . .	172
114	<b>REFERENCES</b>	175

# Listing of figures

116	I.1	The particles of the Standard Model and their properties [6]. . . . .	7
117	I.2	The four most common Higgs boson production modes at the LHC: (a) gluon-gluon fusion, (b) vector boson fusion, (c) $W/Z + H$ production, (d) $t\bar{t}H$ production . . . . .	11
118	I.3	Higgs production cross sections as a function of center of mass energy ( $\sqrt{s}$ ) at a $pp$ collider [18]. . . . .	12
119	I.4	Higgs boson branching ratios as a function of $m_H$ [18]. . . . .	15
120	I.5	The two leading diagrams for Standard Model di-Higgs production at the LHC: (a) box diagram, (b) Higgs self coupling. . . . .	16
121	I.6	Diagrams with new vertices for non-resonant Higgs pair production arising in composite Higgs models. . . . .	18
122	I.7	Generic Feynman diagram for resonant Higgs pair production in BSM theories. . . . .	18
123	I.8	Branching ratios for a spin-2 Randall-Sundrum graviton as a function of mass computed in MadGraph with the CP3-Origins implementation [34, 40, 41]. . . . .	19
124	I.9	$\sigma \times \text{BR}(HH)$ for Randall-Sundrum gravitons as a function of mass computed in MadGraph with the CP3-Origins implementation [34, 40, 41]. . . . .	20
125	I.10	Randall-Sundrum graviton width as a function of mass computed in MadGraph with the CP3-Origins implementation [34, 40, 41] . . . . .	21
126	I.11	Branching ratios for heavy Higgs $H$ in Type I (left) and Type II (right) 2HDM models with $\tan \beta = 1.5$ and $\cos(\beta - \alpha) = 0.1(0.01)$ for Type I (Type II) [38]. . . . .	22
127	2.1	A schematic view of the LHC ring [48]. Four main experiments are located at interaction points along the ring. ATLAS and CMS are general purpose experiments, while ALICE is dedicated to heavy ion collisions and LHCb is dedicated to studying $B$ physics. . . . .	24
128	2.2	A full diagram of the ATLAS detector [44]. . . . .	27
129	2.3	The ATLAS coordinate system. The $z$ direction corresponds to the beam axis, while $x$ and $y$ define the transverse plane. $\theta$ is the angle relative to the beam axis and $\phi$ is the azimuthal angle. $\eta$ , the pseudorapidity, approaches infinity at small angles relative to the beam axis. .	28
130	2.4	Layout of the ATLAS Inner Detector system [52]. . . . .	29
131	2.5	Layout of the ATLAS calorimeter system [44]. . . . .	31
132	2.6	Layout of the ATLAS muon system [44]. . . . .	33
133	2.7	Predicted field integral as a function of $ \eta $ for the ATLAS magnet system [44]. . . . .	35

146	2.8	ATLAS trigger rates for Level-1 triggers as a function of instantaneous luminosity in 2012	
147		and 2015 operation. These are single object triggers for electromagnetic clusters (EM),	
148		muons (MU), jets (J), missing energy (XE), and $\tau$ leptons (TAU). The threshold of the	
149		trigger is given in the name in GeV [54]. . . . .	36
150	2.9	Instantaneous luminosity as a function of time for data recorded by ATLAS at different	
151		center of mass energies [55, 56]. . . . .	38
152	2.10	MDT tube hit (solid) and segment (dashed) efficiency as a function of hit rate per tube [57].	39
153	2.11	Trigger rate as a function of $p_T$ threshold with and without the NSW upgrade [57]. . . . .	40
154	2.12	Illustrations of the geometry (left) and operating principle (right) of the micromegas de-	
155		tector [57]. . . . .	41
156	2.13	Geometry of the sTGC detector [57]. . . . .	41
157	2.14	Illustration of particle interactions in ATLAS [60]. . . . .	43
158	2.15	Electron performance: (a) reconstruction efficiency as a function of electron $E_T$ [62] (b)	
159		energy resolution in simulation as a function of $ \eta $ for different energy electrons [63]. . .	44
160	2.16	Muon performance in $\sqrt{s} = 8$ TeV data: (a) reconstruction efficiency as a function of	
161		muon $p_T$ (b) dimuon mass resolution as a function of average $p_T$ [64]. . . . .	46
162	2.17	Jet energy response after calibration as a function of true $p_T$ in simulation [69]. . . . .	47
163	2.18	Summary of the inputs to the MV2 $b$ -tagging algorithm. . . . .	48
164	2.19	Light jet rejection (1/efficiency) vs. $b$ -jet efficiency for MV1 and its input algorithms (a) [70]	
165		and MV2 (b) [71] in simulated $t\bar{t}$ events. The numbers in the algorithm names in (b) refer	
166		to the fraction of charm events used in the MV2 training. . . . .	49
167	2.20	Resolution of $E_T^{\text{miss}}$ components as a function of $\sum E_T$ before pileup suppression with	
168		different pileup techniques [73]. . . . .	51
169	3.1	Branching ratios for a $WW$ system. $q$ refers to quarks. $\ell$ can be either an electron or muon,	
170		and the leptonic branching ratios of the $\tau$ are included. For example, the $\ell\nu qq$ final state	
171		includes one $W$ decaying to $e\nu$ , $\mu\nu$ , or $\tau\nu$ . $\tau_h$ refer to hadronic decays of the $\tau$ . . . . .	55
172	3.2	An illustration of the unique analysis signal regions [74]. The most sensitive regions for	
173		both gluon fusion and vector boson fusion production . . . . .	56
174	3.3	Feynman diagram for Standard Model $WW$ production . . . . .	56
175	3.4	Feynman diagrams for top pair production (left) and $Wt$ production (right) . . . . .	57
176	3.5	An example Feynman diagram of $W$ +jets production . . . . .	58
177	3.6	An example Feynman diagram of $Z$ +jets production . . . . .	58
178	3.7	A graphical illustration of the $E_{T,\text{rel}}^{\text{miss}}$ calculation. . . . .	60
179	3.8	Predicted backgrounds (compared with data) as a function of the number of jets, $n_j$ (a)	
180		and b), and the number of $b$ -tagged jets, $n_b$ (c), after pre-selection requirements. Panel a	
181		shows $n_j$ in the same flavor sample, while panels b and c show the $n_j$ and $n_b$ distributions	
182		in the different flavor sample. . . . .	61

183	3.9	An event display of a $Z/\gamma^*$ + jets event illustrating the effect of pileup interactions . . . . .	63
184	3.10	The RMS of different missing transverse momentum definitions as a function of the average number of interactions per bunch crossing . . . . .	63
185	3.11	The difference between the true and reconstructed values of the missing transverse momentum (a) and $m_T$ (b) in a gluon fusion signal sample using both track-based ( $p_T^{\text{miss}}$ ) and calorimeter-based $E_T^{\text{miss}}$ definitions. . . . .	65
186	3.12	Comparison of $f_{\text{recoil}}$ distributions for $Z/\gamma^* + \text{jets}$ , $H \rightarrow WW^*$ , and other backgrounds with real neutrinos. . . . .	66
187	3.13	Signal significance as a function of required value for $f_{\text{recoil}}$ and $p_{T,\text{rel}}^{\text{miss}(\text{trk})}$ in the ggF $H \rightarrow WW^*$ with $n_j = 0$ . . . . .	67
193	4.1	Jet multiplicity distribution in data and MC after applying lepton, jet, and $E_{T,\text{rel}}^{\text{miss}}$ selections. The $WW$ and top backgrounds have been normalized using control samples, and the hashed band indicates the total uncertainty on the prediction [1]. . . . .	74
194	4.2	Comparison of $m_T$ between data and simulation in the $n_j = 0$ $WW$ (a) and $n_j = 1$ top (b) control samples [1]. . . . .	76
195	4.3	$m_T$ distribution in the $H \rightarrow WW \rightarrow e\nu\mu\nu$ $n_j \leq 1$ channels for 8 TeV data [1]. . . . .	78
196	4.4	Diphoton mass spectrum in 7 and 8 TeV data. Panel a) shows the unweighted data distribution superimposed on the background fit, while panel c) shows the data where each event category is weighted by its signal to background ratio. Panels b) and d) show the respective distributions with background subtracted [1]. . . . .	79
203	4.5	Four lepton invariant mass spectrum ( $m_{4\ell}$ ) in 7 and 8 TeV data compared to background estimate. A 125 GeV SM Higgs signal is shown in blue [1]. . . . .	80
204	4.6	Local $p_0$ distribution as a function of hypothesized Higgs mass for the $H \rightarrow ZZ^* \rightarrow 4\ell$ (a), $H \rightarrow \gamma\gamma$ (b), and $H \rightarrow WW^* \rightarrow \ell\nu\ell\nu$ (c) channels. Dashed curves show expected results, while solid curves show observed. Red curves are from 7 TeV data, blue curves from 8 TeV, and black curved combined [1]. . . . .	82
209	4.7	Combined 95% CL limits (a), local $p_0$ values (b), and signal strength measurement (c) as a function of Higgs mass [1]. . . . .	83
211	4.8	Comparison of measured signal strength $\mu$ for a 126 GeV Higgs in the 7 and 8 TeV datasets [1].	84
212	4.9	Two dimensional likelihood as a function of signal strength $\mu$ and Higgs mass $m_H$ [1]. . .	84
213	5.1	A comparison of the subleading lepton $p_T$ spectrum between VBF $H \rightarrow WW^*$ production and $t\bar{t}$ background. . . . .	87
215	5.2	Leading jet $\eta$ in VBF $H \rightarrow WW^*$ (red) and $t\bar{t}$ (black) . . . . .	96
216	5.3	Distributions of (a) $m_{jj}$ , (b) $\Delta y_{jj}$ , (c) $C_{\ell 1}$ , and (d) $\Sigma m_{\ell j}$ , for the cut-based VBF analysis. The top panels compare simulation and data, while the bottom panels show normalized distributions for all background processes and signal for shape comparisons [74]. . . . .	97

219	5.4	A cartoon of the WW final state. Momenta are represented with thin arrows, spins with thick arrows [74]. . . . .	98
220	5.5	Event display of a VBF candidate event [74]. . . . .	100
221	5.6	Higgs topology variables - $m_{\ell\ell}$ (top left), $\Delta\phi_{\ell\ell}$ (top right), and $m_T$ (bottom) - used in the selection requirements of the cut-based signal region and as inputs to the BDT result. These are plotted after all of the BDT pre-training selection cuts [74]. The VBF Higgs signal cross section is multiplied by a factor of 50 to allow for shape comparisons. . . . .	102
222	5.7	VBF topology variables - $m_{jj}$ (top left), $\Delta y_{jj}$ (top right), $\sum C_\ell$ (bottom) - used in the selection requirements of the cut-based signal region and as inputs to the BDT result. These are plotted after all of the BDT pre-training selection cuts [74]. The VBF Higgs signal cross section is multiplied by a factor of 50 to allow for shape comparisons. . . . .	103
223	5.8	Distributions of $m_{jj}$ (a) and $O_{\text{BDT}}$ (b) in the VBF $n_b = 1$ top CR [74]. . . . .	105
224	5.9	Comparison of $m_{jj}$ shape in a same flavor $Z \rightarrow \ell\ell$ control region and the VBF cut-based signal region. The MC samples used for these distributions are given in table 5.4. . . . .	106
225	5.10	General illustration of the ABCD region definitions for $Z/\gamma^* \rightarrow \ell\ell$ background estimation. . . . .	107
226	5.11	Distribution of $m_{T2}$ in the WW validation region of the VBF analysis [74]. . . . .	109
227	5.12	Extrapolation factors for the $W + \text{jets}$ estimate derived for muons (a) and electrons (b) as a function of lepton $p_T$ [74]. OC refers to the opposite charge $W + \text{jets}$ MC sample, while SC refers to the same charge $W + \text{jets}$ MC. The uncertainty bands have contributions from statistical uncertainty in the data and backgrounds to $Z + \text{jets}$ that are subtracted from the data, as well as systematic uncertainties due to variations in the extrapolation factor between the three MC samples shown. . . . .	III
228	5.13	Background composition in final VBF signal region [74]. . . . .	112
229	5.14	Variations in the top background extrapolation factor in the cut-based analysis due to PDF uncertainties. The uncertainties are shown in the three bins of $m_T$ used in the final cut-based statistical fit. Variations from the eigenvector of the nominal PDF, CT10, as well as the result from an alternate PDF (NNPDF10), are compared. . . . .	115
230	5.15	Variations in the top background extrapolation factor in the cut-based analysis due to QCD scale uncertainties. The uncertainties are shown in the three bins of $m_T$ used in the final cut-based statistical fit. $Q_F$ is the QCD factorization scale, while $Q_R$ is the QCD renormalization scale. . . . .	115
231	5.16	Post-fit distributions in the cut-based VBF analysis. Panel (a) shows the one-dimensional $m_T$ distribution, while (b) shows the data candidates split into the bins of $m_T$ and $m_{jj}$ used in the final fit [74]. . . . .	118
232	5.17	Postfit distributions in the BDT VBF analysis [74]. . . . .	119
233	5.18	Overlap between cut-based and BDT VBF signal region candidates in the $m_{jj}$ - $m_T$ plane. .	119
234	6.1	Post-fit $m_T$ distribution in the $n_j \leq 1$ regions for the same flavor ( $ee/\mu\mu$ ) final states [74].	122

256	6.2 Post-fit $m_T$ distribution in the $n_j \leq 1$ regions [74]. . . . .	124
257	6.3 Best fit signal strength $\hat{\mu}$ as a function of hypothesized $m_H$ [74]. . . . .	125
258	6.4 Local $p_0$ as a function of $m_H$ [74]. . . . .	126
259	6.5 Likelihood as a function of $\mu_{\text{VBF}}/\mu_{\text{ggF}}$ [74]. . . . .	126
260	6.6 Two dimensional likelihood scan as a function of $\mu_{\text{VBF}}$ and $\mu_{\text{ggF}}$ [74]. . . . .	127
261	6.7 Likelihood scan as a function of $\kappa_F$ and $\kappa_V$ , the Higgs coupling scale factors [74]. . . . .	129
262	6.8 Comparison of signal strength measurements in different Higgs decay channels on ATLAS [108].	131
263	7.1 Parton luminosity ratios as a function of resonance mass $M_X$ for 13/8 TeV and 7/8 TeV [109].	134
264	7.2 Summary of $HH$ branching ratios [110]. . . . .	135
265	7.3 Minimum $\Delta R$ between $B$ decay vertices for different RSG masses in a $G_{\text{KK}}^* \rightarrow HH \rightarrow$	
266	$4b$ sample with $c = 1$ . . . . .	136
267	7.4 Trigger efficiency for events passing all signal region selections as a function of mass in	
268	$G_{\text{KK}}^* \rightarrow HH \rightarrow 4b$ samples with $c = 1$ [119]. In the trigger names, “j” refers to a jet	
269	or jets. “ht” refers to $H_T$ , the scalar sum of transverse momenta in the event. “bloose”	
270	refers to a loose $b$ -tagging requirement applied to the jet. “aor” refers to anti- $k_T$ jets with	
271	$R = 1.0$ . The numbers at the end of each trigger name are the thresholds on the given	
272	quantity in GeV. . . . .	138
273	7.5 Comparison of untrimmed and trimmed jet masses for large radius jets in a RSG sample	
274	with $m_{G_{\text{KK}}^*} = 1$ TeV. JES (JMS) refers to the standard jet energy (mass) scale calibration	
275	for ATLAS [69]. . . . .	139
276	7.6 Efficiency of finding two $b$ -jets from each Higgs in an RSG event using calorimeter jets	
277	with $R = 0.3$ and track jet radii of $R = [0.2, 0.3, 0.4]$ [123]. . . . .	140
278	7.7 Illustration of the boosted selection requirements on Higgs candidates. Each large-radius	
279	calorimeter jet (Higgs candidate) must contain two track jets. . . . .	142
280	7.8 Estimated significance as a function of signal mass for RSG $c = 1$ models in the $3b$ (a) and	
281	$4b$ (b) regions for different $b$ -tagging efficiency working points . . . . .	143
282	7.9 Acceptance $\times$ efficiency as a function of mass for (a) RSG and (b) narrow heavy scalar	
283	signal models [126]. . . . .	144
284	7.10 Efficiency of requiring 3 or 4 $b$ -tagged track jets vs. RSG mass. The efficiency quoted is	
285	relative to the previous selection requirements (rather than an absolute efficiency). . . . .	145
286	7.11 MV2c20 $b$ -tagging efficiency for each of the four track jets in the boosted $4b$ selection as a	
287	function of RSG mass for $c = 1$ models. . . . .	146
288	7.12 $M_J^{\text{sublead}}$ vs. $M_J^{\text{lead}}$ in a 2 $b$ -tag data sample. The signal region is defined by the inner black	
289	contour ( $X_{hh} < 1.6$ ) and the sideband region is defined by the outer contour ( $R_{hh} >$	
290	35.8 GeV). The region between the black contours is the control region. The mass region	
291	which is enriched in $t\bar{t}$ background is also shown for illustration [126]. . . . .	147
292	7.13 An illustration of the data-driven background estimation technique for the boosted analysis	149

293	7.14	Leading large-R jet mass in the $3b$ (a) and $4b$ (b) sideband regions. The multijet and $t\bar{t}$ backgrounds are estimated using the data-driven methods described above. Because their normalizations are derived in the sideband region, the total background normalization is constrained by default to match the normalization of the data [126]. . . . .	150
294			
295	7.15	Di-jet invariant mass ( $M_{2J}$ ) in the $3b$ (a) and $4b$ (b) control regions. The multijet and $t\bar{t}$ backgrounds are estimated using the data-driven methods described above [126]. . . . .	151
296			
297	7.16	Di-jet invariant mass ( $M_{2J}$ ) in the $3b$ (a) and $4b$ (b) signal regions. The multijet and $t\bar{t}$ backgrounds are estimated using the data-driven methods described above. In the $3b$ region, a graviton signal with $m_{G_{KK}^*} = 1.8$ TeV and $c = 1$ is overlaid, with the cross section multiplied by a factor of 50 so that the signal is visible. In the $4b$ region, signals with $m_{G_{KK}^*} = 1.0$ TeV and $m_{G_{KK}^*} = 1.5$ TeV are overlaid, both with $c = 1$ and the yields multiplied by factors of 2 and 5 respectively [126]. . . . .	156
298			
299	8.1	Di-jet invariant mass ( $M_{2J}$ ) in the resolved signal region. A graviton signal with $m_{G_{KK}^*} = 800$ GeV and $c = 1$ is overlaid. [126]. . . . .	159
300			
301	8.2	Expected and observed upper limit as a function of mass for $G_{KK}^*$ in the RSG model with (a) $c = 1$ and (b) $c = 2$ , as well as (c) $H$ with fixed $\Gamma_H = 1$ GeV, at the 95% confidence level in the $CL_s$ method [126]. . . . .	162
302			
303	9.1	Combined ATLAS and CMS measurements in Run 1 for (a) Higgs signal strength in gluon fusion and VBF and (b) Higgs couplings normalized to their SM predictions . . . . .	166
304			
305	9.2	Discovery significance for RSG models at the HL-LHC in three different budget scenarios [133]. Systematic uncertainties on the background prediction ( $\sigma_B$ ) of 2.5% and 5.0% are both tested. . . . .	167
306			
307	A.1	$p_T$ of the leading track jet in the leading calorimeter jet for different signal masses in RSG $c = 1$ models . . . . .	169
308			
309	A.2	MV2c2o score for the leading track jet (a) and subleading track jet (b) of the leading calorimeter jet for different signal masses in RSG $c = 1$ models . . . . .	169
310			
311	A.3	IP3D log-likelihood ratio ( $\log(p_b/p_u)$ ) of the leading track jet in the leading calorimeter jet for different signal masses in RSG $c = 1$ models . . . . .	170
312			
313	A.4	Mass (a) and number of tracks (b) for the secondary vertices computed with the SV1 algorithm. When no secondary vertex is found, the quantities are assigned to default negative values. . . . .	171
314			
315	A.5	Mass (a) and number of tracks (b) for vertices computed with the JetFitter algorithm. When no vertices are found, the quantities are assigned to default negative values. . . . .	171
316			
317	A.6	MV2c2o score (a) and SV1 mass (b) for leading track jets with two truth $b$ quarks ( $n_{tb,lead} = 2$ ) compared to those with only one truth $b$ ( $n_{tb,lead} = 1$ ). . . . .	172
318			

328	A.7 Track fit $\chi^2/n_{\text{DOF}}$ (a) and number of pixel detector hits (b) for the leading track of the	
329	leading track jet in different mass RSG $c = 1$ samples . . . . .	173
330	A.8 MV <sub>2c2o</sub> score (a) and SV1 mass (b) for leading track jets whose leading track jet has at least	
331	four pixel hits ( $N_{\text{pix}} \geq 4$ ) compared to those which do not ( $N_{\text{pix}} < 4$ ). . . . .	174

# Listing of tables

332

333	1.1	Production cross sections for a 125 GeV Higgs boson at $\sqrt{s} = 8$ TeV with scale and PDF uncertainties [18]. . . . .	13
334	1.2	Theoretical branching ratios for a 125 GeV Higgs boson, quoted as a percentage of the total width of the Higgs. Uncertainties shown are relative to the branching ratio value [18]. . . . .	15
335	1.3	Possible channels for Higgs searches. Checkmarks denote the most sensitive production modes for each decay channel [5]. . . . .	16
336	1.4	Production cross sections for pair production of a 125 GeV Higgs boson at $\sqrt{s} = 14$ TeV with total uncertainty [29]. The uncertainties include QCD scale and PDF variations as well as uncertainties on $\alpha_S$ . . . . .	17
337	2.1	Evolution of LHC machine conditions [50, 51]. . . . .	26
338	2.2	Performance requirements for the ATLAS detector [44]. . . . .	37
339	2.3	Signal efficiencies for $WH$ production with $H \rightarrow b\bar{b}$ and $H \rightarrow WW^* \rightarrow \mu\nu qq$ under different trigger configurations [57]. . . . .	42
340	3.1	A summary of backgrounds to the $H \rightarrow WW^* \rightarrow \ell\nu\ell\nu$ signal . . . . .	59
341	4.1	Monte carlo generators used to model signal and background for the Higgs search [1]. . . . .	73
342	4.2	Normalization factors (ratio of data and MC yields in a control sample) for the Standard Model $WW$ and top backgrounds in the $H \rightarrow WW^* \rightarrow \ell\nu\ell\nu$ analysis [1]. Only statistical uncertainties are shown. . . . .	76
343	4.3	Data and expected yields for signal and background in the final $H \rightarrow WW^* \rightarrow \ell\nu\ell\nu$ signal region. Uncertainties shown are both statistical and systematic [1]. . . . .	77
344	4.4	Summary of the expected and observed significance and measured signal strengths in the combined 7 and 8 TeV datasets for the Higgs discovery analysis [1]. . . . .	81
345	5.1	Single lepton triggers used for electrons and muons in the $H \rightarrow WW^* \rightarrow \ell\nu\ell\nu$ analysis. A logical “or” of the triggers listed for each lepton type is taken. Units are in GeV, and the $i$ denotes an isolation requirement in the trigger. . . . .	88
346	5.2	Di-lepton triggers used for different flavor combinations in the $H \rightarrow WW^* \rightarrow \ell\nu\ell\nu$ analysis. The two thresholds listed refer to leading and sub-leading leptons, respectively. The di-muon trigger only requires a single lepton at level-1. . . . .	88

361	5.3	Trigger efficiency for signal events and relative gain of adding a dilepton trigger on top of the single lepton trigger selection. The first lepton is the leading, while the second is the sub-leading. Efficiencies shown here are for the ggF signal in the $n_j = 0$ category but are comparable for the VBF signal. . . . .	88
362			
363			
364			
365	5.4	Monte Carlo samples used to model the signal and background processes [74]. The ta- ble lists the cross section for each process, taking into account the branching ratio for the process producing two leptons. . . . .	90
366			
367			
368	5.5	$p_T$ dependent isolation requirements for muons. Muons are required to have their calorime- ter based or track based cone sums be less than this fraction of their $p_T$ . . . . .	92
369			
370	5.6	$p_T$ dependent requirements for electrons. Electrons are required to have their calorimeter based or track based cone sums be less than this fraction of their $E_T$ . . . . .	92
371			
372	5.7	Summary of event selection for the $n_j \geq 2$ VBF analysis in the 8 TeV cut-based analy- sis [74]. . . . .	99
373			
374	5.8	Background composition after each requirement in the $n_j \geq 2$ VBF analysis in the 8 TeV cut-based analysis [74]. . . . .	100
375			
376	5.9	Top normalization factors computed at each stage of the cut-based selection. Uncertainties are statistical only. . . . .	104
377			
378	5.10	Top normalization factors computed for each bin of $O_{\text{BDT}}$ . Uncertainties are statistical only. . . . .	104
379			
380	5.11	$Z/\gamma^* \rightarrow \tau\tau$ correction factors for the VBF cut-based analysis. Uncertainties are statistical only. . . . .	107
381			
382	5.12	$Z/\gamma^* \rightarrow \ell\ell$ normalization factors for cut-based and BDT analyses. Uncertainties are statistical only. . . . .	108
383			
384	5.13	Systematic uncertainties for various processes in the cut-based VBF analysis, given in units of % change in yield. Values are given for the low $m_{jj}$ signal region. . . . .	114
385			
386	5.14	Composition of the post-fit uncertainties (in %) on the total signal ( $N_{\text{sig}}$ ), total back- ground ( $N_{\text{bkg}}$ ), and individual background yields in the VBF analysis [74]. “Stat.” refers to statistical uncertainties, “Expt.” refers to experimental systematic uncertainties, and “Theo.” refers to theoretical systematic uncertainties. . . . .	116
387			
388			
389			
390	5.15	Event selection for the VBF BDT analysis. The event yields in (a) are shown after the pre- selection and the additional requirements applied before the BDT classification (see text). The event yields in (b) are given in bins in $O_{\text{BDT}}$ after the classification [74]. . . . .	117
391			
392			
393	6.1	Post-fit yields in ggF dedicated signal regions for the $ee/\mu\mu$ final states [74]. . . . .	121
394	6.2	All signal regions definitions input into final statistical fit [74]. . . . .	123
395	6.3	Post-fit yields in the both ggF and VBF dedicated signal regions with all lepton flavor final states combined [74]. . . . .	123
396			

397	7.1	Summary of requirements on objects used in the $X \rightarrow HH \rightarrow b\bar{b}b\bar{b}$ search . . . . .	141
398	7.2	Effect of boosted selection on data, RSG signal models, $t\bar{t}$ , and $Z+jets$ . The numbers from simulation are normalized with the MC generator cross section and do not take into account the data driven estimates described in section 7.6 [127]. . . . .	146
399			
400	7.3	Mass region definitions used for background estimation. . . . .	148
401	7.4	Parameters derived for exponential fit to background $M_{2J}$ shape in the 3 $b$ and 4 $b$ signal regions [127]. . . . .	150
402			
403	7.5	The number of events in data and predicted background events in the boosted 3-tag and 4-tag sideband and control regions [126]. The uncertainties shown are statistical only. . . . .	151
404			
405	7.6	Summary of systematic uncertainties in the total background and signal event yields (ex- pressed in %) in the boosted 3-tag and 4-tag signal regions. Systematic uncertainties on the signal normalization are shown for models with $m_{G_{KK}^*} = 1.5$ TeV and both $c = 1$ and $c = 2$ as well as a narrow width heavy scalar. . . . .	153
406			
407	7.7	Alternate fit functions used to model the $M_{2J}$ distribution in the QCD multijet back- ground. In the equations, $x = M_{2J}/\sqrt{s}$ . . . . .	154
408			
409	7.8	Observed yields in the 3-tag and 4-tag signal regions for the boosted analysis compared to the predicted number of background events Errors correspond to the total uncertainties in the predicted event yields. The yields for a graviton with $m_{G_{KK}^*} = 1$ TeV and $c = 1$ are also shown [126]. . . . .	155
410			
411	8.1	Observed yields in the resolved selection 4-tag signal region compared to the predicted number of background events Errors correspond to the total uncertainties in the pre- dicted event yields. The yields for a graviton with $m_{G_{KK}^*} = 800$ GeV and $c = 1$ are also shown [126]. . . . .	158
412			
413			
414			
415			
416			
417			
418			
419			



# Acknowledgments

422 I have been a member of the Harvard ATLAS group for many years now, first as an undergraduate and  
 423 then as a graduate student. As a result, I have had the privilege of interacting with many amazing people  
 424 there over the years and have accumulated a large list of folks to thank.

425 First and foremost, I must thank the two people who have effectively been my academic parents since I  
 426 started in the Harvard group: João Guimarães da Costa and Melissa Franklin. Melissa Franklin and João  
 427 Guimarães da Costa. They have both been so important to both my academic and personal development  
 428 that I can't even put one before the other. João has been an excellent PhD advisor, showing me how to  
 429 look at the big picture and helping me navigate the sometimes complicated politics of ATLAS. He got me  
 430 started on my first projects with ATLAS as a young college sophomore before there was even beam in the  
 431 LHC (go cosmic ray muons!). He has also been a constant source of advice and support, even when we  
 432 have been on different continents. Melissa gave me my start in HEP as a summer student on CDF and  
 433 has been an unbelievable mentor throughout my time at Harvard. I still remember our weekly chalkboard  
 434 particle physics lessons after that first summer. She also graciously took me on as a co-advisee after João  
 435 moved on to his new position at IHEP. I am incredibly lucky to have had both of them as advisors.

436 Another mentor who was essential to my development as a graduate student is Paolo Giromini. His un-  
 437 canny knowledge and intuition about detectors is unmatched and I am very grateful to have had the chance  
 438 to work with him on the micromegas for the ATLAS New Small Wheel upgrade project. I owe essentially  
 439 all my practical knowledge about detectors (and building things in general) to him. I also appreciated his  
 440 unique sense of humor which made sometimes difficult tasks much easier to get through.

441 I am grateful to John Huth and Masahiro Morii for their helpful advice as the other professors in the  
 442 Harvard ATLAS group as well. I especially thank John for helping me get started on the micromegas  
 443 trigger project and being a great professor to TF particle physics for. Additionally I thank Howard Georgi  
 444 for serving as my third committee member and offering me feedback throughout my graduate career.

445 I also owe enormous thanks to Hugh Skottowe, the postdoc that I worked most closely with in my early  
446 years as a graduate student. He was always able to help me through complicated tasks in everything from  
447 writing code to understanding difficult physics concepts. I particularly enjoyed walking down to his office  
448 in Palfrey at random times and talking through whatever problem I was tackling on that day.

449 Alex Tuna, the second postdoc that I worked closely with at Harvard, deserves great thanks as well. He  
450 helped me push through to the end of my graduate career and offered great advice along the way.

451 Being at Harvard, I have seen an incredible array of graduate students graduate before me: Ben Smith,  
452 Verena Martinez Outschoorn, Srivas Prasad, Michael Kagan, Giovanni Zevi Della Porta, Laura Jeanty,  
453 Kevin Mercurio, William Spearman, and Andy Yen. I want to thank them all for showing me what a good  
454 physicist looks like and for patiently answering my questions and offering insightful advice about physics  
455 and life.

456 Getting through graduate school would not have been possible without the support and friendship of  
457 the other students in our group. Thanks to Emma Tolley for geeking out with me about cool comput-  
458 ing stuff, going to taste delicious beers with me, and helping start the Palfrey tradition of Taco Tuesdays.  
459 Thanks to Brian Clark for being a great friend and housing companion both in Kirkland House and in our  
460 tiny summer apartment in Geneva (and thanks to his partner Allison Goff for the same reasons!). Thanks  
461 to Siyuan Sun for giving me my first aikido lesson and always being there for great conversations, big and  
462 small. Tony (Baojia) Tong deserves special recognition for working with me on the  $4b$  analysis and putting  
463 up with my sometimes strange requests (and giving me rides to the Val Thoiry Migros so I wouldn't have  
464 to pay exorbitant Geneva grocery prices!). Stephen Chan is probably the only student in the group who  
465 both understands my references to the Sopranos and makes some of his own. To the younger graduate  
466 students - Karri Di Petrillo, Jennifer Roloff, Julia Gonski, and Ann Wang - I want to say thank you for  
467 making the group a fun and lively place to be and giving all of us energy that the older graduate students  
468 like myself can sometimes lack.

469 I'd like to thank Annie Wei and Gray Putnam, the two undergraduates I have worked with as a graduate  
470 student. Their unbelievable intuition and quickness in picking up difficult particle physics concepts is  
471 inspiring.

472 I would also like to thank all of the postdocs that I have interacted with in my time in the Harvard group:  
473 Kevin Black, Alberto Belloni (who would always ask me “Do you have it?”...I can now say that I do!),  
474 Shulamit Moed, Corrinne Mills, Geraldine Conti, David Lopez Mateos, Chris Rogan, Valerio Ippolito,  
475 and Stefano Zambito.

476 There are many people on ATLAS who have helped me get to this point as well. In the *WW* group, I  
477 have to thank Jonathan Long, Joana Machado Miguens, Ben Cerio, Philip Chang, Bonnie Chow, Richard  
478 Polifka, Heberth Torres, Tae Min Hong, and Jennifer Hsu for being wonderful colleagues and making the  
479 entire analysis run smoothly. In the *4b* group, I have to thank Qi Zeng, Tony Tong, Alex Tuna, Michael  
480 Kagan, Max Bellomo, John Alison, and Patrick Bryant.

481 Kirkland House was my home for the last three years of graduate school and was an wonderful envi-  
482 ronment and support system. I want to thank my fellow tutors, especially Brian Clark and Allison Goff  
483 (again), Zach Abel, Kelly Bodwin, Alex Lupsasca, John and Pam Park, Luke and Erin Walczewski, and  
484 Philip Gant for their friendship and support. I also want to thank Kate Drizos Cavell, Bob Butler, and the  
485 Faculty Deans Tom and Verena Conley.

486 There are still a few friends that haven’t been covered yet and deserve great thanks. Jake Connors and  
487 Meredith MacGregor have been absolutely wonderful friends and I thank them in particular for the many  
488 home-cooked meals and great conversations we’ve had in their apartment. Nihar Shah has been my friend  
489 and confidant since we were both wee freshmen in Harvard Yard. Gareth Kafka, though he sits on the  
490 “neutrino” side of Palfrey House, has made days there more fun and has also been an enthusiastic partici-  
491 pant in the Palfrey Taco Tuesdays.

492 Being at Harvard necessarily means having to navigate through bureaucracy at some point or another.  
493 I thank Lisa Cacciabuado, Carol Davis, Jacob Barandes, Korin Watras, and Angela Allen for always having  
494 open doors and being the most kind, helpful people in the Physics department.

495 I thank Venky Narayananuriti for putting on a great SPU course that I was proud to be a part of and  
496 TF for. I’d also like to thank Jim Waldo for offering me much advice about working in Computer Science  
497 and giving me a fun data project to be a part of in my free time.

498 I grew up in a very tight knit Serbian community on the south side of Chicago which helped make me

499 the person I am today. I would like to thank all of the people at St. Simeon Mirotochivi Serbian Orthodox  
500 Church who have always been sources of enthusiasm and support in my life.

501 I would not be here without the unconditional love and constant support and encouragement of my  
502 family. To my pokojni Deda Branko and Miloje, my pokojni Baba Milka, and my Baba Desa, I want to  
503 say thank you for instilling in me at an early age the love of curiosity and storytelling that I have carried  
504 throughout my life. To my sister Angelina, I want to say thank you for always loving me and being my  
505 partner in crime throughout our childhoods. To my parents, Miroljub and Nada, Tata and Mama, I really  
506 cannot express how grateful I am to you and how much I owe you. As I look back now I see how I am  
507 a combination of both of your best qualities. Every day I am in situations where I better understand the  
508 lessons you taught me and the sacrifices you made to make sure I got the best possible education. I love  
509 you all.

510 Finally, I have to thank my soul mate, the one person in my life who understands me more than anyone  
511 else, my fiancée Kelly Brock. You are my sounding board, my support system, my cheerleader (figuratively  
512 and literally!), my best friend, my role model, and my everything. I would not have gotten through grad-  
513 uate school without you and my life would not be the same without you. I cannot wait to start our new  
514 lives together as the married doctors, tackling whatever comes our way with the same zeal with which we  
515 tackled graduate school. I love you with all my heart and soul.

# 0

516

517

## Introduction

518 The Higgs boson is often described as one of the cornerstones of particle physics. When the Standard  
519 Model was first developed as a theory to describe the fundamental particles and forces of nature, physicists  
520 were faced with a dilemma. The electroweak theory beautifully characterized both electromagnetism and  
521 the weak force with a single underlying framework. However, the mass of the weak  $W$  and  $Z$  bosons  
522 was puzzling given the fact that their electromagnetic counterpart, the photon, is massless. The Higgs  
523 mechanism was developed as the leading theory for the origin of this electroweak symmetry breaking. It  
524 predicted the existence of an additional spin-0 boson in the Standard Model, the Higgs boson. Generations  
525 of collider experiments searched for this elusive particle. This dissertation presents research work on the  
526 Higgs boson from its discovery to its use as a tool in the search for physics beyond the Standard Model  
527 with the ATLAS detector at the Large Hadron Collider (LHC).

528 One of the first priorities for the LHC when it began colliding proton beams in 2010 was the search  
529 for the Higgs boson. This search was initially tackled in the  $H \rightarrow WW^* \rightarrow \ell\nu\ell\nu$  channel, followed by

530 the  $H \rightarrow \gamma\gamma$  and  $H \rightarrow ZZ^* \rightarrow 4\ell$  channels. Each channel has its own merits, but the  $WW^*$  mode is  
531 particularly suited to searching over a wide range of masses. The  $H \rightarrow WW^*$  branching ratio is large and it  
532 is the primary decay channel above the  $2m_W$  mass threshold. Despite the fact that the full Higgs invariant  
533 mass cannot be reconstructed in the  $H \rightarrow WW^* \rightarrow \ell\nu\ell\nu$  channel, its signal to background ratio makes  
534 it ideal for measurement of Higgs properties such as the production cross section and couplings.

535 In 2012, the ATLAS and CMS experiments announced the discovery of a new particle consistent with  
536 the Higgs boson [1, 2]. In ATLAS, this discovery was made with  $4.8 \text{ fb}^{-1}$  collected at  $\sqrt{s} = 7 \text{ TeV}$   
537 and  $5.8 \text{ fb}^{-1}$  at  $\sqrt{s} = 8 \text{ TeV}$ . This dissertation first presents the search for gluon fusion production  
538 of the Higgs in the  $H \rightarrow WW^* \rightarrow \ell\nu\ell\nu$  channel, which played an important role in this discovery.  
539 Selection requirements which were optimized to maximize the discovery significance in this channel, as  
540 well as background estimation procedures, are discussed.

541 After its discovery, interest in the Higgs shifted to focus on the measurement of its properties. As a result,  
542 extensions of the initial discovery analysis in larger datasets had two main goals. Improvement of signal  
543 to background ratio was important to allow for precision measurements. Also, searches for production  
544 modes of the Higgs with lower cross sections than gluon fusion were a priority. The first such extension  
545 presented in this dissertation is a tailored selection for  $\ell\nu\ell\nu$  final states with same flavor leptons. Novel  
546 variables for the reduction of the  $Z+\text{jets}$  background that could remain robust under increasing LHC  
547 instantaneous luminosities are shown. The second post-discovery result shown is the first evidence of  
548 Vector Boson Fusion (VBF) production of the Higgs boson.

549 VBF production of the Higgs boson is particularly interesting in the  $H \rightarrow WW^* \rightarrow \ell\nu\ell\nu$  final state.  
550 In this combination of production and decay modes, the Higgs boson couples exclusively to vector bosons,  
551 allowing for precise measurement of the Higgs- $W$  coupling constant. However, it is challenging to observe  
552 VBF Higgs production because its cross section at the LHC is an order of magnitude lower than gluon  
553 fusion production. The large  $H \rightarrow WW^*$  branching ratio thus presents another advantage over other  
554 final states. Additionally, VBF production of the Higgs boson creates two forward jets in addition to the  
555 Higgs, and these jets can be used to isolate VBF Higgs events from other production modes. The VBF  
556  $H \rightarrow WW^* \rightarrow \ell\nu\ell\nu$  analysis first created a selection requirement based signal region using variables

constructed specifically for the VBF Higgs production topology. This “cut-based” analysis is presented in detail in this dissertation. These VBF topology variables, once validated in the cut-based analysis, were then input into a multivariate boosted decision tree discriminant to achieve the first evidence of VBF Higgs production with the full  $20.3 \text{ fb}^{-1}$  of  $\sqrt{s} = 8 \text{ TeV}$  data in ATLAS. Additionally, combining these results with the dedicated gluon fusion Higgs production analysis allowed for precise measurement of the Higgs couplings.

After a two year shutdown, the LHC restarted in 2015 with a center of mass energy of  $\sqrt{s} = 13 \text{ TeV}$ . This increase improved the LHC’s ability to probe for physics beyond the Standard Model, and the Higgs sector remained one of the largest regions of unprobed phase space where such new physics could be discovered. Production of high mass resonances benefit most from the center of mass energy increase. In particular, the cross section for a generic gluon-initiated  $2 \text{ TeV}$  resonance increased tenfold with the increase from  $8$  to  $13 \text{ TeV}$ . Therefore, a natural next step in studies of the Higgs was a search for a new heavy resonance which decays into a pair of Higgs bosons. The final result shown in this dissertation is a search for resonant di-Higgs production in the  $X \rightarrow HH \rightarrow b\bar{b}b\bar{b}$  final state with  $3.2 \text{ fb}^{-1}$  recorded by ATLAS at  $\sqrt{s} = 13 \text{ TeV}$ . This search has the unique advantage that it can both probe new physics and gain further understanding of the Higgs potential through constraints on SM pair production of the Higgs. It also extends the previous ATLAS results at  $\sqrt{s} = 8 \text{ TeV}$  and probes higher mass resonances that were not previously accessible. Additionally, it is an informative precursor to di-Higgs analyses at the future High Luminosity LHC (HL-LHC), where a projected dataset of  $3000 \text{ fb}^{-1}$  at  $\sqrt{s} = 14 \text{ TeV}$  will begin to become sensitive to the SM Higgs self coupling.

As mentioned above, this dissertation begins by discussing the discovery of the Higgs and the role of the  $H \rightarrow WW^* \rightarrow \ell\nu\ell\nu$  channel. It then presents the first evidence for the VBF production mode using the  $H \rightarrow WW^* \rightarrow \ell\nu\ell\nu$  channel with the full ATLAS Run 1 dataset. It also shows the final combined Run 1 measurements of gluon fusion Higgs production from this channel. Finally, it presents a search for Higgs pair production in the  $HH \rightarrow b\bar{b}b\bar{b}$  channel. It is organized into four parts.

Part 1 presents the theoretical and experimental background required for the subsequent parts. Chapter 1 gives an overview of Higgs physics, particularly single and double Higgs production in the Standard

584 Model and beyond. Chapter 2 presents details regarding the Large Hadron Collider and the ATLAS experi-  
585 ment. The evolution of machine conditions, descriptions of the ATLAS sub-detectors, and an overview of  
586 object reconstruction in ATLAS are all shown. A brief interlude on the ATLAS Muon New Small Wheel  
587 upgrade is also given, as this upgrade has been a focus of my graduate work and will have an important  
588 impact on ATLAS' ability to study the Higgs at the High Luminosity LHC.

589 Part 2 discusses the observation and measurement of the Higgs in the  $H \rightarrow WW^* \rightarrow \ell\nu\ell\nu$  channel  
590 in the ATLAS Run 1 dataset at  $\sqrt{s} = 7$  and 8 TeV. Because I worked in this channel from before the  
591 discovery through to the final analysis of the Run 1 dataset, Part 2 is organized in such a way to allow  
592 easy presentation of multiple analyses on different subsets of the full Run 1 dataset. Chapter 3 presents  
593 a general overview of the  $H \rightarrow WW^*$  analysis strategy and defines many of the variables and common  
594 elements used in the rest of Part 2. Chapter 4 presents the discovery and subsequent measurements of  
595 the Higgs boson, focusing on the role of the  $WW^*$  channel in this discovery. Chapter 5 presents the  
596 first evidence for the VBF production mode of the Higgs, a result from the  $WW^*$  channel in the full  
597 Run 1 ATLAS dataset. In this chapter, the focus is mainly on the cut-based VBF analysis. The cut-based  
598 analysis was an important first step to the final VBF result which used a boosted decision tree. Where  
599 appropriate, connections between the cut-based and BDT analyses are shown and their compatibility is  
600 discussed. Finally, the VBF analysis was an important input into the combined Run 1  $H \rightarrow WW^* \rightarrow$   
601  $\ell\nu\ell\nu$  result, which used both the gluon fusion and VBF channels in a combined fit to infer properties of  
602 the Higgs, including its couplings to the gauge bosons and its production cross section. This is the topic  
603 of Chapter 6.

604 Part 3 presents a search for Higgs pair production in the  $HH \rightarrow b\bar{b}b\bar{b}$  channel. Chapter 7 presents  
605 an overview of this search in the boosted regime, where the Higgs pairs are the result of the decay of a  
606 heavy resonance. Chapter 8 shows the combined results between the boosted regime and the resolved  
607 regime, which is sensitive to lower mass resonances and non-resonant Higgs pair production. Finally, Part  
608 4 presents a conclusion and brief outlook of future Higgs physics with ATLAS.

609

## Part I

610

### Theoretical and Experimental Background

*In modern physics, there is no such thing as “nothing.”*

Richard Morris

# 1

611

612

## The Physics of the Higgs Boson

613 This chapter presents an overview of the Standard Model of Particle Physics and in particular the physics  
614 of the Higgs boson. First, a brief overview of the Standard Model is presented. Then, a description of  
615 the Higgs mechanism of electroweak symmetry breaking is given. Next, the physics of single Higgs boson  
616 production and decay is described. The Standard Model also allows for production of two Higgs bosons  
617 and this is detailed as well. Finally, di-Higgs production in two beyond the Standard Model (BSM) theories  
618 - Randall-Sundrum gravitons (RSG) and Two Higgs Doublet Models (2HDM) - is shown.

### 619 I.I THE STANDARD MODEL OF PARTICLE PHYSICS

620 The Standard Model (SM) of Particle Physics is a quantum field theory describing the fundamental parti-  
621 cles of nature and the forces that govern their interactions. Several comprehensive pedagogical treatments  
622 of the SM already exist in the literature [3–8] and this section will not rehash those. Rather, this section  
623 presents a brief overview of the SM particles and forces in order to define them for subsequent discussions.

624 The Standard Model consists of two primary categories of fundamental particles: fermions (spin 1/2  
 625 particles) and bosons (integer spin particles). The SM also describes three forces: electromagnetism, the  
 626 weak nuclear force, and the strong nuclear force. Gravity is not included in the theory and is largely irrel-  
 627 evant at the scales currently probed by collider experiments. Within the fermions, there are both quarks  
 628 (which interact via all three forces) and leptons. The charged leptons interact via electromagnetic and weak  
 629 interactions, while neutrinos (neutral leptons) interact only via the weak force. Within the bosons, there  
 630 are the  $W^\pm$  and  $Z$  bosons (the mediators of the weak force), the gluon ( $g$ , the mediator of the strong  
 631 force), and the photon ( $\gamma$ , the mediator of the electromagnetic force). Finally, there is the Higgs boson,  
 632 a fundamental spin zero particle resulting from the Higgs mechanism of electroweak symmetry breaking.

633 Figure 1.1 summarizes the fermions and bosons of the SM.

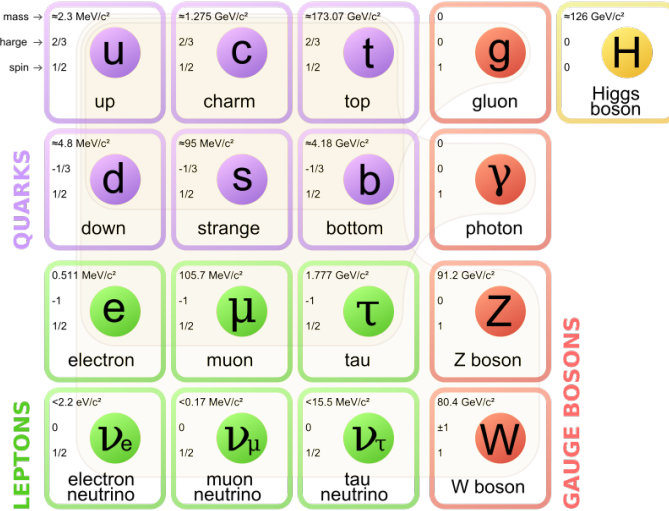


Figure 1.1: The particles of the Standard Model and their properties [6].

634 The Standard Model coalesced into a unified theoretical framework in the 1960s through the work  
 635 of Glashow, Weinberg, Salam, and others on the theory of electroweak interactions [9–12]. This theory  
 636 characterized both the electromagnetic and weak interactions as unified under a single gauge symmetry  
 637 group, namely  $SU(2) \times U(1)$ . At low enough energy scales (on the order of the  $W$  and  $Z$  masses), the  
 638 electroweak symmetry is broken, as evidenced by the fact that the weak bosons have mass while the photon  
 639 does not. The discovery of the Higgs boson in 2012 confirmed the Higgs mechanism as the most likely  
 640 candidate for this electroweak symmetry breaking [1, 2]. The complete SM consists of this electroweak

641 theory combined with the theory of quantum chromodynamics (which models the strong sector as a non-  
642 Abelian  $SU(3)$  gauge group)<sup>1</sup>.

643 **I.2 ELECTROWEAK SYMMETRY BREAKING AND THE HIGGS**

644 In the Standard Model Lagrangian, it is difficult to include mass terms for the  $W$  and  $Z$  bosons without  
645 breaking the fundamental gauge symmetry of the Lagrangian. A traditional mass term does not preserve  
646 the  $SU(2) \times U(1)$  symmetry. Additionally, scattering of massive  $W$  and  $Z$  bosons violate unitarity and  
647 these diagrams diverge at high energy scales. In the 1960s, Higgs, Brout, Englert, Guralnik, Kibble, and  
648 Hagen developed a mechanism for spontaneous symmetry breaking via the addition of a complex scalar  
649 doublet to the SM. Three of the four real degrees of freedom of this complex field would go to the lon-  
650 gitudinal modes of the  $W^\pm$  and  $Z$ , thus allowing them to have mass [14–17]. The remaining degree of  
651 freedom would manifest as an additional scalar, known now as the Higgs boson.

652 The mechanism works by introducing a Lagrangian for the newly introduced field that still respects the  
653 symmetry of the Standard Model inherently, but with a minimum at a non-zero vacuum expectation value  
654 for the field. In this minimum of the potential, the electroweak symmetry is broken. Specifically, consider  
655 a complex scalar doublet  $\Phi$  with four degrees of freedom, as shown in equation I.1.

$$\Phi = \begin{pmatrix} \phi^+ \\ \phi^0 \end{pmatrix} = \frac{1}{\sqrt{2}} \begin{pmatrix} \phi_1^+ + i\phi_2^+ \\ \phi_1^0 + i\phi_2^0 \end{pmatrix} \quad (\text{I.1})$$

656 The simplest potential of a self-interacting Higgs that still respects the SM symmetry is given in equa-  
657 tion I.2.

$$V(\Phi) = \mu^2 \Phi^\dagger \Phi + \lambda (\Phi^\dagger \Phi)^2 \quad (\text{I.2})$$

658 If the  $\mu^2$  term of this potential is positive, then the potential has a minimum at  $\Phi = 0$  and the electroweak

---

<sup>1</sup>For a pedagogical treatment of the physics of quantum chromodynamics, see reference [13].

<sup>659</sup> symmetry is preserved. However, if instead  $\mu^2 < 0$ , then the minimum is at a finite value of  $\Phi$ , namely

$$\Phi_{\min} = \frac{1}{\sqrt{2}} \begin{pmatrix} 0 \\ v \end{pmatrix} \quad (1.3)$$

<sup>660</sup> where  $v = \sqrt{\mu^2/\lambda}$ . Because this is the location of the minimum, it corresponds to the vacuum expecta-  
<sup>661</sup> tion value for the field ( $\langle \Phi \rangle = \Phi_{\min}$ ). The excitations of the Higgs can then be parameterized as

$$\Phi = \frac{1}{\sqrt{2}} \begin{pmatrix} 0 \\ v + H \end{pmatrix} \quad (1.4)$$

<sup>662</sup> The full scalar Lagrangian, including the kinetic term, is then given as

$$\mathcal{L}_s = (D^\mu \Phi)^\dagger (D_\mu \Phi) - V(\Phi) \quad (1.5)$$

<sup>663</sup> where the covariant derivative is defined as

$$D_\mu = \partial_\mu + \frac{ig}{2} \tau^a W_\mu^a + ig' Y B_\mu \quad (1.6)$$

<sup>664</sup> and  $W^1, W^2, W^3$  and  $B$  are the  $SU(2)$  and  $U(1)$  gauge fields of the electroweak theory, respectively.  $g$   
<sup>665</sup> and  $g'$  are the corresponding coupling constants. The Pauli matrices are represented with  $\tau$ . With the  
<sup>666</sup> scalar Lagrangian in place, the physical gauge fields can then be written as

$$W_\mu^\pm = \frac{1}{\sqrt{2}} (W_\mu^1 \mp i W_\mu^2) \quad (1.7)$$

<sup>667</sup>

$$Z_\mu = \frac{-g' B_\mu + g W_\mu^3}{\sqrt{g^2 + g'^2}} \quad (1.8)$$

<sup>668</sup>

$$A_\mu = \frac{g B_\mu + g' W_\mu^3}{\sqrt{g^2 + g'^2}} \quad (1.9)$$

<sup>669</sup> Equation 1.7 corresponds to the charged  $W^+$  and  $W^-$  bosons, equation 1.8 corresponds to the neutral  $Z$   
<sup>670</sup> boson, and equation 1.9 corresponds to the neutral photon. The masses of the particles also arise from the  
<sup>671</sup> Lagrangian. The photon has zero mass, while the masses of the  $W$  and  $Z$  bosons are given in equation 1.10.

<sup>672</sup>

$$\begin{aligned} M_W^2 &= \frac{1}{4}g^2v^2 \\ M_Z^2 &= \frac{1}{4}(g^2 + g'^2)v^2 \end{aligned} \quad (1.10)$$

<sup>673</sup> The fermion masses also arise through a coupling with the Higgs via the Yukawa interaction (for a detailed  
<sup>674</sup> description, see [8]). In this case the coupling between the Higgs and the fermions goes as

$$g_{h\bar{f}\bar{f}} = \frac{m_f}{v} \quad (1.11)$$

<sup>675</sup> The full Lagrangian of Higgs interactions can be written as

$$\mathcal{L}_{\text{Higgs}} = -g_{h\bar{f}\bar{f}}\bar{f}fh + \frac{g_{hhh}}{6}h^3 + \frac{g_{hhhh}}{24}h^4 + \delta_V V_\mu V^\mu \left( g_{hVV}H + \frac{g_{hhVV}}{2}h^2 \right) \quad (1.12)$$

<sup>676</sup> with

$$\begin{aligned} g_{hVV} &= \frac{2m_V^2}{v} & g_{hhVV} &= \frac{2m_V^2}{v^2} \\ g_{hhh} &= \frac{3m_h^2}{v} & g_{hhHH} &= \frac{3m_h^2}{v^2} \end{aligned} \quad (1.13)$$

<sup>677</sup> The last term of the Lagrangian appears twice, once for  $W$  bosons and once for  $Z$  bosons.  $V$  refers to  
<sup>678</sup> the  $W^\pm$  and  $Z$ , and  $\delta_W = 1$  while  $\delta_Z = 1/2$ . Phenomenologically, there are a few features of this  
<sup>679</sup> Lagrangian that are useful to note. First, note that the Higgs mass is a free parameter of the theory that  
<sup>680</sup> must be determined experimentally. Second, note that the coupling of the Higgs to the vector bosons and  
<sup>681</sup> fermions scales as a function of the masses of these particles, a fact that is important when considering  
<sup>682</sup> both the production and decays of the Higgs. Finally, note the presence of the cubic and quartic Higgs self  
<sup>683</sup> interaction terms, which can lead to final states with multiple Higgs bosons produced.

684 1.3 HIGGS BOSON PRODUCTION AND DECAY

685 This section discusses the properties of Higgs production and decay mechanisms. The details presented  
686 here will focus on the properties of a 125 GeV Higgs boson, as this is the mass closest to that of the newly  
687 discovered Higgs.

688 1.3.1 HIGGS PRODUCTION

689 The Higgs is produced by four main production modes at the Large Hadron Collider - gluon-gluon fusion  
690 ( $ggF$ ), vector boson fusion (VBF), associated production with a  $W$  or  $Z$  boson, or associated production  
691 with top quarks ( $t\bar{t}H$ ). Figure 1.2 shows the Feynman diagrams for these four modes.

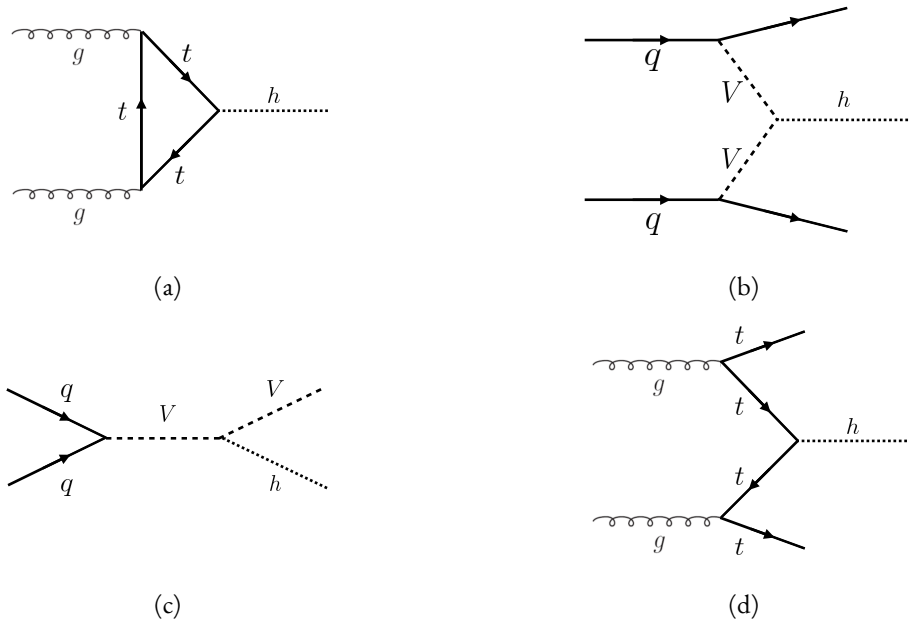


Figure 1.2: The four most common Higgs boson production modes at the LHC: (a) gluon-gluon fusion, (b) vector boson fusion, (c)  $W/Z + H$  production, (d)  $t\bar{t}H$  production

692 In gluon-gluon fusion, gluons from the incoming protons fuse via a top-quark loop to produce a Higgs.  
693 The top quark is the dominant contribution in the loop due to its heavy mass and the fact that the Higgs-  
694 fermion coupling constant scales with fermion mass. In vector boson fusion, the incoming quarks each  
695 radiate a  $W$  or  $Z$  boson which fuse to produce the Higgs. This production mode results in a final state  
696 with a Higgs boson and two additional jets which tend to be forward because they carry the longitudinal

697 momentum of the incoming partons. The Higgs can also be produced in association with a  $W$  or  $Z$  boson.  
 698 The  $W/Z$  is produced normally and then radiates a Higgs<sup>2</sup>. Finally, the Higgs can be produced in asso-  
 699 ciation with two top quarks. Each incoming gluon splits into a  $t\bar{t}$  pair, and one of the top pairs combines to  
 700 create a Higgs. Figure 1.3 shows the production cross section for a 125 GeV Higgs boson in each of these  
 modes at a  $pp$  collider as a function of center of mass energy. In figure 1.3, note that gluon fusion has the

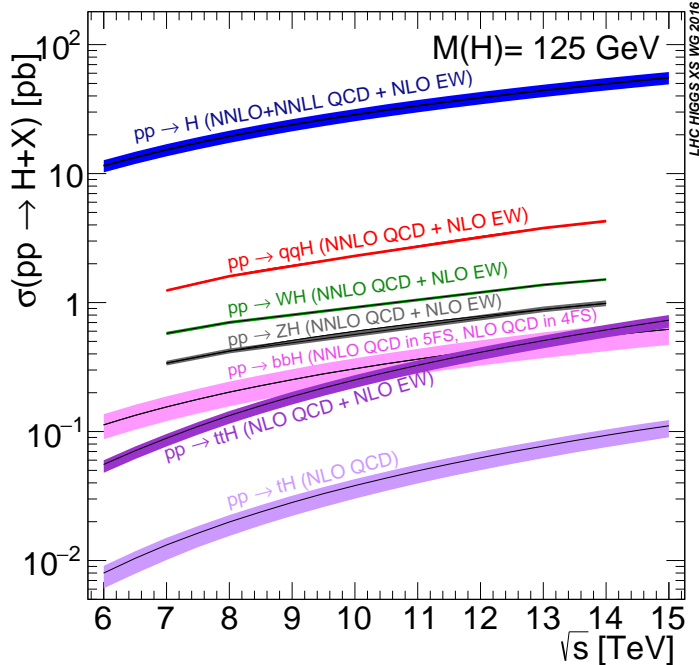


Figure 1.3: Higgs production cross sections as a function of center of mass energy ( $\sqrt{s}$ ) at a  $pp$  collider [18].

701  
 702 largest cross section, while VBF is the second largest at approximately a factor of 10 smaller. The figure also  
 703 includes the less commonly studied  $b\bar{b}H$  and  $tH$  modes. While the  $b\bar{b}H$  mode has a larger cross section  
 704 than  $t\bar{t}H$ , it also has larger backgrounds and is thus less sensitive. The  $tH$  mode is not as sensitive as  $t\bar{t}H$   
 705 due to its lower cross section. At  $\sqrt{s} = 8$  TeV, ggF production of a 125 GeV Higgs has a cross section  
 706 of  $19.47^{+1.54}_{-1.67}$  pb, while VBF has a cross section of  $1.601^{+0.036}_{-0.035}$  pb [18]. Both the gluon fusion and vector  
 707 boson fusion cross sections have been computed to next-to-next-to-leading order (NNLO) in the QCD  
 708 couplings and next-to-leading order in the electroweak couplings [19–26]. The gluon fusion cross section  
 709 also includes next-to-next-to-leading logarithm (NNLL) resummation [27]. The cross sections of all of

---

<sup>2</sup>This mode is also sometimes known as “Higgs-strahlung”.

710 the main Higgs production modes at this center of mass energy, as well as their uncertainties from varying  
 711 the QCD renormalization and factorization scales and PDFs, are summarized in table 1.1 for a 125 GeV  
 712 Higgs. The relative uncertainty of the gluon fusion mode is larger than the relative uncertainty in the  
 713 vector boson fusion mode due to the fact that gluon fusion production happens through a loop.

Production mode	$\sigma$ (pb)	QCD scale uncert. (%)	PDF + $\alpha_s$ uncert. (%)
Gluon fusion	19.47	+7.3 / - 8.0	3.1
Vector boson fusion	1.601	+0.3 / - 0.2	2.2
$WH$	0.7026	+0.6 / - 0.9	2.0
$ZH$	0.4208	+2.9 / - 2.4	1.7
$b\bar{b}H$	0.2021	+20.7 / - 22.3	
$t\bar{t}H$	0.1330	+4.1 / - 9.2	4.3
$tH$ ( $t$ -channel)	0.01869	+7.3 / - 16.5	4.6
$tH$ ( $s$ -channel)	$1.214 \times 10^{-3}$	+2.8 / - 2.4	2.8

Table 1.1: Production cross sections for a 125 GeV Higgs boson at  $\sqrt{s} = 8$  TeV with scale and PDF uncertainties [18].

### 714 1.3.2 HIGGS BRANCHING RATIOS

715 The fact that the Higgs couples more strongly to more massive particles is crucial for understanding its  
 716 branching ratios. The width for Higgs decays to fermions is given by equation 1.14 [5].

$$\Gamma(H \rightarrow f\bar{f}) = \frac{N_c \sqrt{2} G_F m_f^2 m_H}{8\pi} \quad (1.14)$$

717 In this case,  $N_c$  is the number of colors,  $G_F$  is the Fermi constant,  $m_f$  is the mass of the fermion, and  
 718  $m_H$  is the mass of the Higgs. Note that the width scales with the square of the fermion mass. (This also  
 719 assumes that the Higgs mass is large enough to decay with both the fermions on shell.)

720 The decay width to  $WW$ , in the case where both  $W$  bosons are produced on shell ( $m_H \geq 2m_W$ ), is  
 721 given in equation 1.15 [5].

$$\Gamma(H \rightarrow W^+ W^-) = \frac{\sqrt{2} G_F M_W^2 m_H}{16\pi} \frac{\sqrt{1-x_W}}{x_W} (3x_W^2 - 4x_W + 4) \quad (1.15)$$

722 where  $m_W$  is the mass of the  $W$  and  $x_W = 4M_W^2/m_H^2$ . To get the branching ratio to  $ZZ$  (in the regime  
 723 where  $m_H \geq 2m_Z$ ), the equation is divided by 2 to account for identical particles in the final state, and  
 724  $x_W$  is replaced with  $x_Z = 4M_Z^2/m_H^2$ . This is shown in equation 1.16 [5].

$$\Gamma(H \rightarrow ZZ) = \frac{\sqrt{2}G_F M_Z^2 m_H}{32\pi} \frac{\sqrt{1-x_Z}}{x_Z} (3x_Z^2 - 4x_Z + 4) \quad (1.16)$$

725 The more general formula for Higgs branching into  $WW$  or  $ZZ$ , taking into account the case where one  
 726 or both vector bosons is off-shell, is shown in equation 1.17 [28].

$$\Gamma(H \rightarrow V^*V^*) = \frac{1}{\pi^2} \int_0^{M_H^2} \frac{dq_1^2 M_V \Gamma_V}{(q_1^2 - M_V^2)^2 + M_V^2 \Gamma_V^2} \int_0^{(M_H - q_1)^2} \frac{dq_2^2 M_V \Gamma_V}{(q_2^2 - M_V^2)^2 + M_V^2 \Gamma_V^2} \Gamma_0 \quad (1.17)$$

727 Here,  $q_1^2$  and  $q_2^2$  are the invariant masses of the virtual gauge bosons,  $M_V$  is the  $W$  or  $Z$  mass, and  $\Gamma_V$  is  
 728 the  $W$  or  $Z$  width.  $\Gamma_0$  is the squared matrix element, which is given in equation 1.18 [28].

$$\Gamma_0 = \frac{G_F M_H^3}{8\sqrt{2}\pi} \delta_V \sqrt{\lambda(q_1^2, q_2^2, M_H^2)} \left[ \lambda(q_1^2, q_2^2, M_H^2) + \frac{12q_1^2 q_2^2}{M_H^4} \right] \quad (1.18)$$

729 The function  $\lambda$  is defined as  $\lambda(x, y, z) = (1 - x/z - y/z)^2 - 4xy/z^2$ . The integral in the general  
 730 off-shell boson case is much more difficult to interpret than the simpler on-shell branching ratios, but it  
 731 can be evaluated numerically. These branching ratio formulas can also be visualized as a function of Higgs  
 732 mass, as shown in figure 1.4. There are a few interesting features to note in this figure. First, note that at  
 733 high Higgs masses, once on-shell production of both  $W$  and  $Z$  bosons is possible, these two decays are  
 734 dominant due to the large masses of the  $W/Z$ . Also note that the branching ratio to  $W$ s is twice that of  
 735  $Z$ s at these large masses due to the fact that there are two charged  $W$  bosons ( $W^\pm$ ) and only one  $Z$  boson<sup>3</sup>.  
 736 At 125 GeV, the Higgs is accessible through many different decay modes. The largest branching ratio is  
 737 the decay  $H \rightarrow b\bar{b}$  at 58.24% [18]. This branching is larger than the  $WW/ZZ$  decays because one of  
 738 the two bosons must be produced off-shell for  $m_h = 125$  GeV. The second largest branching ratio is  
 739 to  $WW^*$  at 21.37 % (before taking into account the branching ratios of the  $W$ ). Table 1.2 summarizes

---

<sup>3</sup>In the Higgs Lagrangian, this extra symmetry factor is quantified by the  $\delta_V$  noted in equation 1.12.

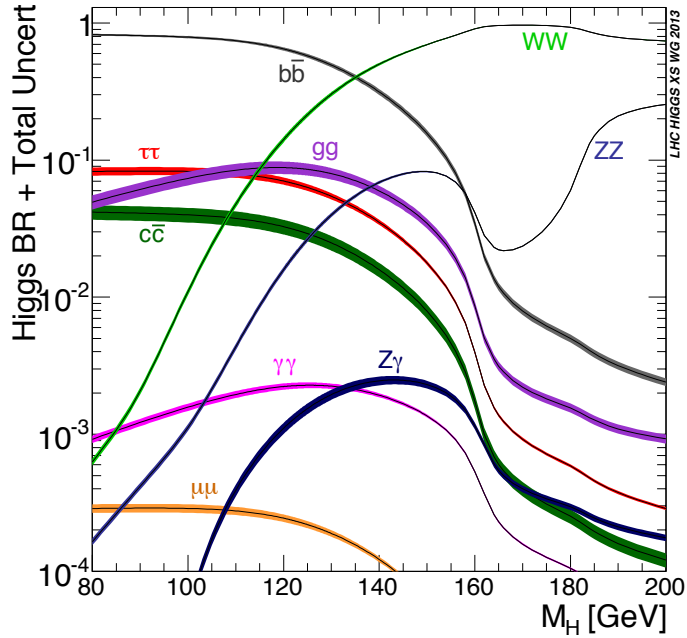


Figure 1.4: Higgs boson branching ratios as a function of  $m_H$  [18].

<sup>740</sup> the theoretical branching ratios for a Higgs with a mass of 125 GeV. Note that there is a Higgs branching  
<sup>741</sup> ratio to  $\gamma\gamma$  even though photons are massless. This decay happens through a loop, which suppresses the  
<sup>742</sup> branching ratio<sup>4</sup>.

Decay	Branching ratio (%)	Relative uncertainty (%)
$bb$	58.24	+0.25 / -0.25
$WW^*$	21.37	+0.99 / -0.99
$gg$	8.187	+3.40 / -3.41
$\tau\tau$	6.272	+1.17 / -1.16
$cc$	2.891	+1.20 / -1.20
$ZZ^*$	2.619	+0.99 / -0.99
$\gamma\gamma$	0.2270	+1.73 / -1.72
$Z\gamma$	0.1533	+5.71 / -5.71
$\mu\mu$	0.02176	+1.23 / -1.23

Table 1.2: Theoretical branching ratios for a 125 GeV Higgs boson, quoted as a percentage of the total width of the Higgs. Uncertainties shown are relative to the branching ratio value [18].

<sup>743</sup> Note that the branching ratios alone do not tell the full story of which Higgs channels are the most

---

<sup>4</sup>The largest contributions to the loop are the top quark and  $W$  boson.

744 sensitive. For example, the  $H \rightarrow b\bar{b}$  channel in gluon fusion production is incredibly difficult to observe  
 745 due to the large QCD dijet background at the LHC. However, in associated production of the Higgs,  
 746 where a  $W$  or  $Z$  gives additional final state particles that can be used to reduce background, a search for  
 747  $H \rightarrow b\bar{b}$  can be sensitive. The combinations of production and decay modes that are most commonly  
 748 studied at the LHC are summarized in table 1.3 [5].

Decay	Inclusive (incl. ggF)	VBF	$WH/ZH$	$t\bar{t}H$
$H \rightarrow \gamma\gamma$	✓	✓	✓	✓
$H \rightarrow b\bar{b}$			✓	✓
$H \rightarrow \tau^+\tau^-$		✓		
$H \rightarrow WW^* \rightarrow \ell\nu\ell\nu$	✓	✓	✓	
$H \rightarrow ZZ \rightarrow 4\ell$	✓			
$H \rightarrow Z\gamma \rightarrow \ell\ell\gamma$	very low			

Table 1.3: Possible channels for Higgs searches. Checkmarks denote the most sensitive production modes for each decay channel [5].

#### 749 1.4 HIGGS PAIR PRODUCTION IN THE STANDARD MODEL

750 The Standard Model also allows for processes that produce two Higgs bosons in the final state, known  
 751 as Higgs pair production or di-Higgs production. The two main production mechanisms are shown in  
 figure 1.5. The two diagrams in figure 1.5 interfere destructively with one another, resulting in a low overall

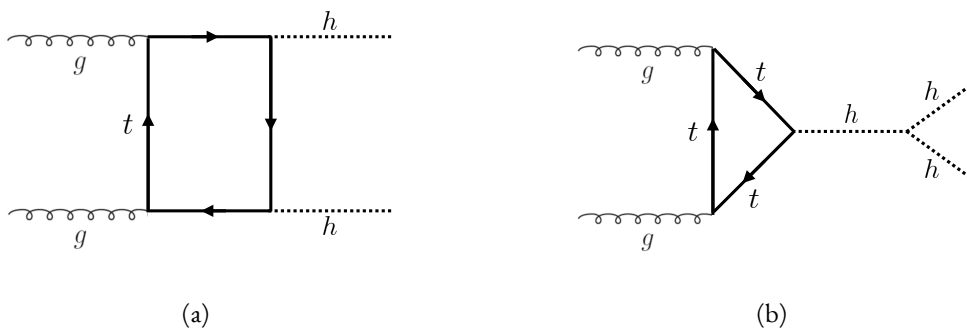


Figure 1.5: The two leading diagrams for Standard Model di-Higgs production at the LHC: (a) box diagram, (b) Higgs self coupling.

752  
 753 cross section for di-Higgs production at the LHC. Nevertheless, Higgs pair production is quite interesting

754 to study because it gives direct access to the  $\lambda$  parameter of the Higgs potential, also known as the Higgs  
755 self coupling. The diagram in figure 1.5(b) is sensitive to this coupling through the triple Higgs vertex.

756 One can substitute the gluon fusion production of diagram 1.5(b) with any of the other production  
757 modes previously discussed. These other modes do not suffer from interference with the box diagram in  
758 figure 1.5(a) due to the presence of additional particles in the final state. They still have a lower cross section  
759 than the gluon fusion mode, however. The cross sections for di-Higgs production in the different modes,  
760 as well as their uncertainties, are shown in table 1.4 [29]. These are shown for  $\sqrt{s} = 14$  TeV as this is the  
761 expected center of mass energy for the High Luminosity LHC and this energy is more sensitive to di-Higgs  
762 production. Note that the scale of cross section quoted is now in fb rather than pb.

Production mode	$\sigma$ (fb)	Total uncert. (%)
Gluon fusion	33.89	+37.2 / - 27.8
Vector boson fusion	2.01	+7.6 / - 5.1
$W H H$	0.57	+3.7 / - 3.3
$Z H H$	0.42	+7.0 / - 5.5
$t \bar{t} H$	1.02	-

Table 1.4: Production cross sections for pair production of a 125 GeV Higgs boson at  $\sqrt{s} = 14$  TeV with total uncertainty [29]. The uncertainties include QCD scale and PDF variations as well as uncertainties on  $\alpha_S$ .

762

## 763 1.5 HIGGS PAIR PRODUCTION IN THEORIES BEYOND THE STANDARD MODEL

764 The Higgs pair production cross section in the Standard Model is rather small, and datasets on the scale of  
765 the full  $3000 \text{ fb}^{-1}$  expected from the High Luminosity LHC will be required to obtain sensitive measure-  
766 ments of the Higgs self-coupling [29]. However, the discovery of the Higgs also gives particle physicists  
767 a new tool that can be exploited in the search for new physics beyond the Standard Model. In particular,  
768 Higgs pair production is a promising channel in the search for new physics. The cross section for di-Higgs  
769 production can be altered through both resonant and non-resonant production of Higgs pairs. In non-  
770 resonant production, di-Higgs production vertices can arise from the presence of a new strong sector and  
771 additional colored particles [30–32]. Figure 1.6 shows examples of the types of vertices that can arise. In  
772 the resonant case, new heavy particle can decay to Higgs pairs. Such new particles can include heavy Higgs

773 bosons arising in two Higgs doublet models (2HDM) or Higgs portal models as well as heavy gravitons in  
 774 Randall-Sundrum theories [30, 33–39]. Figure 1.7 shows a generic diagram for a heavy resonance decaying  
 775 to two Higgs bosons. In the 2HDM,  $X$  corresponds to the heavy CP-even scalar  $H$ . In the Randall-  
 Sundrum model,  $X$  corresponds to a heavy spin-2 graviton  $G_{KK}^*$ . The next sections provide more detail

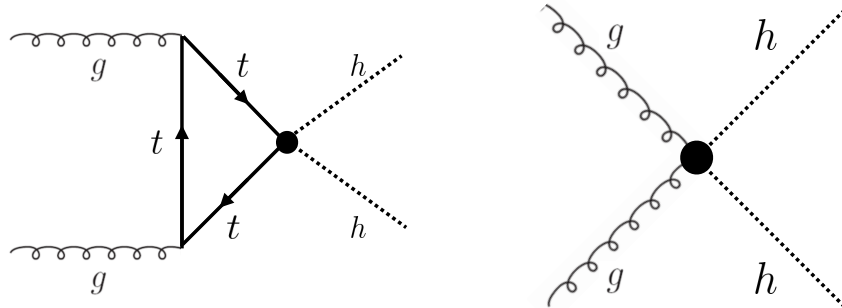


Figure 1.6: Diagrams with new vertices for non-resonant Higgs pair production arising in composite Higgs models.

776  
 777 on the phenomenology of resonant Higgs production in Randall-Sundrum and 2HDM models, as these  
 models will later be tested in a dedicated search for resonant production of boosted Higgs pairs.

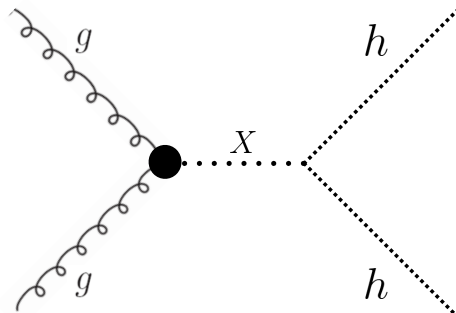


Figure 1.7: Generic Feynman diagram for resonant Higgs pair production in BSM theories.

778

### 779 1.5.1 RANDALL-SUNDRUM GRAVITONS

780 The Randall-Sundrum model is a proposed solution to the hierarchy problem that posits a five-dimensional  
 781 warped spacetime that contains two branes: one where the force of gravity is very strong and a second brane  
 782 at the TeV scale corresponding to the known Standard Model sector [33]. In the theory, the branes are

783 weakly coupled and the graviton probability function drops exponentially going from the gravity brane  
 784 to the SM brane, rendering gravity weak on the SM brane. The experimental consequence of this theory  
 785 is a tower of widely spaced (in mass) Kaluza-Klein graviton resonances. In theories where the fermions  
 786 are localized to the SM brane, production of gravitons from fermion pairs is suppressed and the primary  
 787 mode of production is gluon fusion [34]. These gravitons have a substantial branching fraction to Higgs  
 788 pairs, ranging from 6.43% for gravitons with a mass of 500 GeV to 7.66% at 3 TeV. Figure 1.8 shows the  
 789 branching ratios of the spin-2 Randall Sundrum graviton (RSG) as a function of its mass. The predomi-  
 790 nant decays are to  $t\bar{t}$  above the mass threshold for that channel.

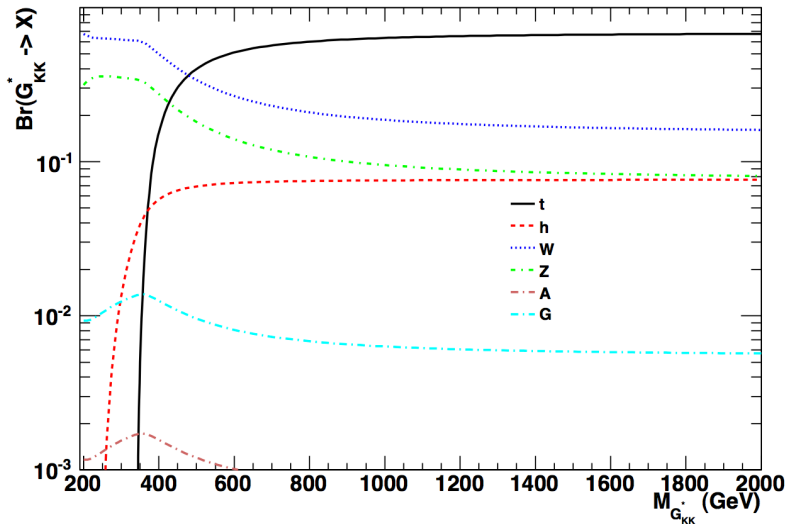


Figure 1.8: Branching ratios for a spin-2 Randall-Sundrum graviton as a function of mass computed in MadGraph with the CP3-Origins implementation [34, 40, 41].

791 Randall-Sundrum models have two free parameters - the mass of the graviton and a curvature parameter  
 792  $k$ . Typically, rather than  $k$ , the theory is parameterized using  $c \equiv k/\bar{M}_{\text{pl}}$ , where  $\bar{M}_{\text{pl}}$  is the reduced  
 793 Planck mass. The cross section for production of the RSG decreases as a function of mass and is strongly  
 794 dependent on the gluon PDF. The increase in center of mass energy from 8 to 13 TeV in LHC Run 2  
 795 greatly increases the cross section at higher mass. Figure 1.9 shows the cross section as a function of graviton  
 796 mass at  $\sqrt{s} = 13$  TeV for RSG models with  $c = 1.0$  and  $c = 2.0$ .

797 Another interesting feature of the theory is that the width of the graviton increases with both  $c$  and  
 798  $m_{G_{\text{KK}}^*}$ . Figure 1.10 shows the graviton width for both  $c = 1.0$  and  $c = 2.0$  as a function of mass. In

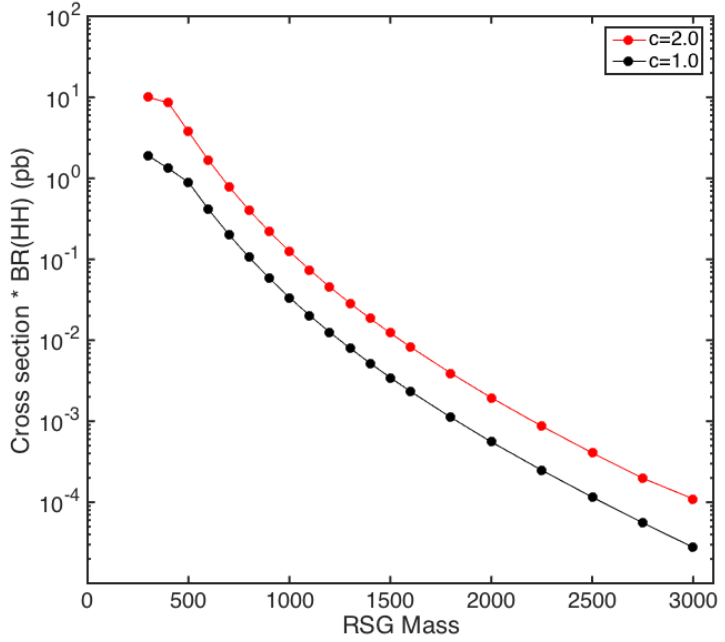


Figure 1.9:  $\sigma \times \text{BR}(HH)$  for Randall-Sundrum gravitons as a function of mass computed in MadGraph with the CP<sub>3</sub>-Origins implementation [34, 40, 41].

<sup>799</sup>  $c = 1.0$ , the width starts at 8.365 GeV for a mass of 300 GeV and increases to 187.2 GeV at a mass of  
<sup>800</sup> 3 TeV. Similarly, with  $c = 2.0$ , the width starts at 33.46 GeV for  $m_G = 300$  GeV and increases to  
<sup>801</sup> 748.8 GeV at a mass of 3 TeV.

### <sup>802</sup> 1.5.2 TWO HIGGS DOUBLET MODELS

<sup>803</sup> In Two Higgs Doublet Models (2HDM), a second complex scalar doublet is added to the Standard Model [36–  
<sup>804</sup> 38]. In this case, all four degrees of freedom in the second doublet correspond to new particles, meaning  
<sup>805</sup> that there are five total scalars from the two Higgs doublets -  $h$  (light CP-even Higgs),  $H$  (heavy CP-even  
<sup>806</sup> Higgs),  $A$  (heavy CP-odd Higgs), and  $H^\pm$  (charged Higgs). The model is parameterized by two main pa-  
<sup>807</sup> rameters. The first,  $\tan \beta \equiv \frac{v_2}{v_1}$ , is the ratio of the vacuum expectation values of the two Higgs doublets  
<sup>808</sup> (where  $v_1$  corresponds to the  $v$  in the SM Higgs model described above). The second parameter is  $\alpha$ , a mix-  
<sup>809</sup> ing angle between the heavy and light Higgs fields. Models are also often parameterized with  $\cos(\beta - \alpha)$   
<sup>810</sup> rather than  $\alpha$  directly. The limit where  $\cos(\beta - \alpha) = 0$  is called the alignment limit, and in this limit the

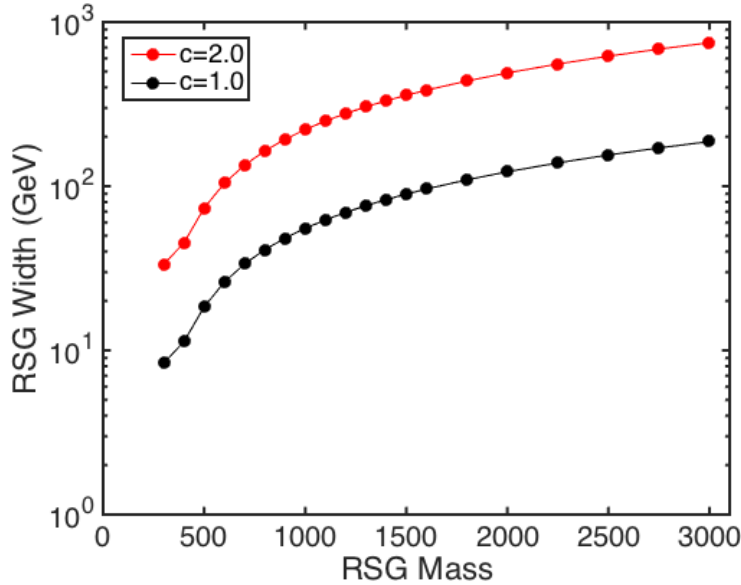


Figure 1.10: Randall-Sundrum graviton width as a function of mass computed in MadGraph with the CP3-Origins implementation [34, 40, 41]

811 light Higgs  $h$  has the same couplings as a Standard Model Higgs. Measurements of the Higgs boson have  
 812 put constraints on these two parameters, but near the alignment limit there is still much unprobed phase  
 813 space depending on the exact models and values of  $\tan \beta$  being considered [42].

814 2HDM models are usually separated into two main types - Type I and Type II. In Type I models, the  
 815 charged fermions only couple to the second Higgs doublet, leading to a fermiophobic light Higgs. In  
 816 Type II models, up-type quarks couple to the first doublet while down-type quarks couple to the second  
 817 doublet. One specific realization of a Type II 2HDM is the Minimal Supersymmetric Standard Model  
 818 (MSSM).

819 Resonant di-Higgs production in 2HDM models can proceed through decays of the heavy CP-even  
 820 Higgs  $H \rightarrow hh$ . The branching ratio for  $H \rightarrow hh$  depends on the model type as well as the values of  
 821  $\tan \beta$  and  $\cos \beta - \alpha$ . Figure 1.11 shows the branching ratios as a function of the mass of the heavy scalar  
 822  $H$  for both Type I and Type II models. Depending on the type of model  $hh$  can be a substantial fraction  
 823 of the decays of  $H$ .

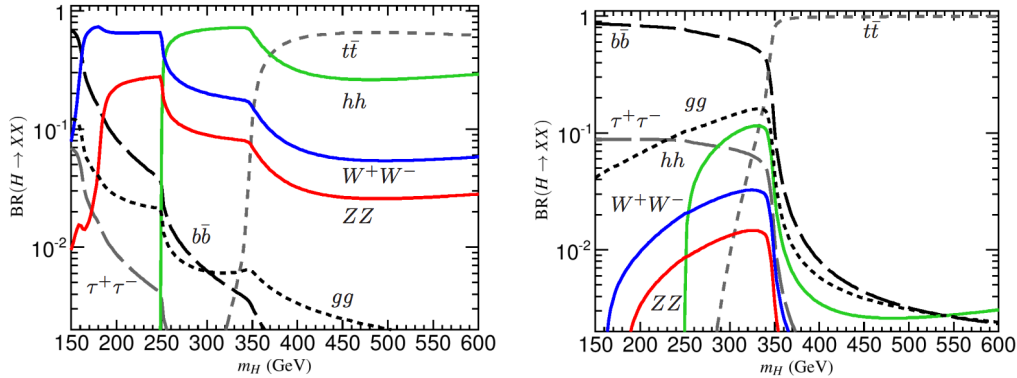


Figure 1.II: Branching ratios for heavy Higgs  $H$  in Type I (left) and Type II (right) 2HDM models with  $\tan \beta = 1.5$  and  $\cos(\beta - \alpha) = 0.1$  (0.01) for Type I (Type II) [38].

## 824 1.6 CONCLUSION

825 Studying the Higgs sector is essential for understanding the details of how mass arises in the Standard  
 826 Model and how the electroweak symmetry is broken. The discovery of the Higgs boson also opens the  
 827 door for its use as a tool to search for new physics, and Higgs pair production is an ideal candidate for  
 828 this study. Even if no BSM physics is found in Higgs pair production, searches for Higgs pairs will put  
 829 constraints on the Higgs self coupling and thus improve knowledge of the Standard Model and the details  
 830 of the Higgs potential.

*The enthusiasm and motivation to explore particle physics  
at the high-energy frontier knows no borders between the  
nations and regions of the planet.*

Peter Jenni

# 2

831

832

833

## The ATLAS detector and the Large Hadron Collider

834 This chapter presents an overview of the experimental systems used to conduct the measurements in this  
835 thesis. First, a brief overview of the accelerator, the Large Hadron Collider, will be given. In this section,  
836 the accelerator conditions relevant to data-taking are presented as well. Next, an overview of the ATLAS  
837 experiment is given. The basics of each sub-detector's role are summarized, as well as the details of the  
838 datasets accumulated. Then, a brief interlude on the ATLAS Muon New Small Wheel upgrade is pre-  
839 sented. While this new detector does not have a direct impact on any of the datasets recorded so far, it will  
840 have an impact on future analyses and the work done on it is briefly summarized here. Finally, an overview  
841 of object reconstruction in ATLAS is given. While the details of all of the algorithms will not be presented  
842 in detail, aspects of the reconstruction performance are shown as these are relevant to the results presented  
843 later in this thesis.

844 2.1 THE LARGE HADRON COLLIDER

845 The Large Hadron Collider (LHC) is a proton-proton collider at the CERN laboratory in Geneva, Switzer-  
846 land [43]. It was designed for a maximum collision center of mass energy of  $\sqrt{s} = 14 \text{ TeV}$  and has a  
847 circumference of 26.7 kilometers. Four main experiments are located at the interaction points (IP) of  
848 the accelerator: ATLAS (A Toroidal LHC ApparatuS), CMS (the Compact Muon Solenoid), ALICE (A  
849 Large Ion Collider Experiment), and LHCb [44–47]. Figure 2.1 shows a schematic of the LHC ring and  
850 its experiments.

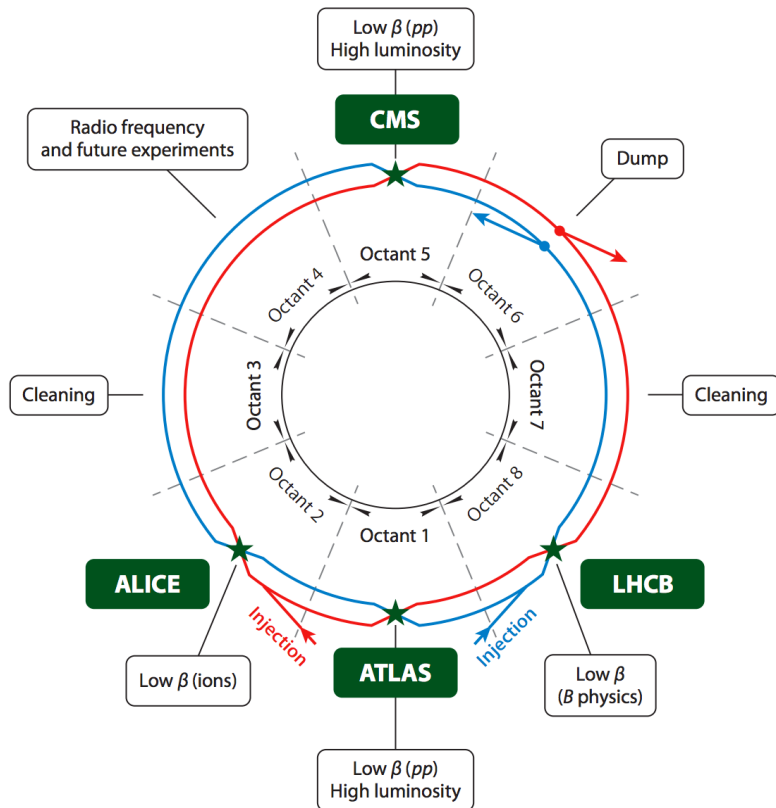


Figure 2.1: A schematic view of the LHC ring [48]. Four main experiments are located at interaction points along the ring. ATLAS and CMS are general purpose experiments, while ALICE is dedicated to heavy ion collisions and LHCb is dedicated to studying  $B$  physics.

851 One of the most interesting features of the LHC is its magnet design. Because the tunnel does not have  
852 room for separate superconducting magnets for each of the beam pipes, the LHC employs a twin-bore  
853 magnet design. Each magnet must hold an 8.3 Tesla magnetic field in order to bend the proton beams at

854  $\sqrt{s} = 14$  TeV. The superconducting magnets are cooled to a temperature of 1.9 Kelvin with superfluid  
 855 helium.

856 2.1.1 INSTANTANEOUS LUMINOSITY

857 The rate of physics events expected from the accelerator is dependent on the instantaneous luminosity  
 858 of the machine and the cross section of the physics process,  $R_{\text{events}} = L\sigma$ . Here,  $R_{\text{events}}$  is the num-  
 859 ber of events per second,  $L$  is the instantaneous luminosity of the machine, and  $\sigma$  is the cross section for  
 860 the physics process being measured. The instantaneous luminosity of the LHC is determined by numer-  
 861 ous factors related to beam conditions. Equation 2.1 gives the equation for instantaneous luminosity of a  
 862 Gaussian beam profile [48].

$$L = \frac{N_b^2 n_b f_{\text{rev}} \gamma_r}{4\pi \epsilon_n \beta^*} F \quad (2.1)$$

863 The LHC collides protons in bunches, and in the above equation  $N_b$  is the number of protons per bunch  
 864 while  $n_b$  is the number of bunches per beam. Nominally, the LHC can hold up to 2808 proton bunches.  
 865  $f_{\text{rev}}$  is the revolution frequency.  $\epsilon_n$  is the normalized transverse beam emittance, a measurement of the  
 866 average spread of the particles in position-momentum space which has the dimension of length.  $\beta^*$  is the  
 867 value of the  $\beta$  function for the beam at the interaction point. It relates the emittance to the Gaussian  
 868 width of the beam with  $\sigma_{\text{beam}} = \sqrt{\epsilon \cdot \beta}$ .  $F$  is a reduction factor that corrects for the fact that the beams  
 869 are colliding at an angle at the IP.

870 Another way of writing the instantaneous luminosity is shown in equation 2.2. In this case, the instan-  
 871 taneous luminosity is written as the ratio of the rate of inelastic collisions to the inelastic cross section [49].

872

$$L = \frac{R_{\text{inel}}}{\sigma_{\text{inel}}} = \frac{\mu n_b f_{\text{rev}}}{\sigma_{\text{inel}}} \quad (2.2)$$

873 In this case,  $\mu$  is the average number of interactions per bunch crossing in the accelerator.  $\mu$  is a useful  
 874 parameter for characterizing the amount of activity recorded in an experiment. As the instantaneous lu-  
 875 minosity and thus  $\mu$  increase, there are more interactions per bunch crossing and more activity is present  
 876 in the detector. The level of activity is often characterized with  $\langle \mu \rangle$ , the measured per bunch crossing  $\mu$

877 value averaged over all bunch crossings. The interactions inside each bunch crossing that are not the main  
 878 physics process of interest are often referred to as “pileup” interactions, and  $\langle \mu \rangle$  is a measurement of the  
 879 level of pileup in the detector.

### 880 2.1.2 EVOLUTION OF MACHINE CONDITIONS

881 This thesis uses datasets taken at three different center of mass energies:  $\sqrt{s} = 7$  TeV data taken in the  
 882 year 2011,  $\sqrt{s} = 8$  TeV data taken in the year 2012, and  $\sqrt{s} = 13$  TeV data taken in the year 2015. In  
 883 addition to increasing center of mass energy, the instantaneous luminosity and parameters that determine  
 884 it were evolving. Table 2.1 summarizes that machine conditions in each of these datasets.

	2011	2012	2015	Design
$\sqrt{s}$ [ TeV ]	7	8	13	14
Number of bunches	1380	1380	1825	2808
Max. protons per bunch	$1.45 \times 10^{11}$	$1.7 \times 10^{11}$	$1.2 \times 10^{11}$	$1.15 \times 10^{11}$
Bunch spacing [ns]	50	50	25	25
Max. instantaneous luminosity [ $\text{cm}^{-2}\text{s}^{-1}$ ]	$3.7 \times 10^{33}$	$7.7 \times 10^{33}$	$5 \times 10^{33}$	$10^{34}$
$\beta^*$ [m]	1.0	0.6	0.8	0.55
$\langle \mu \rangle$	11.6	20.7	13.7	-

Table 2.1: Evolution of LHC machine conditions [50, 51].

## 885 2.2 THE ATLAS DETECTOR

886 The ATLAS detector is the multi-purpose particle detector experiment located at the LHC’s Point 1 [44].  
 887 It has nearly  $4\pi$  coverage in solid angle around the interaction point. It consists of an inner detector for  
 888 measuring charged particles, electromagnetic and hadronic calorimeters, and a muon spectrometer. Fig-  
 889 ure 2.2 gives an overview of the detector.

### 890 2.2.1 COORDINATE SYSTEM

891 Before defining the properties of the individual detectors, it is important to establish the coordinate system  
 892 used. Figure 2.3 shows a schematic of the coordinate system. The azimuthal plane (perpendicular to the

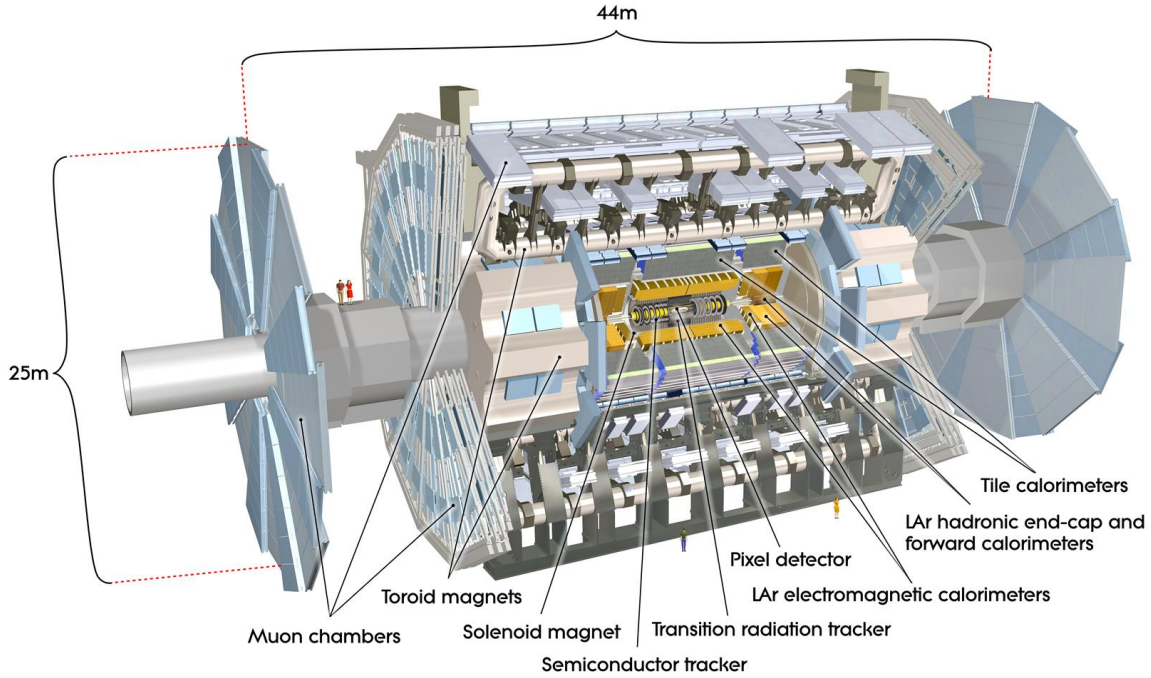


Figure 2.2: A full diagram of the ATLAS detector [44].

beam line) is defined as the  $x$ - $y$  plane. The angle in this plane is referred to as  $\phi$ . The angle relative to the beam axis is referred to as  $\theta$ . Rather than using  $\theta$  directly as a coordinate, the experiment often uses the pseudorapidity  $\eta$ , defined in equation 2.3.

$$\eta = -\ln \left( \tan \left( \frac{\theta}{2} \right) \right) \quad (2.3)$$

Pseudorapidity is the massless approximation of rapidity, the angle used to parameterize boosts in special relativity. This coordinate is useful in particle physics for two reasons. First, it means that differences in  $\eta$  are Lorentz invariant. Second, particle production is roughly constant in pseudorapidity. Particles with  $\eta$  close to zero are referred to as “central”, while those at high  $|\eta|$  are called “forward”. In general, two main detector configurations can be seen in figure 2.2. There are “barrel” elements, which surround the beam line cylindrically and are in the central region of the detector. In the forward region, there are “endcap” regions which are arranged as disks perpendicular to the beam line.

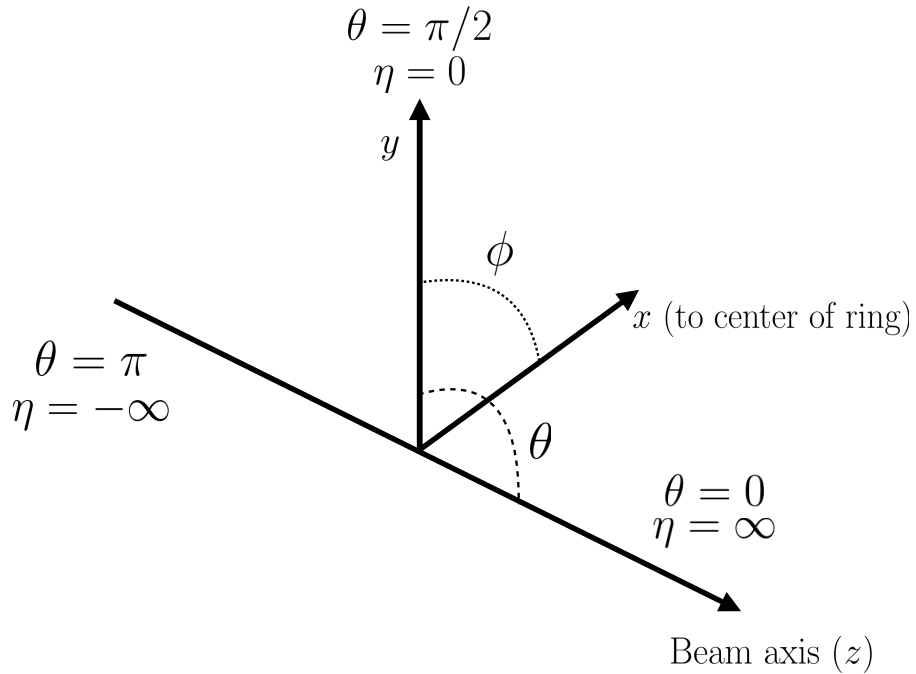


Figure 2.3: The ATLAS coordinate system. The *z* direction corresponds to the beam axis, while *x* and *y* define the transverse plane.  $\theta$  is the angle relative to the beam axis and  $\phi$  is the azimuthal angle.  $\eta$ , the pseudorapidity, approaches infinity at small angles relative to the beam axis.

903    2.2.2    INNER DETECTOR

904    The ATLAS Inner Detector (ID) system is built for precision tracking of charged particles. It covers the  
 905    range  $|\eta| < 2.5$ . In this range, approximately 1000 particles are generated every bunch crossing in the de-  
 906    tector [44]. This requires having fine granularity to achieve the resolutions required for good momentum  
 907    measurement and vertex reconstruction.

908    The ID consists of three sub-components: the pixel detector, semiconductor tracker (SCT), and trans-  
 909    sition radiation tracker (TRT). It is surrounded by a solenoid providing a 2 T axial magnetic field which  
 910    bends particles in the transverse plane to allow for momentum measurement. Figure 2.4 shows the layout  
 911    of each of these components.

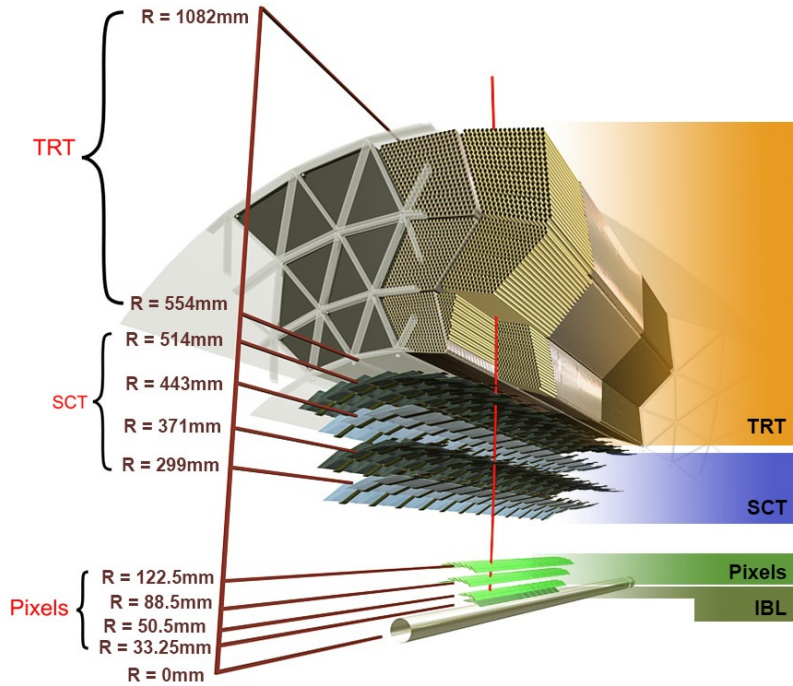


Figure 2.4: Layout of the ATLAS Inner Detector system [52].

## 912 PIXEL DETECTOR

913 The pixel detector is the first detector particles traverse after being generated in proton collisions and is  
 914 the most granular detector. Its operation is crucial for precision tracking and vertex reconstruction as well  
 915 as higher level object reconstruction like tagging of jets from  $b$ -quarks. The basic sensing element in this  
 916 subdetector is a silicon pixel detector. The operating principle for the silicon pixels is that of a  $p-n$  junction.  
 917 When a charged particle passes through, it creates electron-hole pairs that are then separated by the electric  
 918 field. The sensors are  $250 \mu\text{m}$  thick and use oxygenated  $n$ -type wafers with readout pixels on the  $n^+$  side  
 919 of the detector [44]. Overall, the pixel detector has 1744 sensors and 80.4 million readout channels.

920 In the barrel region, the pixel detector has three concentric layers of sensors surrounding the beamline.  
 921 In the endcap region, it consists of disks perpendicular to the beam axis. The detector is segmented in  
 922 the  $R-\phi$  plane and in  $z$ . Usually, three pixel layers are crossed by a charged particle track. The intrinsic  
 923 accuracies of the sensors are  $10 \mu\text{m}$  in  $R-\phi$  and  $115 \mu\text{m}$  in  $z$  (or  $R$  for the endcap).

924 **INSERTABLE B-LAYER**

925 In Run 2, a new innermost pixel layer, known as the insertable B-layer (IBL), was added to the Inner  
926 Detector [53]. This layer was added to cope with the higher luminosities planned in LHC Run 2 and at the  
927 high luminosity HL-LHC. Additionally it improves tracking position resolution which in turn improves  
928 the vertexing and *b*-tagging capabilities in ATLAS. The detector sits directly on a new beam pipe, only  
929 33.25 mm away from the collision points in the azimuthal plane.

930 **SEMICONDUCTOR TRACKER (SCT)**

931 The semiconductor tracker (SCT) consists of silicon microstrips and comprises the next four layers of  
932 the ID. This sub-detector has 6.4 cm long sensors that are daisy-chained into strips with a strip pitch of  
933 80  $\mu\text{m}$  [44]. Some of the strips have a small stereo angle to allow for measurement of both angular co-  
934 ordinates. In total there are 6.3 million readout channels. The intrinsic accuracies are 17  $\mu\text{m}$  in  $R\text{-}\phi$  and  
935 580  $\mu\text{m}$  in  $z$  (or  $R$  in the endcap).

936 **TRANSITION RADIATION TRACKER (TRT)**

937 The transition radiation tracker (TRT) serves two purposes. First, it consists of 4 mm diameter straw tubes  
938 filled with a 70/27/3% gas mixture of xenon, carbon dioxide, and oxygen to provide tracking of charged  
939 particles. Particles typically have 36 TRT straw tube hits per track. The material in between the straws  
940 is designed to induce transition radiation which can be useful for particle identification. As particles pass  
941 between media with different dielectric constants, they emit transition radiation that can cause additional  
942 showers in the TRT. In particular it is useful for discrimination between electrons and pions or other  
943 charged hadrons, as the amount of transition radiation is proportional to the Lorentz factor of the particle.

944 **2.2.3 CALORIMETERS**

945 The calorimeter system consists of two main sub-components: a fine granularity electromagnetic calorime-  
946 ter tailored for the measurement of photons and electrons and multiple coarser hadronic calorimeters ded-  
947 icated to the measurement of hadronic showers [44]. The calorimeter system has broader coverage than

948 the inner detector, covering the region out to  $|\eta| < 4.9$ . It is also designed to deliver good containment of  
949 showers so as to limit leakage into the muon system. Figure 2.5 shows the layout of the calorimeter system.

950 Both the electromagnetic and hadronic calorimeters are sampling calorimeters. They alternate active  
951 material for energy measurement with passive material for energy absorption. The materials used for each  
952 purpose vary based on the type of calorimeter and its location in the detector.

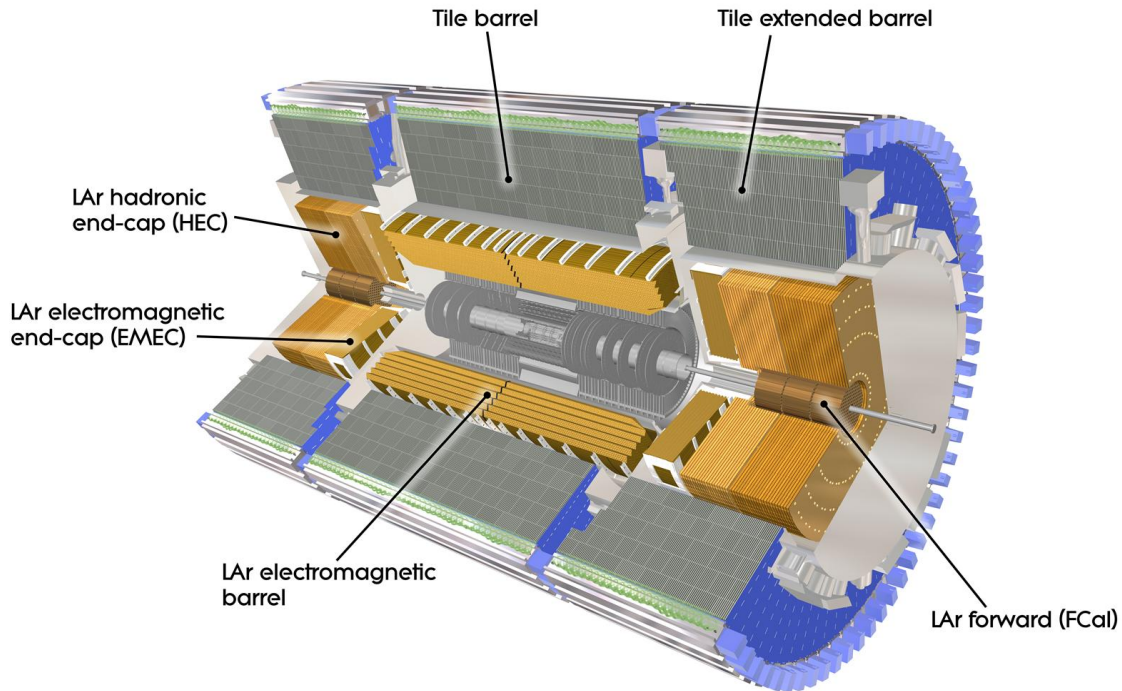


Figure 2.5: Layout of the ATLAS calorimeter system [44].

### 953 ELECTROMAGNETIC CALORIMETER

954 The electromagnetic calorimeter (EM calorimeter) use liquid Argon (LAr) as its active material and lead  
955 as its passive material. It is arranged in an accordion geometry to increase the absorption area while still  
956 allowing it to have no azimuthal cracks (complete symmetry in  $\phi$ ). The EM calorimeter is divided into a  
957 barrel portion that extends to  $|\eta| < 1.475$  and an endcap portion going from  $1.375 < |\eta| < 3.2$ . The  
958 region where these two units overlap is called the “transition region”.

959 In order to provide good containment the calorimeter depth must be optimized. Typically, for elec-  
960 tromagnetic calorimeters the depth is measured in radiation lengths. In general, the intensity of a particle  
961 beam attenuates exponentially in distance with an attenuation constant equal to the radiation length. That  
962 is,  $I(x) = I_0 e^{-x/X_0}$ , where  $I$  is the intensity,  $x$  is the distance traveled, and  $X_0$  is the radiation length.  
963 The ATLAS EM calorimeter is designed to have  $> 22$  radiation lengths in the barrel and  $> 24$  in the  
964 endcap [44].

965 **HADRONIC CALORIMETERS**

966 There are three types of hadronic calorimeters present in ATLAS: the tile calorimeter (TileCal), hadronic  
967 endcap (HEC), and forward calorimeter (FCal). Each one is optimized for stopping of hadronic showers  
968 and the materials chosen are specific to their placement in the detector.

969 The TileCal is a scintillating tile calorimeter placed directly outside the EM calorimeter. It uses steel as  
970 the absorber and plastic scintillator tiles as the active material. It has coverage in the barrel at  $|\eta| < 1.0$   
971 and in the “extended barrel” region of  $0.8 < |\eta| < 1.7$ .

972 The HEC had two wheels perpendicular to the beam line per endcap and is located directly behind the  
973 EM calorimeter endcap modules. The HEC covers the region from  $1.5 < |\eta| < 3.2$ , overlapping slightly  
974 with both the tile calorimeter and the forward calorimeter. Like the EM calorimeter, it uses liquid Argon  
975 as the active material, but it uses copper as the absorber.

976 The FCal covers the most forward regions of the calorimeter system, extending to the region of  $3.1 <$   
977  $|\eta| < 4.9$ . It again uses liquid argon as its active material. For absorber, it consists of an innermost module  
978 made of copper followed by a module made of tungsten.

979 The hadronic equivalent of radiation length is called the interaction length and is denoted as  $\lambda$ . In the  
980 barrel, the hadronic calorimeter depth is approximately  $9.7\lambda$ , while in the endcap is is  $10\lambda$ . The outer  
981 supports contribute an additional  $1.3\lambda$ . This is been shown to be sufficient to limit punch-through of  
982 showers to the muon system [44].

983 2.2.4 MUON SPECTROMETER

984 The muon spectrometer is dedicated to measuring the momentum and position of muons. It consists  
985 of tracking and trigger chambers which are unique in the barrel and endcap regions. The magnetic field  
986 for bending of muons is provided by a system of three large air-core toroid magnets (from which ATLAS  
987 derives its name.) These magnets provide 1.5 to 5.5 Tm of bending power at  $0 < |\eta| < 1.4$  and approx-  
988 imately 1 to 7.5 Tm in the endcap region of  $1.6 < |\eta| < 2.7$ . The entire muon system covers the range  
989  $0 < |\eta| < 2.7$ . Monitored drift tubes (MDTs) are used for tracking in the barrel and the two outer layers  
990 of the endcap, while cathode strip chambers (CSCs) are used to provide tracking in the innermost endcap  
991 wheel. In the barrel, resistive plate chambers (RPCs) are used as trigger chambers while thin gap chambers  
992 (TGCs) are used in the endcap. Figure 2.6 shows the layout of the ATLAS muon system. The entire muon  
993 system is designed with the specification of providing a 10% momentum resolution for a 1 TeV muon.

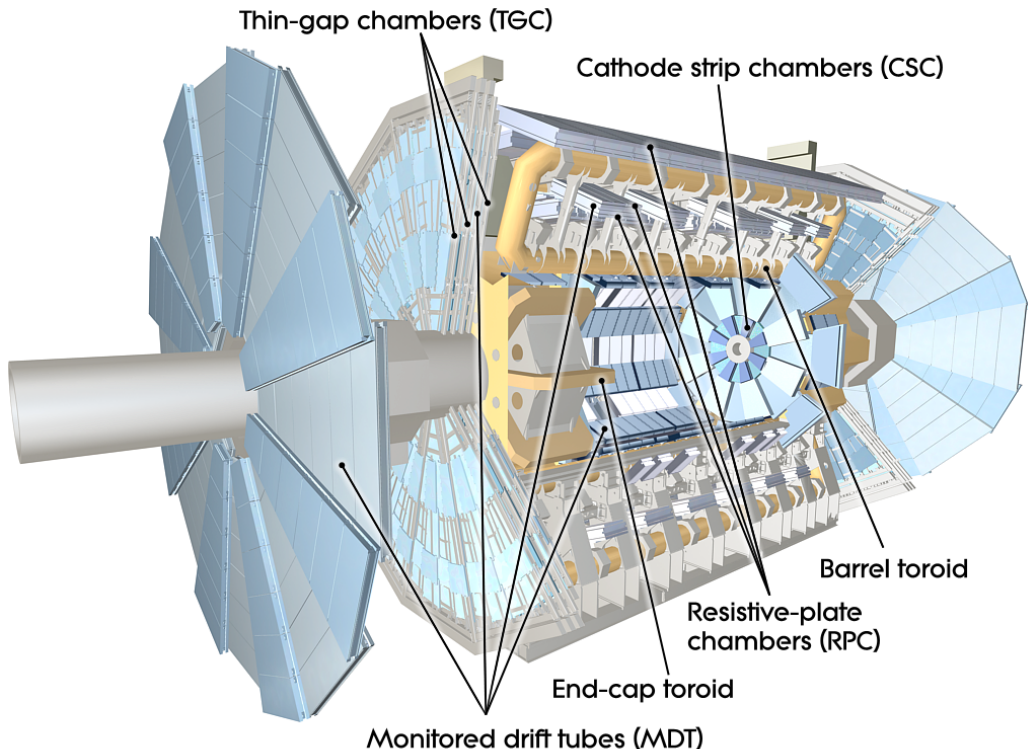


Figure 2.6: Layout of the ATLAS muon system [44].

994 MONITORED DRIFT TUBES (MDTs)

995 The monitored drift tubes (MDTs) are aluminum 3 cm diameter tubes filled with a 93/7 % mixture of  
996 Argon and CO<sub>2</sub>, with trace amounts of water. As a charged particle traverses the tube, it ionizes the gas  
997 and the ions drift to a wire at the center of the tube. The radial distance of traversal of the particle in the  
998 tube is determined by the drift time of the electrons, allowing for fine position resolution. The tubes have  
999 an average resolution of 80  $\mu\text{m}$  per tube and a maximum drift time of approximately 700 ns. The tubes  
1000 are oriented so that they give precision measurement in  $\eta$  and run along  $\phi$ . They cover  $|\eta| < 2.7$ , except  
1001 in the innermost layer of the endcap where they only go to  $|\eta| < 2.0$  [44].

1002 CATHODE STRIP CHAMBERS (CSCs)

1003 The cathode strip chambers cover a narrow window of the innermost endcap region at  $2.0 < |\eta| <$   
1004 2.7. In this region the background rates in the cavern are particularly high and the CSCs are designed to  
1005 handle these higher rates. The CSCs are multiwire proportional chambers with wires pointing in the radial  
1006 direction (away from the beam pipe). The wire serves as an anode and there are two types of segmented  
1007 cathode strip, one perpendicular to the wires which gives the precision measurement and one parallel which  
1008 provides the transverse coordinate. It has an 80/20% gas mixture of Argon and CO<sub>2</sub> [44].

1009 RESISTIVE PLATE CHAMBERS (RPCs)

1010 The resistive plate chambers (RPCs) are gaseous electrode-plate detectors covering the region  $|\eta| < 1.05$ .  
1011 They consist of two resistive plates separated by a distance of 2 mm. The gas mixture used is a 94.7/5/0.3%  
1012 mixture of C<sub>2</sub>H<sub>2</sub>F<sub>4</sub>, Iso-C<sub>4</sub>H<sub>10</sub>, and SF<sub>6</sub>. It has readout strips with a pitch of 23-35 mm for both  $\eta$  and  
1013  $\phi$  measurement and thus provides measurement of the azimuthal coordinate in the barrel. The thin gas  
1014 gap allows for a quick response time which makes it ideal for use in the trigger. Signals in the RPC have  
1015 a width of approximately 5 ns. There are three layers of RPCs which are referred to as the three trigger  
1016 stations. They allow for programmable thresholds in both a low  $p_T$  and high  $p_T$  trigger. The coincidence  
1017 of hits in the innermost chambers allows for setting muon trigger thresholds between 6 and 9 GeV, while  
1018 the outermost layer allows the trigger to set trigger thresholds in the range of 9 to 40 GeV [44].

1019 THIN GAP CHAMBERS (TGCs)

1020 The thin gap chambers (TGCs) are multiwire proportional chambers where the wire to cathode distance  
1021 (1.4mm) is smaller than the wire-to-wire distance (1.8 mm). They contain a gas mixture of CO<sub>2</sub> and *n*-  
1022 pentane and use a high electric field to gain good time resolution. They serve two functions in the end-cap  
1023 system. First, they serve as the trigger chambers. Second, they also provide azimuthal coordinate measure-  
1024 ment. They sit on the inner and middle layers of the endcap. The outermost layer's azimuthal coordinate  
1025 is determined by extrapolation [44]. As with the RPCs, the TGCs also are capable of triggering with pro-  
1026 grammable thresholds in the same  $p_T$  range specified for the RPCs above.

1027 2.2.5 MAGNET SYSTEM

1028 As mentioned previously, there are two independent magnet systems in ATLAS. The first is a 2 T solenoid  
1029 field in the inner detector which provides bending in the azimuthal plane. The second is an approximately  
1030 0.5 T toroidal field in the muon system which provides bending in  $\eta$ . Figure 2.7 shows the predicted field  
1031 integral as a function of  $|\eta|$  [44].

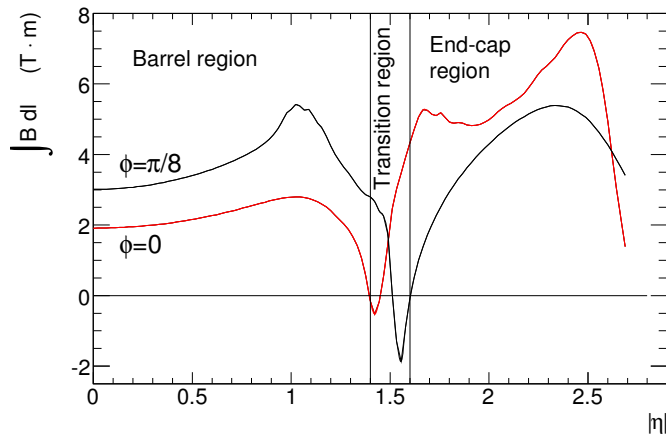


Figure 2.7: Predicted field integral as a function of  $|\eta|$  for the ATLAS magnet system [44].

1032    2.2.6    TRIGGER SYSTEM

1033    The ATLAS trigger system searches for signatures of muons, electrons, photons, hadronically decaying  $\tau$   
 1034    leptons, and jets in order to save these events for further analysis. The trigger system in ATLAS is designed  
 1035    to reduce the maximum LHC event rate of 40 MHz to a more reasonable rate that can be recorded. The  
 1036    trigger first consists of a fast, hardware based system called the Level-1 (L1) trigger. The L1 trigger consists  
 1037    of independent dedicated detector sub-components that can seed regions of interest (RoIs) for further  
 1038    analysis downstream. For muons, the RPCs and TGCs are used, while in the calorimeter coarsely grained  
 1039    sections of calorimeter cells called towers are used. Once regions of interest are seeded, a software based  
 1040    system called the High Level Trigger (HLT) is used to reconstruct objects and integrate information from  
 1041    different parts of the detector. In Run 1 of ATLAS, the HLT consisted of two separate stages: the level 2  
 1042    (L2) trigger and the event filter (EF).

1043    The maximum trigger rate that the L1 trigger can handle is 75 kHz. In the HLT, the rate of events  
 1044    written to disk is approximately 400 Hz. Figure 2.8 shows the trigger rates for different L1 triggers in 2012  
 1045    and 2015 for ATLAS [54].

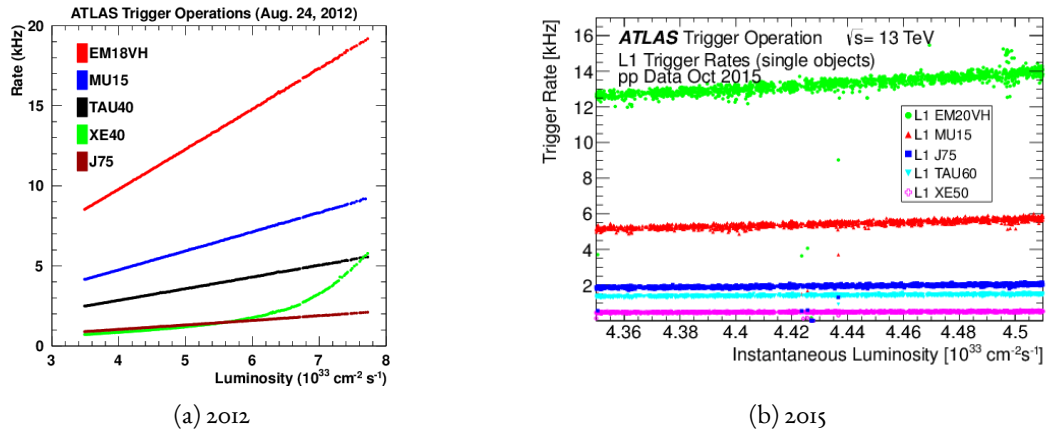


Figure 2.8: ATLAS trigger rates for Level-1 triggers as a function of instantaneous luminosity in 2012 and 2015 operation. These are single object triggers for electromagnetic clusters (EM), muons (MU), jets (J), missing energy (XE), and  $\tau$  leptons (TAU). The threshold of the trigger is given in the name in GeV [54].

1046 2.2.7 ATLAS DATASETS

1047 ATLAS has collected data at center of mass energies of 7, 8, and 13 TeV. Figure 2.9 shows the integrated  
1048 luminosity as a function of time for each of the three datasets. In the 2011 dataset with  $\sqrt{s} = 7 \text{ TeV}$ ,  
1049 ATLAS recorded  $5.08 \text{ fb}^{-1}$ . Increased instantaneous luminosity in 2012 led to a larger dataset of  $21.3 \text{ fb}^{-1}$   
1050 recorded at  $\sqrt{s} = 8 \text{ TeV}$ . After Long Shutdown 1 (LS1) of the LHC and a restart in 2015, ATLAS  
1051 recorded  $3.9 \text{ fb}^{-1}$  of data at  $\sqrt{s} = 13 \text{ TeV}$  [55, 56]. The data recorded by ATLAS can only be used for  
1052 analysis if the required sub-detectors were in a stable state when the data was being taken. The fraction  
1053 of recorded ATLAS data that was labeled as being good for physics analysis was 90%, 95%, and 82% in  
1054 the 7, 8, and 13 TeV data respectively. Thus, the Run 1 results presented in this thesis use  $4.6 \text{ fb}^{-1}$  at  
1055  $\sqrt{s} = 7 \text{ TeV}$  and  $20.3 \text{ fb}^{-1}$  at  $\sqrt{s} = 8 \text{ TeV}$ <sup>1</sup>. The Run 2 results use  $3.2 \text{ fb}^{-1}$  at  $\sqrt{s} = 13 \text{ TeV}$ .

1056 2.2.8 DETECTOR PERFORMANCE

1057 Table 2.2 summarizes the design requirements for each of the different sub-detectors. This table shows the  
1058 energy and momentum resolution of tracking, calorimetry, and muon measurements.

	Required resolution
Tracking	$\sigma_{p_T}/p_T = 0.05\% p_T \oplus 1\%$
EM calorimetry	$\sigma_E/E = 10\%/\sqrt{E} \oplus 0.7\%$
Hadronic calorimetry	
Barrel and end-cap	$\sigma_E/E = 50\%/\sqrt{E} \oplus 3\%$
Forward	$\sigma_E/E = 100\%/\sqrt{E} \oplus 10\%$
Muon spectrometer	$\sigma_{p_T}/p_T$ at $p_T = 1 \text{ TeV}$

Table 2.2: Performance requirements for the ATLAS detector [44].

1059 2.3 THE ATLAS MUON NEW SMALL WHEEL UPGRADE

1060 As the LHC continues operation, it is scheduled to be upgraded in several phases to allow it to reach higher  
1061 instantaneous luminosities and thus collect larger datasets. These conditions will open new doors for study

---

<sup>1</sup>The analyses combined in the Higgs discovery (presented in chapter 4) use between  $4.6$  and  $4.8 \text{ fb}^{-1}$  at  $7 \text{ TeV}$  depending on which detectors are required to be in a stable state. The discovery also only uses the  $5.8 \text{ fb}^{-1}$  of  $8 \text{ TeV}$  data that was available at the time of the analysis.

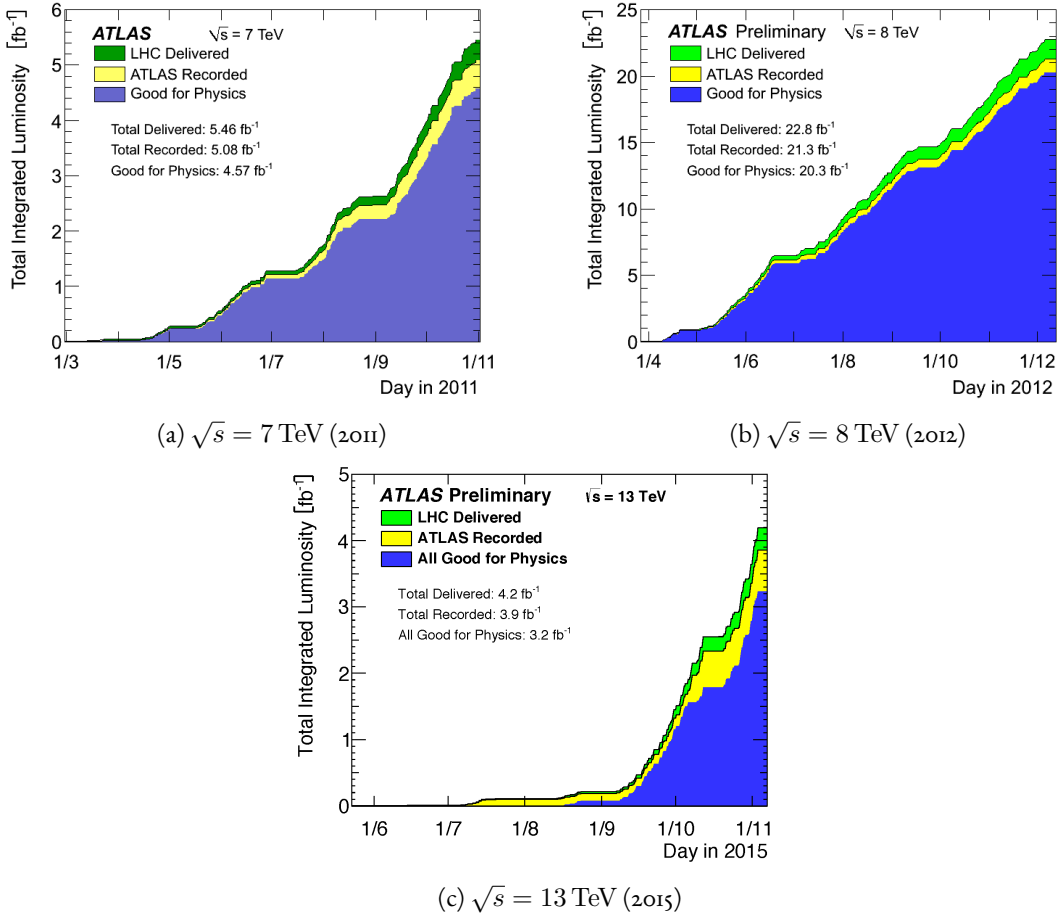


Figure 2.9: Instantaneous luminosity as a function of time for data recorded by ATLAS at different center of mass energies [55, 56].

of rare physics processes but will also present interesting challenges that must be faced. ATLAS will require new detector technologies to cope with the increased background rates in the cavern in these high luminosity conditions. One such upgrade, scheduled to be installed during Long Shutdown 2 (LS2) of the LHC in 2018, is the ATLAS Muon New Small Wheel (NSW) [57]. The NSW will replace the innermost end-cap wheel of the muon system with new technologies. This is the part of the muon detector closest to the beam line and thus experiences the highest rates of particle flux in the muon system.

1068 2.3.1 MOTIVATION

1069 The motivation of the NSW is two-fold. The first objective is to alleviate the decreased tracking efficiency  
1070 that comes in a high rate environment. As shown in figure 2.10, at the LHC design luminosity both the  
1071 efficiency of recording hits and reconstructing track segments in the MDTs decreases. While the MDTs  
1072 were designed to cope with the hit rates at the LHC design luminosity, the High Luminosity LHC will  
1073 exceed these design specifications and the MDTs will have to be replaced.

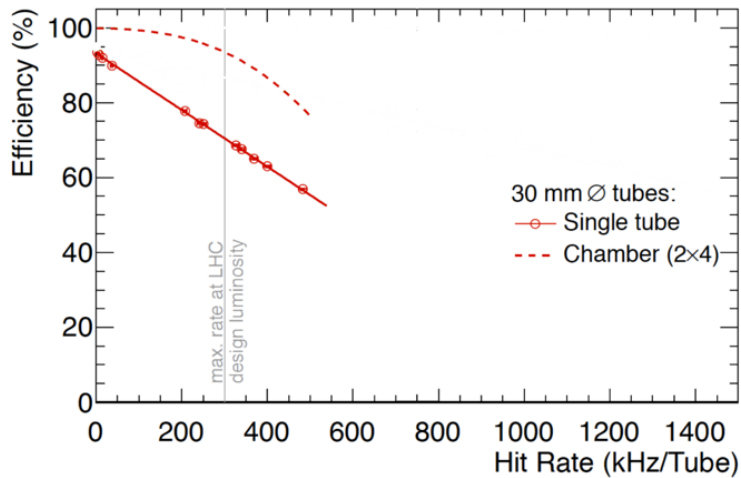


Figure 2.10: MDT tube hit (solid) and segment (dashed) efficiency as a function of hit rate per tube [57].

1074 The NSW will also work to alleviate the rate of fake triggers arising in the endcap. Figure 2.11 shows the  
1075 extrapolated trigger rates as a function of the  $p_T$  threshold with and without the NSW upgrade. As the  
1076 figure shows, the NSW upgrade will reduce the trigger rate considerably compared to the current endcap  
1077 trigger system. At a  $p_T$  threshold of 20 GeV, the level-1 trigger rate drops from 20 kHz to 7 kHz. This  
1078 reduction allows the  $p_T$  thresholds on muons to remain low, increasing the phase space of possible physics  
1079 studies and in particular maintaining good acceptance for Higgs physics.

1080 2.3.2 NSW DETECTOR TECHNOLOGIES

1081 The NSW will use two new detector technologies - micromesh gaseous structure detectors (micromegas)  
1082 and small-strip thin gap chambers (sTGCs) [57, 58]. The micromegas is more suited to tracking because

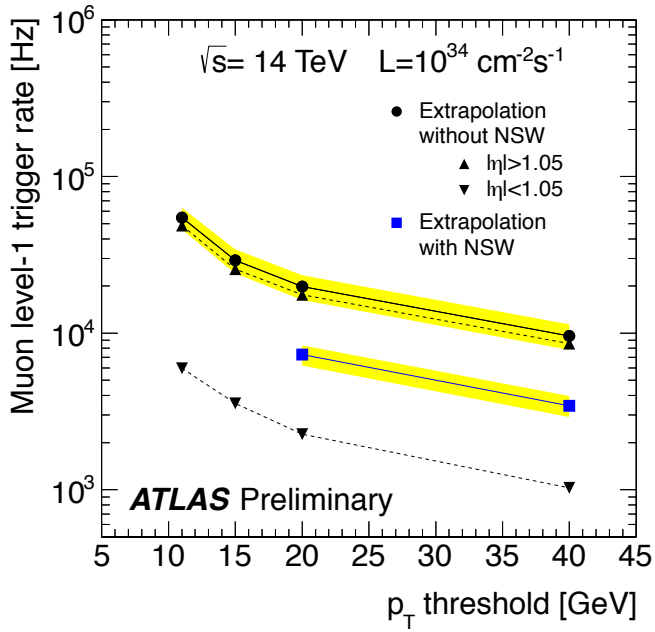


Figure 2.11: Trigger rate as a function of  $p_T$  threshold with and without the NSW upgrade [57].

of its good spatial resolution, while the sTGCs have better time resolution and are more suited for the trigger. However, both systems are capable of providing tracking and trigger information. To maintain full redundancy in cases of detector failure, both technologies will be used for tracking and trigger in the NSW.

## 1087 MICROMEGAS

1088 Micromegas detectors operate using a thin metallic mesh that sits approximately  $100\ \mu\text{m}$  away from the  
 1089 readout electrodes to create the amplification region. Above this mesh, there is a drift region on the order  
 1090 of a few mm in length capped by a drift electrode. As a charged particle traverses the detector, it ionizes gas  
 1091 and the electrons drift down towards readout strips. The timing of the drift can be used to reconstruct the  
 1092 angle of traversal of the particle. This is illustrated in figure 2.12. The micromegas used in ATLAS will be  
 1093 resistive micromegas, where the readout electrodes are topped with resistive strips [59]. This alleviates the  
 1094 risk of sparking in the large area detectors that ATLAS will use.

1095 In ATLAS, the micromegas drift gap will be 5 mm and the amplification gap will be  $128\ \mu\text{m}$ . They are

1096 filled with the same gas mixture as the MDTs. They will be stacked in an octuplet in an XXUV-UVXX  
 1097 geometry, where X refers to nominal strips and U and V refer to stereo strips at an angle of  $\pm 1.5^\circ$ . This  
 1098 arrangement allows for measurement of the azimuthal coordinate and gives a large lever arm between the  
 1099 straight strips for triggering purposes. Figure 2.12 shows the geometry of a single micromegas detector as  
 1100 well as its operating principle [57].

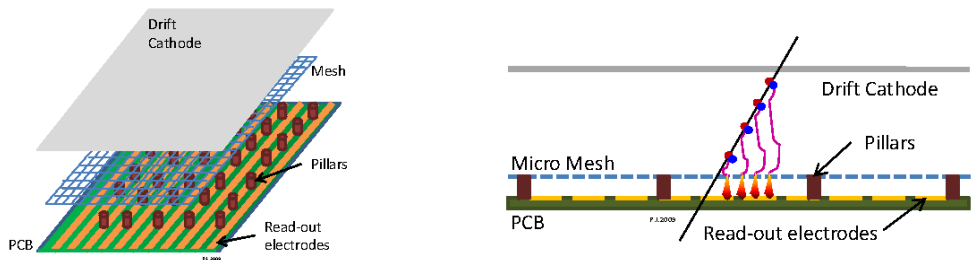


Figure 2.12: Illustrations of the geometry (left) and operating principle (right) of the micromegas detector [57].

## sTGCs

1101 sTGCs  
 1102 The sTGCs are similar to the TGCs currently in the ATLAS endcap muon system [44]. They consist  
 1103 of gold-plated tungsten wires (with a 1.8 mm pitch) between two cathode planes 1.4 mm away from the  
 1104 wire plane. One cathode plane consists of strips with a 3.2 mm pitch (much smaller pitch than the TGCs),  
 1105 while the other consists of coarser pads that are used for defining regions of interest in the sTGC trigger  
 1106 algorithm. Figure 2.13 shows the basic detector geometry.

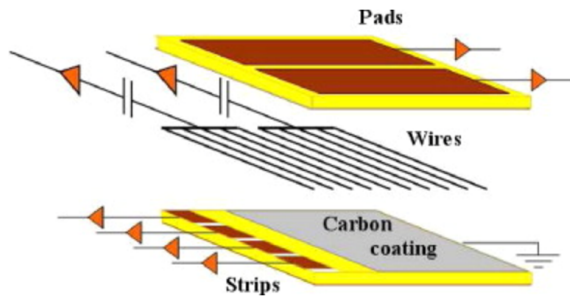


Figure 2.13: Geometry of the sTGC detector [57].

1107 2.3.3 PHYSICS IMPACT

1108 Maintaining low  $p_T$  thresholds for muons while still staying within the trigger rate budget at Level 1 for the  
1109 muon system (20 kHz) is crucial for physics analyses to be successful in high luminosity conditions. One  
1110 realm where the lepton trigger threshold is especially important is in Higgs physics. In the  $H \rightarrow WW^*$   
1111 analysis, one of the  $W$  bosons is off shell and tends to decay to soft leptons. In associated production of a  
1112 Higgs with a  $W$ , the lepton is also important because it provides the main handle which allows the event  
1113 to be triggered. Without the NSW, analyses would be required to either raise the muon  $p_T$  threshold or  
1114 only use muons triggered from the barrel muon system. Table 2.3 shows that both of these alternatives  
1115 significantly reduce the Higgs signal efficiency. With the NSW, the signal efficiency is largely maintained  
1116 and the triggers can remain unprescaled at lower  $p_T$  thresholds.

Threshold	$H \rightarrow b\bar{b}$ (%)	$H \rightarrow WW^*$ (%)
$p_T > 20 \text{ GeV}$	93	94
$p_T > 40 \text{ GeV}$	61	75
$p_T > 20 \text{ GeV} (\text{barrel only})$	43	72
$p_T > 20 \text{ GeV} (\text{with NSW})$	90	92

Table 2.3: Signal efficiencies for  $WH$  production with  $H \rightarrow b\bar{b}$  and  $H \rightarrow WW^* \rightarrow \mu\nu qq$  under different trigger configurations [57].

1117 2.4 OBJECT RECONSTRUCTION IN ATLAS

1118 ATLAS analyses first start by requiring the presence of certain reconstructed physics objects in the event.  
1119 This section will present a brief overview of the algorithms used to reconstruct electrons, muons, jets (in-  
1120 cluding  $b$ -jets), and missing energy<sup>2</sup>. The performance of physics object reconstruction and identification  
1121 will also be discussed as these are relevant to the analyses presented later. Figure 2.14 gives an overview of  
1122 the different sub-detectors that each type of particle will interact with in ATLAS.

---

<sup>2</sup>Reconstruction algorithms for other objects, such as photons and hadronically decaying  $\tau$  leptons, are not detailed here as these objects are not used in the results presented in this dissertation.

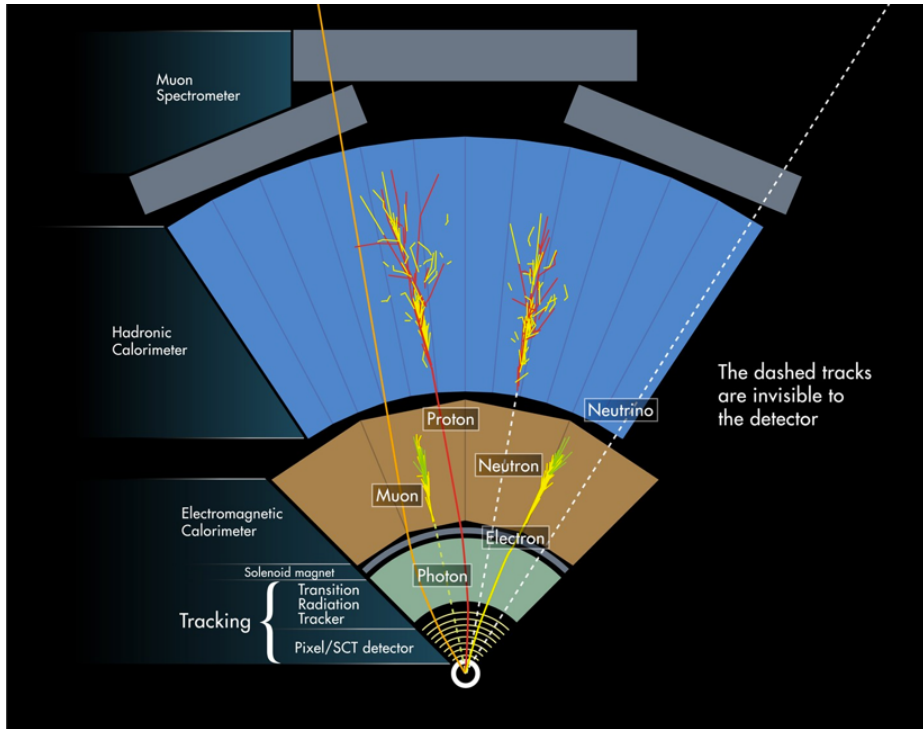


Figure 2.14: Illustration of particle interactions in ATLAS [60]

1123 2.4.I ELECTRONS

1124 Electrons in ATLAS will leave tracks in the inner detector and energy deposits in the electromagnetic  
 1125 calorimeter. The algorithm for recognizing the signature of electrons proceeds in two steps: reconstruction  
 1126 and identification.

1127 In reconstruction, an electron candidate is formed by matching EM calorimeter deposits with ID tracks.  
 1128 The algorithm first chooses seed clusters in the EM calorimeter by using a sliding window algorithm that  
 1129 searches for towers with transverse energy larger than 2.5 GeV. In addition to seed clusters, track candi-  
 1130 dates must be identified in the ID. The algorithm selects seed tracks with  $p_T > 1$  GeV that do not fit well  
 1131 with a pion hypothesis. Once candidate tracks are selected, they are re-fit with a Gaussian Sum Filter (GSF)  
 1132 algorithm to estimate electron parameters [61]. Finally, an electron candidate is formed if at least one track  
 1133 matches to a seed cluster in the calorimeter. The full details of the reconstruction algorithm can be found  
 1134 in reference [62].

1135 Once an electron candidate is present, identification criteria must be applied in order to reject fake elec-

trons from background. Many different variables are used for this identification. They include information about the shower shape in the EM calorimeter and the amount of leakage into the hadronic calorimeter, as well as information from the ID and in particular the TRT. There are both selection requirement based and likelihood-based criteria that range from “loose” to “very tight”. For details, see reference [62].  
 In the  $H \rightarrow WW^*$  analysis, both medium and very tight likelihood electrons are used depending on the electron  $p_T$ .

Figure 2.15 shows the algorithm’s reconstruction efficiency for true electrons with different identification criteria as well as the electron energy resolution in simulation [62, 63]. The reconstruction efficiency is measured using both the  $Z$  and  $J/\psi$  with 8 TeV data.

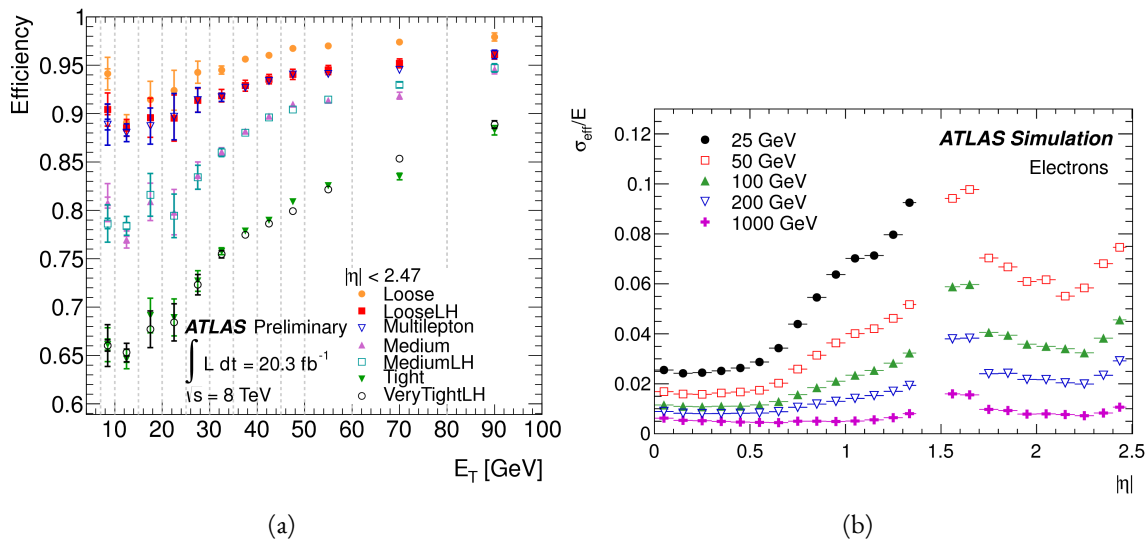


Figure 2.15: Electron performance: (a) reconstruction efficiency as a function of electron  $E_T$  [62] (b) energy resolution in simulation as a function of  $|\eta|$  for different energy electrons [63].

#### 2.4.2 MUONS

The ATLAS detector is designed to stop most particles before they reach the muon spectrometer. Muons, however, are minimum ionizing particles, meaning that they will not lose a significant amount of energy through interactions with the detector and will thus pass through. Therefore, the muon reconstruction works to match tracks in the muon spectrometer with tracks in the inner detector.

1150      The first step of reconstruction is to reconstruct local straight line tracks, called segments, in each muon  
1151      chamber. Segments are then fit to larger tracks that traverse the entire muon spectrometer. Such muon  
1152      tracks are referred to as “standalone” tracks (SA) as they only use information from the muon spectrometer.  
1153      The standalone tracks are then matched to tracks in the inner detector to form “combined” (CB) muons,  
1154      and both tracks are used to determine the momentum and direction of the muon. To improve acceptance,  
1155      segment-tagged and calorimeter-tagged muons are also reconstructed. In these cases, ID tracks are matched  
1156      to segments in the MS and calorimeter deposits consistent with a minimum ionizing particle, respectively.  
1157      The details of the reconstruction can be found in reference [64].

1158      As with electrons, once muon candidates are reconstructed they have identification criteria applied to  
1159      reduce background. These criteria include the  $\chi^2$  match between the ID and MS tracks, the number of  
1160      hits in the ID, overall ID and MS track fit quality, and additional variables. In Run 1, the muons used are  
1161      simply referred to as combined muons [64]. In Run 2, an improved reconstruction algorithm is used and  
1162      criteria ranging from “loose” to “tight” are defined (similar to what is done with electrons) [65]. Figure 2.16  
1163      shows the muon reconstruction efficiency (measured with the  $Z$  and  $J/\psi$ ) and invariant mass resolution  
1164      in  $\sqrt{s} = 8$  TeV data.

#### 1165      2.4.3 JETS

1166      When a quark or gluon is produced in collisions, it is not measured directly in ATLAS. Rather, due to  
1167      QCD effects, it produces a collimated spray of hadrons in the direction of the original parton, which is  
1168      known as a jet. Jets are reconstructed in ATLAS using energy deposits in the hadronic calorimeter. The  
1169      first step is build “topological clusters” out of energy deposits in calorimeter cells [66, 67]. This is done  
1170      using strategy where seed cells are chosen by picking cells whose energy measurements are four times the  
1171      amount of noise expected for that cell. Adjacent cells with at least  $2\sigma$  energy measurements are added to  
1172      the cluster, then a final layer of clusters with energy above  $0\sigma$  are added. Once calorimeter clusters are  
1173      formed, they are clustered further into jet candidates. The analyses presented in this thesis use the anti- $k_T$   
1174      jet clustering algorithm [68]. This algorithm defines a parameter  $R$  that appears in the denominator of  
1175      the clustering distance metric and defines the radial size of the jet in  $\eta$ - $\phi$  space.

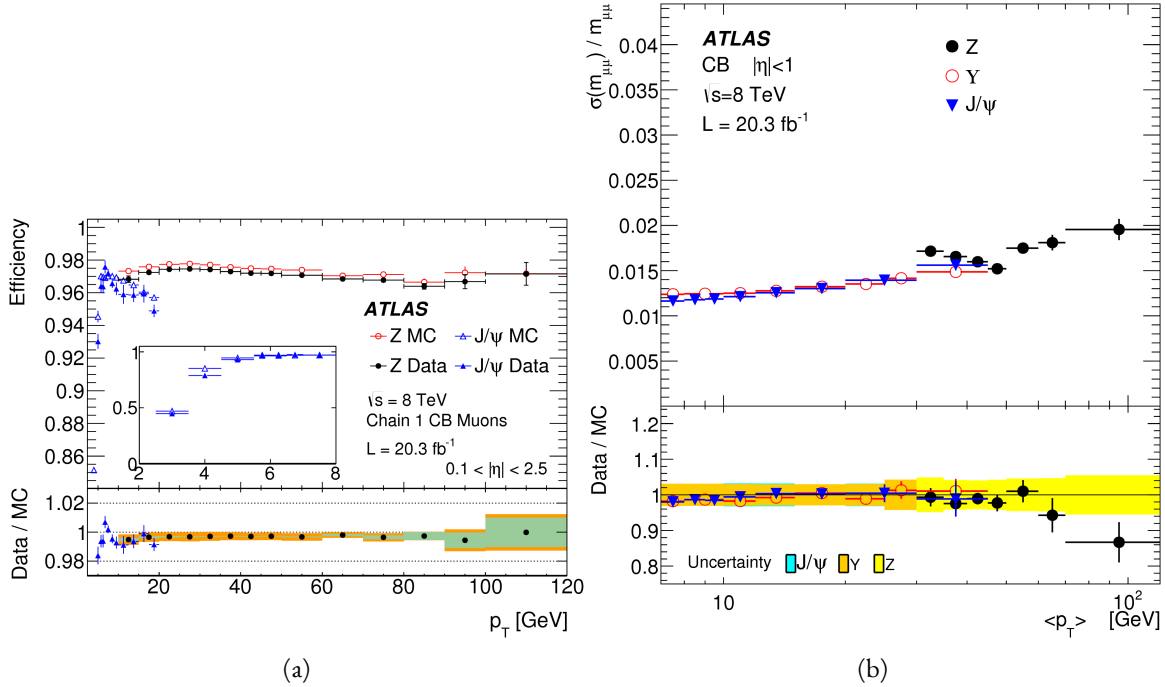


Figure 2.16: Muon performance in  $\sqrt{s} = 8$  TeV data: (a) reconstruction efficiency as a function of muon  $p_T$  (b) dimuon mass resolution as a function of average  $p_T$  [64].

The energy response of the calorimeter must be properly characterized in order to reconstruct the true jet energy. Calorimeter clusters can be calibrated either with the EM calibration, where each cluster is assumed to have come from the energy deposit of an electron or photon, or the LCW calibration, where local cluster weights are computed to allow for local calibration of clusters as hadronic or electromagnetic. The details of the jet energy calibration are not discussed here and are presented in reference [69]. Figure 2.17 shows the jet energy response after calibration in Monte Carlo as a function of the true  $p_T$  of the jet [69]. Analyses often need to know how consistent a particular jet is with the primary vertex of the event in order to avoid contamination from pileup interactions. One measure of this consistency is known as the jet vertex fraction (JVF). The JVF is the ratio of tracks associated with a primary vertex to the total number of tracks inside a jet. Jets from the primary interaction in the event should have a large fraction of tracks consistent with the primary vertex and therefore have a large JVF value.

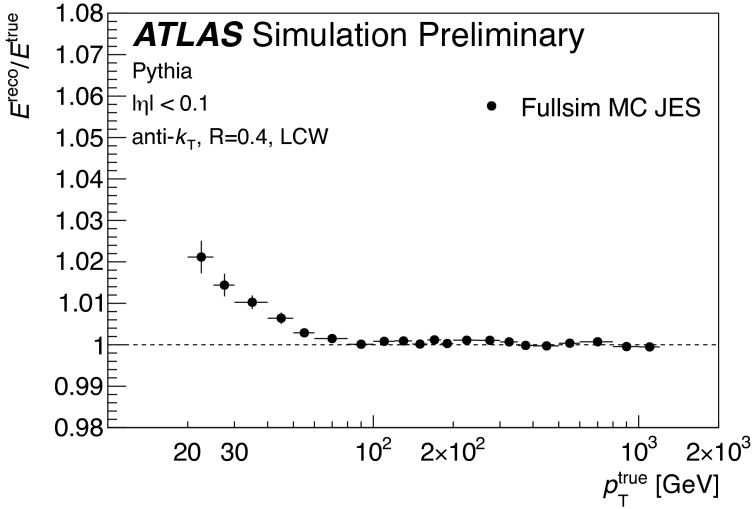


Figure 2.17: Jet energy response after calibration as a function of true  $p_T$  in simulation [69].

1187    2.4.4    *b*-TAGGING

1188    One important aspect of jet physics is the task of identifying the flavor of parton that produced the mea-  
 1189    sured jet. While in general this is very difficult, jets from *b*-quarks offer an interesting case where such  
 1190    identification is possible. *B* mesons have a lifetime on the order of  $10^{-12}$  seconds, which makes a  $c\tau$  of  
 1191    0.5 mm [6]. This type of displaced decay vertex can be identified in detectors like ATLAS and allows *b*-jets  
 1192    to be distinguished from other flavors of jets<sup>3</sup>. With boosts, *B* mesons can travel for several millimeters  
 1193    before decaying.

1194    ATLAS uses several algorithms, including a multivariate machine learning technique, to identify jets  
 1195    from *b*-quarks. The inputs to the multivariate algorithm are determined from lower level reconstruction  
 1196    algorithms. There are three distinct algorithms that reconstruct variables which are used as input to the  
 1197    multivariate technique.

1198    The first family of algorithms is referred to as IPxD (where the x can either be 2 or 3). These algorithms  
 1199    use the transverse and longitudinal impact parameters  $d_0$  and  $z_0$  of the tracks inside a jet to determine their  
 1200    consistency with the primary vertex. They use two or three dimensional (hence the x) templates for light

---

<sup>3</sup>Jets from charm quarks can also be detected in this way but they do not live quite as long so the displacement of the vertex is harder to distinguish

1201 flavor, charm, and bottom jets and then evaluate the likelihood of the jet coming from each of these types.

1202 The likelihood ratios are used as inputs to the multivariate algorithm.

1203 The next two algorithms used as input are referred to as the secondary vertex (SV) and JetFitter (JF)  
1204 algorithms. The SV algorithm uses tracks inside the jet to fit for vertices that are displaced from the pri-  
1205 mary vertex. The JF algorithm attempts to reconstruct the full flight path of the  $b$  by looking for multiple  
1206 displaced vertices along the same line (as  $B$  decays often result in subsequent charm meson decays).

1207 In Run 1, the multivariate  $b$ -tagging algorithm used a neural network and was referred to as MV1. The  
1208 details of this algorithm and its inputs are given in reference [70]. This algorithm is used for defining  
1209 a veto on  $b$ -jets in the  $H \rightarrow WW^* \rightarrow \ell\nu\ell\nu$  analysis presented in Part 2. In Run 2, the number of  
1210 inputs was simplified and a boosted decision tree with 24 input variables was used, referred to as MV2 [71].  
1211 The MV2 algorithm is a boosted decision tree incorporating twenty-four input variables constructed from  
1212 three lower level input algorithms described above. This algorithm is used for  $b$ -tagging in the  $X \rightarrow$   
1213  $HH \rightarrow b\bar{b}b\bar{b}$  search presented in Part 3. Figure 2.18 summarizes the inputs to MV2. Figure 2.19 shows the  
1214 performance of each of these algorithms in Run 1 and Run 2.

IP2D and IP3D (6 inputs)	SV1 (8 inputs)	JetFitter (8 inputs)
$\log(p_b/p_u)$	Mass	Mass
$\log(p_b/p_c)$	Energy fraction	Energy fraction
$\log(p_c/p_u)$	# tracks at vertex	# vertices
	# 2 track vertices	# tracks at vertex
	Lxy	# 1 track vertices
	L3d	# 2 track vertices
	3D significance	3D significance
	$\Delta R$	$\Delta R$
Kinematics (2 inputs)		
	$p_T$	
	$\eta$	

Figure 2.18: Summary of the inputs to the MV2  $b$ -tagging algorithm.

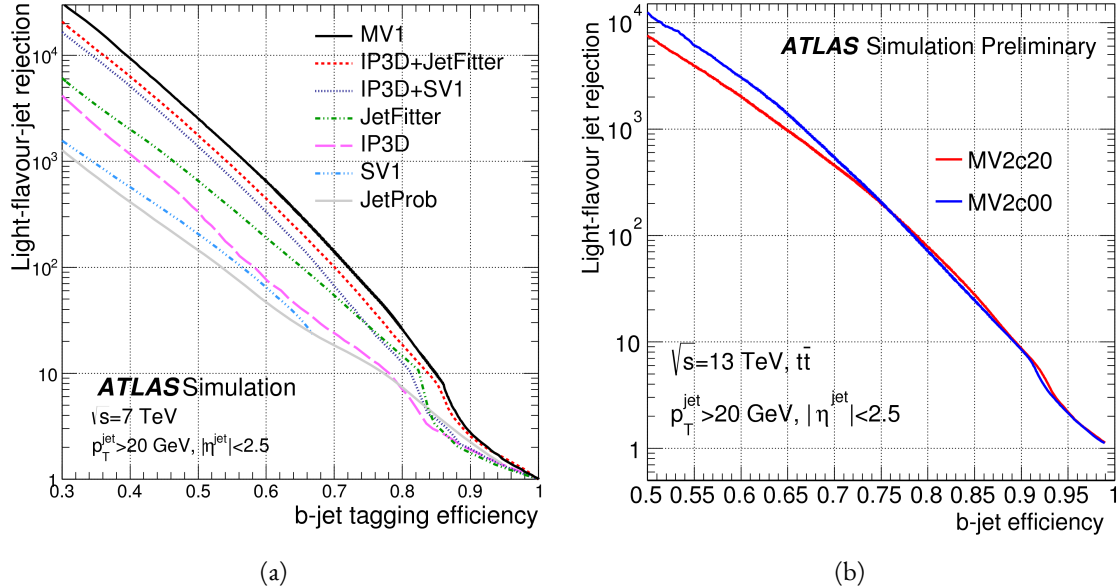


Figure 2.19: Light jet rejection ( $1/\text{efficiency}$ ) vs.  $b$ -jet efficiency for MV1 and its input algorithms (a) [70] and MV2 (b) [71] in simulated  $t\bar{t}$  events. The numbers in the algorithm names in (b) refer to the fraction of charm events used in the MV2 training.

## 1215 2.4.5 MISSING TRANSVERSE ENERGY

1216 As noted in figure 2.14, neutrinos produced in ATLAS will pass through the detector without interacting.  
1217 The only way of detecting the presence of weakly interacting particles like neutrinos (or BSM particles  
1218 that are long-lived) is to use missing transverse momentum. The basic principle of missing transverse en-  
1219 ergy is to use the momentum balance of the incoming protons to infer the presence of missing particles.  
1220 The net longitudinal momentum of the incoming partons that collide is not known (since each carries  
1221 an unknown fraction of the proton's momentum). However, the protons (and thus incoming partons)  
1222 have essentially no net momentum in the plane transverse to the beam line (the  $x$ - $y$ ) plane. Therefore, if  
1223 there are no undetected particles in the final state, the transverse momenta of all of the final state particles  
1224 should balance. The magnitude of the imbalance in the transverse plane is known as missing transverse  
1225 momentum ( $E_T^{\text{miss}}$ ).

The basic calculation of missing transverse momentum from calorimeter cells is given in equation 2.4 [72].

1227

$$\begin{aligned} E_x^{\text{miss}} &= -\sum_{i=1}^{N_{\text{cell}}} E_i \sin \theta_i \cos \phi_i \\ E_y^{\text{miss}} &= -\sum_{i=1}^{N_{\text{cell}}} E_i \sin \theta_i \sin \phi_i \end{aligned} \quad (2.4)$$

1228 The  $E_T^{\text{miss}}$  calculation is separated into different terms based on the objects that the calorimeter clusters  
 1229 are associated with. This way, each cell's contribution is calibrated appropriately according to the object.  
 1230 This separation of terms used to define the  $E_T^{\text{miss}}$  in Run 1 is shown in equation 2.5 [72].

$$\begin{aligned} E_{x(y)}^{\text{miss,calo}} &= E_{x(y)}^{\text{miss},e} + E_{x(y)}^{\text{miss},\gamma} + E_{x(y)}^{\text{miss},\tau} + E_{x(y)}^{\text{miss,jets}} \\ &\quad + E_{x(y)}^{\text{miss,softjets}} + E_{x(y)}^{\text{miss},\mu} + E_{x(y)}^{\text{miss,CellOut}} \end{aligned} \quad (2.5)$$

1231 The CellOut term of the above equation corresponds to calorimeter cells with energy deposits that are  
 1232 not associated with other objects. The soft jets term comes from cells associated to jets with  $p_T$  between  
 1233 7 and 20 GeV, while the jets term comes from jets with  $p_T > 20$  GeV. Because muons do not deposit  
 1234 significant energy in the calorimeter, the muon momentum (after correction for the energy deposited in  
 1235 the calorimeter for non-isolated muons) is used for the muon term [72]. The final  $E_T^{\text{miss}}$  is calculated using  
 1236 equation 2.6.

$$E_T^{\text{miss}} = \sqrt{(E_x^{\text{miss}})^2 + (E_y^{\text{miss}})^2} \quad (2.6)$$

1237 Figure 2.20 shows the resolution of the components of the  $E_T^{\text{miss}}$  with different pileup suppression tech-  
 1238 niques [73].

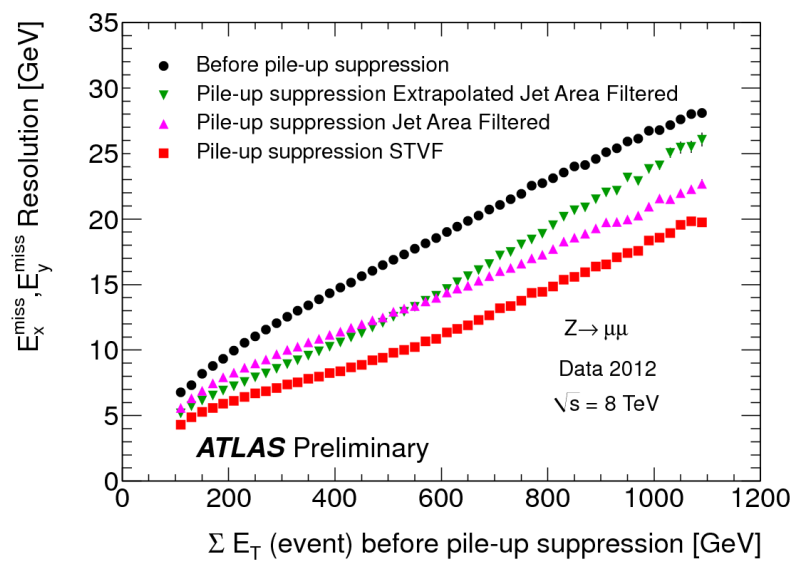


Figure 2.20: Resolution of  $E_T^{\text{miss}}$  components as a function of  $\sum E_T$  before pileup suppression with different pileup techniques [73].

1239

## Part II

1240

Observation and measurement of Higgs

1241

boson decays to  $WW^*$  in LHC Run I at

1242

$\sqrt{s} = 7$  and 8 TeV

*Basic research is what I am doing when I don't know what  
I am doing.*

Wernher von Braun

# 3

1243

1244

## $H \rightarrow WW^* \rightarrow \ell\nu\ell\nu$ Analysis Strategy

### 1245 3.1 INTRODUCTION

1246 This chapter presents an overview of the strategy for searching for a Higgs boson in the  $H \rightarrow WW^* \rightarrow$   
1247  $\ell\nu\ell\nu$  decay topology. Its purpose is to define in broad terms how the search and measurement are under-  
1248 taken, discussing common aspects of the analysis before going into the details of individual sub-categories.  
1249 First, the properties of the Higgs signal are discussed and the associated backgrounds are presented. Next,  
1250 the observables used to enhance the signal to background ratio are defined. Finally, the parameters of in-  
1251 terest in the search and measurement will be shown, along with a brief overview of the statistical treatment  
1252 of the final Higgs candidates.

1253 Following this chapter, three different results from the  $H \rightarrow WW^* \rightarrow \ell\nu\ell\nu$  channel are shown.  
1254 Chapter 4 presents the discovery and subsequent measurement of Higgs boson production in gluon fusion  
1255 mode and the role of the  $H \rightarrow WW^*$  channel. Chapter 5 shows the search and first evidence in ATLAS  
1256 for the Vector Boson Fusion (VBF) production mode of the Higgs. Finally, chapter 6 shows the combined

1257 Run 1  $H \rightarrow WW^*$  results for the measurement of the Higgs cross section and relative coupling strengths  
1258 to other SM particles.

1259 3.2 THE  $H \rightarrow WW^* \rightarrow \ell\nu\ell\nu$  SIGNAL IN ATLAS

1260 The signal studied in this and subsequent chapters is the Higgs boson in the  $WW^*$  final state, where each  
1261  $W$  boson subsequently decays into a charged lepton and a neutrino. In the simplest decay path, the final  
1262 state consists of two neutrinos and two charged leptons, each of which can be either an electron or a muon.  
1263 If a  $W$  decays to a  $\tau$  lepton, only leptonic decays of the  $\tau$  are considered. The  $\tau$  leptons produce additional  
1264 neutrinos in the final state but still yield two charged leptons (where each lepton is an electron or muon).  
1265 Neutrinos are not detected in ATLAS, so the final state ultimately consists of two reconstructed leptons  
1266 and missing transverse momentum. Final states where both of the charged leptons are electrons or muons  
1267 are referred to as the “same flavor” ( $ee/\mu\mu$ ) final states, while those with one electron and one muon are  
1268 referred to as “different flavor” ( $e\mu$  or  $\mu e$ ).

1269 There can be additional jets produced in association with the Higgs boson. As described in detail in  
1270 Chapter 1, if the Higgs is produced via vector boson fusion production, there will be two additional forward  
1271 jets in the event. In gluon fusion, one or more jets can be produced through initial state radiation from  
1272 the incoming gluons. Because of the varying background composition as a function of jet multiplicity,  
1273 each bin in this variable has its own dedicated requirements applied in the search and measurement. The  
1274  $n_j = 0$  and  $n_j = 1$  bins are dedicated to gluon fusion production, while the  $n_j \geq 2$  bin has separate  
1275 dedicated searches for ggF and VBF production.

1276 Figure 3.1 shows the relative branching fractions for the  $H \rightarrow WW^*$  process, calculated from the Par-  
1277 ticle Data Group values for the  $W$  and  $\tau$  branching ratios [6]. The largest branching ratio corresponds  
1278 to both  $W$  bosons decaying to quark pairs at 45.44%. The second largest ratio is for one  $W$  decaying lep-  
1279 tonically and the other decaying to quarks, a branching ratio of 34.18%. In all cases,  $\ell$  denotes either an  
1280 electron or muon, and the leptonic branching ratios of the  $\tau$  are included. For example, the  $\ell\nu qq$  final  
1281 state includes one  $W$  decaying to  $e\nu$ ,  $\mu\nu$ , or  $\tau\nu$ . In the case of the  $W \rightarrow \tau\nu$  decay, the  $\tau$  lepton then  
1282 decays to an electron or muon via  $\tau \rightarrow \nu_\tau \ell \nu_\ell$ . Final states with a  $\tau_h$  refer to hadronic decays of the  $\tau$ . The



Figure 3.1: Branching ratios for a  $WW$  system.  $q$  refers to quarks.  $\ell$  can be either an electron or muon, and the leptonic branching ratios of the  $\tau$  are included. For example, the  $\ell\nu qq$  final state includes one  $W$  decaying to  $e\nu$ ,  $\mu\nu$ , or  $\tau\nu$ .  $\tau_h$  refer to hadronic decays of the  $\tau$ .

branching ratio of the  $\ell\nu\ell\nu$  final state is 6.43%.

While the  $\ell\nu\ell\nu$  final state is not a large fraction of the branching ratio, there are significant advantages to using this channel in an analysis. First, both the  $qqqq$  and  $\ell\nu qq$  channels suffer from a large QCD multijet background, which is often difficult to model. Second, events in the the  $\ell\nu\ell\nu$  channel in data can be triggered more efficiently due to the presence of two leptons.

Figure 3.2 delineates the different signal regions used in the gluon fusion and vector boson fusion analyses of  $H \rightarrow WW^*$ . Signal regions are defined using jet multiplicity and the flavor combination of the final state leptons.

### 3.3 BACKGROUND PROCESSES

Many processes from the Standard Model can also produce a final state with two leptons and missing transverse momentum. This section describes the dominant backgrounds to Higgs production and further explains how they can be reduced. Table 3.1 summarizes the different background processes.

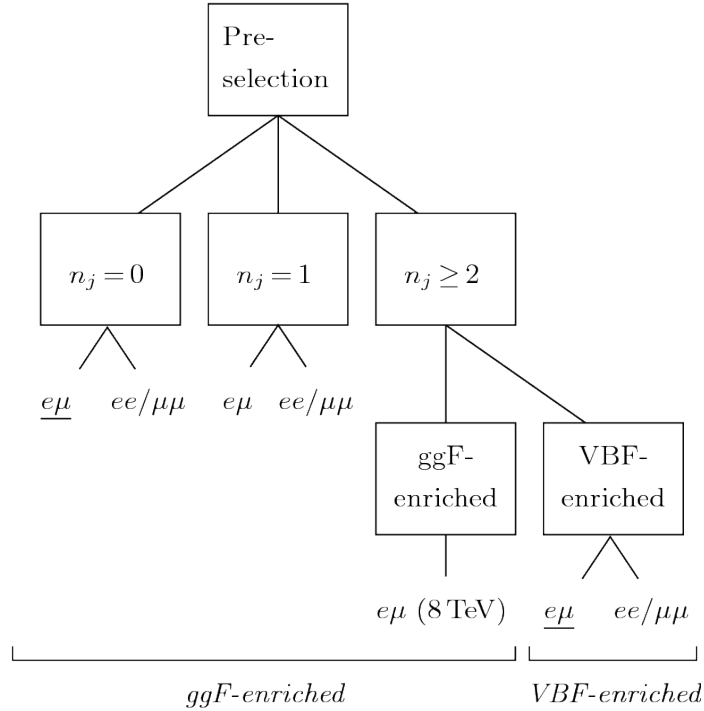


Figure 3.2: An illustration of the unique analysis signal regions [74]. The most sensitive regions for both gluon fusion and vector boson fusion production are underlined.

1295 3.3.1 STANDARD MODEL WW PRODUCTION

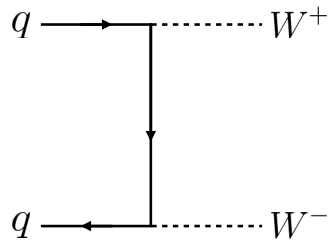


Figure 3.3: Feynman diagram for Standard Model WW production

1296 Non-resonant Standard Model diboson production, as shown in figure 3.3, is an irreducible background  
1297 to Higgs boson production in the WW final state. It produces the same exact final state objects, namely  
1298 leptonically decaying W bosons. There are no additional objects in the final state that allow for back-  
1299 ground reduction. Therefore the analysis solely relies on the correlations between the leptons to reduce  
1300 this background.

1301    3.3.2    TOP QUARK PRODUCTION

1302    Top quark production can mimic the Higgs in the  $WW^*$  final state as well. Top quarks can be produced  
1303    either in pairs ( $t\bar{t}$  production) or singly ( $s$ -channel,  $t$ -channel, or associated production  $Wt$ ). The domi-  
1304    nant top background are  $t\bar{t}$  and  $Wt$  production.

1305    Because top quarks decay via  $t \rightarrow Wb$ , top pair production can produce a final state with two  $W$  bosons  
1306    that then decay leptonically. In  $Wt$  production, there are two real  $W$  bosons produced, as with  $t\bar{t}$ . In  
1307    both cases, there is at least one  $b$ -jet in the final state. By vetoing on the presence of  $b$ -jets, these top quark  
1308    backgrounds can be reduced. Figure 3.4 shows the Feynman diagrams for  $t\bar{t}$  and  $Wt$  production.

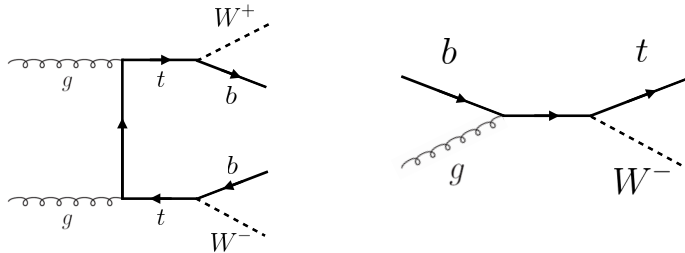


Figure 3.4: Feynman diagrams for top pair production (left) and  $Wt$  production (right)

1309    3.3.3     $W$ +JETS BACKGROUND

1310    Single  $W$  boson production in association with jets is a unique background to Higgs production. The  
1311    other backgrounds considered thus far have all included two prompt leptons, each decaying from a  $W$   
1312    boson, in the final state. In  $W$ +jets production, however, only one reconstructed lepton originates from  
1313    a  $W$ . The second reconstructed lepton is either an algorithmic “fake” or the result of non-prompt decays.  
1314    In the first case, the lepton is a jet misidentified as a lepton by either the electron or muon reconstruction  
1315    algorithms. In the second case, the lepton may be a real lepton but coming from semi-leptonic decays of  
1316    particles inside the shower of the jet. This background can be reduced by requiring that the reconstructed  
1317    lepton have little activity in the surrounding region of the calorimeter (also known as an “isolation”). Fig-  
1318    ure 3.5 shows the Feynman diagram for  $W$ +jets production.

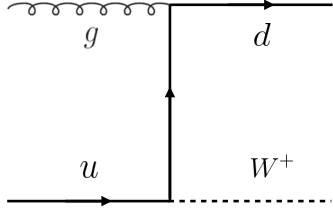


Figure 3.5: An example Feynman diagram of  $W$ +jets production

### 1319 3.3.4 $Z/\gamma^*$ +JETS BACKGROUND

1320 Production of a  $Z$  boson or virtual photon (also known as Drell-Yan and denoted with  $Z/\gamma^*$ ) in associa-  
1321 tion with jets is also a background to Higgs production. The  $Z$  boson decays to two leptons of the same  
1322 flavor. However, the background is present in both the same flavor and different flavor samples. When the  
1323  $Z/\gamma^*$  decays directly to electrons or muons, the background enters the same flavor final state sample, and  
1324 when it decays to two  $\tau$  leptons the background can enter the different flavor sample as well. Figure 3.6  
1325 shows the production of a  $Z$  in association with one jet. Because there are no neutrinos in this final state,  
1326 variables like  $E_T^{\text{miss}}$  can be used to reduce the background<sup>1</sup>.

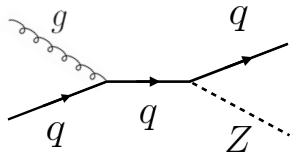


Figure 3.6: An example Feynman diagram of  $Z$ +jets production

### 1327 3.3.5 SUBDOMINANT BACKGROUNDS

1328 There are additional processes which contribute to the background composition. These backgrounds are  
1329 subdominant and contribute less to the total background estimate than those discussed previously. The

---

<sup>1</sup>The  $E_T^{\text{miss}}$  cut is much more effective for the reduction of  $Z/\gamma^*$  production in the same flavor final state. If the background enters the different flavor final state through  $\tau$  decays, there will be neutrinos present. Other requirements on the lepton invariant mass are made to reduce the  $Z/\gamma^* \rightarrow \tau\tau$  background.

1330 first process is referred to as  $VV$  or “Other diboson” processes and includes multiple Standard Model  
 1331 diboson processes, including  $WZ$ ,  $ZZ$ ,  $W\gamma$ ,  $W\gamma^*$ , and  $Z\gamma$  production. Additionally, there is a back-  
 1332 ground contribution from QCD multijet production. While the cross section for this process is large, its  
 1333 contribution to the  $WW^*$  final state is small because two jets must be misidentified as leptons.

Category	Process	Description
SM $WW$	$WW \rightarrow \ell\nu\ell\nu$	Real leptons and neutrinos
Top quark production	$t\bar{t} \rightarrow WbW\bar{b} \rightarrow \ell\nu b\bar{b}\nu\bar{b}$	Real leptons, untagged $b$ s
	$tW \rightarrow WbW \rightarrow \ell\nu b\nu b$	Real leptons, untagged $b$
	$t\bar{b}, t\bar{q}\bar{b}$	Untagged $b$ , jet misidentified as lepton
Drell-Yan	$Z/\gamma^* \rightarrow ee, \mu\mu$	“Fake” $E_T^{\text{miss}}$
	$Z/\gamma^* \rightarrow \tau\tau \rightarrow \ell\nu\nu\ell\nu\nu$	Real leptons and neutrinos
Other dibosons	$ZZ \rightarrow \ell\ell\nu\nu$	Real leptons and neutrinos
	$W\gamma^*, WZ \rightarrow \ell\nu\ell\ell, ZZ \rightarrow \ell\ell\ell\ell$	Unreconstructed leptons
	$W\gamma, Z\gamma$	$\gamma$ reconstructed as $e$ , unreconstructed lepton
$W + \text{jets}$	$Wj \rightarrow \ell\nu j$	Jet reconstructed as lepton
QCD multijet	$jj$	Jets reconstructed as leptons

Table 3.1: A summary of backgrounds to the  $H \rightarrow WW^* \rightarrow \ell\nu\ell\nu$  signal

### 1334 3.4 SHARED SIGNAL REGION SELECTION REQUIREMENTS

1335 As presented in section 3.2, there are many different combinations of physics objects that can define a  
 1336  $H \rightarrow WW^* \rightarrow \ell\nu\ell\nu$  final state. The multiplicity of jets and the flavor combinations of the leptons  
 1337 both lead to many potential signal regions. Additionally, signal regions can be optimized separately to be  
 1338 sensitive to the distinct production modes of the Higgs. Gluon fusion, vector boson fusion, and associated  
 1339 production of a Higgs all lead to unique final state topologies. While there are different optimizations  
 1340 possible in each signal region, there are also some commonly shared selections that will be described here.

#### 1341 3.4.1 EVENT PRE-SELECTION

1342 Before being sorted into the distinct signal regions, basic requirements are applied to the reconstructed  
 1343 objects in the event to select Higgs-like event candidates. First, two oppositely charged leptons are required.  
 1344 Once the leptons are selected, the last requirement for event pre-selection is the presence of neutrinos.  
 1345  $E_T^{\text{miss}}$  is used as a proxy for the combined neutrino momentum in the transverse plane.

1346 In general, the signal tends to have higher values of  $E_T^{\text{miss}}$  than backgrounds, especially if these back-  
 1347 grounds do not contain neutrinos in the final state. It is possible mis-measurements of objects in the detec-  
 1348 tor can lead to imbalances in the transverse plane. When such a mis-measurement occurs, the  $E_T^{\text{miss}}$  vector  
 1349 in the transverse plane will often point in the same direction as the mis-measured object. Therefore, a new  
 1350 variable,  $E_{T,\text{rel}}^{\text{miss}}$ , is used in the pre-selection.  $E_{T,\text{rel}}^{\text{miss}}$  is defined in equation 3.1.

$$E_{T,\text{rel}}^{\text{miss}} = \begin{cases} E_T^{\text{miss}} \sin \Delta\phi_{\text{near}} & \text{if } \Delta\phi_{\text{near}} < \pi/2 \\ E_T^{\text{miss}} & \text{otherwise,} \end{cases} \quad (3.1)$$

1351 If the closest object to the  $E_T^{\text{miss}}$  vector is within  $\pi/2$  radians in the transverse plane, the  $E_T^{\text{miss}}$  is projected  
 1352 away from this object. Otherwise, the normal  $E_T^{\text{miss}}$  vector is used. Figure 3.7 shows a graphical illustration  
 of this concept.

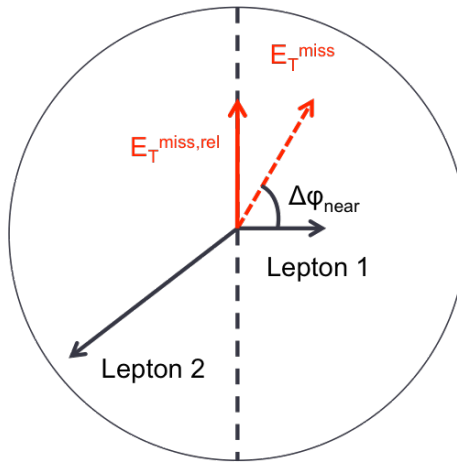


Figure 3.7: A graphical illustration of the  $E_{T,\text{rel}}^{\text{miss}}$  calculation.

1353  
 1354 Once the lepton and  $E_T^{\text{miss}}$  pre-selections are made, the analysis is divided into different regions accord-  
 1355 ing to jet multiplicity.

#### 1356 3.4.2 JET MULTIPLICITY

1357 Jet multiplicity, denoted as  $n_j$ , is used to sub-divide the analysis into distinct signal regions. By creating  
 1358 separate signal regions, each bin in jet multiplicity becomes sensitive to different modes of Higgs produc-  
 1359 tion and different backgrounds. For example, the  $n_j \geq 2$  region is more sensitive to VBF production

1360 because of the two high momentum jets produced at matrix element level. For gluon fusion production  
1361 to enter this bin, two initial state radiation jets must be emitted.

1362 Figure 3.8 shows the jet multiplicity in both the different flavor and same flavor regions after the pre-  
1363 selection. It also shows the background composition in the bins of the number of  $b$ -tagged jets,  $n_b$ . A  
1364 few trends from this distribution are worth noting. The first is that the Drell-Yan background dominates  
1365 in the same flavor channels for  $n_j \leq 1$ . Second, the top background becomes a clear contributor to the  
1366 total background for  $n_j \geq 1$ . Lastly, the SM WW production dominates in the  $n_j = 0$  bin, as it is an  
1367 irreducible background to  $H \rightarrow WW^*$  production. Because of these distinct features, each jet multiplicity  
1368 bin is treated separately.

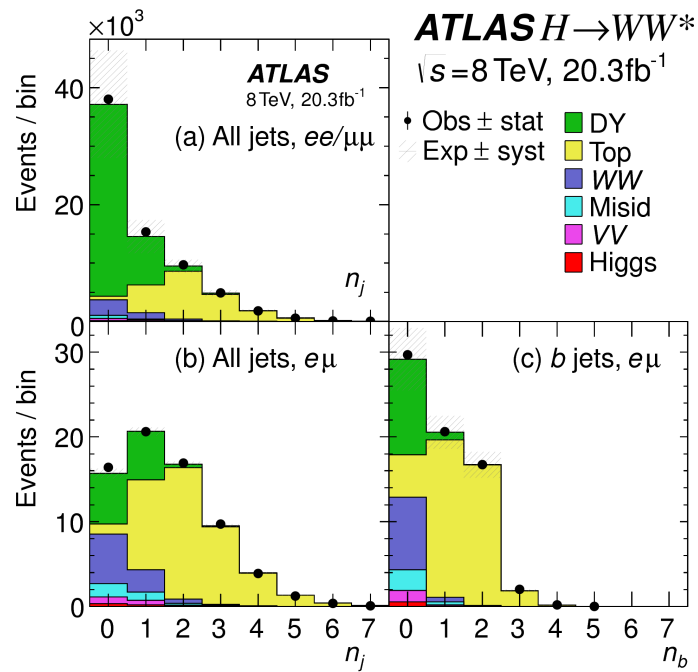


Figure 3.8: Predicted backgrounds (compared with data) as a function of the number of jets,  $n_j$  (a and b), and the number of  $b$ -tagged jets,  $n_b$  (c), after pre-selection requirements. Panel a shows  $n_j$  in the same flavor sample, while panels b and c show the  $n_j$  and  $n_b$  distributions in the different flavor sample.

1369 3.5 BACKGROUND REDUCTION IN SAME-FLAVOR FINAL STATES

1370 As described in section 3.4.2, the background composition of the same flavor final states is different from  
1371 that of the different flavor states. In particular, Drell Yan processes play a much larger role because the

1372  $Z/\gamma^*$  decays to same flavor leptons. Because real neutrinos are absent in the  $Z/\gamma^*$  decays to  $ee$  and  $\mu\mu$ , a  
1373 requirement on  $E_T^{\text{miss}}$  should largely reduce the background. However, as this section will demonstrate,  
1374 with increasing pileup conditions the resolution of the calorimeter-based  $E_T^{\text{miss}}$  degrades greatly. There-  
1375 fore, two new variables for  $Z/\gamma^*$  background reduction are constructed and described in this section.

1376 **3.5.1 PILEUP AND  $E_T^{\text{miss}}$  RESOLUTION**

1377 Secondary interactions of protons in the colliding bunches of the LHC (known as pileup interactions,  
1378 described in detail in Chapter 2) deposit energy into the ATLAS calorimeter in addition to the energy that  
1379 comes from the hard scatter process of interest. The calculation of  $E_T^{\text{miss}}$  is fundamentally like a Poisson  
1380 process - summing up all of the energy deposits in individual calorimeter cells or clusters is similar to a  
1381 counting experiment. The error on a mean of  $N$  in a Poisson distribution is  $\sqrt{N}$ , so the energy resolution  
1382 scales as  $\sqrt{E}$ . As more energy is deposited in the calorimeter, the  $E_T^{\text{miss}}$  resolution degrades, meaning that  
1383 the  $E_T^{\text{miss}}$  resolution is particularly sensitive to LHC instantaneous luminosity conditions.

1384 Figure 3.9 shows an event display of a  $Z/\gamma^* + \text{jets}$  event candidate with the twenty-five reconstructed  
1385 primary vertices. This display illustrates that while the interaction of interest only has tracks coming from  
1386 the hardest primary vertex, all of the secondary interactions deposit energy in the calorimeter as well.

1387 Figure 3.10 shows the RMS of the  $E_T^{\text{miss}}$  distribution in  $Z \rightarrow \mu\mu$  events (where there are no real neu-  
1388 trinos) as a function of the number of the average number of interactions. Under 2011 LHC conditions,  
1389 this RMS was approximately 9 GeV, while under 2012 running conditions the resolution worsened to 12  
1390 GeV. The increase in pileup dilutes the ability of the  $E_T^{\text{miss}}$  variable to reduce the  $Z/\gamma^*$  background.

1391 **3.5.2 TRACK-BASED DEFINITIONS OF MISSING TRANSVERSE MOMENTUM**

1392 Because the increasing number of secondary proton-proton interactions degrades calorimeter-based  $E_T^{\text{miss}}$   
1393 resolution, a new variable using only contributions from the primary interaction vertex is necessary to  
1394 further reduce the  $Z/\gamma^*$  background. While it is not possible to associate calorimeter energy deposits  
1395 with a particular vertex, individual charged particle tracks in the Inner Detector are associated to unique  
1396 vertices. Thus, two track-based definitions of missing transverse momentum, using only tracks coming

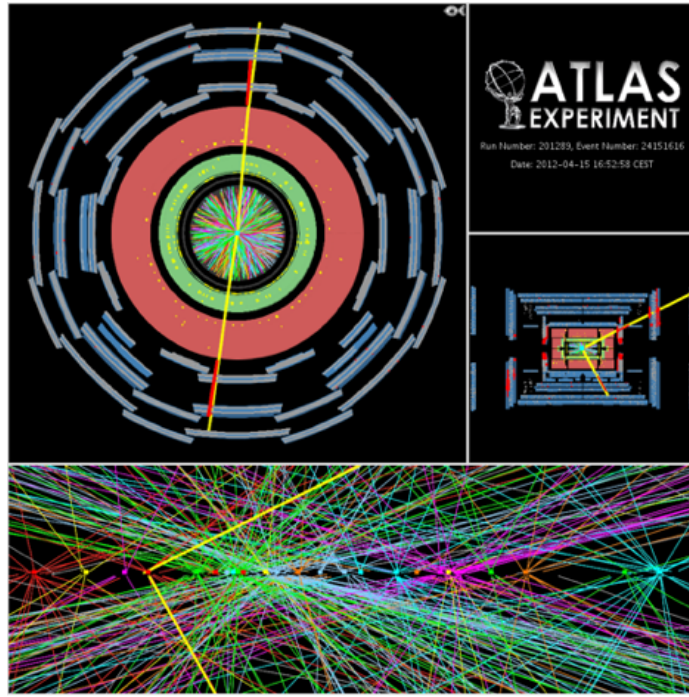


Figure 3.9: An event display of a  $Z/\gamma^* + \text{jets}$  event illustrating the effect of pileup interactions

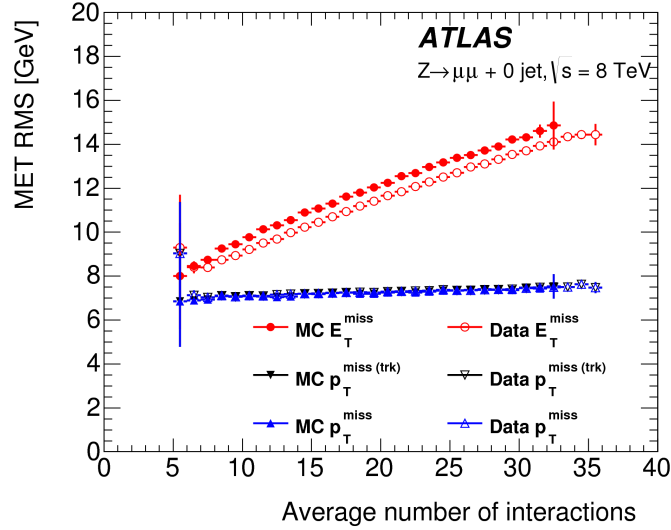


Figure 3.10: The RMS of different missing transverse momentum definitions as a function of the average number of interactions per bunch crossing

from the primary vertex in the event, are used in the analysis. These variables are not intended to substitute  $E_T^{\text{miss}}$ , as they only account for charged particles and do not measure neutrals. However, the track-based variables serve as a confirmation that any measured momentum imbalance is coming from real particles

1400 and not detector effects. The simplest variable,  $p_T^{\text{miss}(\text{trk})}$ , is the vectorial sum of the  $p_T$  of all of the tracks  
 1401 from the primary vertex and the selected leptons (excluding the tracks associated with the selected leptons  
 1402 to avoid double counting). Equation 3.2 defines  $p_T^{\text{miss}(\text{trk})}$ .

$$p_T^{\text{miss}(\text{trk})} = - \left( \sum_{\text{selected leptons}} p_T + \sum_{\text{other tracks}} p_T \right), \quad (3.2)$$

1403 To further improve the resolution on the missing transverse momentum, the variable  $p_T^{\text{miss}}$  is used as de-  
 1404 fined in equation 3.3. For selected leptons and jets, the nominal  $p_T$  measurements are used, as the calorime-  
 1405 ter information improves the  $p_T$  resolution of the objects by taking into account the presence of neutral  
 1406 particles in showers. The soft component of the missing transverse momentum, which is more suscep-  
 1407 tible to spurious contributions from pileup interactions, is estimated using tracks instead of calorimeter  
 1408 measurements.

$$p_T^{\text{miss}} = - \left( \sum_{\text{selected leptons}} p_T + \sum_{\text{selected jets}} p_T + \sum_{\text{other tracks}} p_T \right), \quad (3.3)$$

1409 Figure 3.10 illustrates that these two new variables accomplish their intended purpose. The resolution as a  
 1410 function of mean number of interactions for both  $p_T^{\text{miss}(\text{trk})}$  and  $p_T^{\text{miss}}$  is much flatter than the dependence  
 1411 for  $E_T^{\text{miss}}$ . Figure 3.11a shows the difference between the true and reconstructed values of missing transverse  
 1412 momentum using both the track-based  $p_T^{\text{miss}}$  and calorimeter based  $E_T^{\text{miss}}$ . The RMS of the distribution  
 1413 improves by 3.5 GeV when using  $p_T^{\text{miss}}$ .

### 1414 3.5.3 DISTINGUISHING $Z/\gamma^*$ +JETS AND $H \rightarrow WW^*$ TOPOLOGIES

1415 In addition to measuring missing transverse momentum, another variable can be constructed to exploit  
 1416 kinematic and topological differences between the  $Z/\gamma^*$  background and  $H \rightarrow WW^*$  signal. Because  
 1417 there are no real neutrinos in the final state (in the case of  $Z/\gamma^* \rightarrow ee, \mu\mu$  decays), the dilepton system  
 1418 will be balanced with the jets produced in the hard scatter. A new variable,  $f_{\text{recoil}}$ , is constructed to es-  
 1419 timate the balance between the dilepton system and recoiling jets and is defined in equation 3.4. The  
 1420 transverse plane is divided into four sections, or quadrants, with one quadrant centered on the dilepton

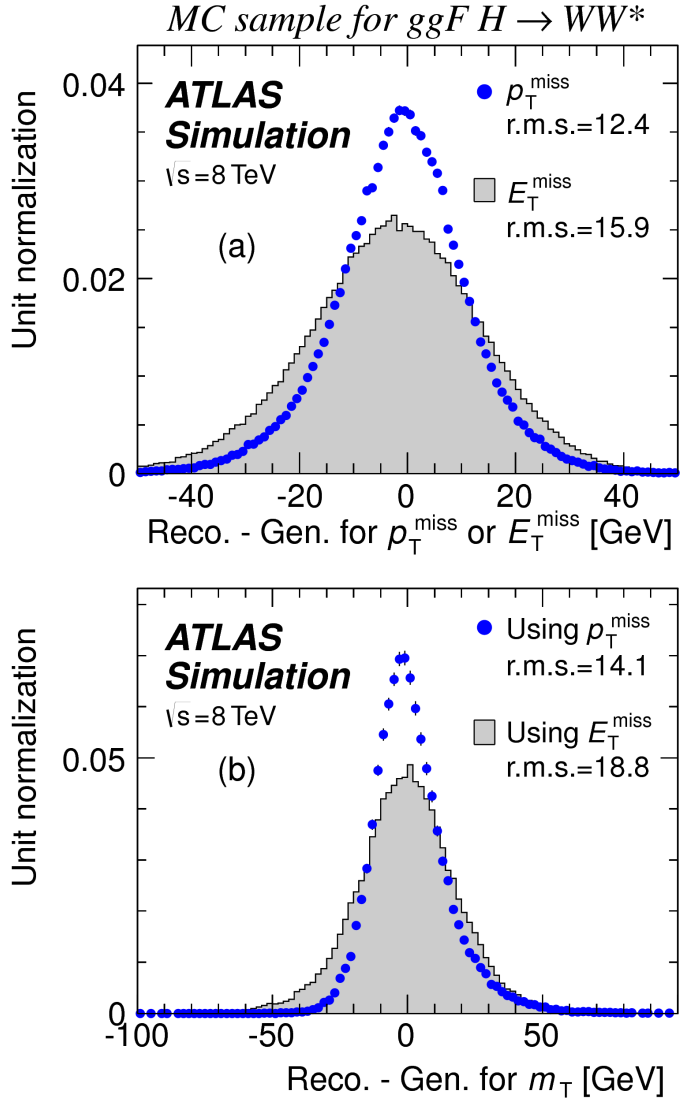


Figure 3.11: The difference between the true and reconstructed values of the missing transverse momentum (a) and  $m_T$  (b) in a gluon fusion signal sample using both track-based ( $p_T^{\text{miss}}$ ) and calorimeter-based  $E_T^{\text{miss}}$  definitions.

vector. The numerator of  $f_{\text{recoil}}$  is the magnitude of the vectorial sum of the  $p_T$  of jets in the quadrant opposite the dilepton system, weighted the Jet Vertex Fraction (JVF, described in chapter 2) of each jet. The denominator is the magnitude of the dilepton  $p_T$ .

$$f_{\text{recoil}} = \left| \sum_{\text{jets } j \text{ in } \wedge} \text{JVF}_j \cdot \mathbf{p}_T^j \right| / p_T^{\ell\ell}. \quad (3.4)$$

1424 Figure 3.12 shows a shape comparison of the  $f_{\text{recoil}}$  distribution in a simulated  $Z/\gamma^* + \text{jets}$  sample, a  
 1425  $H \rightarrow WW^*$  signal sample, and other backgrounds that contain real neutrinos. The  $Z/\gamma^* + \text{jets}$  events  
 1426 tend to be more balanced between the dilepton system and recoiling jets, while the processes containing  
 1427 real neutrinos are less balanced in the transverse plane. Thus, a requirement on  $f_{\text{recoil}}$  will reduce the  $Z/\gamma^*$   
 1428 + jets background while maintaining a good signal efficiency.

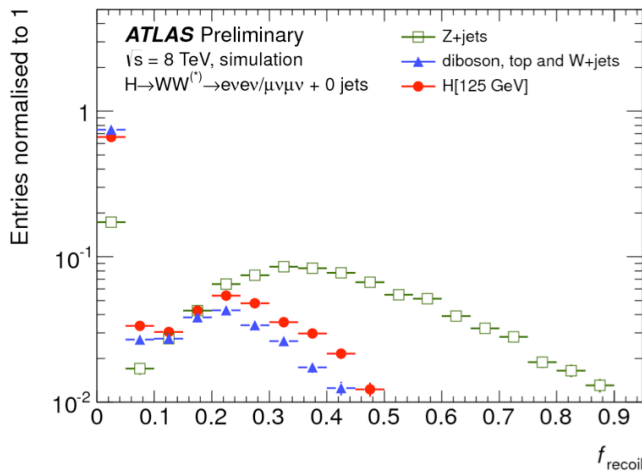


Figure 3.12: Comparison of  $f_{\text{recoil}}$  distributions for  $Z/\gamma^* + \text{jets}$ ,  $H \rightarrow WW^*$ , and other backgrounds with real neutrinos.

#### 1429 3.5.4 OPTIMIZING BACKGROUND REDUCTION SELECTION REQUIREMENTS

1430 The requirements on  $p_T^{\text{miss}(\text{trk})}$  and  $f_{\text{recoil}}$  used to reduce the  $Z + \text{jets}$  background must be optimized to  
 1431 maximize expected signal significance in the same flavor channels. Figure 3.13 shows an optimization of the  
 1432 combination of the two requirements in the gluon fusion zero jet bin. Each bin shows the expected signal  
 1433 significance if the  $p_{T,\text{rel}}^{\text{miss}(\text{trk})}$  (the track-based version of  $E_{T,\text{rel}}^{\text{miss}}$ ) is required to be greater than the left edge  
 1434 of the bin and the  $f_{\text{recoil}}$  is required to be less than the top edge of the bin. The figure shows that the best  
 1435 signal significance comes from requiring low values of  $f_{\text{recoil}}$  ( $< 0.05$ ) and  $p_{T,\text{rel}}^{\text{miss}(\text{trk})}$  values greater than  
 1436 45 GeV.

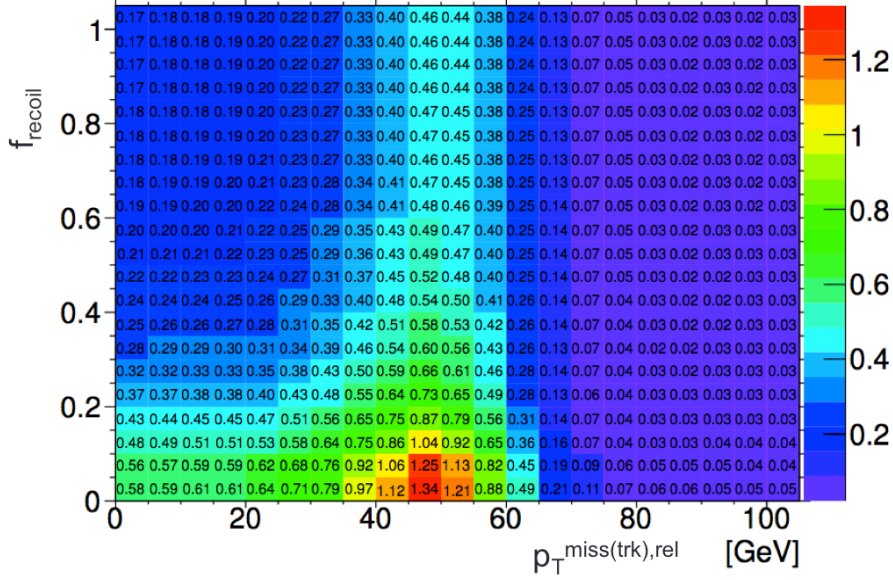


Figure 3.13: Signal significance as a function of required value for  $f_{\text{recoil}}$  and  $p_{T,\text{rel}}^{\text{miss}(\text{trk})}$  in the ggF  $H \rightarrow WW^*$  with  $n_j = 0$

### 1437 3.6 PARAMETERS OF INTEREST AND STATISTICAL TREATMENT

1438 As with any search or measurement, there are particular parameters of the Higgs that the  $H \rightarrow WW^*$   
 1439 analysis is interested in measuring. In this case, the parameters of interest are the mass of the Higgs boson  
 1440 and its production cross section. In the  $H \rightarrow WW^* \rightarrow \ell\nu\ell\nu$  final state, it is not possible to measure  
 1441 the full invariant mass of the Higgs due to the presence of neutrinos. However, a proxy for the invariant  
 1442 mass is defined using transverse plane information and detailed in section 3.6.1. The second parameter of  
 1443 interest is the cross section  $\sigma$ , which in this analysis is measured relative to the theoretical prediction for a  
 1444 Standard Model Higgs. This ratio,  $\mu$ , is defined in equation 3.5.

$$\mu = \frac{\sigma}{\sigma_{\text{SM}}} \quad (3.5)$$

1445 All of the likelihoods used in the statistical analysis of the final signal region events are parameterized as a  
 1446 function of  $\mu$ .  $\mu$  is a natural variable for hypothesis testing, as  $\mu = 0$  corresponds to a background only  
 1447 hypothesis and  $\mu = 1$  corresponds exactly to a Standard Model Higgs.

1448    3.6.1 TRANSVERSE MASS

1449    The  $H \rightarrow WW^* \rightarrow \ell\nu\ell\nu$  analysis cannot reconstruct the full invariant mass of the Higgs because of the  
1450    neutrinos in the final state. The transverse mass serves as a proxy for the full invariant mass by exploiting  
1451    information from the transverse plane. The transverse mass is defined in equation 3.6.

$$m_T = \sqrt{(E_T^{\ell\ell} + p_T^{\text{miss}})^2 - |\vec{p}_T^{\ell\ell} + \vec{p}_T^{\text{miss}}|^2}, \quad (3.6)$$

1452    Here the  $E_T^{\ell\ell}$  and  $p_T^{\ell\ell}$  are the transverse energy and momentum of the dilepton system, while  $p_T^{\text{miss}}$  is a  
1453    proxy for the transverse momentum of the di-neutrino system. The track-based  $p_T^{\text{miss}}$  is used in the  $m_T$   
1454    rather than the calorimeter based  $E_T^{\text{miss}}$  because it has a better resolution on the true transverse mass.  
1455    Figure 3.11b shows the improvement in the RMS of the difference between the true and reconstructed  
1456    transverse mass in a ggF signal sample. The RMS improves by 4.7 GeV using  $p_T^{\text{miss}}$  in the  $m_T$  calculation.

1457    3.6.2 STATISTICAL TREATMENT

1458    LIKELIHOOD FUNCTION

1459    The statistical analysis<sup>2</sup> of final event candidates is framed as a hypothesis test, where the null hypothesis is  
1460    background-only (no Standard Model Higgs). The first step in the analysis is to form a likelihood function  
1461    for the data. In its simplest form, this likelihood is the probability of observing the number of events seen  
1462    in the final signal region given knowledge of the signal strength. Because observation of events is funda-  
1463    mentally a Poisson counting experiment, this simple likelihood can be expressed as a Poisson probability of  
1464    observing  $N$  events given a total number of predicted signal and background events. This basic likelihood  
1465    is shown in equation 3.7.

$$\mathcal{L}(\mu) = P(N|\mu S + B) \quad (3.7)$$

1466    Here,  $P$  is the Poisson probability density function,  $N$  is the total number of observed events,  $\mu$  is the  
1467    signal strength,  $S$  is the predicted number of signal events, and  $B$  is the predicted number of background  
1468    events.

---

<sup>2</sup>Many thanks to Aaron Armbruster, whose thesis [75] inspired parts of this section.

1469      Generally, in searches, certain background estimates are commonly normalized in so-called “control” re-  
 1470      gions and those predictions are scaled by the same normalization factor in the signal region. This method  
 1471      allows for more precise background estimation by using data as a constraint, reducing the impact of theo-  
 1472      retical uncertainties on the background model. This leads to a slightly more complicated likelihood, which  
 1473      is a function of both the signal strength and the background normalization. This is shown in equation 3.8.

1474

$$\mathcal{L}(\mu, \theta) = P(N|\mu S + \theta B) P(N_{\text{CR}}|\theta B_{\text{CR}}) \quad (3.8)$$

1475      Here,  $\theta$  serves as a “nuisance parameter”, or a parameter that is not of primary interest but still enters the  
 1476      likelihood. The second Poisson term enforces that the background normalization be consistent with the  
 1477      number of observed events in data in the control region,  $N_{\text{CR}}$ .

1478      So far, these two formulations of likelihoods have assumed a single signal region and do not take into  
 1479      account any shape information of potential discriminating variables. The  $H \rightarrow WW^*$  analysis is divided  
 1480      into many different categories, and the counting experiment described above can be performed in each  
 1481      individual category. As mentioned in section 3.6.1, the transverse mass is used as the primary discriminating  
 1482      variable in many of the  $H \rightarrow WW^*$  signal regions. The same counting experiment can be performed  
 1483      in each bin of the  $m_T$  distribution to incorporate some shape information. Thus, the total likelihood  
 1484      becomes a product over signal regions and bins of the  $m_T$  distribution. Finally, there are usually many  
 1485      background sources that are normalized in control regions. The new formulation of the likelihood takes  
 1486      this into account by including a product over control regions in the second Poisson term. All of these  
 1487      modifications are shown in equation 3.9.

$$\mathcal{L}(\mu, \theta) = \prod_{\substack{\text{SRs } i \\ \text{bins } b}} P\left(N_{ib} \middle| \mu S_{ib} + \sum_{\text{bkg } k} \theta_k B_{kib}\right) \prod_{\text{CRs } l} P\left(N_l \middle| \sum_{\text{bkg } k} \theta_k B_{kl}\right) \quad (3.9)$$

1488      Here, the variable  $i$  counts over the different signal regions,  $b$  counts over bins of  $m_T$ ,  $k$  counts over the  
 1489      backgrounds, and  $l$  counts over the control regions.

1490      The final step to obtain the full likelihood used in the analysis is to add nuisance parameters for the  
 1491      systematic uncertainties. In cases where the uncertainty does not affect the shape of  $m_T$  bin-by-bin, each

systematic uncertainty  $\epsilon$  is allowed to affect the expected event yields through a linear response function of the nuisance parameter, namely  $\nu(\theta) = (1 + \epsilon)\theta$ . If instead the uncertainty does affect the shape, the effect is instead parameterized by  $\nu_b(\theta) = 1 + \epsilon_b\theta$ . The value of the nuisance parameters for the systematic uncertainty are constrained with a Gaussian term that is added to the likelihood as well. This is of the form  $g(\delta|\theta) = e^{-(\delta-\theta)^2/2}/\sqrt{2\pi}$ , where  $\delta$  is the central value and  $\theta$  is a nuisance parameter. Finally, a last term is added to account for the statistical uncertainty in the Monte Carlo samples used, which adds an additional poisson term. The full likelihood used in the final statistical analysis is defined in equation 3.10.

$$\begin{aligned}
 \mathcal{L}(\mu, \boldsymbol{\theta}) = & \prod_{\substack{\text{SRs i} \\ \text{bins b}}} P \left( N_{ib} \middle| \mu S_{ib} \cdot \prod_{\substack{\text{sig.} \\ r}} \nu_{br}(\theta_r) + \sum_{\text{bkg k}} \theta_k B_{kib} \cdot \prod_{\substack{\text{bkg.} \\ s}} \nu_{bs}(\theta_s) \right) \\
 & \cdot \prod_{\text{CRs l}} P \left( N_l \middle| \sum_{\text{bkg k}} \theta_k B_{kl} \right) \\
 & \cdot \prod_{\substack{\text{syst} \\ t}} g(\delta_t|\theta_t) \cdot \prod_{\text{bkg k}} P(\xi_k|\zeta_k\theta_k)
 \end{aligned} \tag{3.10}$$

Here,  $\boldsymbol{\theta}$  represents the full vector of nuisance parameters,  $r$  is an index for signal systematics,  $s$  is an index for background systematics, and  $t$  is an index for Monte Carlo samples. The fourth term of the equation quantifies the uncertainty due to finite Monte Carlo sample size. Here,  $\xi$  represents the central value of the background prediction,  $\theta$  is the associated nuisance parameter,  $\zeta = (B/\delta B)^2$ , where  $\delta B$  is the statistical uncertainty of  $B$ .

The best fit value of the signal strength  $\mu$  is determined by finding the values of  $\mu$  and  $\boldsymbol{\theta}$  that maximize the likelihood, while setting  $\delta = 0$  and  $\xi = \zeta$ . Once the likelihood is defined, a test statistic must be built for use in hypothesis testing.

## TEST STATISTIC

To distinguish whether the data match a background only or background and signal hypothesis, a test statistic must be used. The  $H \rightarrow WW^*$  analysis uses the profile likelihood technique [76]. The first step

1510 in formulating this test statistic is to define the profile likelihood ratio, shown in equation 3.11.

$$\lambda(\mu) = \frac{\mathcal{L}(\mu, \hat{\theta}_\mu)}{\mathcal{L}(\hat{\mu}, \hat{\theta})} \quad (3.11)$$

1511 Here  $\hat{\theta}_\mu$  is the value of  $\theta$  that maximizes the likelihood for the choice of  $\mu$  being tested. Additionally,  $\hat{\theta}$   
1512 and  $\hat{\mu}$  represent the values of  $\theta$  and  $\mu$  that gives the overall maximum value of the likelihood.

1513 Once this is defined, a test statistic  $q_\mu$  is constructed. This is shown in equation 3.12.

$$q_\mu = -2 \ln \lambda(\mu) \quad (3.12)$$

1514 A higher value of  $q_\mu$  indicates that the data are more incompatible with the hypothesized value of  $\mu$ , and  
1515  $q_0$  then corresponds to the value of the test statistic for the background only hypothesis. A  $p_0$  value is  
1516 then defined to quantify the compatibility between the data and the null hypothesis. The  $p_0$  value is the  
1517 probability of obtaining a value of  $q_0$  larger than the observed value, and this is shown in equation 3.13.

$$p_0 = \int_{q_0^{\text{obs}}}^{\infty} f(q_\mu | \mu = 0) dq_\mu \quad (3.13)$$

1518 Here  $f(q_\mu)$  is the probability distribution function of the test statistic. Finally, the  $p_0$  value can be con-  
1519 verted into a signal significance, using the formula in equation 3.14, or the one-sided tail of the Gaussian  
1520 distribution.

$$Z_0 = \sqrt{2} \operatorname{erf}^{-1}(1 - 2p_0) \quad (3.14)$$

1521 The threshold for discovery used in particle physics is  $Z_0 \geq 5$ , more commonly known as a value of  $5\sigma$ .

*The real voyage of discovery consists not in seeking new landscapes, but in having new eyes.*

Marcel Proust

# 4

1522

## 1523 The discovery of the Higgs boson and the role 1524 of the $H \rightarrow WW^* \rightarrow \ell\nu\ell\nu$ channel

### 1525 4.1 INTRODUCTION

1526 This chapter presents the results of the search for the Higgs boson in  $4.8 \text{ fb}^{-1}$  collected at  $\sqrt{s} = 7 \text{ TeV}$   
1527 and  $5.8 \text{ fb}^{-1}$  at  $\sqrt{s} = 8 \text{ TeV}$ . The results of three searches at  $\sqrt{s} = 8 \text{ TeV}$  in the  $H \rightarrow WW^* \rightarrow$   
1528  $\ell\nu\ell\nu$ ,  $H \rightarrow \gamma\gamma$ , and  $H \rightarrow ZZ \rightarrow 4\ell$  channels are shown. These results at  $8 \text{ TeV}$  are combined  
1529 with the results of searches at  $\sqrt{s} = 7 \text{ TeV}$  in the same channels along with  $H \rightarrow \tau\tau$  production and  
1530 associated production searches for  $H \rightarrow b\bar{b}$ . The results of this combination are a  $5.9\sigma$  detection of a  
1531 new particle consistent with a Higgs boson produced via gluon fusion. Rather than going into detail for  
1532 all of the different Higgs decay searches, this chapter will discuss the three most sensitive channels and in  
1533 particular focus on  $H \rightarrow WW^* \rightarrow \ell\nu\ell\nu$ . While the focus is on  $WW^*$ , some of the  $ZZ^*$  and  $\gamma\gamma$  results

1534 are shown for completeness. The results not discussed here can be found in the ATLAS Higgs discovery  
1535 publication [1].

1536 **4.2 DATA AND SIMULATION SAMPLES**

1537 The data sample used for the following results was taken in 2011 and 2012 at center of mass energies of 7 and  
1538 8 TeV, respectively, with  $4.8 \text{ fb}^{-1}$  collected at 7 TeV and  $5.8 \text{ fb}^{-1}$  collected at 8 TeV. Higgs production  
1539 in the gluon fusion and vector boson fusion modes is modeled with POWHEG for the hard scattering event  
1540 and PYTHIA for the showering and hadronization. Associated production of a Higgs with a vector boson  
1541 or top quarks is modeled via PYTHIA . Table 4.1 shows the Monte Carlo generators used for modeling the  
1542 signal and background processes relevant for the three analyses to be discussed.

Process	Generator
ggF, VBF $H$	POWHEG + PYTHIA
$WH, ZH, t\bar{t}H$	PYTHIA
$W + \text{jets}, Z/\gamma^* + \text{jets}$	ALPGEN + HERWIG
$t\bar{t}, tW, tb$	MC@NLO + HERWIG
$tqb$	ACERMC + PYTHIA
$q\bar{q} \rightarrow WW$	MC@NLO + HERWIG
$gg \rightarrow WW$	GG2WW+ HERWIG
$q\bar{q} \rightarrow ZZ$	POWHEG + PYTHIA
$gg \rightarrow ZZ$	GG2ZZ+ HERWIG
$WZ$	MADGRAPH+ PYTHIA , HERWIG
$W\gamma + \text{jets}$	ALPGEN + HERWIG
$W\gamma^*$	MADGRAPH+ PYTHIA
$q\bar{q}/gg \rightarrow \gamma\gamma$	SHERPA

Table 4.1: Monte carlo generators used to model signal and background for the Higgs search [1].

1543 **4.3  $H \rightarrow WW \rightarrow e\nu\mu\nu$  SEARCH**

1544 The  $H \rightarrow WW \rightarrow e\nu\mu\nu$  search is unique compared to the  $ZZ$  and  $\gamma\gamma$  channels. The Higgs mass  
1545 cannot be fully reconstructed due to the presence of neutrinos in the final state, so the transverse mass  $m_T$   
1546 is used as the final discriminating variable. This channel also has a wider variety of backgrounds compared  
1547 to other channels, as discussed in chapter 3. The same flavor final states are excluded from the 8 TeV dataset

1548 due to high pileup conditions<sup>1</sup>. These final states are later included in results with the full Run 1 dataset,  
1549 as discussed in chapters 5 and 6.

1550 **4.3.1 EVENT SELECTION**

1551 The analysis requires to opposite charge isolated leptons, with the leading (sub-leading) lepton required to  
1552 have  $p_T > 25(15)$  GeV. The events are separated into different signal regions depending on which flavor  
1553 of lepton is leading ( $e\mu$  for leading electron,  $\mu e$  for leading muon). Strict lepton quality cuts are applied  
1554 to the sample to reduce backgrounds from mis-reconstructed leptons.

1555 Jets are reconstructed with the anti- $k_T$  algorithm with a radius parameter  $R = 0.4$ . The jets are re-  
1556 quired to have  $p_T > 25$  GeV and  $|\eta| < 4.5$ , with jets in the tracking volume required to have a jet vertex  
1557 fraction of 0.5 and jets in the forward region required to have  $p_T > 30$  GeV. The analysis is separated  
1558 into three different signal regions based on jet multiplicity:  $n_j = 0, 1, \geq 2$ .

1559 To indicate the presence of neutrinos in the event, a requirement of  $E_{T,\text{rel}}^{\text{miss}} > 25$  GeV is made<sup>2</sup>. This  
1560 requirement significantly reduces the QCD multijet and  $Z/\gamma^*$  + jets backgrounds. Figure 4.1 shows the  
1561 distribution of  $n_j$  in data and simulation after applying these “pre-selection” requirements.

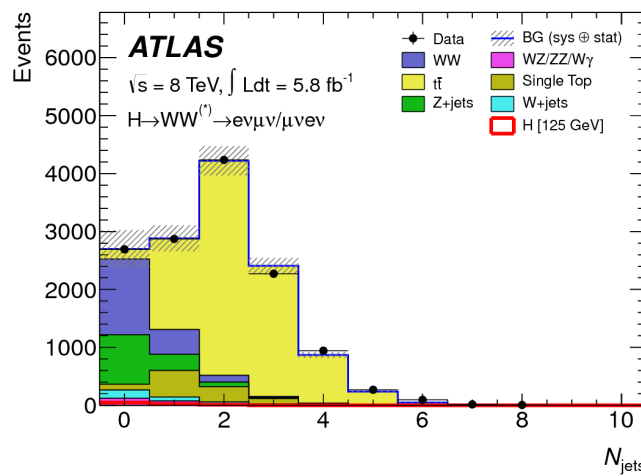


Figure 4.1: Jet multiplicity distribution in data and MC after applying lepton, jet, and  $E_{T,\text{rel}}^{\text{miss}}$  selections. The  $WW$  and top backgrounds have been normalized using control samples, and the hashed band indicates the total uncertainty on the prediction [1].

<sup>1</sup>The less sensitive 7 TeV search result includes both different flavor and same flavor final states.

<sup>2</sup>For the definition of  $E_{T,\text{rel}}^{\text{miss}}$ , see section 3.4.1.

1562        Additional selections are applied to require the dilepton topology to correspond to that of a Standard  
1563        Model Higgs boson. The requirements are presented here - more detailed discussion on the motivation  
1564        for each requirement is saved for Chapter 5. In all of the jet multiplicity channels, the dilepton system  
1565        is required to have a small gap in azimuthal angle,  $\Delta\phi_{\ell\ell} < 1.8$ . Similarly, the dilepton invariant mass,  
1566         $m_{\ell\ell}$ , is required to be less than 50 GeV in the lower jet multiplicity channels and less than 80 GeV in the  
1567         $n_j \geq 2$  channel. In the  $n_j = 0$  channel, the magnitude of the dilepton  $p_T$ ,  $p_T^{\ell\ell}$ , is required to be greater  
1568        than 30 GeV.

1569        In the higher jet multiplicity channels ( $n_j \geq 1$ ), the top background is a larger fraction of the total  
1570        background and must be reduced more carefully. The total transverse momentum  $p_T^{\text{sum}}$  is thus required  
1571        to be less than 30 GeV. Additionally, the di- $\tau$  invariant mass  $m_{\tau\tau}$  (dilepton mass computed under the  
1572        assumption that the neutrinos from the  $\tau$  decay are emitted collinear to the charged leptons [77]) is used  
1573        to reject  $Z \rightarrow \tau\tau$  events by requiring  $|m_{\tau\tau} - m_Z| > 25$  GeV. These variables are also discussed in more  
1574        detail in Chapter 5.

1575        In the  $n_j \geq 2$  channel, requirements are made to isolate the VBF contribution to Higgs production.  
1576        The kinematics of the two leading jets are used to make these requirements. In particular, the event must  
1577        have  $\Delta y_{jj} > 3.8$  and  $m_{jj} > 500$  GeV, along with a veto on having any additional jets with rapidity  
1578        between the two leading jets.

#### 1579        4.3.2 BACKGROUND ESTIMATION

1580        The details of the background estimation techniques used in the  $H \rightarrow WW^* \rightarrow \ell\nu\ell\nu$  analysis are  
1581        discussed in section 5.5. The dominant backgrounds are SM  $WW$  production and top (both pair and  
1582        single) production, and these backgrounds have their normalizations estimated from dedicated control  
1583        regions while their shapes are taken from simulation.

1584        The control sample for the Standard Model  $WW$  background is defined by making the same require-  
1585        ments as the signal region with the  $m_{\ell\ell}$  requirement inverted (now requiring  $m_{\ell\ell} > 80$  GeV) and remov-  
1586        ing the  $\Delta\phi_{\ell\ell}$  requirement. This creates a control sample that is 70% (40%) pure in the 0(1)-jet region. The  
1587        correction to the pure MC-based background estimate is quantified by defining a normalization factor  $\beta$

1588 which is the ratio of the data yield to the MC yield ( $N_{\text{data}}/N_{\text{MC}}$ ) in this control sample. Table 4.2 shows  
 1589 the  $WW$  normalization factors in the  $n_j = 0$  and  $n_j = 1$  bins (the  $n_j \geq 2$  estimate is taken directly  
 1590 from MC).

$n_j$	$\beta_{WW}$	$\beta_t$
= 0	$1.06 \pm 0.06$	$1.11 \pm 0.06$
= 1	$0.99 \pm 0.15$	$1.11 \pm 0.05$
$\geq 2$	-	$1.01 \pm 0.26$

Table 4.2: Normalization factors (ratio of data and MC yields in a control sample) for the Standard Model  $WW$  and top backgrounds in the  $H \rightarrow WW^* \rightarrow \ell\nu\ell\nu$  analysis [1]. Only statistical uncertainties are shown.

1591 The top background estimate is also computed separately in each jet multiplicity bin. In the  $n_j = 0$   
 1592 channel, the background is first normalized using data after pre-selection requirements with no selection  
 1593 on  $n_j$ . Then, a dedicated  $b$ -tagged control sample is used to evaluate the ratio of one-jet to two-jet events in  
 1594 data. The details of this technique are shown in reference [78]. In the  $n_j = 1$  and the  $n_j \geq 2$  regions, the  
 1595 top background is normalized in a control sample where the signal region selections are applied, but the  
 1596  $b$ -jet veto is reversed and the Higgs topology requirements on  $m_{\ell\ell}$  and  $\Delta\phi_{\ell\ell}$  are removed. The resulting  
 1597 normalization factors for these techniques are shown in table 4.2.

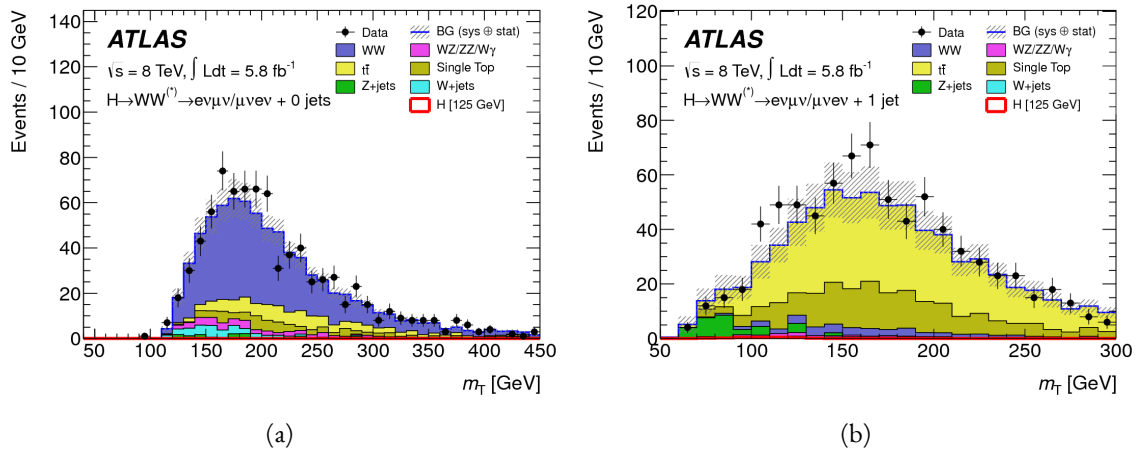


Figure 4.2: Comparison of  $m_T$  between data and simulation in the  $n_j = 0$   $WW$  (a) and  $n_j = 1$  top (b) control samples [1].

1598 The control samples which are used for background normalization can also be used to validate the mod-  
 1599 eling of the  $m_T$  distribution for each background. Figure 4.2 shows the comparison between data and MC

1600 for the  $m_T$  distribution after correcting the normalization of the backgrounds in the  $WW$  and top control  
1601 regions. Good agreement between data and simulation is seen in both cases.

1602 The  $W + \text{jets}$  background estimate is taken entirely from data using a control sample with one well recon-  
1603 structed lepton and one anti-identified lepton. All other backgrounds are taken purely from simulation.

#### 1604 4.3.3 SYSTEMATIC UNCERTAINTIES

1605 The systematic uncertainties that have the largest impact on the analysis are the theoretical uncertainties  
1606 associated with the signal cross section. These are shared with the  $ZZ^*$  and  $\gamma\gamma$  channels. The uncertainties  
1607 resulting from variations of the QCD scale are  $+7\% / -8\%$  on the final signal yield. Those coming from  
1608 variations of the parton distribution function (PDF) used in the simulation add a  $\pm 8\%$  uncertainty on  
1609 the yield. The uncertainties on the branching ratios of the Higgs are  $\pm 5\%$ .

1610 The main experimental uncertainties come from variations of the jet energy scale (JES), jet energy reso-  
1611 lution, pile-up,  $E_T^{\text{miss}}$ ,  $b$ -tagging efficiency,  $W + \text{jets}$  background estimate, and integrated luminosity. For  
1612 more details, see reference [1].

#### 1613 4.3.4 RESULTS

1614 Table 4.3 shows the signal and background yields in the final signal region after normalizing the back-  
1615 grounds according to the methods described above.

	$n_j = 0$	$n_j = 1$	$n_j \geq 2$
Signal	$20 \pm 4$	$5 \pm 2$	$0.34 \pm 0.07$
$WW$	$101 \pm 13$	$12 \pm 5$	$0.10 \pm 0.14$
Other dibosons	$12 \pm 3$	$1.9 \pm 1.1$	$0.10 \pm 0.10$
$t\bar{t}$	$8 \pm 2$	$6 \pm 2$	$0.15 \pm 0.10$
Single top	$3.4 \pm 1.5$	$3.7 \pm 1.6$	-
$Z/\gamma^* + \text{jets}$	$1.9 \pm 1.3$	$0.10 \pm 0.10$	-
$W + \text{jets}$	$15 \pm 7$	$2 \pm 1$	-
Total background	$142 \pm 16$	$26 \pm 6$	$0.35 \pm 0.18$
Observed in data	185	38	0

Table 4.3: Data and expected yields for signal and background in the final  $H \rightarrow WW^* \rightarrow \ell\nu\ell\nu$  signal region.  
Uncertainties shown are both statistical and systematic [1].

1616      Figure 4.3 shows the  $m_T$  distribution in the  $n_j \leq 1$  channels for 8 TeV data. (No events are observed  
 1617      in data in the  $n_j \geq 2$  channels in this dataset). The excess shown here relatively flat as a function of  
 1618      hypothesized Higgs mass. The combined 7 and 8 TeV data gives an excess with local significance of  $2.8\sigma$   
 1619      with an expected significance of  $2.3\sigma$ , corresponding to a  $\mu$  measurement of  $1.3 \pm 0.5$ .

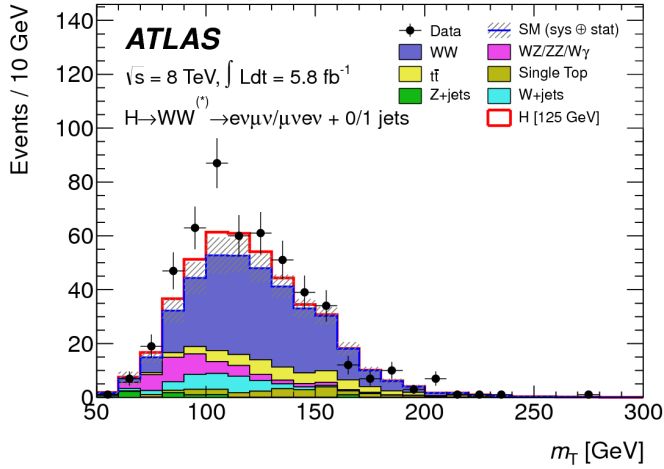


Figure 4.3:  $m_T$  distribution in the  $H \rightarrow WW \rightarrow e\nu\mu\nu$   $n_j \leq 1$  channels for 8 TeV data [1].

#### 1620    4.4    $H \rightarrow \gamma\gamma$ SEARCH

1621    The  $H \rightarrow \gamma\gamma$  search is a search for a peaked excess above the falling SM diphoton mass spectrum, with  
 1622     $m_{\gamma\gamma}$  as the ultimate discriminating variable. Events are selected by requiring two isolated photons, with  
 1623    the leading (sub-leading) photon required to have  $E_T > 40(30)$  GeV. In the 8 TeV data, the photons are  
 1624    required to pass identification criteria consistent with a photonic shower in the electromagnetic calorimeter  
 1625    and little leakage in the hadronic calorimeter.

1626    The main challenges for this analysis are accurate mass reconstruction and background estimation. In  
 1627    order to accurately reconstruct the invariant mass of the di-photon system, both the energy and direction  
 1628    of the photons must be measured well. Therefore, the identification of the primary vertex of the hard  
 1629    interaction is particularly important, and is done using a multivariate likelihood which combines informa-  
 1630    tion about the photon direction and vertex position. The background is modeled with a falling spectrum  
 1631    in  $m_{\gamma\gamma}$  that is parameterized by different functions depending on the category of the event.

1632    4.4.1    RESULTS

1633    The resulting diphoton mass spectrum is shown in figure 4.4. The best fit mass value in the  $\gamma\gamma$  channel  
 1634    alone in the combined 7 and 8 TeV data is 126.5 GeV. The local significance at this point is  $4.5\sigma$ , with  
 1635    an expected significance of  $2.5\sigma$ . Therefore, the measured signal strength  $\mu$  is  $1.8 \pm 0.5$  in this channel.

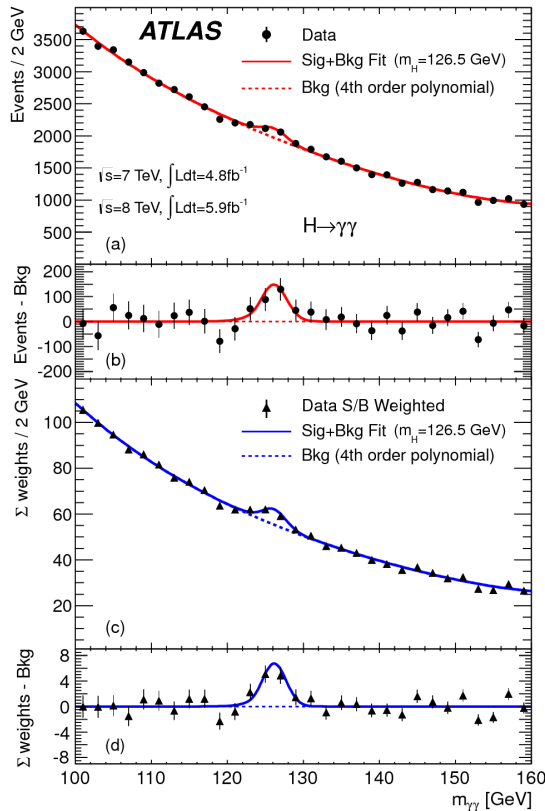


Figure 4.4: Diphoton mass spectrum in 7 and 8 TeV data. Panel a) shows the unweighted data distribution superimposed on the background fit, while panel c) shows the data where each event category is weighted by its signal to background ratio. Panels b) and d) show the respective distributions with background subtracted [1].

1636    4.5     $H \rightarrow ZZ \rightarrow 4\ell$  SEARCH

1637    The  $H \rightarrow ZZ \rightarrow 4\ell$  analysis searches for a Standard Model Higgs boson decaying to two  $Z$  bosons, each  
 1638    of which decays to a pair of same flavor, opposite charge isolated leptons. The ultimate discriminating  
 1639    variable is  $m_{4\ell}$ , or the invariant mass of the four selected leptons. The  $\ell$  denotes an  $e$  or  $\mu$  as with the  
 1640     $H \rightarrow WW^* \rightarrow \ell\nu\ell\nu$  analysis.

1641 Four distinct signal regions are constructed depending on the flavors of the final state, additionally sep-  
 1642 arated by the flavor of the leading lepton pair. These are referred to as  $4e$ ,  $2e2\mu$ ,  $2\mu2e$ ,  $4\mu$ .

1643 The main backgrounds in the  $H \rightarrow ZZ \rightarrow 4\ell$  search are continuum  $ZZ^*$  production,  $Z + \text{jets}$  pro-  
 1644 duction, and  $t\bar{t}$ . The  $m_{4\ell}$  distribution for background is estimated from simulation. The normalization  
 1645 of the SM  $ZZ^*$  background is also taken from MC simulation, while the  $Z + \text{jets}$  and  $t\bar{t}$  normalizations are  
 1646 taken from data-driven methods.

#### 1647 4.5.1 RESULTS

1648 Figure 4.5 shows the  $m_{4\ell}$  spectrum measured in the 7 and 8 TeV datasets. The total number of events  
 1649 observed in the window between 120 and 130 GeV is 13, with 6 events in the  $4\mu$  channel, 2 events in  
 1650 the  $4e$  channel, and 5 events in the  $2e2\mu/2\mu2e$ . The best fit  $\mu$  value in the combined 7 and 8 TeV data  
 1651 occurs at 125 GeV and is measured to be  $1.2 \pm 0.6$ . The observed significance at this mass is  $3.6\sigma$ , with  
 1652 an expected significance of  $2.7\sigma$ .

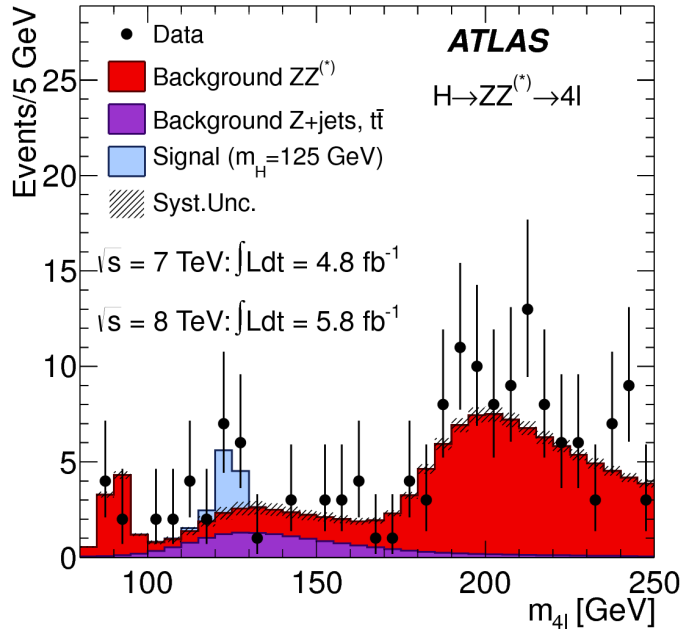


Figure 4.5: Four lepton invariant mass spectrum ( $m_{4\ell}$ ) in 7 and 8 TeV data compared to background estimate. A 125 GeV SM Higgs signal is shown in blue [1].

1653    4.6 COMBINED RESULTS

1654    The statistical interpretation of the combined results is undertaken as described in section 3.6.2, with a hy-  
1655    pothesis test based on a likelihood ratio parameterized by the Higgs signal strength  $\mu$ . The null hypothesis  
1656    corresponds to  $\mu = 0$ , while the SM Higgs corresponds to  $\mu = 1$ .

1657    Table 4.4 summarizes the properties of the individual channels as well as the significances of the excesses  
1658    seen. The most significant observed local excess comes from the  $\gamma\gamma$  channel. Figure 4.6 shows a com-  
1659    parison of the observed local  $p_0$  values as a function of hypothesized mass for the three different search  
1660    channels. Both the  $ZZ^*$  and  $\gamma\gamma$  channels have very peaked excesses, while the  $WW^*$  excess can be seen as  
1661    very broad because the  $m_T$  distribution does not provide detailed information about the true Higgs mass.  
1662    Figure 4.7 shows the combined exclusion limit,  $p_0$ , and signal strength. The highest local excess comes at  
1663    a value of 126.5 GeV and corresponds to a  $6.0\sigma$  observed excess.

Channel	Fit var.	Observed $Z_l$	Expected $Z_l$	$\hat{\mu}$
$H \rightarrow ZZ^* \rightarrow 4\ell$	$m_{4\ell}$	3.6	2.7	$1.2 \pm 0.6$
$H \rightarrow \gamma\gamma$	$m_{\gamma\gamma}$	4.5	2.5	$1.8 \pm 0.5$
$H \rightarrow WW^* \rightarrow e\nu\mu\nu$	$m_T$	2.8	2.3	$1.3 \pm 0.5$
Combined	-	6.0	4.9	$1.4 \pm 0.3$

Table 4.4: Summary of the expected and observed significance and measured signal strengths in the combined 7 and 8 TeV datasets for the Higgs discovery analysis [1].

1664    Figure 4.8 shows a comparison of the measured signal strengths between the different Higgs search  
1665    channels. All measured  $\mu$  are consistent with unity within their uncertainty, and the combined  $\mu$  mea-  
1666    surement is  $1.4 \pm 0.3$ .

1667    The likelihood can also be computed in a two-dimensional plane of  $m_H$  and  $\mu$ , and this is shown in  
1668    figure 4.9. The figure shows that while the  $\gamma\gamma$  and  $ZZ^*$  channels have very good mass resolution, the  
1669    excess in  $WW^*$  covers a broad mass range. The banana shape of the  $WW^*$  result is due to the fact that  
1670    the excess in this channel can either be explained by increasing the signal strength or by changing the mass  
1671    (and thus the cross section). The two parameters are correlated due to the lack of mass sensitivity in this  
1672    channel.

1673    Because multiple Higgs mass points are searched for, the local significance must be corrected for a look-

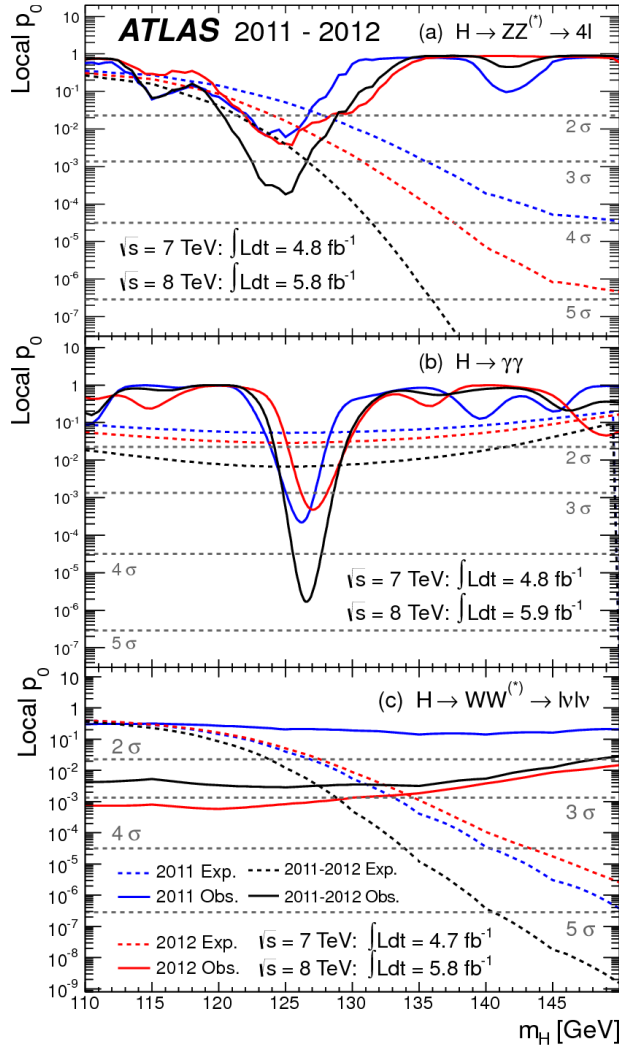


Figure 4.6: Local  $p_0$  distribution as a function of hypothesized Higgs mass for the  $H \rightarrow ZZ^* \rightarrow 4\ell$  (a),  $H \rightarrow \gamma\gamma$  (b), and  $H \rightarrow WW^* \rightarrow \ell\nu\ell\nu$  (c) channels. Dashed curves show expected results, while solid curves show observed. Red curves are from 7 TeV data, blue curves from 8 TeV, and black curved combined [1].

1674 elsewhere effect to compute a true global significance. The global significance for finding a Higgs anywhere  
 1675 in the mass range of 110 GeV to 600 GeV is  $5.1\sigma$ . This increases slightly to  $5.3\sigma$  if only mass range from  
 1676 110 to 150 GeV.

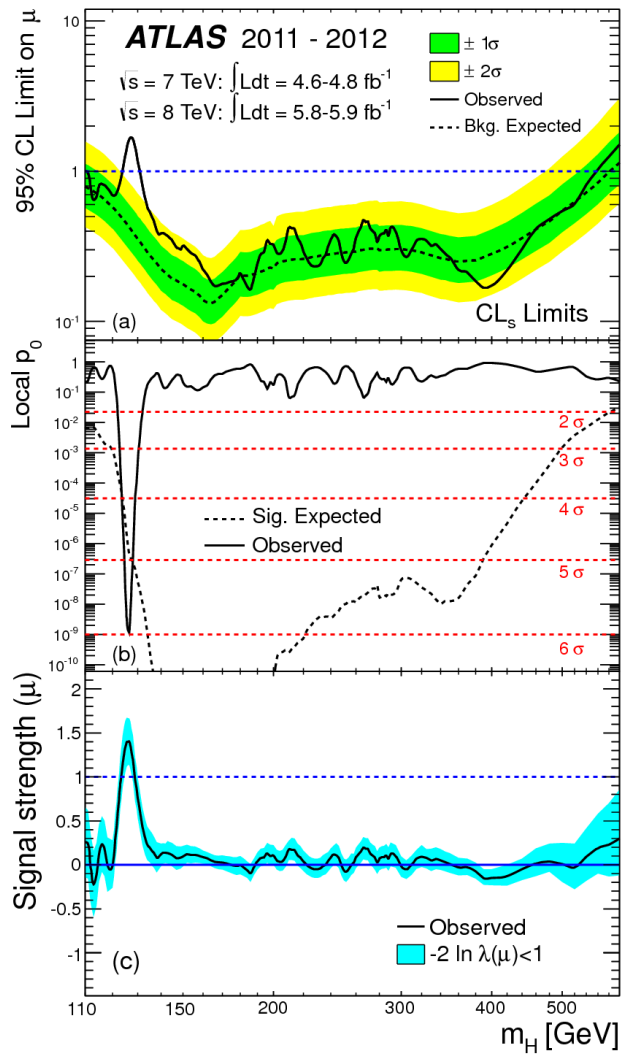


Figure 4.7: Combined 95% CL limits (a), local  $p_0$  values (b), and signal strength measurement (c) as a function of Higgs mass [1].

1677    4.7 CONCLUSION

1678    A search for the production of a Standard Model Higgs boson was conducted in  $4.8 \text{ fb}^{-1}$  collected at  
 1679     $\sqrt{s} = 7 \text{ TeV}$  and  $5.8 \text{ fb}^{-1}$  at  $\sqrt{s} = 8 \text{ TeV}$ . A new particle consistent with the Higgs boson was observed,  
 1680    with a mass of  $126.5 \text{ GeV}$  and a global (local) significance of  $5.1(6.0)\sigma$ . This is the first discovery level  
 1681    observation of a particle consistent with the Higgs.

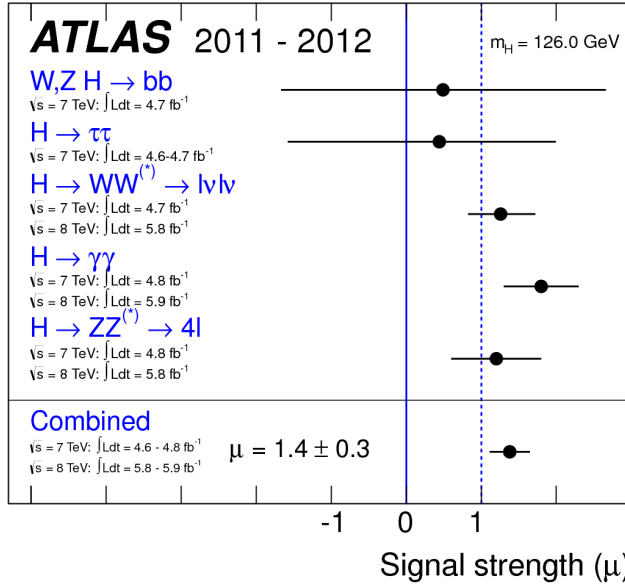


Figure 4.8: Comparison of measured signal strength  $\mu$  for a 126 GeV Higgs in the 7 and 8 TeV datasets [1].

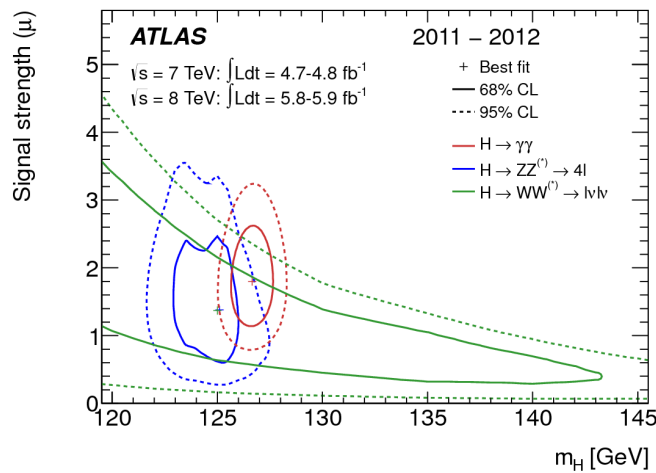


Figure 4.9: Two dimensional likelihood as a function of signal strength  $\mu$  and Higgs mass  $m_H$  [1].

*The imagination of nature is far, far greater than the  
imagination of man.*

Richard Feynman

1682

# 5

1683

## Evidence for Vector Boson Fusion production

1684

of  $H \rightarrow WW^* \rightarrow \ell\nu\ell\nu$

1685

### 5.1 INTRODUCTION

1686 After the discovery of the Higgs boson, the  $H \rightarrow WW^*$  analysis had two main goals. The first goal was  
1687 to increase the sensitivity of the analysis to fully confirm that the  $H \rightarrow WW^*$  process did indeed exist.  
1688 The second goal was to characterize the particle as much as possible, including searching for the lower  
1689 cross-section production modes. This chapter presents a dedicated search for Vector Boson Fusion (VBF)  
1690 production of a Higgs boson decaying via the  $H \rightarrow WW^* \rightarrow \ell\nu\ell\nu$  mode. First, the data and Monte  
1691 Carlo samples are detailed, along with trigger and physics object selections. Then, the details of the analysis  
1692 are shown, including signal region definition, background estimation techniques, and systematic uncer-  
1693 tainties. Finally, the results of the analysis are presented. As will be shown, this analysis is the first and

1694 most sensitive evidence for VBF production of the Higgs at the LHC.

1695 The VBF  $H \rightarrow WW^* \rightarrow \ell\nu\ell\nu$  analysis defines two signal regions. The first is a more standard  
1696 selection, referred to as “cut-based”, that applies requirements on VBF topology variables and uses  $m_T$  as  
1697 the final discriminating variable. The second is a looser selection that uses an algorithm known as a Boosted  
1698 Decision Tree (BDT). A BDT is a multivariate technique that uses an ensemble of decision trees to split the  
1699 phase space of input variables into signal-like and background-like regions in order to provide separation  
1700 power [79–81]. The output score of a BDT trained to distinguish the VBF Higgs signal from background  
1701 processes is used as the final discriminating variable in the second signal region. While the BDT-based  
1702 signal region is ultimately more sensitive, the cut-based result is an important component of the analysis.  
1703 First, the cut-based analysis allows for confirming the modeling and validity of the variables used as input  
1704 to the BDT. Second, because this is the first use of a multivariate technique in the  $H \rightarrow WW^*$  analysis,  
1705 the cut-based selection allows confirmation of the final BDT result with a more traditional analysis. The  
1706 cut-based techniques are the focus of this chapter, but connections to the BDT result will be illustrated  
1707 when appropriate.

1708 One important note is that because this analysis is dedicated to the measurement of the VBF pro-  
1709 duction mode of the Higgs, events coming from gluon fusion production with the Higgs decaying via  
1710  $H \rightarrow WW^* \rightarrow \ell\nu\ell\nu$  are treated as background events. This will be seen throughout the background  
1711 predictions shown below.

1712 **5.2 DATA AND SIMULATION SAMPLES**

1713 The results presented here are with  $20.3 \text{ fb}^{-1}$  taken at  $\sqrt{s} = 8 \text{ TeV}$  and  $4.5 \text{ fb}^{-1}$  taken at  $\sqrt{s} = 7 \text{ TeV}$ .  
1714 The details of the LHC and detector conditions during this period are given in Chapter 2. The trigger  
1715 selection defining the dataset is discussed in section 5.2.1. The simulation samples used for signal and back-  
1716 ground modeling are given in section 5.2.2.

1717 5.2.1 TRIGGERS

1718 The analysis uses a combination of single lepton and dilepton triggers to allow lowering of the  $p_T$  thresh-  
1719 olds and increased signal acceptance. The  $p_T$  threshold on the leptons is a particularly important con-  
1720 sideration for this signal. Because the  $W^*$  produced in the decay is off-shell, it tends to produce lower  
1721 momentum leptons. Thus, being able to lower the  $p_T$  threshold while still maintaining a low background  
1722 rate is critical. Figure 5.1 shows an example of the subleading lepton  $p_T$  for a VBF  $H \rightarrow WW^*$  signal com-  
1723 pared to the corresponding  $t\bar{t}$  background. Note that the lepton  $p_T$  spectrum is considerably softer in the  
1724 signal sample. The spectrum shown here is also similar in gluon fusion production of the Higgs as well.

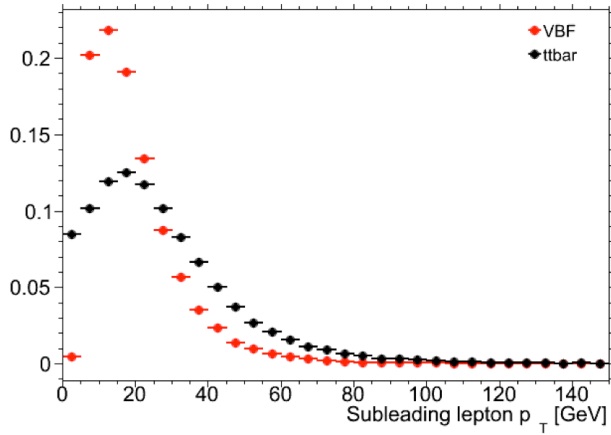


Figure 5.1: A comparison of the subleading lepton  $p_T$  spectrum between VBF  $H \rightarrow WW^*$  production and  $t\bar{t}$  background.

1725 As discussed in Chapter 2, there are multiple levels in the ATLAS trigger system, and there are different  
1726  $p_T$  thresholds imposed for the leptons at each level. Additionally, some triggers have a loose selection on  
1727 the isolation of the lepton (looser than that applied offline in the analysis object selection). Table 5.1 shows  
1728 the  $p_T$  thresholds used for single lepton triggers, while table 5.2 shows the  $p_T$  thresholds coming from  
1729 di-lepton triggers. The single lepton trigger efficiency for muons that pass the analysis object selection is  
1730 70% for muons in the barrel region ( $|\eta| < 1.05$ ) and 90% in the endcap region. The electron trigger  
1731 efficiency increases with electron  $p_T$  but the average is approximately 90%. These efficiencies are measured  
1732 by combined performance and trigger signature groups [82, 83].

	Level-1 threshold	High-level threshold
Electron	18	$24i$
	30	60
Muon	15	$24i$
		36

Table 5.1: Single lepton triggers used for electrons and muons in the  $H \rightarrow WW^* \rightarrow \ell\nu\ell\nu$  analysis. A logical “or” of the triggers listed for each lepton type is taken. Units are in GeV, and the  $i$  denotes an isolation requirement in the trigger.

	Level-1 threshold	High-level threshold
$ee$	10 and 10	12 and 12
$\mu\mu$	15	18 and 8
$e\mu$	10 and 6	12 and 8

Table 5.2: Di-lepton triggers used for different flavor combinations in the  $H \rightarrow WW^* \rightarrow \ell\nu\ell\nu$  analysis. The two thresholds listed refer to leading and sub-leading leptons, respectively. The di-muon trigger only requires a single lepton at level-1.

1733        The combination of all listed triggers gives good efficiency for signal events. This efficiency is summa-  
 1734        rized in table 5.3. The relative improvement in efficiency by adding the dilepton triggers is also shown  
 1735        in the same table. The largest gain comes in the  $\mu\mu$  channel. Overall the trigger selection shows a good  
 1736        efficiency for  $H \rightarrow WW^*$  signal events.

Channel	Trigger efficiency	Gain from $2\ell$ trigger
$ee$	97%	9.1%
$\mu\mu$	89%	18.5%
$e\mu$	95%	8.3%
$\mu e$	81%	8.2%

Table 5.3: Trigger efficiency for signal events and relative gain of adding a dilepton trigger on top of the single lepton trigger selection. The first lepton is the leading, while the second is the sub-leading. Efficiencies shown here are for the ggF signal in the  $n_j = 0$  category but are comparable for the VBF signal.

### 1737     5.2.2 MONTE CARLO SAMPLES

1738        In both the gluon fusion and vector boson fusion focused analyses, modeling of signal and background  
 1739        processes in the signal region is an important consideration for the final interpretation of the analysis.  
 1740        Therefore, careful consideration must be paid to which Monte Carlo (MC) generators are used for specific

1741 processes. With the exception of the  $W + \text{jet}$  and multijet backgrounds, the  $m_T$  shape used as the final  
1742 discriminant is taken from simulation<sup>1</sup>.

1743 Table 5.4 shows the MC generators used for the signal and background processes, as well as the cross  
1744 sections of each process. In order to include corrections up to next-to-leading order (NLO) in the QCD  
1745 coupling constant  $\alpha_s$ , the `POWHEG` [84] generator is often used. In some cases, only leading order gener-  
1746 ators like `ACERMC` [85] and `GG2VV` [86] are available for the process in question. If the process requires  
1747 good modeling for very high parton multiplicities, the `SHERPA` [87] and `ALPGEN` [88] generators are used  
1748 to provide merged calculations for five or fewer additional partons. These matrix element level calculations  
1749 must then be additionally matched to models of the underlying event, hadronization, and parton shower.  
1750 There are four generators used for this purpose: `SHERPA`, `PYTHIA 6` [89], `PYTHIA 8` [90], or `HERWIG`  
1751 [91] + `JIMMY` [92]. The simulation additionally requires an input parton distribution function (PDF).  
1752 The `CT10` [93] PDFs are used for `SHERPA` and `POWHEG` simulated samples, while `CTEQ6L1` [94] is used  
1753 for `ALPGEN + HERWIG` and `ACERMC` simulations. The Drell-Yan samples are reweighted to the `MRST` [95]  
1754 PDFs, as these are found to give the best agreement between data and simulation. The branching ratio  
1755 for Higgs to  $WW^*$  and  $ZZ^*$  is computed with `PROPHECY4f` [96], while the width of all other decays is  
1756 computed with `HDECAY`[97].

1757 Once the basic hard scattering process is simulated, it must be passed through a detector simulation and  
1758 additional pile-up events must be overlaid. The pile-up events are modeled with `PYTHIA 8`, and the ATLAS  
1759 detector is simulated with `GEANT4` [98]. Because of the unique phase space of the  $H \rightarrow WW^*$  analysis,  
1760 events are sometimes filtered at generator level to allow for more efficient generation of relevant events.  
1761 The efficiency of the trigger in MC simulation does not always match the measured efficiency in data, so  
1762 trigger scale factors are applied to correct the MC efficiency to the data. The details of these corrections are  
1763 given in reference [82] for muons and reference [83] for electrons.

---

<sup>1</sup>Many backgrounds are normalized from data, as described in section 5.5.

Process	MC generator	$\sigma \cdot \mathcal{B}$ (pb)
Signal		
ggF $H \rightarrow WW^*$	POWHEG +PYTHIA 8	0.435
VBF $H \rightarrow WW^*$	POWHEG +PYTHIA 8	0.0356
VH $H \rightarrow WW^*$	PYTHIA 8	0.0253
$WW$		
$q\bar{q} \rightarrow WW$ and $qg \rightarrow WW$	POWHEG +PYTHIA 6	5.68
$gg \rightarrow WW$	GG2VV +HERWIG	0.196
$(q\bar{q} \rightarrow W) + (q\bar{q} \rightarrow W)$	PYTHIA 8	0.480
$q\bar{q} \rightarrow WW$	SHERPA	5.68
VBS $WW + 2$ jets	SHERPA	0.0397
Top quarks		
$t\bar{t}$	POWHEG +PYTHIA 6	26.6
$Wt$	POWHEG +PYTHIA 6	2.35
$t\bar{q}\bar{b}$	ACERMC +PYTHIA 6	28.4
$t\bar{b}$	POWHEG +PYTHIA 6	1.82
Other dibosons ( $VV$ )		
$W\gamma$ ( $p_T^\gamma > 8$ GeV)	ALPGEN +HERWIG	369
$W\gamma^*$ ( $m_{\ell\ell} \leq 7$ GeV)	SHERPA	12.2
$WZ$ ( $m_{\ell\ell} > 7$ GeV)	POWHEG +PYTHIA 8	12.7
VBS $WZ + 2$ jets	SHERPA	0.0126
( $m_{\ell\ell} > 7$ GeV)		
$Z\gamma$ ( $p_T^\gamma > 8$ GeV)	SHERPA	163
$Z\gamma^*$ (min. $m_{\ell\ell} \leq 4$ GeV)	SHERPA	7.31
$ZZ$ ( $m_{\ell\ell} > 4$ GeV)	POWHEG +PYTHIA 8	0.733
$ZZ \rightarrow \ell\ell\nu\nu$ ( $m_{\ell\ell} > 4$ GeV)	POWHEG +PYTHIA 8	0.504
Drell-Yan		
$Z$ ( $m_{\ell\ell} > 10$ GeV)	ALPGEN +HERWIG	16500
VBF $Z + 2$ jets	SHERPA	5.36
( $m_{\ell\ell} > 7$ GeV)		

Table 5.4: Monte Carlo samples used to model the signal and background processes [74]. The table lists the cross section for each process, taking into account the branching ratio for the process producing two leptons.

### 1764 5.3 OBJECT SELECTION

1765 In order to define the signal region, the analysis must first select the reconstructed physics objects to be  
1766 considered. The details of the object reconstruction algorithms were discussed in Chapter 2, while this

1767 section gives specific selection requirements used in the  $H \rightarrow WW^*$  analysis. The first step in this process  
1768 is to select a primary vertex candidates. The event's primary vertex is chosen to be the vertex with the largest  
1769 sum of  $p_T^2$  for its associated tracks. It is required to have at least three tracks with  $p_T > 450$  MeV. Many  
1770 of the object selection cuts are then made relative to this chosen primary vertex.

### 1771 5.3.1 MUONS

1772 The analysis uses combined muon candidates, where a track in the Inner Detector has been matched to a  
1773 standalone track in the Muon Spectrometer. The track parameters are combined statistically in the muon  
1774 reconstruction algorithm [64]. The muons are required to be within  $|\eta| < 2.5$  and have a  $p_T > 10$  GeV.  
1775 To reduce backgrounds coming from mis-reconstructed leptons, there are requirements on the impact  
1776 parameter of the muon relative to the primary vertex. The transverse impact parameter  $d_0$  is required to  
1777 be small relative to its estimated uncertainty, the exact cut value being  $d_0/\sigma_{d_0} < 3$ . The longitudinal  
1778 impact parameter  $z_0$  must satisfy  $|z_0 \sin \theta| < 1$  mm.

1779 As discussed previously, the muons must also be isolated. There are two types of lepton isolations  
1780 that are calculated: track-based and calorimeter-based. For muons, the track-based isolation is defined  
1781 using the scalar sum  $\sum p_T$  for tracks with  $p_T > 1$  GeV (excluding the muon track) within a cone of  
1782  $\Delta R = 0.3$  (0.4) around the track for muons with  $p_T > 15$  GeV ( $10 < p_T < 15$  GeV). The final  
1783 isolation requirement is made by requiring that this scalar sum be no more than a certain fraction of the  
1784 muon  $p_T$ . This requirement varies with muon  $p_T$  and the exact requirements are defined in table 5.5.

1785 The calorimeter-based muon isolation is defined using the  $\sum E_T$  calculated from calorimeter cells with  
1786 the same cone size as the track-based isolation but excluding cells within  $\Delta R < 0.05$  around the muon.  
1787 This isolation is also defined as a requirement on the ratio of the sum to the muon  $p_T$  and varies with  
1788 muon  $p_T$ . The requirement values as a function of  $p_T$  are also given in table 5.5.

1789 The isolation requirements loosen as a function of  $p_T$  to allow for larger signal acceptance. At low  $p_T$ ,  
1790 the isolation is tightened to reduce the  $W + \text{jets}$  background which arises from a misidentified lepton.

$p_T$ range (GeV)	Calorimeter isolation	Track isolation
10 – 15	0.06	0.06
15 – 20	0.12	0.08
20 – 25	0.18	0.12
> 25	0.30	0.12

Table 5.5:  $p_T$  dependent isolation requirements for muons. Muons are required to have their calorimeter based or track based cone sums be less than this fraction of their  $p_T$ .

1791    5.3.2 ELECTRONS

1792    Electrons are identified and reconstructed using the methods previously described in chapter 2. The elec-  
 1793    trons are required to have  $|\eta| < 2.47$ , and candidates in the transition region between the barrel and  
 1794    endcap ( $1.37 < |\eta| < 1.52$ ) are excluded. As the muons, the electrons are required to have transverse  
 1795    impact parameter significance  $< 3$ , while in the longitudinal direction they must have  $|z_0 \sin \theta| < 0.4$   
 1796    mm. Some electron requirements also vary with electron  $E_T$ , and these requirements are summarized in  
 1797    table 5.6.

1798    The isolation for electrons is defined similarly to the muons but with unique requirements on the ob-  
 1799    jects included. The track-based isolation is constructed using tracks with  $p_T > 400$  MeV with cone sizes  
 1800    as defined for the muons. The calorimeter-based isolation also uses the same cone size as the muon, but  
 1801    here the cells within a  $0.125 \times 0.175$  area in  $\eta \times \phi$  around the electron cluster's barycenter are excluded.  
 1802    The other difference with respect to muons is that the denominator of the isolation ratio is the electron  
 1803     $E_T$  rather than  $p_T$ . The isolation cuts very with electron  $E_T$  and are defined in table 5.6. The electron is  
 1804    also required to not be consistent with a vertex coming from a photon conversion.

$p_T$ range (GeV)	Quality cut	Calorimeter isolation	Track isolation
10 – 15	Very tight LH	0.20	0.06
15 – 20	Very tight LH	0.24	0.08
20 – 25	Very tight LH	0.28	0.10
> 25	Medium	0.28	0.10

Table 5.6:  $p_T$  dependent requirements for electrons. Electrons are required to have their calorimeter based or track based cone sums be less than this fraction of their  $E_T$ .

1805 5.3.3 JETS

1806 Jets are clustered with the anti- $k_T$  reconstruction algorithm using a radius parameter of  $R = 0.4$ . They  
1807 are required to have a jet vertex fraction (JVF) of at least 50%, meaning that half of the tracks associated with  
1808 the jet originated from the primary vertex. Jets with no tracks associated (i.e. those outside the acceptance  
1809 of the ID) do not have this requirement applied. Jets are required to have  $p_T > 25$  GeV if they are within  
1810 the tracking acceptance ( $|\eta| < 2.4$ ). Jets with  $2.4 < |\eta| < 4.5$  are required to have  $p_T > 30$  GeV. This  
1811 tighter requirement reduces jets from pileup in the region where JVF requirements cannot be applied. The  
1812 two highest  $p_T$  jets in the event are referred to as the “VBF” jets and used to compute variables used in the  
1813 analysis selection.

1814 Identification of  $b$ -jets is done using the MV<sub>1</sub> algorithm and is limited to the acceptance of the ID ( $|\eta| <$   
1815 2.5) [70]. The operating point of MV<sub>1</sub> used is 85% efficient for identifying true  $b$ -jets. This operating  
1816 point has a 10.3% probability of mis-tagging a light quark jet as a  $b$ -jet. The analysis vetoes events that  
1817 contain  $b$ -tagged jets with  $p_T > 20$  GeV.

1818 5.3.4 OVERLAP REMOVAL

1819 There are some cases where reconstructed objects will overlap and one will have to be chosen (for example,  
1820 an electron and a jet in the calorimeter). First, the case of lepton overlap is dealt with. If an electron  
1821 candidate extends into the muon spectrometer, it is removed. If a muon and electron are within  $\Delta R < 0.1$   
1822 of each other, the electron is removed and the muon is kept. If two electron candidates overlap within the  
1823 same radius, then the higher  $E_T$  electron is kept. Next, the overlap between leptons and jets is considered.  
1824 If an electron and jet are within  $\Delta R < 0.3$  of one another, the electron is kept and the jet is removed.  
1825 However, if a muon and jet overlap within  $\Delta R < 0.3$ , the jet is kept (as it is likely that the muon is the  
1826 result of a semileptonic decay inside the jet). Once the overlap removal is complete, the final set of objects  
1827 used in the analysis is defined.

1828    **5.4 ANALYSIS SELECTION**

1829    This section discusses the variables used to distinguish VBF production of the Higgs in the  $H \rightarrow WW^* \rightarrow$   
1830     $\ell\nu\ell\nu$  final state. First, pre-selection requirements are presented. Then, the definitions of analysis variables  
1831    and the cut-based signal region are shown. Finally, the BDT signal region is defined and the commonalities  
1832    between the two signal regions are discussed.

1833    **5.4.1 PRE-SELECTION**

1834    Both the cut-based and BDT analyses have a common pre-selection that is applied before the signal region  
1835    requirements. The requirements on leptons are common to all  $n_j$  bins. The analysis requires two oppo-  
1836    sitely charged leptons, with the leading lepton required to have  $p_T > 22$  GeV while the subleading lepton  
1837    must have  $p_T > 10$  GeV. Next, to remove low mass  $Z/\gamma^*$  events, a requirement on the dilepton mass  
1838     $m_{\ell\ell} > 10$  (12) GeV is applied in the different (same) flavor channel. In the same flavor channels, there is  
1839    an additional veto placed on the region around the Z peak, requiring that  $|m_{\ell\ell} - m_Z| > 15$  GeV.

1840    There are also requirements on the amount of missing transverse momentum in the event. These  
1841    are only applied in the same flavor channels, where  $Z/\gamma^* + \text{jets}$  production is one of the dominant back-  
1842    grounds. The BDT analysis requires  $p_T^{\text{miss}} > 40$  GeV and  $E_T^{\text{miss}} > 45$  GeV. The cut-based analysis  
1843    must select more tightly on these variables to have maximal sensitivity and thus requires  $p_T^{\text{miss}} > 50$  GeV  
1844    and  $E_T^{\text{miss}} > 55$  GeV.

1845    Finally, because this analysis is focused on VBF Higgs production, a requirement on the jet multiplicity  
1846    is placed, with  $n_j \geq 2$ . Additionally, the analysis requires that there are no jets identified as b-quarks in  
1847    the event, or  $n_b = 0$ .

1848    **5.4.2 ANALYSIS VARIABLE DEFINITIONS AND CUT-BASED SELECTION**

1849    The cut-based selection places sequential requirements on variables reconstructed from the VBF jets in  
1850    order to increase the signal to background ratio. This section defines the variables that are used in the  
1851    cut-based selection and details the requirements that are placed on these variables.

1852 GENERAL BACKGROUND REDUCTION

1853 Top pair production is the primary background in the  $n_j \geq 2$  bin. Even though  $n_b = 0$  is required, an  
1854 additional variable is constructed to further suppress the top background. There is often additional QCD  
1855 radiation that accompanies the  $t\bar{t}$  system when it is produced. Therefore, a variable which tests for the  
1856 presence of this additional radiation,  $p_T^{\text{sum}}$ , is constructed. It is defined in equation 5.1.

$$p_T^{\text{sum}} = p_T^{\ell\ell} + p_T^{\text{miss}} + \sum p_T^j \quad (5.1)$$

1857 After pre-selection, the cut-based analysis requires the event to have  $p_T^{\text{sum}} < 15$  GeV to further suppress  
1858  $t\bar{t}$  production.

1859 In the different flavor channels, a requirement is made to reduce the contamination from  $Z \rightarrow \tau\tau$   
1860 decays. The di- $\tau$  invariant mass,  $m_{\tau\tau}$ , is constructed by assuming that the neutrinos from the  $\tau$  decays  
1861 were collinear with the leptons [77]. The analysis requires that this mass satisfy  $m_{\tau\tau} < m_Z - 25$  GeV so  
1862 that it is not consistent with the mass of the  $Z$  boson.

1863 VBF TOPOLOGICAL CUTS

1864 The characteristic feature of VBF production of the Higgs is the presence of two additional forward jets  
1865 coming from the incoming partons which radiate the vector bosons that make the Higgs. These jets are  
1866 forward because the outgoing partons still carry the longitudinal momentum of the incoming partons.  
1867 Figure 5.2 shows the distribution of the  $\eta$  for the leading jet in a VBF event compared to a background top  
1868 pair production event. As can be seen, the VBF jets tend to be more forward in  $\eta$ , while the  $t\bar{t}$  jets are more  
1869 central. Because the cross section for VBF production is an order of magnitude smaller than gluon fusion  
1870 production, these forward jets must be used in order to reduce background and achieve a good signal to  
1871 background ratio. The dedicated VBF search selection requirements are constructed to maximally exploit  
1872 the features of the unique VBF topology.

1873 Requirements on the VBF jets are collectively referred to as the “VBF topological cuts”. First, a require-  
1874 ment on the dijet invariant mass of the VBF jets,  $m_{jj}$ , is placed, requiring  $m_{jj} > 600$  GeV. Next, the

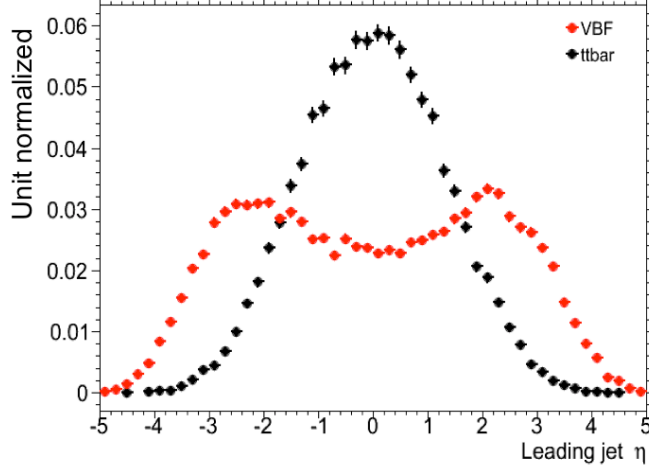


Figure 5.2: Leading jet  $\eta$  in VBF  $H \rightarrow WW^*$  (red) and  $t\bar{t}$  (black)

event is required to have a large gap in rapidity between the two VBF jets, or  $\Delta y_{jj} > 3.6$ . Both of these are tight requirements on the presence of two forward, high  $p_T$  jets moving in opposite directions in the longitudinal plane.

Beyond requiring the presence of the two forward VBF jets, the analysis also vetoes on the presence of any additional jets that fall between the two VBF jets. This requirement is referred to as the central jet veto, or CJV. Events are vetoed if they have a third jet with  $p_T > 20$  GeV whose rapidity is between the region defined by the two VBF jets. This requirement can be expressed in terms of a variable called the jet centrality, defined in equation 5.2.

$$C_{j3} = \left| \eta_{j3} - \frac{\eta_{j1} + \eta_{j2}}{2} \right| / \frac{|\eta_{j1} - \eta_{j2}|}{2}, \quad (5.2)$$

Here,  $\eta_{j1}$  and  $\eta_{j2}$  are the pseudorapidities of the leading and subleading jets, respectively, while  $\eta_{j3}$  is the pseudorapidity of the extra jet in the event (if one exists). Intuitively,  $C_{j3}$  is zero when  $\eta_{j3}$  is directly centered between the two jets and unity when  $\eta_{j3}$  is aligned with either of the VBF jets. Thus, the CJV can be expressed as a requirement that  $C_{j3} > 1$ .

The decay products of the Higgs tend to be central as well. Thus, the analysis also requires that both

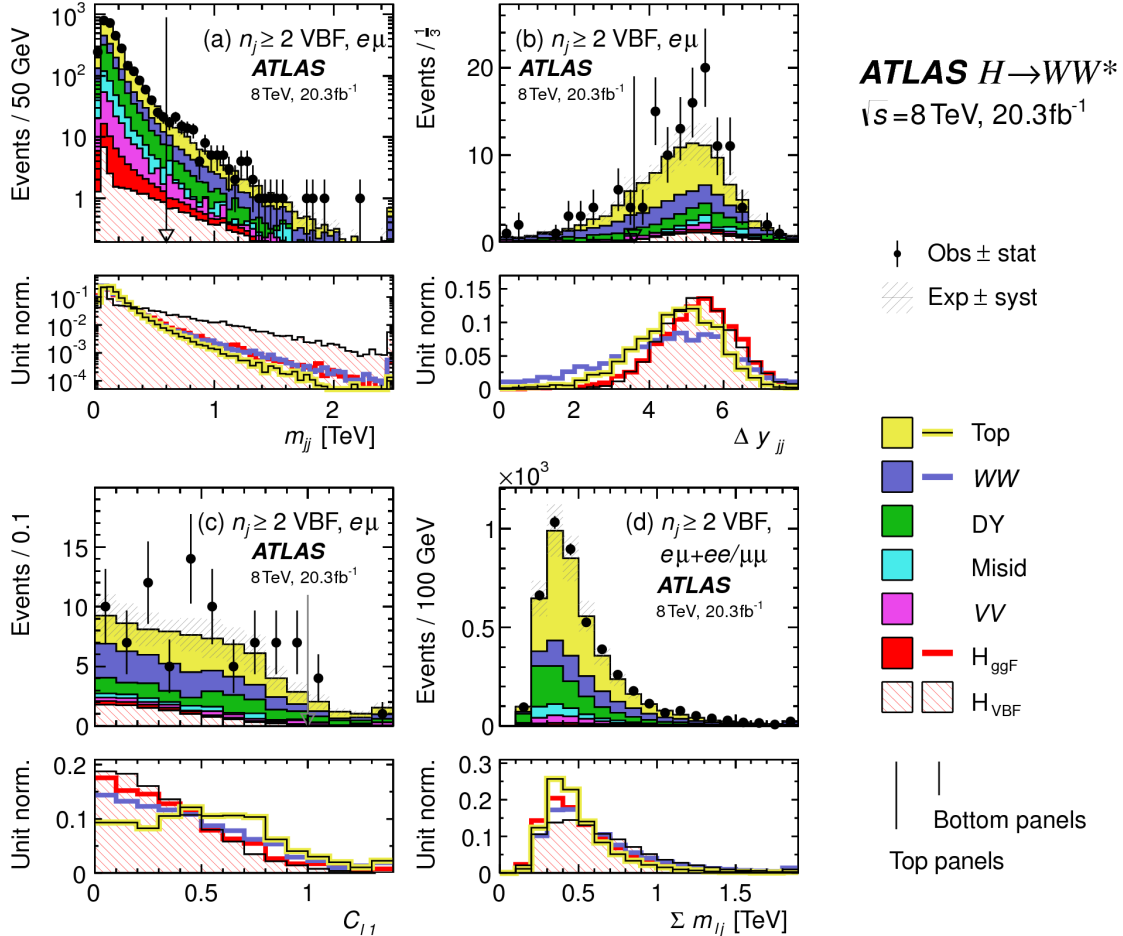


Figure 5.3: Distributions of (a)  $m_{jj}$ , (b)  $\Delta y_{jj}$ , (c)  $C_{\ell 1}$ , and (d)  $\Sigma m_{\ell j}$ , for the cut-based VBF analysis. The top panels compare simulation and data, while the bottom panels show normalized distributions for all background processes and signal for shape comparisons [74].

leptons in the analysis fall within the rapidity gap defined by the jets. This cut is referred to as the outside lepton veto, or OLV. Stated another way, leptons are required to have a centrality (defined analogously to that of the third jet in equation 5.2) within the jet rapidity gap, or  $C_{\ell} < 1$  for both leptons.

Figure 5.3a-c shows the  $m_{jj}$ ,  $\Delta y_{jj}$ , and  $C_{\ell 1}$  variables at the stage where all previous requirements in the sequence have been made. The agreement between data and Monte Carlo is good, and the bottom panels show their power in discriminating the VBF signal from the background processes.

The final signal region is also split into two bins of  $m_{jj}$ , with the first bin corresponding to  $600 \text{ GeV} < m_{jj} < 1 \text{ TeV}$  and the second bin corresponding to  $m_{jj} > 1 \text{ TeV}$ . The first bin has more events but also

1896 a larger contribution from background, while the second bin has a lower expected number of events but a  
1897 1:1 signal to background ratio.

1898 HIGGS TOPOLOGICAL CUTS

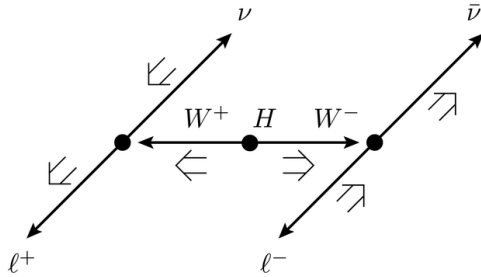


Figure 5.4: A cartoon of the WW final state. Momenta are represented with thin arrows, spins with thick arrows [74].

1899 The final state leptons will exhibit unique correlations due to the fact that they arise from the decay of  
1900 a spin zero resonance. These characteristics are present in  $H \rightarrow WW^* \rightarrow \ell\nu\ell\nu$  decays regardless of the  
1901 production mode being studies. In particular, the spins of the final state leptons and neutrinos must all  
1902 cancel, as shown in figure 5.4. Because the neutrino has a left handed chirality and the anti-neutrino has a  
1903 right handed chirality (in the massless neutrino approximation), the spin and momentum of the particles  
1904 will be anti-aligned and aligned, respectively. In the transverse plane, the momenta of all four final state  
1905 objects must cancel as well. With the constraint of having both the momenta and the spin alignments  
1906 cancel, the final state kinematics strongly prefer having a small angle between the leptons in the transverse  
1907 plane (low  $\Delta\phi_{\ell\ell}$ ). This angular correlation will also lead to low values of the di-lepton invariant mass  $m_{\ell\ell}$ .  
1908 These unique signal final state kinematic correlations are exploited to define the ultimate signal region.

1909 Two requirements on dilepton kinematics are made that are common with lower multiplicity jet bins  
1910 as well. The angle between leptons in the transverse plane,  $\Delta\phi_{\ell\ell}$ , is required to be less than 1.8 radians.  
1911 Additionally, the dilepton invariant mass,  $m_{\ell\ell}$ , is required to be less than 50 GeV.

1912 The cut-based analysis uses  $m_T$  as the final discriminating variable as in the ggF focused analysis. The  
1913 optimal number of bins in  $m_T$  was found to be three bins, with the bin boundaries at 80 and 130 GeV.

1914      Table 5.7 shows a summary of the data and estimated signal and background yields from simulation  
 1915      as each requirement described above is made. The table shows how the overall signal to background ra-  
 1916      tio grows through the various selection requirements. Table 5.8 shows the background composition after  
 1917      each selection requirement, illustrating which backgrounds are reduced most by certain requirements. Fig-  
 1918      ure 5.5 shows an ATLAS event display of a candidate event in the final signal region.

Selection	Summary					
	$N_{\text{obs}}/N_{\text{bkg}}$	$N_{\text{obs}}$	$N_{\text{bkg}}$	$N_{\text{signal}}$		
				$N_{\text{ggF}}$	$N_{\text{VBF}}$	$N_{\text{VH}}$
$e\mu$ sample	$1.00 \pm 0.00$	61434	61180	85	32	26
$n_b = 0$	$1.02 \pm 0.01$	7818	7700	63	26	16
$p_T^{\text{sum}} < 15$	$1.03 \pm 0.01$	5787	5630	46	23	13
$m_{\tau\tau} < m_Z - 25$	$1.05 \pm 0.02$	3129	2970	40	20	9.9
$m_{jj} > 600$	$1.31 \pm 0.12$	131	100	2.3	8.2	—
$\Delta y_{jj} > 3.6$	$1.33 \pm 0.13$	107	80	2.1	7.9	—
$C_{j3} > 1$	$1.36 \pm 0.18$	58	43	1.3	6.6	—
$C_{\ell 1} < 1, C_{\ell 2} < 1$	$1.42 \pm 0.20$	51	36	1.2	6.4	—
$m_{\ell\ell}, \Delta\phi_{\ell\ell}, m_T$	$2.53 \pm 0.71$	14	5.5	0.8	4.7	—
<hr/>						
$ee/\mu\mu$ sample	$0.99 \pm 0.01$	26949	27190	31	14	10.1
$n_b, p_T^{\text{sum}}, m_{\tau\tau}$	$1.03 \pm 0.03$	1344	1310	13	8.0	4.0
$m_{jj}, \Delta y_{jj}, C_{j3}, C_\ell$	$1.39 \pm 0.28$	26	19	0.4	2.9	0.0
$m_{\ell\ell}, \Delta\phi_{\ell\ell}, m_T$	$1.63 \pm 0.69$	6	3.7	0.3	2.2	0.0

Table 5.7: Summary of event selection for the  $n_j \geq 2$  VBF analysis in the 8 TeV cut-based analysis [74].

### 1919      5.4.3    BDT-BASED SELECTION

1920      The boosted decision tree based analysis uses many of the variables defined in the cut-based selection as  
 1921      inputs to the BDT. The output BDT score ( $O_{\text{BDT}}$ ) is used as the final discriminant rather than  $m_T$ <sup>2</sup>.  
 1922      The BDT is trained with the VBF  $H \rightarrow WW^*$  simulation as the signal samples and all other processes as  
 1923      background, including ggF  $H \rightarrow WW^*$  production. While the BDT based analysis is ultimately treated  
 1924      as a separate result, it has significant overlap with the cut-based selection.

---

<sup>2</sup>For the final discriminant analysis, the  $O_{\text{BDT}}$  distribution is divided into four bins, with boundaries at  $[-1, -0.48, -0.3, 0.78, 1]$ .

	Composition of $N_{\text{bkg}}$									
	$N_{WW}$		$N_{t\bar{t}}$		$N_{\text{misid}}$		$N_{VV}$		$N_{\text{Drell-Yan}}$	
	$N_{WW}^{\text{QCD}}$	$N_{WW}^{\text{EW}}$	$N_{t\bar{t}}$	$N_t$	$N_{Wj}$	$N_{jj}$	$N_{VV}$	$N_{ee/\mu\mu}$	$N_{\tau\tau}^{\text{QCD}}$	$N_{\tau\tau}^{\text{EW}}$
$e\mu$ sample	1350	68	51810	2970	847	308	380	51	3260	46
$n_b = 0$	993	43	3000	367	313	193	273	35	2400	29
$p_T^{\text{sum}} < 15$	781	38	1910	270	216	107	201	27	2010	23
$m_{\tau\tau} < m_Z - 25$	484	22	1270	177	141	66	132	7.6	627	5.8
$m_{jj} > 600$	18	8.9	40	5.3	1.8	2.4	5.1	0.1	15	1.0
$\Delta y_{jj} > 3.6$	11.7	6.9	35	5.0	1.6	2.3	3.3	—	11.6	0.8
$C_{j3} > 1$	6.9	5.6	14	3.0	1.3	1.3	2.0	—	6.8	0.6
$C_{\ell 1} < 1, C_{\ell 2} < 1$	5.9	5.2	10.8	2.5	1.3	1.3	1.6	—	5.7	0.6
$m_{\ell\ell}, \Delta\phi_{\ell\ell}, m_T$	1.0	0.5	1.1	0.3	0.3	0.3	0.6	—	0.5	0.2
$ee/\mu\mu$ sample	594	37	23440	1320	230	8.6	137	690	679	16
$n_b, p_T^{\text{sum}}, m_{\tau\tau}$	229	12.0	633	86	26	0.9	45	187	76	1.5
$m_{jj}, \Delta y_{jj}, C_{j3}, C_\ell$	3.1	3.1	5.5	1.0	0.2	0.0	0.7	3.8	0.7	0.1
$m_{\ell\ell}, \Delta\phi_{\ell\ell}, m_T$	0.4	0.2	0.6	0.2	0.2	0.0	0.1	1.5	0.3	0.1

Table 5.8: Background composition after each requirement in the  $n_j \geq 2$  VBF analysis in the 8 TeV cut-based analysis [74].

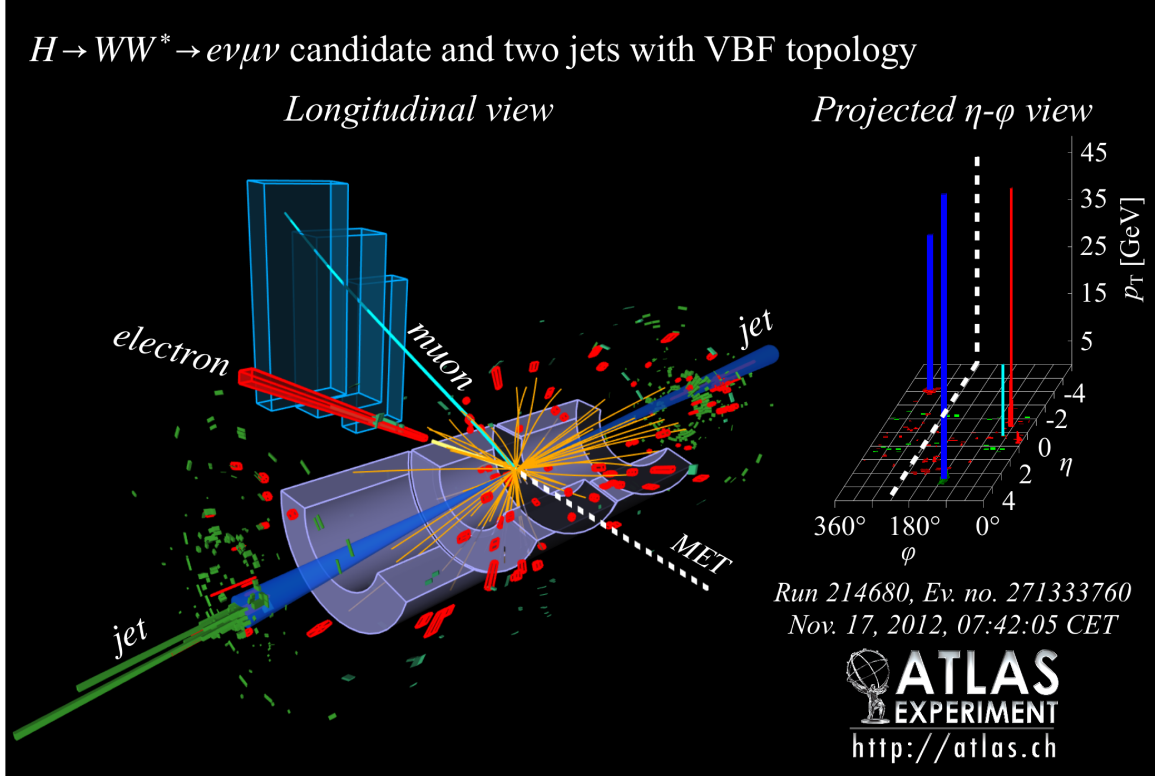


Figure 5.5: Event display of a VBF candidate event [74].

1925    **PRE-TRAINING SELECTION AND BDT INPUTS**

1926    Before training, the common pre-selection cuts described in section 5.4.1 are applied. Additionally, the  
1927    central jet veto and outside lepton veto described in section 5.4.2 are applied. The BDT has eight input  
1928    variables, six of which are also variables that are used in the cut-based analysis. The six shared variables  
1929    are  $p_T^{\text{sum}}$ ,  $m_{jj}$ ,  $\Delta y_{jj}$ ,  $m_{\ell\ell}$ ,  $\Delta\phi_{\ell\ell}$ , and  $m_T$ . The seventh variable input in the BDT is a combination of  
1930    the variables used to define the OLV in the cut-based analysis. The BDT uses as input the sum of lepton  
1931    centralities, or  $\sum C_\ell = C_{\ell 1} + C_{\ell 2}$ . The final BDT input variable,  $\Sigma m_{\ell j}$ , is constructed to account for  
1932    the correlations between the jets and leptons in the event. It is the sum of the invariant masses of all four  
1933    possible lepton-jet combinations.

1934    Figure 5.3d shows the agreement between data and simulation for the  $\Sigma m_{\ell j}$  variable, as well as showing  
1935    its discriminating power. Figure 5.6 shows the distributions of the Higgs topological variables that are  
1936    shared between the cut-based and BDT analyses. Figure 5.7 shows the distributions of the VBF topological  
1937    variables shared between the cut-based and BDT analyses. In both cases, the VBF yield has been scaled by  
1938    a factor of 50 to better show the shape difference compared to the backgrounds.

1939    **5.5 BACKGROUND ESTIMATION**

1940    This section describes the procedures used to estimate backgrounds for the VBF analysis in both the cut-  
1941    based and BDT analyses.

1942    **5.5.1 GENERAL STRATEGY**

1943    Most of the backgrounds in both the gluon fusion and VBF Higgs analyses have shapes estimated from  
1944    Monte Carlo simulation but normalizations derived from control regions in data. In essence, a normaliza-  
1945    tion factor (denoted with  $\beta$  or abbreviated as NF) is derived by scaling the MC yield in the control region  
1946    to the corresponding yield in data. Once this factor is derived, it can be used to scale the MC estimate of  
1947    the background in the signal region. This is illustrated in equation 5.3.

$$B_{\text{SR}}^{\text{est}} = B_{\text{SR}} \times \frac{N_{\text{CR}}}{B_{\text{CR}}} \equiv B_{\text{SR}} \times \beta \quad (5.3)$$

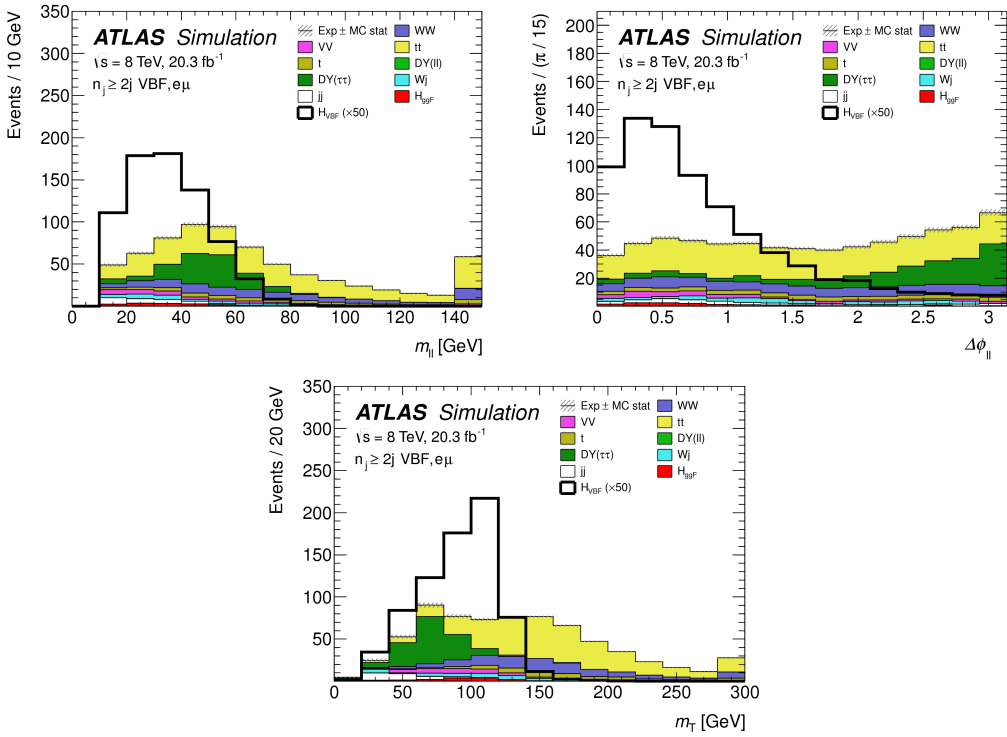


Figure 5.6: Higgs topology variables -  $m_{\ell\ell}$  (top left),  $\Delta\phi_{\ell\ell}$  (top right), and  $m_T$  (bottom) - used in the selection requirements of the cut-based signal region and as inputs to the BDT result. These are plotted after all of the BDT pre-training selection cuts [74]. The VBF Higgs signal cross section is multiplied by a factor of 50 to allow for shape comparisons.

1948 Here,  $B$  is the MC yield prediction in the denoted region, while  $N$  is the observed number of events in  
 1949 data in the denoted region.

1950 There is an alternative way of writing the same equation in terms of an extrapolation factor  $\alpha$  rather  
 1951 than a normalization factor  $\beta$ . The overall calculation is exactly the same. However, when phrased in  
 1952 this way, it shows how the uncertainty on the background estimation can be reduced. This is shown in  
 1953 equation 5.4.

$$B_{\text{SR}}^{\text{est}} = N_{\text{CR}} \times \frac{B_{\text{SR}}}{B_{\text{CR}}} \equiv N_{\text{CR}} \times \alpha \quad (5.4)$$

1954 Phrased this way, the equation shows that with enough events in the control region, a large theoretical  
 1955 uncertainty on the overall background yield in the signal region can be replaced by a small statistical un-  
 1956 certainty coming from the number of data events in the CR and a smaller theoretical uncertainty on the  
 1957 extrapolation from the control region to the signal region.

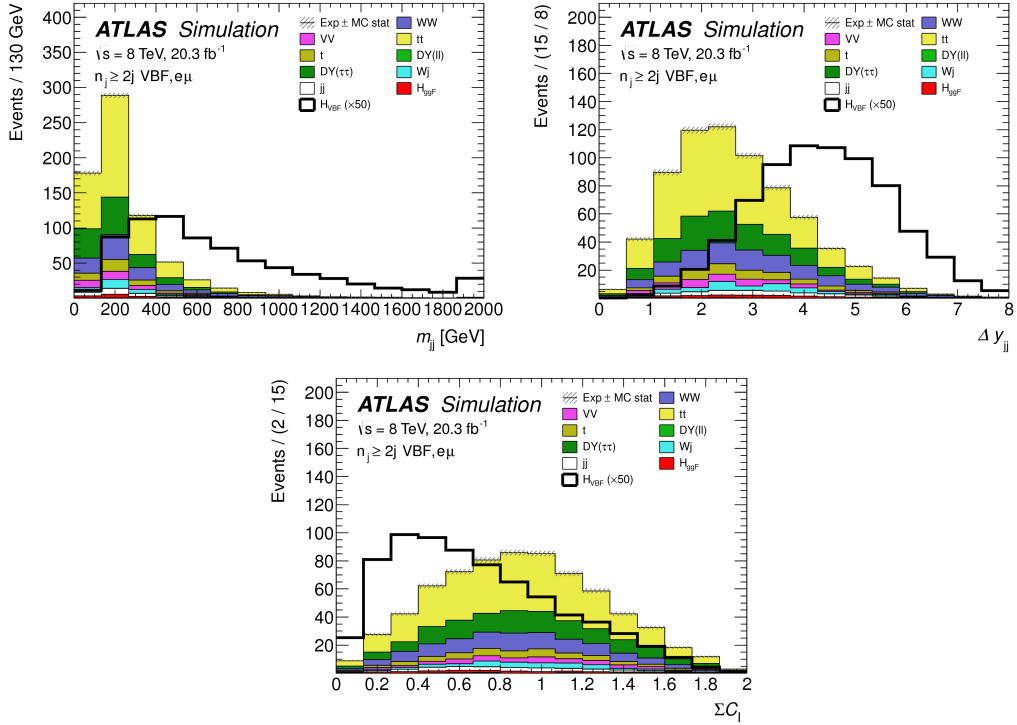


Figure 5.7: VBF topology variables -  $m_{jj}$  (top left),  $\Delta y_{jj}$  (top right),  $\sum C_\ell$  (bottom) - used in the selection requirements of the cut-based signal region and as inputs to the BDT result. These are plotted after all of the BDT pre-training selection cuts [74]. The VBF Higgs signal cross section is multiplied by a factor of 50 to allow for shape comparisons.

### 5.5.2 TOP BACKGROUND

The normalization factor  $\beta_t$  for the top background in the VBF analysis is derived in a region required to have one  $b$ -tagged jet, or  $n_b = 1$ . In the cut-based analysis, normalization factors are computed after every selection requirement by making the same requirements in the CR. These NF are then applied to the  $t\bar{t}$  and single top event yields in the SR. In the BDT analysis, a single normalization factor is computed for each bin of  $O_{\text{BDT}}$  after applying the BDT pre-training cuts described previously. The computed normalization factors are derived with all flavor combinations combined in order to decrease statistical uncertainty. Additionally, in the BDT analysis, BDT bins 2 and 3 are merged for the same reason.

Table 5.9 shows the evolution of the  $\beta_t$  through the cut-based selection. Table 5.10 shows the value of the  $\beta_t$  in each bin of  $O_{\text{BDT}}$ . The computed factors are almost all relatively consistent with unity, except for bin 1 of  $O_{\text{BDT}}$  which requires a larger correction. The normalization factors in bins 2 and 3 of  $O_{\text{BDT}}$  are also

<sup>1969</sup> consistent with those derived in the cut-based signal region, increasing confidence in the BDT estimation.

Figure 5.8 shows the  $m_{jj}$  and  $O_{\text{BDT}}$  distributions in the top control region. Overall the modeling looks

Cut	$\beta_t$
$p_T^{\text{sum}} < 15 \text{ GeV}$	$1.03 \pm 0.01$
$m_{\tau\tau} < m_Z - 25$	$1.05 \pm 0.01$
$m_{jj} > 600 \text{ GeV}$	$0.96 \pm 0.06$
$\Delta y_{jj} > 3.6$	$1.02 \pm 0.08$
CJV	$1.13 \pm 0.16$
OLV	$1.01 \pm 0.19$
$m_{jj} < 1 \text{ TeV}$	$0.94 \pm 0.19$
$m_{jj} > 1 \text{ TeV}$	$1.48 \pm 0.66$

Table 5.9: Top normalization factors computed at each stage of the cut-based selection. Uncertainties are statistical only.

$O_{\text{BDT}}$	$\beta_t$
Bin 0	$1.09 \pm 0.02$
Bin 1	$1.58 \pm 0.15$
Bin 2	$0.95 \pm 0.31$
Bin 3	$0.95 \pm 0.31$

Table 5.10: Top normalization factors computed for each bin of  $O_{\text{BDT}}$ . Uncertainties are statistical only.

<sup>1970</sup>

<sup>1971</sup> consistent with the data. While these normalization factors can be computed and applied to the expected  
<sup>1972</sup> background yields listed in tables like table 5.8, the final normalization of the top background is profiled  
<sup>1973</sup> (meaning there is a dedicated Poisson constraint) and allowed to float in the final statistical fit.

### <sup>1974</sup> 5.5.3 $Z/\gamma^* \rightarrow \tau\tau$ BACKGROUND

<sup>1975</sup> In the different flavor channels, the  $Z/\gamma^* \rightarrow \tau\tau$  background is an important one. Di-tau production can  
<sup>1976</sup> produce an  $e\mu$  final state if each  $\tau$  lepton decays to a different flavor lepton.

<sup>1977</sup> In the BDT analysis, a single normalization factor for the background is derived. A control region  
<sup>1978</sup> is defined using the pre-training selection cuts, except requiring that  $|m_{\tau\tau} - m_Z| < 25 \text{ GeV}$  so that  
<sup>1979</sup> the region is enriched in  $Z/\gamma^* \rightarrow \tau\tau$  background. Additional requirements of  $m_{\ell\ell} < 80(75) \text{ GeV}$   
<sup>1980</sup> in the different (same) flavor channel, as well as  $O_{\text{BDT}} > -0.48$  are applied to increase the purity of the

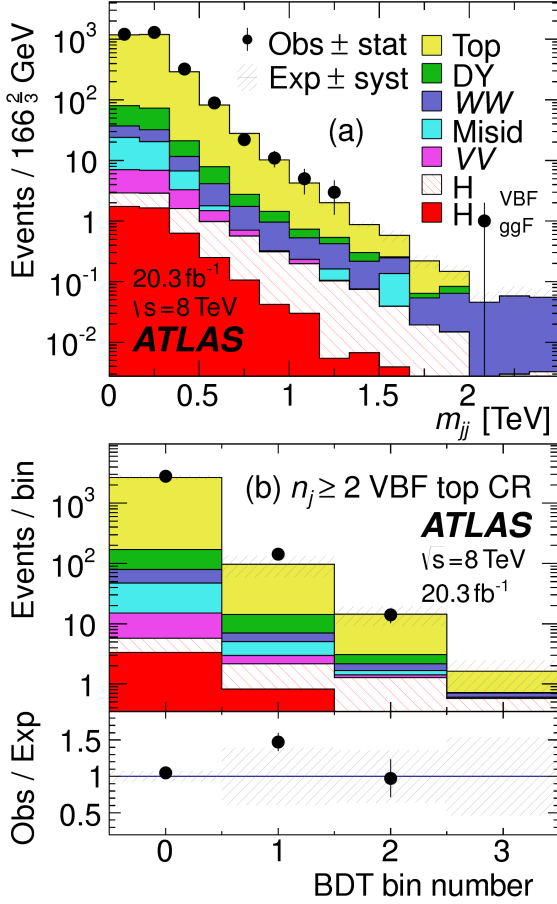


Figure 5.8: Distributions of  $m_{jj}$  (a) and  $O_{\text{BDT}}$  (b) in the VBF  $n_b = 1$  top CR [74].

region. The final  $\beta_{Z/\gamma^* \rightarrow \tau\tau}$  is calculated to be  $0.9 \pm 0.3$  (statistical uncertainty only). Because of the small contribution of this background in the BDT analysis and the large statistical uncertainty, no additional systematics are calculated. The final SR estimate is scaled by this  $\beta$  and not allowed to float in the fit.

The cut-based corrections are a bit more involved because they need to be applied selection by selection, as well as in the final signal region for the fit. The control region is defined including all SR requirements up to the  $Z/\gamma^* \rightarrow \tau\tau$  veto, which is instead turned into a Z mass peak requirement as for the BDT region. The  $m_{\ell\ell}$  cut from the BDT region is included as well. The cut-based approach aims to correct the normalization of the  $Z/\gamma^* \rightarrow \tau\tau$  background in two ways. First, an overall normalization factor is computed from the control region. However, the VBF topological cuts are not included in this region, and applying them as is done in the top CR is not feasible due to limited statistics. So, instead, correction

1991 factors (CF) to the cut efficiencies of the VBF cuts are derived in a same flavor  $Z \rightarrow \ell\ell$  control region,  
 1992 which has significantly more statistics. The CF is simply the ratio of the cut efficiencies in data and MC  
 1993 derived in this region. In the end, the overall background estimate is given by equation 5.5.

$$N_{Z/\gamma^* \rightarrow \tau\tau}^{\text{est}} = B_{Z/\gamma^* \rightarrow \tau\tau}^{\text{SR}} \times \beta_{\tau\tau} \times \frac{\epsilon_{\text{VBF cuts}}^{\text{data}}}{\epsilon_{\text{VBF cuts}}^{\text{MC}}} \quad (5.5)$$

1994 The hypothesis is that while the normalization correction must be derived in a dedicated region, the effi-  
 1995 ciency of the VBF topology requirements should not be sensitive to the type of  $Z/\gamma^*$  process and thus the  
 1996 higher number of events can be exploited to derive the CF. Figure 5.9 shows a shape comparison for the  
 1997  $m_{jj}$  variable in  $Z \rightarrow \tau\tau$  events in the signal region and  $Z \rightarrow \ell\ell$  events in the control region. The figure  
 1998 shows that the shapes are indeed comparable and thus any CF derived in the same flavor control region  
 1999 can reliably be applied in the signal region.

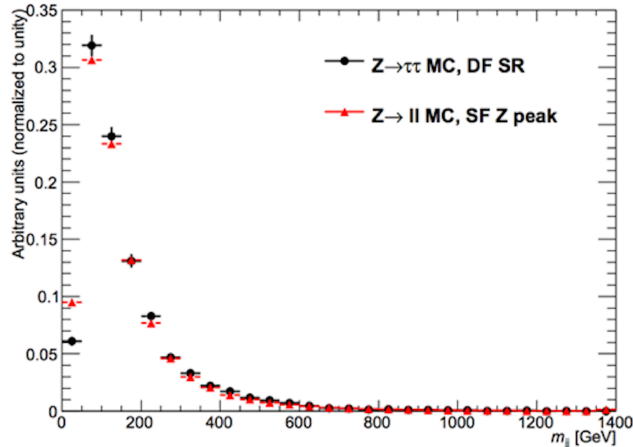


Figure 5.9: Comparison of  $m_{jj}$  shape in a same flavor  $Z \rightarrow \ell\ell$  control region and the VBF cut-based signal region.  
The MC samples used for these distributions are given in table 5.4.

2000 Table 5.11 shows the overall normalization factor  $\beta_{\tau\tau}$  and the efficiency correction factors for the various  
 2001 VBF topological cuts. In general, the statistical uncertainties on the cut efficiency corrections are quite  
 2002 good, and the MC tends to underestimate the efficiency of the VBF cuts for the  $Z/\gamma^* \rightarrow \tau\tau$  background.  
 2003 The overall normalization factor is also consistent with that calculated for the BDT analysis.

$\beta_{\tau\tau}$	$0.97 \pm 0.04$
Cut	Correction factors (CF)
$m_{jj} > 600 \text{ GeV}$	$1.09 \pm 0.01$
$\Delta y_{jj} > 3.6$	$1.14 \pm 0.02$
CJV	$1.20 \pm 0.02$
OLV	$1.17 \pm 0.03$
$m_{jj} < 1 \text{ TeV}$	$1.17 \pm 0.06$
$m_{jj} > 1 \text{ TeV}$	$1.18 \pm 0.13$

Table 5.II:  $Z/\gamma^* \rightarrow \tau\tau$  correction factors for the VBF cut-based analysis. Uncertainties are statistical only.

2004 5.5.4  $Z/\gamma^* \rightarrow \ell\ell$  BACKGROUND

2005 In the same flavor channels, the  $Z/\gamma^* \rightarrow \ell\ell$  background is dominant and thus must be estimated cor-  
 2006 rectly. In both the BDT and cut-based analyses, the background is estimated using the so-called “ABCD”  
 2007 method. The ABCD method creates four different regions by defining requirements on two variables.  
 2008 One of the regions (A) is the signal region, while the other regions are defined by inverting one of both of  
 2009 the requirements. in this case, the two variables used are  $m_{\ell\ell}$  and  $E_T^{\text{miss}}$ , because inverting either of the  
 2010 SR cuts on these variables will give regions rich in the  $Z/\gamma^* \rightarrow \ell\ell$  background. Figure 5.10 illustrates the  
 2011 definitions of each region.

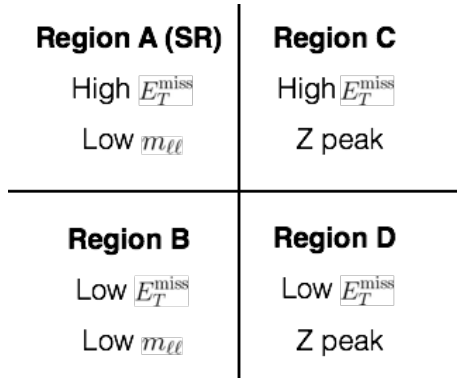


Figure 5.10: General illustration of the ABCD region definitions for  $Z/\gamma^* \rightarrow \ell\ell$  background estimation.

2012 In both of the cut-based and BDT analyses, the Z peak region is defined with  $|m_{\ell\ell} - m_Z| < 15 \text{ GeV}$ .  
 2013 In the cut-based analysis, low  $m_{\ell\ell}$  corresponds to  $m_{\ell\ell} < 50 \text{ GeV}$  (this defines the cut-based SR) while  
 2014 in the BDT it is  $m_{\ell\ell} < 75 \text{ GeV}$ . In the cut-based, high and low  $E_T^{\text{miss}}$  are defined as opposite ends of

2015 the 55 GeV cut applied for the signal region definition. The BDT low  $E_T^{\text{miss}}$  region is between 25 and  
 2016 45 GeV, while the high  $E_T^{\text{miss}}$  region is  $E_T^{\text{miss}} > 45$  GeV.

2017 Once the regions are defined, the background in the signal region is estimated by extrapolating the  
 2018 estimate in region B to region A. This extrapolation is done by multiplying the number of events in region  
 2019 B by the ratio of the number of events in regions C and D. Effectively, the Z peak region is used to estimate  
 2020 the efficiency of the  $E_T^{\text{miss}}$  requirement in data, and then this efficiency is applied in the low  $m_{\ell\ell}$  region.  
 2021 The method assumes that the  $E_T^{\text{miss}}$  efficiency is uncorrelated with  $m_{\ell\ell}$ . The method can be applied in  
 2022 MC as a check on this assumption, and an additional correction,  $f_{\text{corr}}$ , is applied for the non-closure of  
 2023 the method in MC. This is summarized in equations 5.6 and 5.7.

$$N_{Z/\gamma^* \rightarrow \ell\ell}^{\text{SR}} = N_{Z/\gamma^* \rightarrow \ell\ell}^{\text{B}} \times \frac{N_{Z/\gamma^* \rightarrow \ell\ell}^{\text{C}}}{N_{Z/\gamma^* \rightarrow \ell\ell}^{\text{D}}} \times f_{\text{corr}} \quad (5.6)$$

$$f_{\text{corr}} = \frac{B_{\text{MC}}^{\text{A}}/B_{\text{MC}}^{\text{B}}}{B_{\text{MC}}^{\text{C}}/B_{\text{MC}}^{\text{D}}} \quad (5.7)$$

2024 Here, the  $N$  refer to data yields in each region with the non  $Z/\gamma^*$  backgrounds subtracted, while  $B$  refer  
 2025 to the  $Z/\gamma^*$  yields in MC in each region.

2027 A normalization factor  $\beta_{\ell\ell}$  is computed for each analysis as the ratio of the predicted data yield to the  
 2028 MC yield in the SR. The shape of the BDT distribution is taken from data region B, while the shape of  
 2029 the  $m_T$  distribution in the cut-based analysis is taken from  $Z/\gamma^*$  MC in the SR. The values of  $\beta_{\ell\ell}$  in the  
 2030 cut-based and BDT analyses from this method are summarized in table 5.12. They are quite consistent  
 2031 with one another within the statistical uncertainties. The value of  $f_{\text{corr}}$  is found to be  $0.77 \pm 0.13$ . In the  
 2032 cut-based analysis, the same cut efficiency correction factors shown in table 5.11 are also applied (in product  
 2033 with the  $\beta_{\ell\ell}$ ) to obtain the final estimate of the  $Z/\gamma^*$  background in the same flavor channels.

	$\beta_{\ell\ell}$
BDT Bin 1	$1.01 \pm 0.15$
BDT Bin 2	$0.89 \pm 0.28$
Cut-based	$0.81 \pm 0.21$

Table 5.12:  $Z/\gamma^* \rightarrow \ell\ell$  normalization factors for cut-based and BDT analyses. Uncertainties are statistical only.

2034 5.5.5  $WW$  AND OTHER DIBOSON BACKGROUNDS

2035 The Standard Model  $WW$  and other diboson backgrounds ( $WZ$ ,  $ZZ$ ,  $W\gamma$ ,  $W\gamma^*$ , and  $Z\gamma$ ) have both  
 2036 their shape and normalization taken from MC simulation as they are subdominant in the VBF analysis.  
 2037 They are validated in dedicated control regions and found to agree with data well.

2038 As SM  $WW$  production is the largest of these backgrounds and is irreducible, validating the estimate  
 2039 is of particular importance. A validation region is constructed by requiring the pre-selection requirements  
 2040 on leptons and  $m_{\ell\ell}, n_b = 0$ , and  $m_T > 100$  GeV. The  $m_{T2}$  variable is an additional discriminant that  
 2041 has been shown to have the ability to isolate the SM  $WW$  background [99]. It is calculated by scanning  
 2042 over all possible values of neutrino momentum for both  $W$  bosons and taking the minimum result. A  
 2043 requirement of  $m_{T2} > 160$  GeV is placed to define the  $WW$  validation region. This requirement gives a  
 2044 60% purity for the validation region. The derived normalization factor in this region is  $1.15 \pm 0.19$  and  
 2045 is thus consistent with unity. Figure 5.11 shows the  $m_{T2}$  distribution and how it distinguishes the  $WW$   
 2046 background.

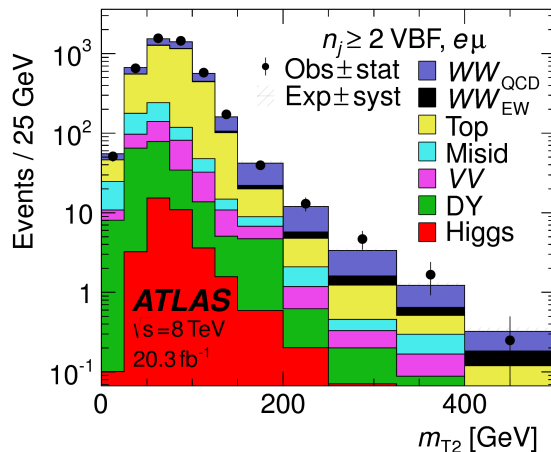


Figure 5.11: Distribution of  $m_{T2}$  in the  $WW$  validation region of the VBF analysis [74].

2047 5.5.6 HIGGS PRODUCTION VIA GLUON-GLUON FUSION

2048 Because this analysis is dedicated to measuring the VBF contribution to Higgs production, the component  
 2049 of Higgs production from gluon-gluon fusion is treated as a background. The shape is taken directly from

2050 simulation, using the generators described in table 5.4. In the final combined fit of all different Higgs  
2051 signal regions, the normalization is controlled by either a combined signal strength parameter  $\mu$ , which  
2052 controls the normalization of both ggF and VBF production, or a separate parameter  $\mu_{\text{ggF}}$  depending on  
2053 the interpretation being presented in the final results.

### 2054 5.5.7 BACKGROUNDS WITH MISIDENTIFIED LEPTONS

2055 As discussed previously, the  $W+\text{jets}$  and QCD multijet backgrounds are derived with fully data-driven  
2056 methods. These backgrounds do not make a large contribution to the final VBF signal region but their es-  
2057 timation methods are discussed briefly here. Because both backgrounds involve at least one mis-identified  
2058 lepton, they are labeled as “misid” throughout this chapter.

#### 2059 $W+\text{jets}$ BACKGROUND

2060 The  $W+\text{jets}$  background enters the signal region by having one of the jets mis-reconstructed as a lepton.  
2061 The background is estimated by constructing a control sample with two leptons, where one lepton passes  
2062 the usual lepton quality requirements but the second lepton fails one of those requirements (also known  
2063 as the “anti-identified” lepton). This control region is rich in the  $W+\text{jets}$  contribution because if a second  
2064 lepton is reconstructed in a  $W+\text{jets}$  event it is likely to be of poor quality. The purity of this  $W+\text{jets}$  control  
2065 sample is 85% to 90% depending on the exact configuration of leptons in the final state.

2066 The  $W+\text{jets}$  content of the signal region is estimated by extrapolation from the control sample to the  
2067 signal region using extrapolation factors derived in a  $Z+\text{jets}$  control sample in data. The assumption of  
2068 the method is that the probability of a jet being misidentified as a lepton does not change between  $W+\text{jets}$   
2069 and  $Z+\text{jets}$  samples, and systematic uncertainties are assigned for differences in sample composition. The  
2070 extrapolation factor is defined as the ratio of the number of lepton candidates satisfying all quality criteria  
2071 to the number of lepton candidates anti-identified. This ratio is measured in bins of  $p_T$  and  $\eta$ . Thus, the  
2072 final signal region estimate (binned as the extrapolation factor is binned) is simply the number of events in  
2073 the anti-identified lepton control sample multiplied by the extrapolation factor derived from the  $Z+\text{jets}$   
2074 control sample. Figure 5.12 shows the extrapolation factors derived for electrons and muons. The extrap-

2075 olation factor can be seen in the figure to be an order of magnitude larger for muons than electrons, but  
 2076 this does not indicate that jets have a larger probability to be mis-identified as a muon than an electron.  
 2077 Values of the extrapolation factor are actually determined by the specific requirements used to define an  
 2078 anti-identified lepton. The difference between the muon and electron extrapolation factors comes from  
 2079 different definitions of the anti-identified lepton in each case.

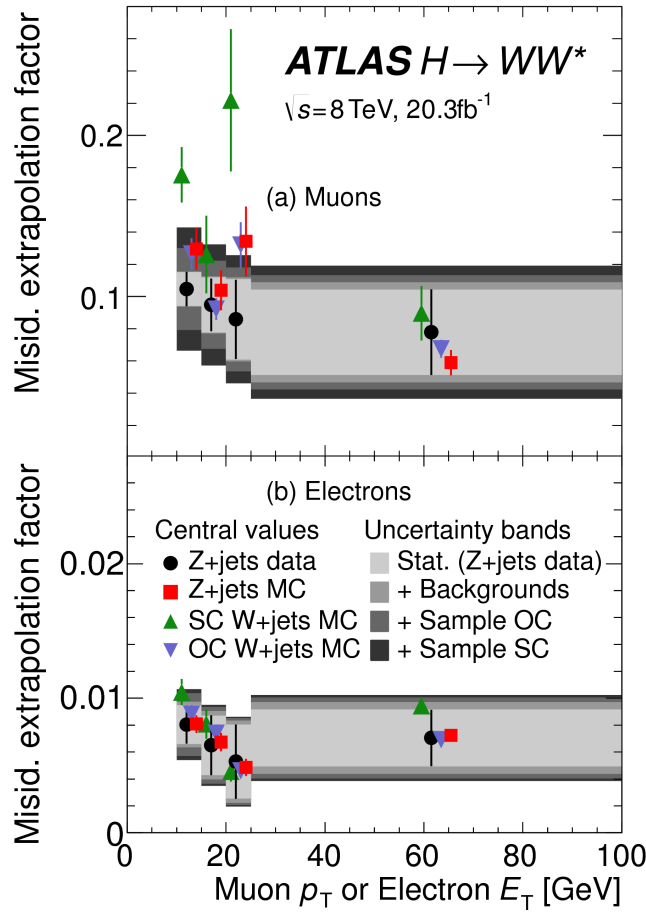


Figure 5.12: Extrapolation factors for the  $W + \text{jets}$  estimate derived for muons (a) and electrons (b) as a function of lepton  $p_T$  [74]. OC refers to the opposite charge  $W + \text{jets}$  MC sample, while SC refers to the same charge  $W + \text{jets}$  MC. The uncertainty bands have contributions from statistical uncertainty in the data and backgrounds to  $Z + \text{jets}$  that are subtracted from the data, as well as systematic uncertainties due to variations in the extrapolation factor between the three MC samples shown.

2080 **QCD MULTIJET BACKGROUND**

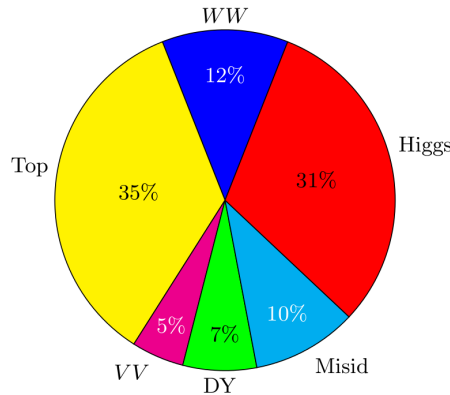
2081 The method for estimating the multijet background is very similar to the  $W + \text{jets}$  estimation method. The  
2082 control sample in this case has two anti-identified leptons but otherwise satisfies all signal region require-  
2083 ments. The extrapolation factor is estimated from a multijet sample and applied twice to the control sam-  
2084 ple.

2085 **5.5.8 BACKGROUND COMPOSITION IN SIGNAL REGION**

2086 After all of these estimation procedures, the signal region background composition can be calculated. The  
2087 estimated yields are all shown in table 5.8. Figure 5.13 shows the relative percentages of the different back-  
2088 ground for the different flavor and same flavor final states. In  $e\mu$ , the leading backgrounds are top back-  
2089 grounds, ggF Higgs, and SM  $WW$  production. In  $ee/\mu\mu$ , the leading background is Drell-Yan, followed  
2090 by top and ggF Higgs.

---

(a)  $n_j \geq 2$  VBF,  $e\mu$



(b)  $n_j \geq 2$  VBF,  $ee/\mu\mu$

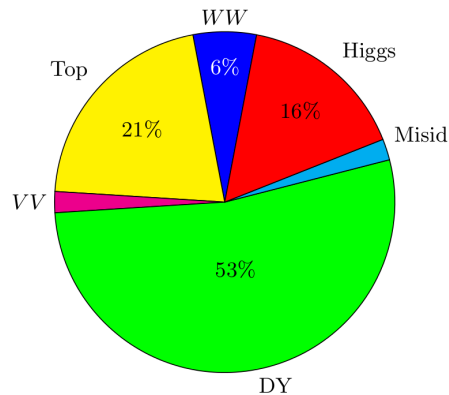


Figure 5.13: Background composition in final VBF signal region [74].

2091 **5.6 SYSTEMATIC UNCERTAINTIES**

2092 There are two main types of systematic uncertainties that are assessed for the analysis. First, theoretical  
2093 uncertainties associated with the signal and background yield estimates are discussed. Then, experimental  
2094 uncertainties due to detector effects are shown. Normalization uncertainties refer to uncertainties that

2095 affect the cross section of the process in question in the signal region being probed. Shape uncertainties  
2096 refer to systematic uncertainties that affect the shape of the final discriminating variable (either  $m_T$  or  
2097  $O_{\text{BDT}}$ ).

2098 **5.6.1 THEORETICAL UNCERTAINTIES**

2099 There are four main components to theoretical uncertainties assigned to signal and background processes  
2100 taken from Monte Carlo. Each one is a different source of variation in the overall acceptance for that  
2101 process. The first involves variation of the QCD renormalization and factorization scales used in the cal-  
2102 culation. In this case, the two scales are varied both independently and simultaneously by factors of two  
2103 high or low. The resulting variation in normalization and shape for the process is taken as a systematic  
2104 uncertainty (referred to as scale uncertainty). This uncertainty approximates the level of the correction  
2105 to the cross section that would come from including the next order of the QCD calculation. Next, there  
2106 is an uncertainty associated with the PDF set used in generating the events. The uncertainty eigenvec-  
2107 tors for the given PDF set are inspected, and the envelope of maximal variation is taken as an uncertainty  
2108 (referred to as PDF uncertainty). Finally, there are two uncertainties associated with the choice of MC  
2109 software. An uncertainty associated with the generator chosen for the hard scattering process is evaluated  
2110 by keeping the parton showering software constant but varying the matrix element generator and taking  
2111 the maximal variation as an uncertainty (referred to as the generator uncertainty). The converse variation  
2112 can also be done, where the matrix element generator remains constant and the generator used for the un-  
2113 derlying event/parton shower modeling is varied (referred to as the UE/PS uncertainty). In cases where  
2114 the background is normalized in a control region, the systematic uncertainty arises from variations of the  
2115 extrapolation factor  $\alpha$  between the CR and the SR, which can affect the normalization of the background  
2116 in the SR.

2117 There are two additional uncertainties that are applied to the Higgs processes as well. First, there are  
2118 uncertainties assigned to the Higgs total production cross section. Then, there are uncertainties assigned  
2119 based on the fact that the analysis is done in exclusive jet bins and it is possible for signal events to migrate  
2120 from one bin to the next depending on the presence or absence of jets. These are assigned using the Jet Veto

2121 Efficiency (JVE) procedure [18, 100] for ggF events and the Stewart-Tackmann (ST) method [101] for VBF  
 2122 production. Table 5.13 shows the total theory uncertainties on the backgrounds in the cut-based analysis.  
 2123 These are the sum in quadrature of the uncertainties from each of the variations described above.

Process	Theory syst. (%)
ggF $H$	48
Top	26
QCD $WW$	37
$Z/\gamma^* \rightarrow \tau\tau$	6.1

Table 5.13: Systematic uncertainties for various processes in the cut-based VBF analysis, given in units of % change in yield. Values are given for the low  $m_{jj}$  signal region.

2124 Figures 5.14 and 5.15 show the variations in the extrapolation factor from the PDF and QCD uncertain-  
 2125 ties on the top background estimate, binned in  $m_T$ , for the cut-based analysis. In both cases, there was  
 2126 no significant shape uncertainty but normalization uncertainties were assigned according to the maximal  
 2127 variation. These uncertainties enter into the 26% total uncertainty on top quark production quoted in  
 2128 table 5.13

2129 While the estimate for the same-flavor  $Z/\gamma^* \rightarrow \ell\ell$  background is data-driven, there is still a systematic  
 2130 uncertainty taken for the non-closure of the method in Monte Carlo. This is taken as the maximum of the  
 2131 deviation of the non-closure factor  $f_{\text{corr}}$  from unity and its uncertainty, or  $\max(|1 - f_{\text{corr}}|, \delta f_{\text{corr}})$ . For  
 2132 the cut-based analysis this non-closure uncertainty 23%, while for the BDT analysis it is 17%.

### 2133 5.6.2 EXPERIMENTAL UNCERTAINTIES

2134 In this analysis, the theoretical uncertainties are the most dominant after statistical, but there are some  
 2135 experimental uncertainties that make a contribution as well. The first is the uncertainty on the measured  
 2136 integrated luminosity, which affects the signal estimate and backgrounds whose normalizations are taken  
 2137 from MC. It is measured to be 2.8% in the 8 TeV dataset [102]. The dominant sources of uncertainty over-  
 2138 all are uncertainties on the jet energy scale and resolution and the  $b$ -tagging efficiency. Additional sources  
 2139 include lepton uncertainties on identification, resolution, and trigger efficiency, as well as uncertainties on  
 2140 the missing transverse momentum.

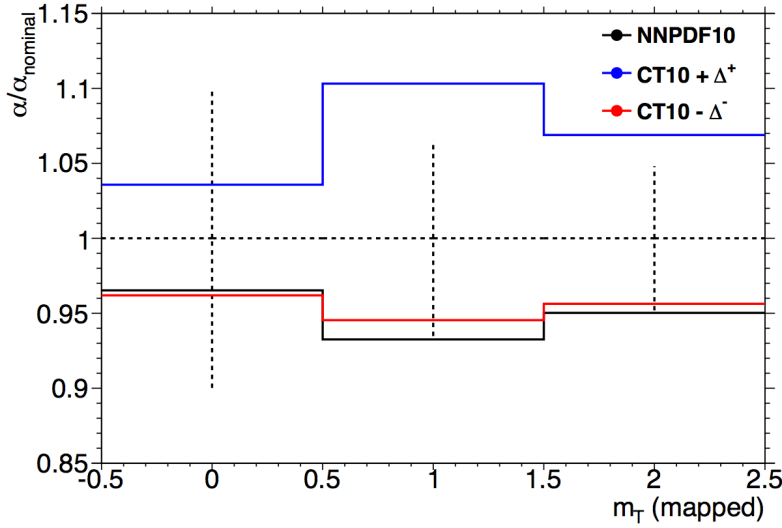


Figure 5.14: Variations in the top background extrapolation factor in the cut-based analysis due to PDF uncertainties. The uncertainties are shown in the three bins of  $m_T$  used in the final cut-based statistical fit. Variations from the eigenvector of the nominal PDF, CT10, as well as the result from an alternate PDF (NNPDF10), are compared.

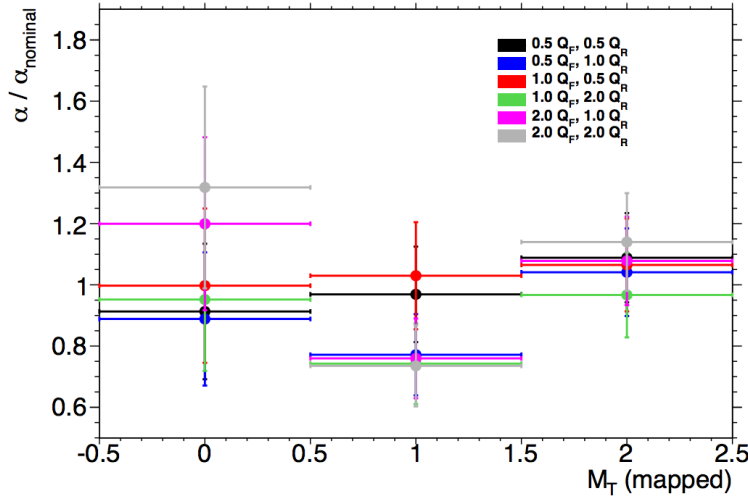


Figure 5.15: Variations in the top background extrapolation factor in the cut-based analysis due to QCD scale uncertainties. The uncertainties are shown in the three bins of  $m_T$  used in the final cut-based statistical fit.  $Q_F$  is the QCD factorization scale, while  $Q_R$  is the QCD renormalization scale.

The jet energy scale uncertainty is split into several independent components, including jet-flavor dependent calorimeter response uncertainties, uncertainties on modeling of pile-up interactions, uncertainties on extrapolation from the central to forward detector regions, and MC non-closure [103]. The uncer-

Sample	Total uncert.	Stat. uncert.	Expt. uncert.	Theo. uncert.
$n_j \geq 2$ VBF-enriched				
$N_{\text{sig}}$	13	—	6.8	12
$N_{\text{bkg}}$	9.2	4.7	6.4	4.5
$N_{WW}$	32	—	14	28
$N_{\text{top}}$	15	9.6	7.6	8.5
$N_{\text{misid}}$	22	—	12	19
$N_{VV}$	20	—	12	15
$N_{\tau\tau}$ (DY)	40	25	31	2.9
$N_{ee/\mu\mu}$ (DY)	19	11	15	—

Table 5.14: Composition of the post-fit uncertainties (in %) on the total signal ( $N_{\text{sig}}$ ), total background ( $N_{\text{bkg}}$ ), and individual background yields in the VBF analysis [74]. “Stat.” refers to statistical uncertainties, “Expt.” refers to experimental systematic uncertainties, and “Theo.” refers to theoretical systematic uncertainties.

tainty on energy scale for jets used in this analysis ranges from 1% to 7% depending on the jet  $p_{\text{T}}$  and  $\eta$ .  
 The jet energy resolution varies from 5% to 20%, with uncertainties ranging from 2% to 40% (the largest uncertainties occurring at the selection threshold).

The b-tagging efficiency is independently measured in data samples enriched in dileptonic decays of  $t\bar{t}$  events or in events where a muon is reconstructed in the vicinity of a jet [104, 105]. The efficiencies and their uncertainties are binned in  $p_{\text{T}}$  and decomposed into uncorrelated components using an eigenvector method [106]. Uncertainties on the efficiency range from 1% to 7.8%. The uncertainty on the rate of misidentification of  $c$ -jets as  $b$ -jets ranges from 6-14%, while the uncertainty on the rate of light jet mis-tagging ranges from 9-19% depending on  $p_{\text{T}}$  and  $\eta$ . These efficiency uncertainties are applied to each individual jet in the event.

The total experimental uncertainties on different signal and background components are summarized in table 5.14. They are compared to the level of other statistical and systematic uncertainties as well. Overall, the experimental uncertainties are sub-dominant compared to the statistical and theoretical uncertainties.

## 5.7 RESULTS

While the combined results of all the  $H \rightarrow WW^*$  sub-analyses will be discussed in the next chapter, this section presents the results of the VBF specific analysis and interpretations. As table 5.7 shows, the final

2160 cut-based signal region contains 20 events in data with  $m_T < 150$  GeV, 14 coming from the  $e\mu$  channel  
2161 and 6 coming from the  $ee + \mu\mu$  channel. The BDT analysis has many more candidates due to its looser  
2162 selection, and the yields in each bin of  $O_{\text{BDT}}$  are shown in table 5.15.

(a) Before the BDT classification

Selection	Summary						Composition of $N_{\text{bkg}}$									
	$N_{\text{obs}}/N_{\text{bkg}}$	$N_{\text{obs}}$	$N_{\text{bkg}}$	$N_{\text{signal}}$			$N_{WW}^{\text{QCD}}$	$N_{WW}^{\text{EW}}$	$N_{t\bar{t}}$	$N_t$	$N_{Wj}$	$N_{jj}$	$N_{VV}$	$N_{\text{Drell-Yan}}$	$N_{ee/\mu\mu}^{\text{QCD}}$	$N_{\tau\tau}^{\text{EW}}$
				$N_{\text{ggF}}$	$N_{\text{VBF}}$	$N_{\text{VH}}$										
$e\mu$ sample	$1.04 \pm 0.04$	718	689	13	15	2.0	90	11	327	42	29	23	31	2.2	130	2
$ee/\mu\mu$ sample	$1.18 \pm 0.08$	469	397	6.0	7.7	0.9	37	3	132	17	5.2	1.2	10.1	168	23	1

(b) Bins in  $O_{\text{BDT}}$

$e\mu$ sample																
Bin 0 (not used)	$1.02 \pm 0.04$	661	650	8.8	3.0	1.9	83	9	313	40	26	21	28	2.2	126	1
Bin 1	$0.99 \pm 0.16$	37	37	3.0	4.2	0.1	5.0	1.0	17	3.1	3.3	1.8	2.6	—	4.0	0.2
Bin 2	$2.26 \pm 0.63$	14	6.2	1.2	4.2	—	1.5	0.5	1.8	0.3	0.4	0.3	0.8	—	0.3	0.3
Bin 3	$5.41 \pm 2.32$	6	1.1	0.4	3.1	—	0.3	0.2	0.3	0.1	—	—	0.1	—	0.1	0.1
$ee/\mu\mu$ sample																
Bin 0 (not used)	$1.91 \pm 0.08$	396	345	3.8	1.3	0.8	33	2	123	16	4.1	1.1	8.8	137	20.5	0.5
Bin 1	$0.82 \pm 0.14$	53	45	1.5	2.2	0.1	3.0	0.5	10.4	1.8	0.8	0.2	0.9	26	1.7	0.1
Bin 2	$1.77 \pm 0.49$	14	7.9	0.6	2.5	—	0.8	0.3	1.1	0.2	0.2	—	0.3	4.4	0.3	0.1
Bin 3	$6.52 \pm 2.87$	6	0.9	0.2	1.7	—	0.1	0.2	0.2	—	—	—	—	0.7	—	—

Table 5.15: Event selection for the VBF BDT analysis. The event yields in (a) are shown after the pre-selection and the additional requirements applied before the BDT classification (see text). The event yields in (b) are given in bins in  $O_{\text{BDT}}$  after the classification [74].

2163 Figure 5.16(a) shows the final distribution of data candidates compared to the expected  $m_T$  distribution  
2164 for signal and background. The data are very consistent with a VBF Higgs hypothesis. Figure 5.16(b) shows  
2165 where the data candidates fall in the two-dimensional binning of  $m_T$  and  $m_{jj}$  used in the fit for the cut-  
2166 based analysis. Figure 5.17 shows the distributions of  $O_{\text{BDT}}$  and  $m_T$  in the VBF BDT analysis. Again the  
2167 data are quite consistent with a VBF Higgs hypothesis.

2168 Because the cut-based result is used as a validation for the BDT analysis and the two signal regions are  
2169 not fully orthogonal, it is interesting to explore which events overlap between the two analyses. Of the  
2170 twenty events in the cut-based signal region, only seven were not selected by the BDT analysis, while the  
2171 other thirteen also enter the BDT signal region. Figure 5.18 shows where the different analysis candidates  
2172 lie in the  $m_{jj}$ - $m_T$  plane. This shows clearly that the advantage of the BDT analysis is that it can extract  
2173 signal candidates from the lower  $m_{jj}$  region due to its ability to recognize correlations with other variables.

2174 While the context of these results in the broader  $H \rightarrow WW^*$  statistical analysis will be presented in the

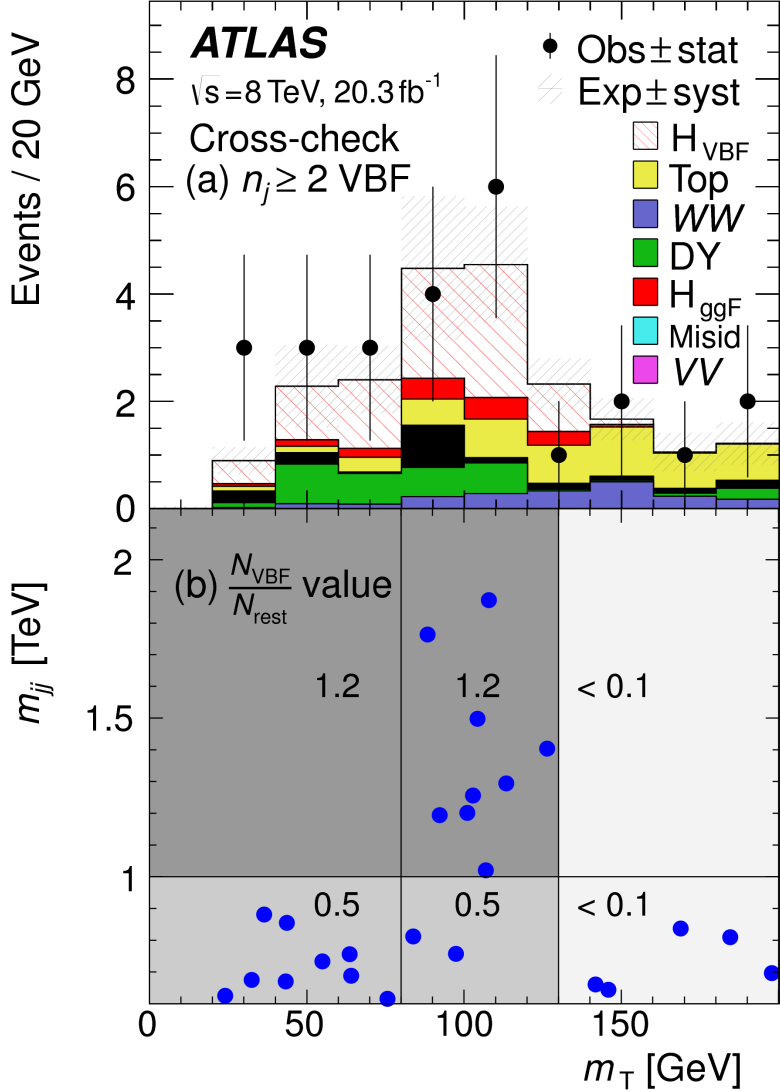


Figure 5.16: Post-fit distributions in the cut-based VBF analysis. Panel (a) shows the one-dimensional  $m_T$  distribution, while (b) shows the data candidates split into the bins of  $m_T$  and  $m_{jj}$  used in the final fit [74].

next chapter, the statistical significance of the VBF Higgs result is shown here. In the BDT analysis, the expected signal significance was  $2.7\sigma$ , while the observed significance was  $3.1\sigma$ . In the cut-based analysis, the expected significance was  $2.1\sigma$  and the observed significance was  $3.0\sigma$ . The compatibility between these two results can be evaluated by computing the probability of observing a larger difference in  $Z_0$  values than the one measured. Using toy Monte Carlo with the ggF signal strength fixed to unity and considering only statistical uncertainties, this probability is computed to be 79%, indicating good agreement between

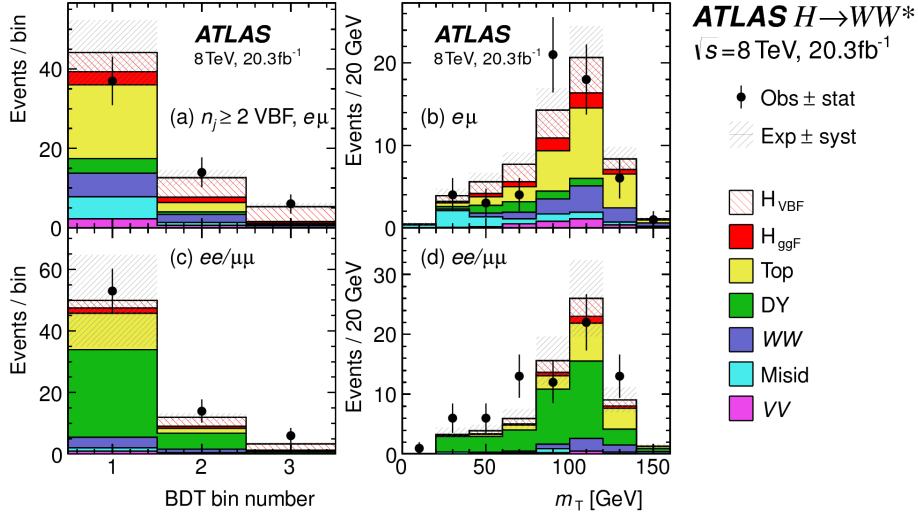


Figure 5.17: Postfit distributions in the BDT VBF analysis [74].

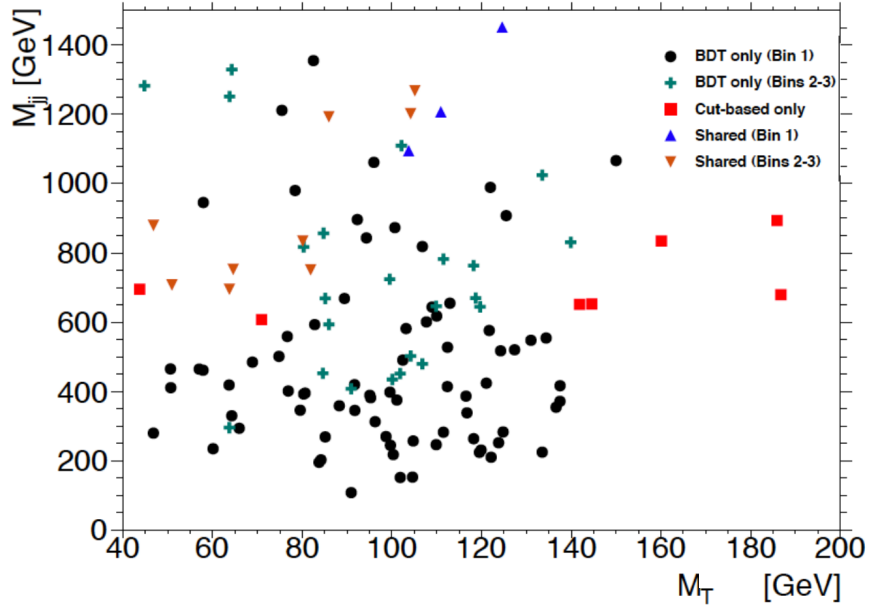


Figure 5.18: Overlap between cut-based and BDT VBF signal region candidates in the  $m_{jj}$ - $m_T$  plane.

2181 the analyses. This result represents the first evidence of the vector boson fusion production of a Higgs  
2182 boson.

*The feeling is less like an ending than just another starting  
point.*

Chuck Palahniuk

# 6

2183

2184

## Combined Run I $H \rightarrow WW^* \rightarrow \ell\nu\ell\nu$

2185

## results

2186

### 6.1 INTRODUCTION

2187 In the final statistical analysis of  $H \rightarrow WW^* \rightarrow \ell\nu\ell\nu$ , the dedicated gluon-gluon fusion and vector  
2188 boson fusion sensitive signal regions are all combined into a single fit to determine the main parameters of  
2189 interest, the Higgs signal strength  $\mu$  and mass  $m_H$ . Therefore, while the specific requirements applied for  
2190 the VBF sensitive analysis are discussed in chapter 5, the final measurement of these parameters can only be  
2191 discussed in combination with the results of the ggF dedicated analysis. For example, because ggF Higgs  
2192 production is considered a background in the VBF analysis, the ggF dedicated signal regions can actually  
2193 constrain the normalization of this background in the VBF dedicated region.

2194 This chapter presents the combined interpretation of results in the  $H \rightarrow WW^* \rightarrow \ell\nu\ell\nu$  analysis

2195 for gluon fusion and vector boson fusion Higgs production. First, the results of the dedicated gluon fu-  
 2196 sion search are presented. Then, a comparison of the individual production mode signal strengths ( $\mu_{\text{ggF}}$   
 2197 and  $\mu_{\text{VBF}}$ ) and a measurement of the combined signal strength ( $\mu$ ) are shown. Subsequently, the mea-  
 2198 sured values of the Higgs couplings to fermions and vector bosons is presented. Finally, the cross section  
 2199 measurement for ggF and VBF production are shown.

## 2200 6.2 RESULTS OF DEDICATION GLUON FUSION $H \rightarrow WW^* \rightarrow \ell\nu\ell\nu$ ANALYSIS

2201 The details of the dedicated gluon fusion  $H \rightarrow WW^* \rightarrow \ell\nu\ell\nu$  analysis are not discussed in this thesis  
 2202 and instead left to more comprehensive sources [74]. However, a brief summary of the results is essen-  
 2203 tial for describing the measurements of Higgs properties and interpreting the the dedicated VBF Higgs  
 2204 production search in a broader context. Additionally, the final Run 1 results on gluon fusion production  
 2205 make use of the dedicated variables for same flavor final states developed in section 3.5. The results in the  
 2206 same flavor final states will be shown here as well.

### 2207 6.2.1 RESULTS IN SAME FLAVOR ( $ee/\mu\mu$ ) FINAL STATES

2208 Final states of the  $H \rightarrow WW^* \rightarrow \ell\nu\ell\nu$  channel where both leptons have the same flavor ( $ee/\mu\mu$ )  
 2209 were not included in the discovery result due to increased pileup conditions in the  $\sqrt{s} = 8$  TeV data.  
 2210 Dedicated techniques for background reduction in the same flavor final states were developed, as described  
 2211 in section 3.5. The results shown in this section are the first published results using the same flavor channels  
 2212 in the  $H \rightarrow WW^*$  analysis.

2213 Table 6.1 shows the background estimate, expected signal yield, and event count in data for the same  
 2214 flavor channels in the  $n_j \leq 1$  signal regions. The dedicated same flavor background reduction techniques  
 2215 allow this channel to preserve a signal to background ratio similar to that of the different flavor channels.

	$N_{\text{obs}}$	$N_{\text{bkg}}$	$N_{\text{ggF}}$	$N_{\text{VBF}}$
$n_j = 0$	1108	$1040 \pm 40$	$77 \pm 15$	$2.4 \pm 1.7$
$n_j = 1$	467	$427 \pm 21$	$22 \pm 6$	$3.6 \pm 1.8$

Table 6.1: Post-fit yields in ggF dedicated signal regions for the  $ee/\mu\mu$  final states [74].

2216     Figure 6.1 shows the final  $m_T$  distribution in data for the  $n_j \leq 1$  same flavor channels. The data is very  
 2217     consistent with the Higgs hypothesis and it can be seen that the same flavor channels are indeed sensitive  
 2218     to gluon fusion production of the Higgs.

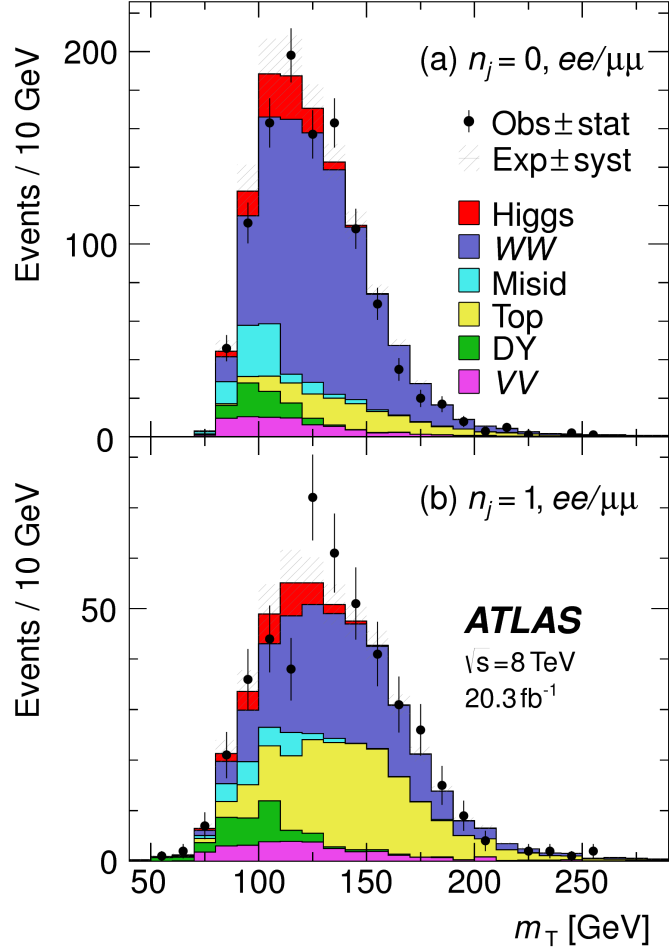


Figure 6.1: Post-fit  $m_T$  distribution in the  $n_j \leq 1$  regions for the same flavor ( $ee/\mu\mu$ ) final states [74].

### 2219     6.2.2 COMBINED GLUON FUSION RESULTS

2220     Table 6.2 shows the individual signal regions that were input into the final statistical fit. The ggF dedicated  
 2221     bins use  $m_T$  as their discriminating variable and are separated into bins of  $p_T$  of the subleading lepton as  
 2222     well. The VBF dedicated bin uses the  $O_{BDT}$  distribution as its final discriminant.

2223     Table 6.3 shows the yields in the various signal regions in both data and expected signal and back-  
 2224     grounds. The yields for signal and background are all scaled according to the final normalizations cal-

SR category $i$				Fit var.	
$n_j$ , flavor	$\otimes m_{\ell\ell}$	$\otimes p_T^{\ell 2}$	$\otimes \ell_2$		
$n_j = 0$	$e\mu$	$\otimes [10, 30, 55]$	$\otimes [10, 15, 20, \infty]$	$\otimes [e, \mu]$	$m_T$
	$ee/\mu\mu$	$\otimes [12, 55]$	$\otimes [10, \infty]$		$m_T$
$n_j = 1$	$e\mu$	$\otimes [10, 30, 55]$	$\otimes [10, 15, 20, \infty]$	$\otimes [e, \mu]$	$m_T$
	$ee/\mu\mu$	$\otimes [12, 55]$	$\otimes [10, \infty]$		$m_T$
$n_j \geq 2$ ggF	$e\mu$	$\otimes [10, 55]$	$\otimes [10, \infty]$		$m_T$
$n_j \geq 2$ VBF	$e\mu$	$\otimes [10, 50]$	$\otimes [10, \infty]$		$O_{\text{BDT}}$
	$ee/\mu\mu$	$\otimes [12, 50]$	$\otimes [10, \infty]$		$O_{\text{BDT}}$

Table 6.2: All signal regions definitions input into final statistical fit [74].

culated in the fit.

	$N_{\text{obs}}$	$N_{\text{bkg}}$	$N_{\text{ggF}}$	$N_{\text{VBF}}$
$n_j = 0$	3750	$3430 \pm 90$	$300 \pm 50$	$8 \pm 4$
$n_j = 1$	1596	$1470 \pm 40$	$102 \pm 26$	$17 \pm 5$
$n_j \geq 2$ , ggF $e\mu$	1017	$960 \pm 40$	$37 \pm 11$	$13 \pm 1.4$
$n_j \geq 2$ , VBF	130	$99 \pm 9$	$7.7 \pm 2.6$	$21 \pm 3$

Table 6.3: Post-fit yields in the both ggF and VBF dedicated signal regions with all lepton flavor final states combined [74].

Figure 6.2 shows the final post-fit  $m_T$  distribution in the  $n_j \leq 1$  regions. The data are very consistent with the hypothesis of ggF Higgs production. These yields are used as input, along with the VBF results in chapter 5, for the physical interpretation of results presented in subsequent sections.

### 6.3 SIGNAL STRENGTH MEASUREMENTS IN GGF AND VBF PRODUCTION

When all of the signal regions are combined in the fit, there can be a combined measurement of the signal strength as well as the individual ggF and VBF signal strengths. The combined signal strength is the ratio of the measured cross section in the combined gluon fusion and VBF signal regions to the theory prediction

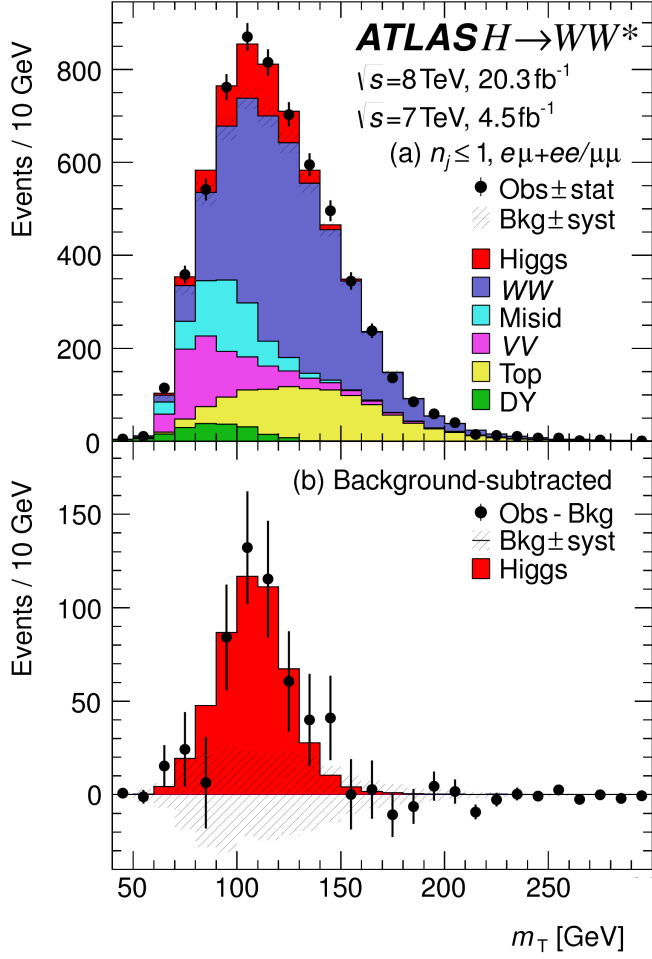


Figure 6.2: Post-fit  $m_T$  distribution in the  $n_j \leq 1$  regions [74].

for the sum of of these two processes. It is a signal strength measurement for the total Higgs production cross section that this analysis is sensitive to. The final measured combined signal strength  $\mu$  is measured shown in equation 6.1.

$$\begin{aligned}
 \mu &= 1.09 \quad {}^{+0.16}_{-0.15} (\text{stat.}) \quad {}^{+0.08}_{-0.07} \left( \frac{\text{expt}}{\text{syst}} \right) \quad {}^{+0.15}_{-0.12} \left( \frac{\text{theo}}{\text{syst}} \right) \quad \pm 0.03 \left( \frac{\text{lumi}}{\text{syst}} \right) \\
 &= 1.09 \quad {}^{+0.16}_{-0.15} (\text{stat}) \quad {}^{+0.17}_{-0.14} (\text{syst}) \\
 &= 1.09 \quad {}^{+0.23}_{-0.21}.
 \end{aligned} \tag{6.1}$$

2236 Figure 6.3 gives the best fit signal strength  $\hat{\mu}$  as a function of the hypothesized Higgs mass. The value at  
 2237 a mass of 125.36 GeV corresponds to the  $\mu$  quoted in equation 6.1. This value of the Higgs mass is used  
 2238 because it is the most precise mass measurement from ATLAS, a result of the combined  $\gamma\gamma$  and  $ZZ$  mass  
 2239 measurements [107].

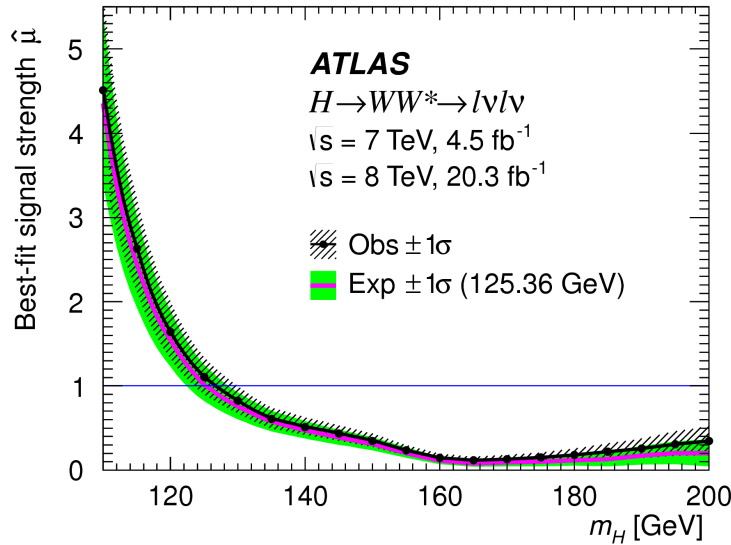


Figure 6.3: Best fit signal strength  $\hat{\mu}$  as a function of hypothesized  $m_H$  [74].

2240 As explained in chapter 3, a probability  $p_0$  can be computed using the test statistic  $q_0$  to quantify the  
 2241 probability that the background could fluctuate to produce an excess at least as large as the one observed  
 2242 in the data. The local  $p_0$  value is shown in figure 6.4 as a function of  $m_H$ . The minimum  $p_0$  value is at  
 2243  $m_H = 130$  GeV and corresponds to a significance of  $6.1\sigma$ . The curve is relatively flat and the significance  
 2244 is the same at 125.36 GeV within the quoted precision. The expected significance for a signal with strength  
 2245  $\mu = 1.0$  is  $5.8\sigma$ . This represents the first discovery level observation of Higgs production using only the  
 2246  $H \rightarrow WW^* \rightarrow \ell\nu\ell\nu$  analysis.

2247 All the results presented so far in this section have been for the combined gluon fusion and VBF pro-  
 2248 duction modes. However, each signal strength can be calculated separately in the likelihood as well. There  
 2249 are two ways to do this. First, the likelihood can be parameterized in terms of a single parameter, the ratio  
 2250 of the VBF and gluon fusion signal strengths. With this method, the statistical significance of the VBF  
 2251 Higgs result can be evaluated. Figure 6.5 shows the likelihood as a function of the ratio  $\mu_{\text{VBF}}/\mu_{\text{ggF}}$ .

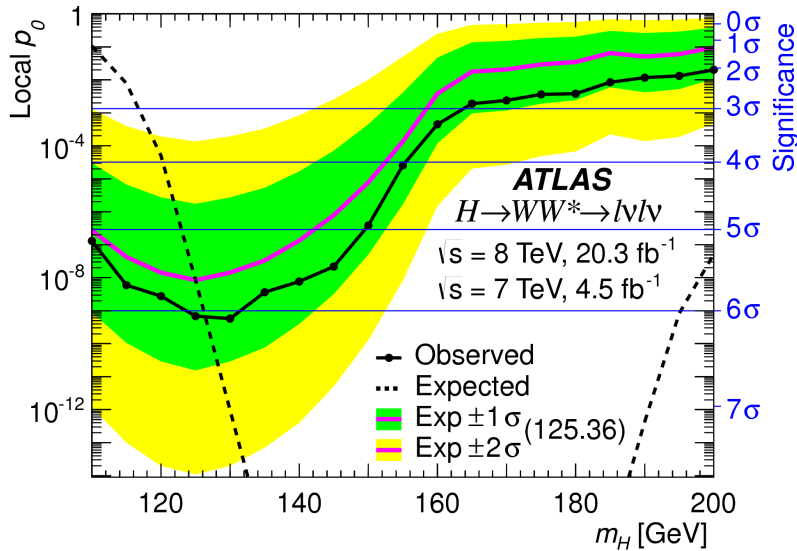


Figure 6.4: Local  $p_0$  as a function of  $m_H$  [74].

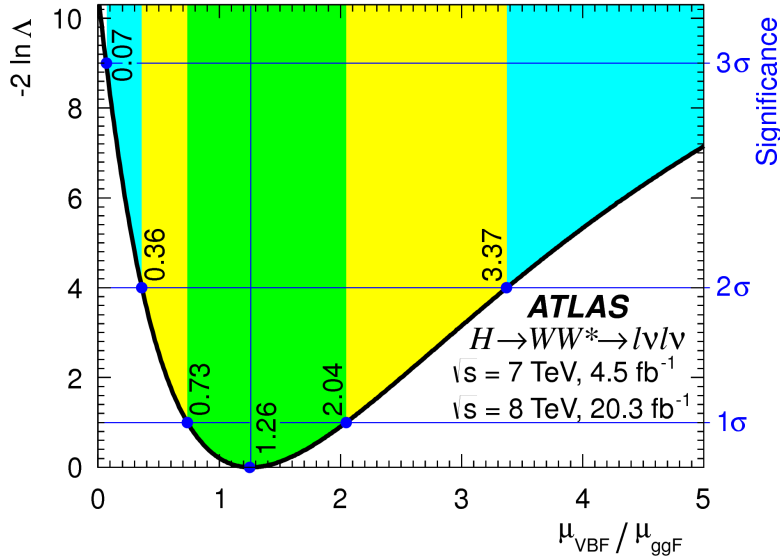


Figure 6.5: Likelihood as a function of  $\mu_{\text{VBF}} / \mu_{\text{ggF}}$  [74].

2252        The best fit value of the ratio of signal strengths is shown in equation 6.2. Within the quoted uncer-  
 2253        tainties, it is consistent with a ratio of unity.

$$\frac{\mu_{\text{VBF}}}{\mu_{\text{ggF}}} = 1.26^{+0.61} (\text{stat.})^{+0.50} (\text{syst.}) = 1.26^{+0.79}_{-0.53} \quad (6.2)$$

2254 The null hypothesis for VBF production corresponds to a ratio of  $\mu_{\text{VBF}}/\mu_{\text{ggF}} = 0$ . The likelihood in  
 2255 figure 6.5 gives a significance of  $3.2\sigma$  at  $\mu_{\text{VBF}}/\mu_{\text{ggF}} = 0$ , as quoted in chapter 5.

2256 In addition to the ratio of signal strengths, each signal strength can be varied independently in the like-  
 2257 lihood as well. Figure 6.6 shows the two dimensional likelihood scan in the  $\mu_{\text{ggF}}-\mu_{\text{VBF}}$  plane. The best fit  
 2258 values of the two signal strengths are shown in equation 6.3. Both are consistent with unity within their  
 2259 uncertainties.

$$\begin{aligned} \mu_{\text{ggF}} &= 1.02 \pm 0.19^{+0.22}_{-0.18} = 1.02^{+0.29}_{-0.26} \\ \mu_{\text{VBF}} &= 1.27^{+0.44}_{-0.40}^{+0.29}_{-0.21} = 1.27^{+0.53}_{-0.45} \end{aligned} \quad (6.3)$$

(stat.) (syst.)

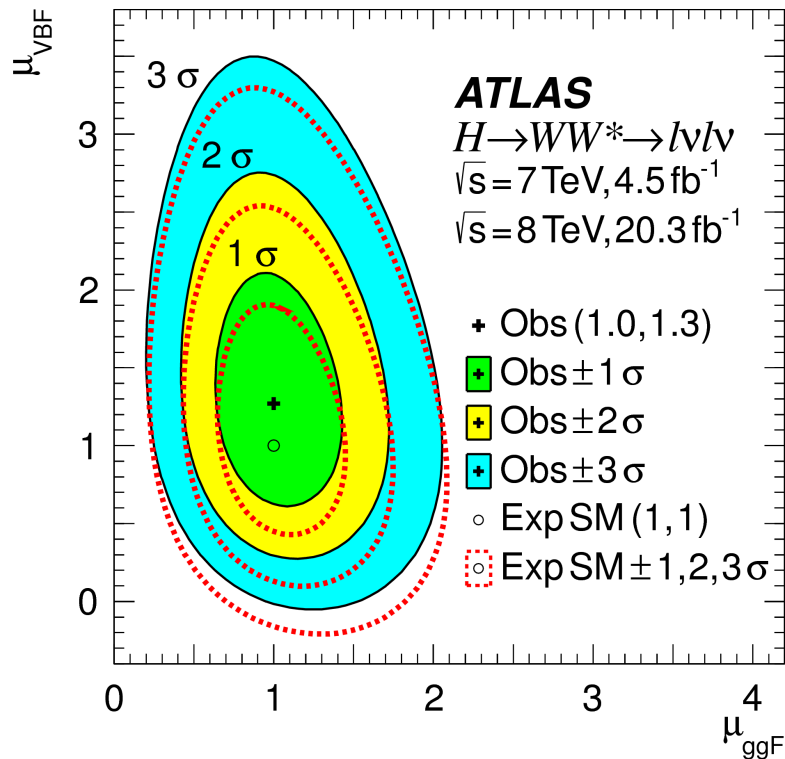


Figure 6.6: Two dimensional likelihood scan as a function of  $\mu_{\text{VBF}}$  and  $\mu_{\text{ggF}}$  [74].

2260 6.4 MEASUREMENT OF HIGGS COUPLINGS TO VECTOR BOSONS AND FERMIONS

2261 Similar to the parameterization of signal strength, the couplings of the Higgs to fermions and bosons can  
 2262 also be parameterized. The parameter of interest in this case is  $\kappa$ , or the ratio of the measured coupling to  
 2263 the Standard Model expectation. Both the fermion and boson couplings have these so-called scale factors,  
 2264  $\kappa_F$  for fermions and  $\kappa_V$  for bosons. Gluon fusion production is sensitive to the fermion couplings through  
 2265 the top quark loops in its production, while VBF production is sensitive to the vector boson couplings in  
 2266 its production. Both modes are sensitive to the vector boson couplings in their decays. The signal strengths  
 2267 will have dependence on the coupling scale factors as described in equation 6.4 [18].

$$\begin{aligned}\mu_{\text{ggF}} &\propto \frac{\kappa_F^2 \cdot \kappa_V^2}{(\mathcal{B}_{H \rightarrow f\bar{f}} + \mathcal{B}_{H \rightarrow gg}) \kappa_F^2 + (\mathcal{B}_{H \rightarrow VV}) \kappa_V^2} \\ \mu_{\text{VBF}} &\propto \frac{\kappa_V^4}{(\mathcal{B}_{H \rightarrow f\bar{f}} + \mathcal{B}_{H \rightarrow gg}) \kappa_F^2 + (\mathcal{B}_{H \rightarrow VV}) \kappa_V^2}.\end{aligned}\quad (6.4)$$

2268 Figure 6.7 shows the two-dimensional likelihood scan of  $\kappa_F$  and  $\kappa_V$ . The best-fit values are given in equa-  
 2269 tion 6.5. The best-fit values are consistent with unity within their uncertainties.

$$\begin{aligned}\kappa_F &= 0.93 & {}^{+0.24}_{-0.18} & {}^{+0.21}_{-0.14} & = 0.93 & {}^{+0.32}_{-0.23} \\ \kappa_V &= 1.04 & {}^{+0.07}_{-0.08} & {}^{+0.07}_{-0.08} & = 1.04 & \pm 0.11.\end{aligned}\quad (6.5)$$

(stat.) (syst.)

2270

2271 6.5 HIGGS PRODUCTION CROSS SECTION MEASUREMENT

2272 Another measurement that comes naturally from the signal strength measurements quoted earlier is the  
 2273 production cross section and 7 and 8 TeV for both gluon fusion and VBF production. The general equa-

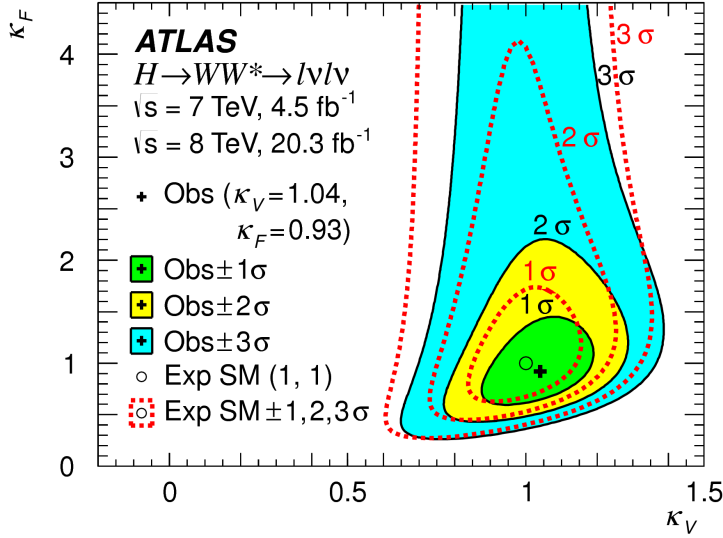


Figure 6.7: Likelihood scan as a function of  $\kappa_F$  and  $\kappa_V$ , the Higgs coupling scale factors [74].

tion for calculating the cross section is given in equation 6.6.

$$\begin{aligned}
 (\sigma \cdot \mathcal{B}_{H \rightarrow WW^*})_{\text{obs}} &= \frac{(N_{\text{sig}})_{\text{obs}}}{\mathcal{A} \cdot \mathcal{C} \cdot \mathcal{B}_{WW \rightarrow l\bar{l}l\nu}} \cdot \frac{1}{\int L dt} \\
 &= \hat{\mu} \cdot (\sigma \cdot \mathcal{B}_{H \rightarrow WW^*})_{\text{exp}}
 \end{aligned} \tag{6.6}$$

$(N_{\text{sig}})_{\text{obs}}$  is the number of events observed in data.  $\mathcal{A}$  is the geometric and kinematic acceptance of the detector, while  $\mathcal{C}$  is the efficiency of the signal region selection for events that are reconstructed in the detector. The branching ratio of a  $WW$  system to leptons must also be divided out. The production cross section depends on the center of mass energy and the production mode desired (gluon fusion or VBF), and so three separate cross section measurements are quoted in equation 6.7.

$$\begin{aligned}
 \sigma_{\text{ggf}}^{7\text{TeV}} \cdot \mathcal{B}_{H \rightarrow WW^*} &= 2.0 \pm 1.7 \stackrel{+1.2}{-1.1} = 2.0 \stackrel{+2.1}{-2.0} \text{ pb} \\
 \sigma_{\text{ggf}}^{8\text{TeV}} \cdot \mathcal{B}_{H \rightarrow WW^*} &= 4.6 \pm 0.9 \stackrel{+0.8}{-0.7} = 4.6 \stackrel{+1.2}{-1.1} \text{ pb} \\
 \sigma_{\text{VBF}}^{8\text{TeV}} \cdot \mathcal{B}_{H \rightarrow WW^*} &= 0.51 \stackrel{+0.17}{-0.15} \stackrel{+0.13}{-0.08} = 0.51 \stackrel{+0.22}{-0.17} \text{ pb.}
 \end{aligned} \tag{6.7}$$

(stat.) (syst.)

2280 The predicted cross section values (including the branching ratio of  $H \rightarrow WW^*$ ) for gluon fusion are  
2281  $3.3 \pm 0.4$  pb at 7 TeV and  $4.2 \pm 0.5$  pb at 8 TeV, consistent with the measured values within their uncer-  
2282 tainties. For vector boson fusion, the predicted cross section is  $0.35 \pm 0.02$  pb, again consistent with the  
2283 measured value.

2284 **6.6 CONCLUSION**

2285 The combined analysis of the gluon fusion and vector boson fusion processes in  $H \rightarrow WW^* \rightarrow \ell\nu\ell\nu$  in  
2286 the 7 and 8 TeV datasets has yielded the first discovery level significance for Higgs production in this decay  
2287 channel. Additionally, precise measurements of the couplings to vector bosons and fermions are given.  
2288 Finally, signal strengths and cross sections for each production mode are measured. Figure 6.8 shows the  
2289  $H \rightarrow WW^* \rightarrow \ell\nu\ell\nu$  measurements in comparison with other Higgs decay channels in ATLAS. The  
2290 measurement of signal strength from this channel remains the most sensitive in both the gluon fusion and  
2291 VBF production modes for the Run 1 dataset.

**ATLAS**

Individual analysis

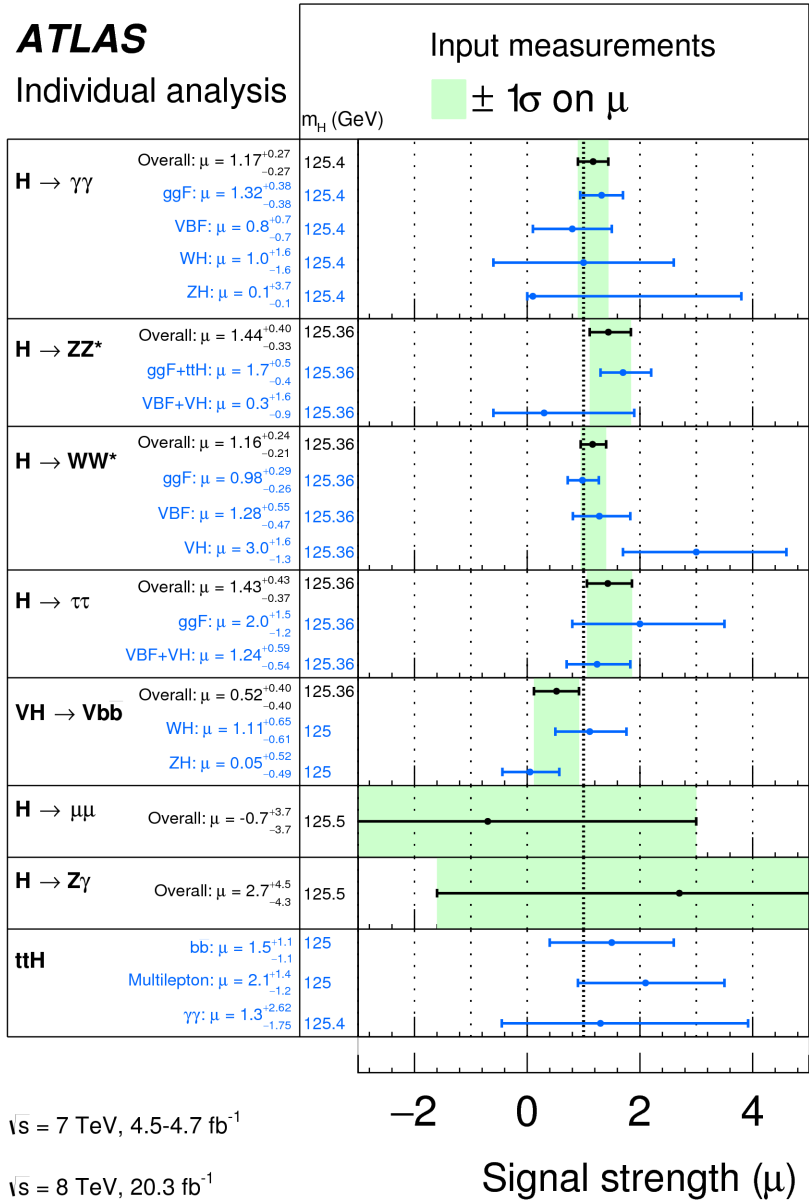


Figure 6.8: Comparison of signal strength measurements in different Higgs decay channels on ATLAS [io8].

2292

## Part III

2293

Search for Higgs pair production in the

2294

$HH \rightarrow b\bar{b}b\bar{b}$  channel in LHC Run 2 at  $\sqrt{s} =$

2295

13 TeV

*Passion is in all great searches and is necessary to all creative endeavors.*

W. Eugene Smith

# 7

2296

## 2297 Search for Higgs pair production in boosted 2298 $b\bar{b}b\bar{b}$ final states

### 2299 7.1 INTRODUCTION

2300 This chapter presents a search for resonant production of a Higgs pair in the  $X \rightarrow HH \rightarrow b\bar{b}b\bar{b}$  final  
2301 state in  $3.2 \text{ fb}^{-1}$  of data collected at  $\sqrt{s} = 13 \text{ TeV}$ . In particular, this chapter focuses on a search for this  
2302 final state in the regime where  $m_X$  is large ( $\gtrsim 1 \text{ TeV}$ ) and the Higgs bosons in the decay are significantly  
2303 boosted. A tailored selection for this boosted selection, using novel techniques in jet substructure and  $b$ -  
2304 tagging, is discussed. Then, the data-driven background estimate is presented. Finally, the results of the  
2305 search are shown. The signal models used as benchmarks are a spin-2 Randall Sundrum graviton (RSG)  
2306 and a narrow width spin zero resonance. These models are described in more detail in Chapter 1. Limits  
2307 on signal models are reserved for the next chapter where the results of this chapter are combined with the

2308 results of a separate selection dedicated to the lower  $m_X$  regime.

2309 **7.2 MOTIVATION**

2310 With the center of mass energy increase from  $\sqrt{s} = 8 \text{ TeV}$  to  $\sqrt{s} = 13 \text{ TeV}$ , the LHC and ATLAS are  
2311 able to probe new resonances at higher mass scales than previously accessible in Run 1. This is a powerful  
2312 motivator for searching for a new resonance in the early 13 TeV data. Figure 7.1 shows the ratios of parton  
2313 luminosities between 8 and 13 TeV for different resonance masses. For a resonance of  $M_X = 2 \text{ TeV}$ , the  
2314 cross section at  $\sqrt{s} = 13 \text{ TeV}$  is roughly a factor of 10 larger than at  $\sqrt{s} = 8 \text{ TeV}$ .

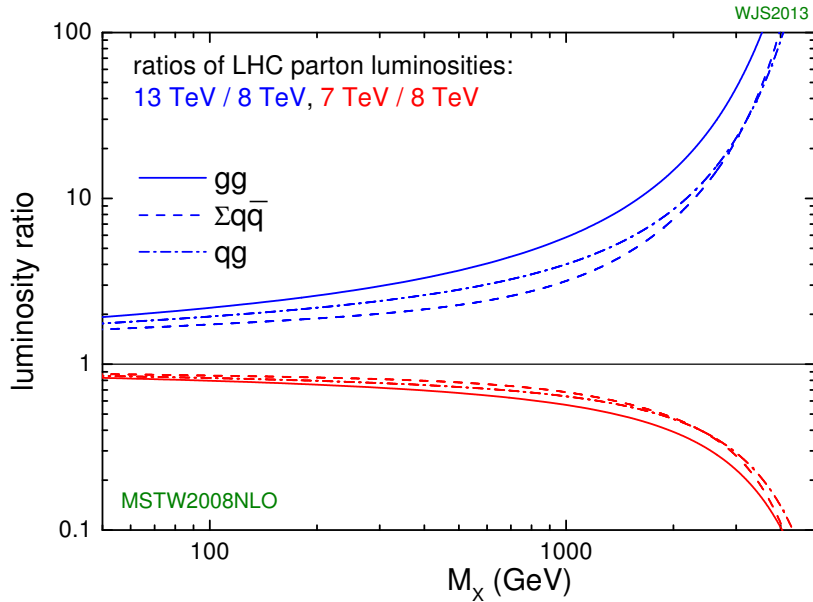


Figure 7.1: Parton luminosity ratios as a function of resonance mass  $M_X$  for 13/8 TeV and 7/8 TeV [109].

2315 Higgs pair production offers a vast array of unprobed regions of phase space where searches for BSM  
2316 physics can be made. Chapter 1 discusses some possibilities for both resonant and non-resonant enhance-  
2317 ment of the di-Higgs production cross section. Given the increased mass reach of the LHC in Run 2, it is  
2318 particularly important to focus on resonant searches at high  $m_X$ . When conducting a search in the  $HH$   
2319 final state, the different possible decay modes of each Higgs must be considered. Figure 7.2 shows the  
2320 branching ratio of the  $HH$  final state for different combinations of decays of each individual Higgs. As

2321 the largest branching ratio for the 125 GeV Higgs is  $H \rightarrow b\bar{b}$ , the  $HH \rightarrow b\bar{b}b\bar{b}$  branching ratio is also the  
2322 largest at 33%.

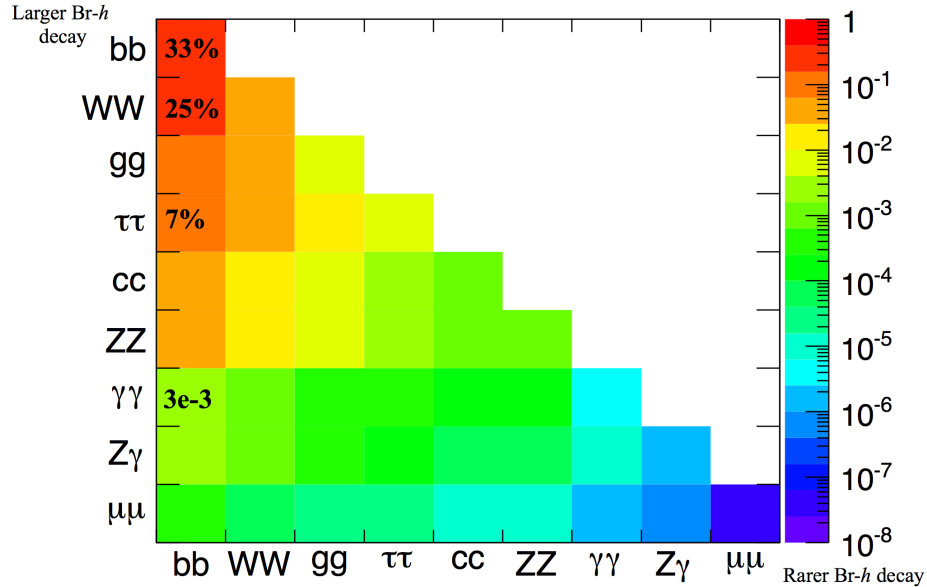


Figure 7.2: Summary of  $HH$  branching ratios [110].

2323 At high  $m_X$ , the Higgs bosons resulting from the decay of a heavy resonance will have large  $p_T$ <sup>1</sup>. The  
2324 angular separation between the decay products of the Higgs,  $\Delta R \equiv \sqrt{(\Delta\eta)^2 + (\Delta\phi)^2}$ , is inversely  
2325 proportional to the Higgs  $p_T$ , as shown in equation 7.1.

$$\Delta R \approx \frac{2m}{p_T} \quad (7.1)$$

2326 Figure 7.3 shows the minimum  $\Delta R$  between truth level  $B$  decay vertices in simulation samples for Randall-  
2327 Sundrum gravitons of different masses. The figure shows that as the mass of the graviton increases, the  $\Delta R$   
2328 distribution between the  $b$  quarks in the Higgs decay tends to shift to lower values. Because of this effect,  
2329 it is necessary to tailor a selection to target these merged  $b$ -jets.

---

<sup>1</sup>In the limit that the resonance mass is much larger than the Higgs mass, the Higgs  $p_T$  is roughly  $m_X/2$ .

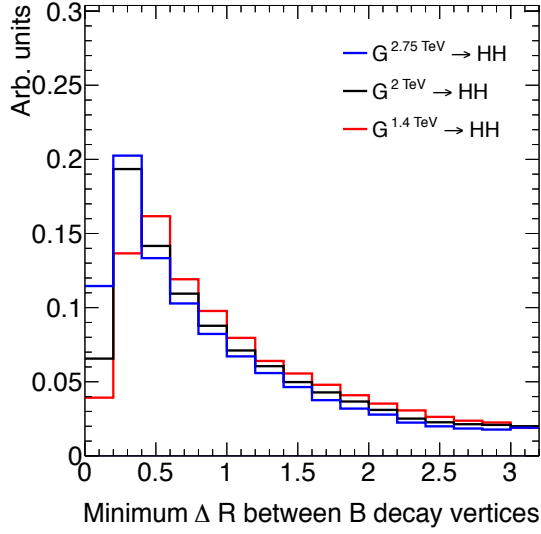


Figure 7.3: Minimum  $\Delta R$  between  $B$  decay vertices for different RSG masses in a  $G_{KK}^* \rightarrow HH \rightarrow 4b$  sample with  $c = 1$ .

2330 7.3 DATA AND SIMULATION SAMPLES

2331 7.3.1 SIGNAL MODELS

2332 While the resonance search is by its nature generic (as it is a simple search for a peak in the  $4b$  invariant mass  
 2333 spectrum), there are two signal models that the selection requirements have been optimized for. The first  
 2334 is Randall-Sundrum (RSG) model, where a tower of massive spin-2 Kaluza-Klein gravitons is predicted.  
 2335 The second is a heavy narrow scalar resonance, the so-called “heavy Higgs”. This type of resonance arises,  
 2336 for example, in the two Higgs doublet model (2HDM). More details about the physics of these models  
 2337 and their motivation is given in chapter 1.

2338 Signal graviton ( $G_{KK}^*$ ) events are generated at leading order (LO) with **MADGRAPH5 v2.2.2** [ii]. The  
 2339 PDF set used is the **NNPDF2.3 LO** set [ii]. For modeling parton shower and hadronization in jets, **PYTHIA**  
 2340 8.186 is used with the A14 tune [90, ii]. The free parameters in the RSG model are the graviton mass  
 2341 and the coupling constant  $c \equiv k/\bar{M}_{\text{Pl}}^2$ . Both the production cross section and width of the graviton are  
 2342 proportional to  $c^2$ . Samples are generated at both  $c = 1$  and  $c = 2$  for a variety of mass points between

---

<sup>2</sup> $k$  is the curvature constant for the warped extra dimension and  $\bar{M}_{\text{Pl}}$  is the Planck mass divided by  $8\pi$

2343 300 GeV and 3 TeV.

2344 The second signal sample is a heavy spin-0 resonance  $H$  with a fixed width of  $\Gamma_H = 1$  GeV. This  
2345 is generated with **MADGRAPH5** and uses the **CT10** PDF set [93]. The parton shower and hadronization  
2346 are handled by **HERWIG ++** with the **CTEQ6L1** PDF set and the **UEEE5** event tune [94, 114, 115]. Because  
2347 the width and branching ratios depend on 2HDM parameters, each mass point generated with this fixed  
2348 width corresponds to a different point in the 2HDM parameter phase space. Mass points are generated  
2349 between 300 GeV and 1 TeV as with the RSG signal samples.

2350 **7.3.2 BACKGROUND SAMPLES**

2351 While the dominant **QCD** multijet background is estimated with a fully data-driven method, the sub-  
2352 dominant backgrounds  $t\bar{t}$  and  $Z$ +jets are modeled with some input from simulation.

2353  $t\bar{t}$  events are simulated at next-to-leading order (NLO) with the **POWHEG-BOX** version 1 generator us-  
2354 ing the **CT10** PDF set [116]. The parton shower, hadronization, and underlying event are simulated with  
2355 **PYTHIA 6.428** with the **CTEQ6L1** PDF set [89]. The Perugia 2012 tune is used [117]. NNLO **QCD** correc-  
2356 tions to the cross sections are computed in **Top++ 2.0** [118]. The top quark mass is set to 172.5 GeV. The  
2357 shapes of distributions in  $t\bar{t}$  are taken from MC while the normalization is taken from data.

2358 Finally, the  $Z$ +jets background is simulated with **PYTHIA 8.186** and the **NNPDF2.3** LO PDF set. This  
2359 background is negligible compared to the others and is taken fully from MC.

2360 **7.3.3 DATA SAMPLE AND TRIGGER**

2361 This analysis is done on  $3.2 \text{ fb}^{-1}$  of data taken in 2015 at  $\sqrt{s} = 13$  TeV. The details of the machine  
2362 conditions during this time can be found in Chapter 2. Only data which was taken during stable beam  
2363 conditions with all detectors functioning is used. Events must pass a trigger which requires a single large  
2364 radius ( $R = 1.0$ ) jet with  $p_T > 360$  GeV to be reconstructed in the HLT. Figure 7.4 shows the trigger  
2365 efficiency for various trigger options as a function of graviton mass. Above  $m_{G_{KK}^*} > 1$  TeV, the single  
2366 large radius jet trigger is 99% efficient for events passing the signal selection.

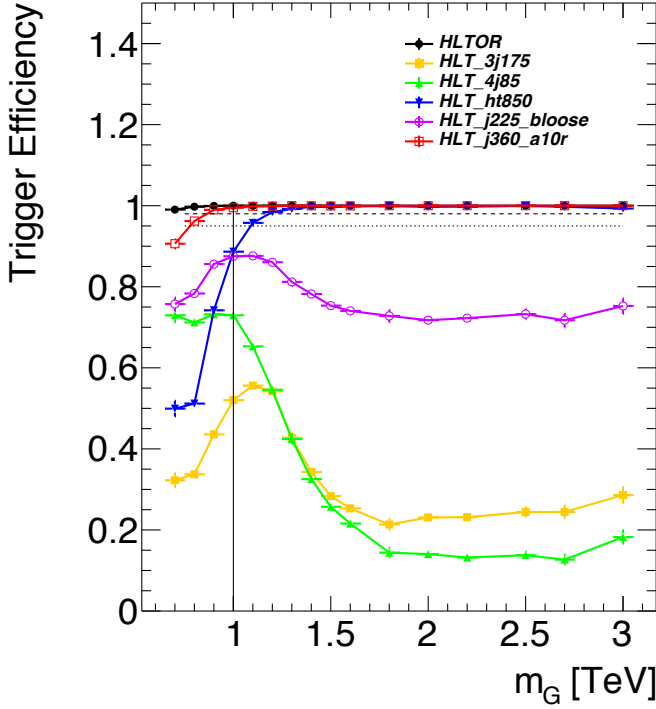


Figure 7.4: Trigger efficiency for events passing all signal region selections as a function of mass in  $G_{KK}^* \rightarrow HH \rightarrow 4b$  samples with  $c = 1$  [119]. In the trigger names, “j” refers to a jet or jets. “ht” refers to  $H_T$ , the scalar sum of transverse momenta in the event. “bloose” refers to a loose  $b$ -tagging requirement applied to the jet. “a10r” refers to anti- $k_T$  jets with  $R = 1.0$ . The numbers at the end of each trigger name are the thresholds on the given quantity in GeV.

## 2367 7.4 EVENT RECONSTRUCTION AND OBJECT SELECTION

2368 The boosted selection first begins by defining a unique set of objects that can be exploited to increase signal  
 2369 efficiency in the kinematic regime where the final state  $b$ -jets are very merged.

### 2370 7.4.1 LARGE RADIUS ( $R = 1.0$ ) JETS

2371 The first step towards reconstructing the final state is to define objects that can be used to measure the  
 2372 kinematics of the Higgs bosons. In the boosted selection anti- $k_T$  jets with a radius parameter of 1.0 are  
 2373 used. These jets are much larger in angular size than the typical  $R = 0.4$  jets and are intended to encompass  
 2374 all of the products of the Higgs decay<sup>3</sup>. The jets are built from clusters in the calorimeter calibrated with

---

<sup>3</sup>This is in contrast to the resolved selection, which uses two  $R = 0.4$  anti- $k_T$  jets for each Higgs.

local calibration weighting [69].

Because of the large extent of these jets, great care must be taken to remove potential contributions of calorimeter clusters from pile-up. This is done using a technique called jet trimming [120]. With trimming, the constituents of the large radius jet are re-clustered with a smaller radius using the  $k_T$  algorithm. Then, these so-called subjets are removed from the larger jet if  $p_T^{\text{subjett}} / p_T^{\text{jet}} < f_{\text{cut}}$ . In this analysis, the subjet radius is  $R = 0.2$  and  $f_{\text{cut}} = 0.05$ . Trimming has been shown to improve the mass resolution of large radius jets. Figure 7.5 shows the effect of trimming on the large radius jet mass ( $M_J$ ). Because the large radius jet fully contains the Higgs decay products, its invariant mass should correspond to the 125 GeV mass of the Higgs. The trimming algorithm brings the jet mass much closer to the expected Higgs mass and improves the mass resolution.

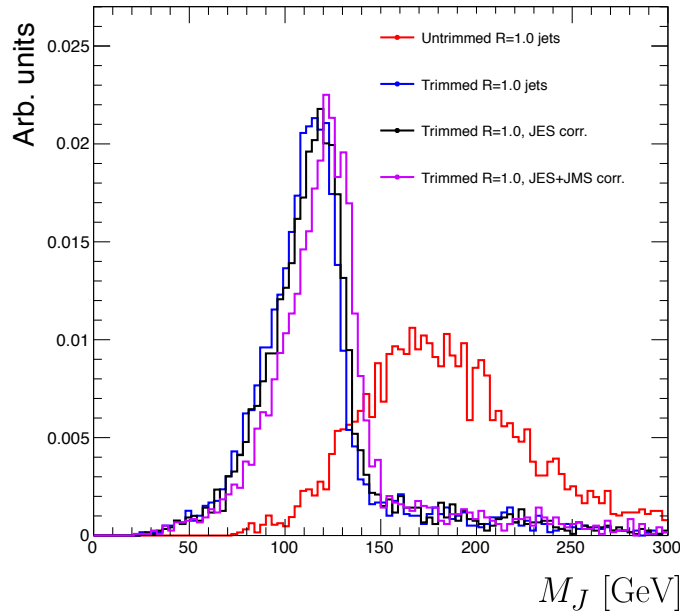


Figure 7.5: Comparison of untrimmed and trimmed jet masses for large radius jets in a RSG sample with  $m_{G_{\text{KK}}^*} = 1 \text{ TeV}$ . JES (JMS) refers to the standard jet energy (mass) scale calibration for ATLAS [69].

The large radius jets are required to satisfy  $250 < p_T < 1500 \text{ GeV}$ . They must also be within  $|\eta| < 2.0$  in order to ensure that the full jet is within the inner detector tracking volume. Finally, they are required to have  $M_J > 50 \text{ GeV}$ . The upper  $p_T$  cut and lower threshold on mass are applied to correspond to the kinematic range where uncertainties are available in ATLAS calibrations [121, 122].

2389 7.4.2 TRACK JETS AND  $b$ -TAGGING

2390 Because the  $b$ -jets from boosted Higgs decays are so close together (as illustrated in figure 7.3), narrow radius  
2391 jets are required to fully resolve both  $b$ -jets. The minimum radius feasible for jets based on calorimeter  
2392 deposits is determined by the calorimeter granularity. However, because  $b$ -tagging relies on information  
2393 from the inner detector, it is possible to define another type of jet that can have a smaller radius and better  
2394  $b$ -tagging resolution. These jets are called “track jets” [122, 123].

2395 Track jets are formed by applying the usual anti- $k_T$  clustering algorithm to tracks that are required to be  
2396 consistent with the primary vertex. After the jet axis has been determined using these tracks, a second step  
2397 of track association is also performed to add tracks that can be useful for  $b$ -tagging [123]. In this analysis,  
2398 the tracks are clustered with a radius parameter of  $R = 0.2$ . This radius has been shown to give good  
2399 performance in boosted Higgs tagging [122, 123]. Figure 7.6 shows a comparison among different track jet  
2400 radii of the efficiency for reconstructing two  $b$ -jets from each Higgs in a RSG sample as a function of mass.  
Track jets with radius of 0.2 give the best performance, especially at high mass. In this analysis, track jets

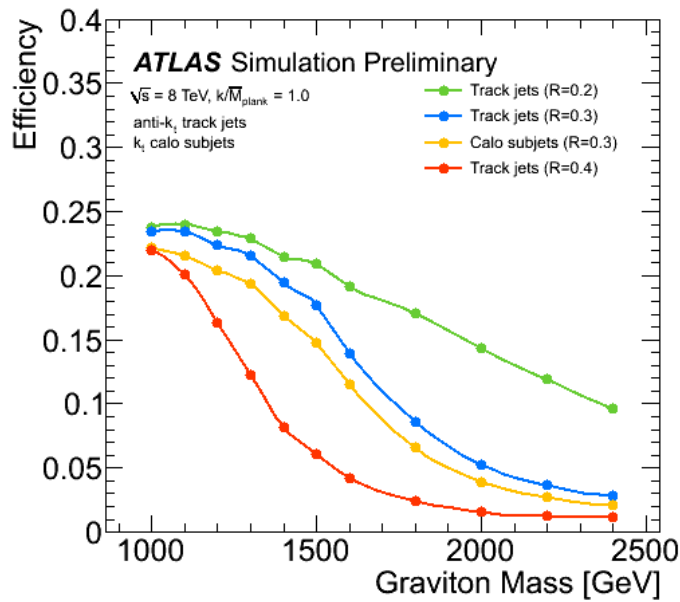


Figure 7.6: Efficiency of finding two  $b$ -jets from each Higgs in an RSG event using calorimeter jets with  $R = 0.3$  and track jet radii of  $R = [0.2, 0.3, 0.4]$  [123].

2401

2402 are required to have  $p_T > 10$  GeV and  $|\eta| < 2.5$ . They must also have at least two tracks.

2403 **7.4.3 MUONS**

2404 Muons are used in this study to correct the four-momenta of calorimeter jets by accounting for semi-  
2405 leptonic  $b$  decays. The muons used are combined ID and MS muons which must satisfy tight identification  
2406 requirements [65]. The muons must have  $p_T > 4 \text{ GeV}$  and  $|\eta| < 2.5$ . Table 7.1 summarizes the object  
2407 requirements described in this section.

	$R$	$p_T$	$ \eta $	$M$
Calorimeter jets	1.0	$250 < p_T < 1500 \text{ GeV}$	$< 2.0$	$> 50 \text{ GeV}$
Track jets	0.2	$> 10 \text{ GeV}$	$< 2.5$	-
Muons	-	4 GeV	$< 2.5$	-

Table 7.1: Summary of requirements on objects used in the  $X \rightarrow HH \rightarrow b\bar{b}b\bar{b}$  search

2408 **7.5 EVENT SELECTION**

2409 The first requirement in the boosted event selection is for  $\geq 2$  large radius jets satisfying the selections  
2410 outlined above. The two highest momentum large-R jets in the event are referred to as “Higgs candidates”.  
2411 The leading jet is required to have  $p_T > 350 \text{ GeV}$ .

2412 Track jets satisfying the object selections are matched to Higgs candidate jets via ghost association [124].  
2413 Each Higgs candidate must have at least 2 track jets associated with it. These basic requirements are illus-  
2414 trated graphically in figure 7.7.

2415 The QCD multijet background produces less central jets than high mass resonances, so there is an ad-  
2416 dditional requirement that the two Higgs candidates be close together in  $\eta$ . The large-R jets are required to  
2417 satisfy  $|\Delta\eta(JJ)| < 1.7$ .

2418 **7.5.1 MASS REQUIREMENTS**

2419 The final set of requirements ensures that the Higgs candidates are consistent with expected properties of  
2420 the 125.0 GeV Higgs. First, a variable ( $X_{hh}$ ) is defined to measure the consistency of both of the Higgs

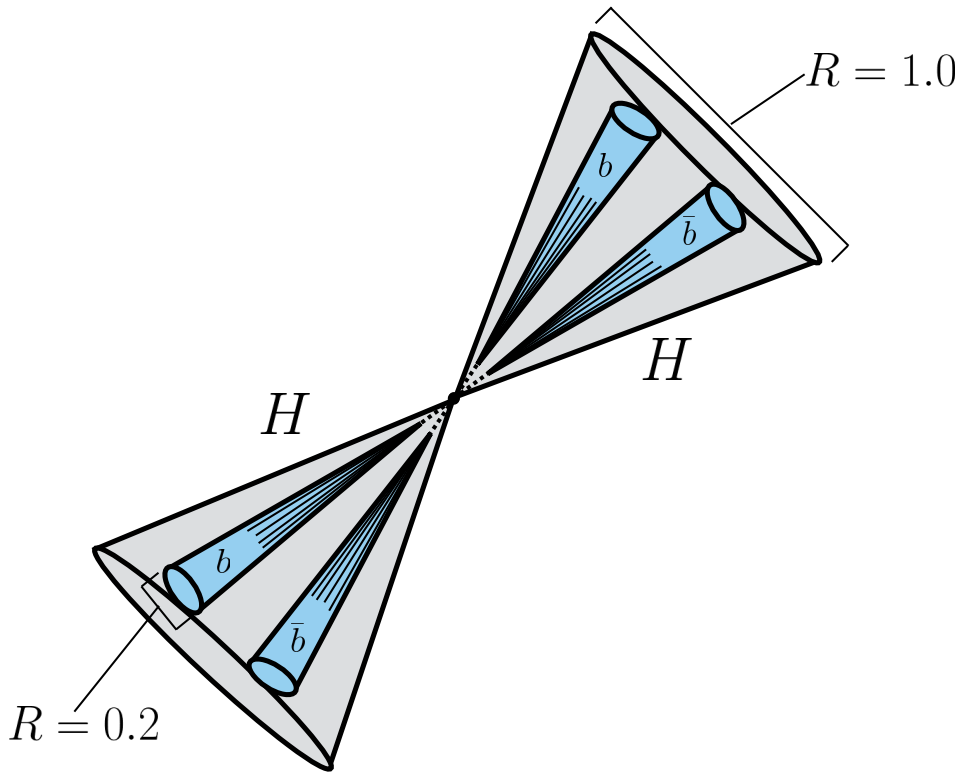


Figure 7.7: Illustration of the boosted selection requirements on Higgs candidates. Each large-radius calorimeter jet (Higgs candidate) must contain two track jets.

<sup>2421</sup> candidate jets with the SM Higgs mass. This is shown in equation 7.2.

$$X_{hh} = \sqrt{\left(\frac{M_J^{\text{lead}} - 124 \text{ GeV}}{0.1 M_J^{\text{lead}}}\right)^2 + \left(\frac{M_J^{\text{sublead}} - 115 \text{ GeV}}{0.1 M_J^{\text{sublead}}}\right)^2} \quad (7.2)$$

<sup>2422</sup> The mass values in the  $X_{hh}$  formula are optimized to maximize signal efficiency. The sub-leading jet typ-  
<sup>2423</sup> ically has a lower mass due to semi-leptonic  $b$  decays and final state radiation.  $X_{hh}$  effectively acts as a  $\chi^2$   
<sup>2424</sup> measurement of the consistency of the two Higgs candidate masses with the signal hypothesis. The de-  
<sup>2425</sup> nominators of each term ( $0.1 M$ ) give the uncertainty on the mass measurement for the large radius jets.  
<sup>2426</sup> Events are required to satisfy  $X_{hh} < 1.6$ .

<sup>2427</sup> Before making the requirement on  $X_{hh}$ , the masses of the Higgs candidates are corrected for semi-  
<sup>2428</sup> leptonic  $b$  decays using muons with the criteria outlined in the previous section. Any muons within a  
<sup>2429</sup>  $\Delta R < 0.2$  of a  $b$ -tagged track jet (as described in the next section) have their four-momenta added to the

2430 four-momentum of the Higgs candidate. This correction does not affect the pre-selection requirements  
 2431 but does affect the  $X_{hh}$  requirement and the final invariant mass discriminant.

2432 **7.5.2 b-TAGGING REQUIREMENTS**

2433 The last requirement applied is on the number of  $b$ -tagged track jets. There are two signal regions defined.  
 2434 The first requires exactly four  $b$ -tagged track jets, two in each Higgs candidate (known as the  $4b$  signal re-  
 2435 gion). At high resonance masses, this requirement is inefficient, so an additional signal region requiring  
 2436 only three  $b$ -tagged track jets is also defined (known as the  $3b$  signal region). While this has a larger back-  
 2437 ground it is also more efficient for high resonance masses. For both signal regions, the MV2c2o algorithm,  
 2438 where the training sample for the algorithm has 20% charm events is used. More details for this algorithm  
 2439 can be found in Chapter 2.

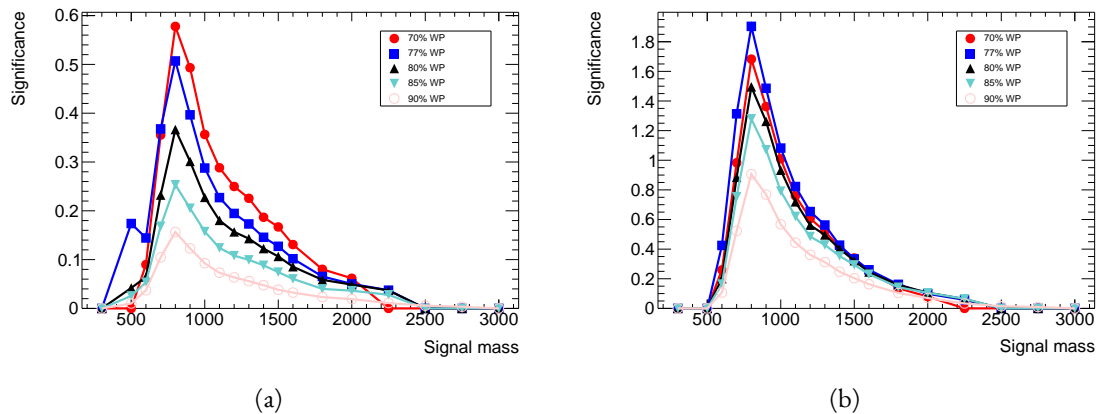


Figure 7.8: Estimated significance as a function of signal mass for RSG  $c = 1$  models in the  $3b$  (a) and  $4b$  (b) regions for different  $b$ -tagging efficiency working points

2440 Once the algorithm is selected, an efficiency working point must also be chosen. This working point  
 2441 defines the efficiency with which true  $b$ -jets are tagged and also fixes the overall background rejection of the  
 2442 algorithm. Higher efficiency working points accept more true  $b$ -jets but also allow for more background.  
 2443 Five different working points (70%, 77%, 80%, 85%, 90%) are tested. With each working point, the  
 2444 full data driven background estimation method is run to quantify the amount of background that will be  
 2445 present in the final signal region. The significance is quantified using the median discovery significance for

2446 signal and background with Poisson errors, given in equation 7.3 [125].

$$Z = \sqrt{2 \left( (s + b) \ln \left( 1 + \frac{s}{b} \right) - s \right)} \quad (7.3)$$

2447 Here,  $s$  is the expected number of signal events and  $b$  is the expected number of background events. This  
 2448 formula is derived using Poisson statistics with errors on both the signal and background. It is used because  
 2449 it is valid in the regime where  $s$  and  $b$  are of the same order. Note that in the limit where  $s$  is much smaller  
 2450 than  $b$ , this equation reduces to the more well known  $s/\sqrt{b}$ . Figure 7.8 shows the estimated significance as  
 2451 a function of signal mass in RSG  $c = 1$  models for the  $3b$  and  $4b$  signal regions. The 77% working point  
 2452 gives the best performance over a wide range of masses in the  $4b$  signal region. As this is the region which  
 2453 contributes the most to the total discovery significance, the 77% efficiency working point is chosen for the  
 2454 analysis.

### 2455 7.5.3 SELECTION EFFICIENCY

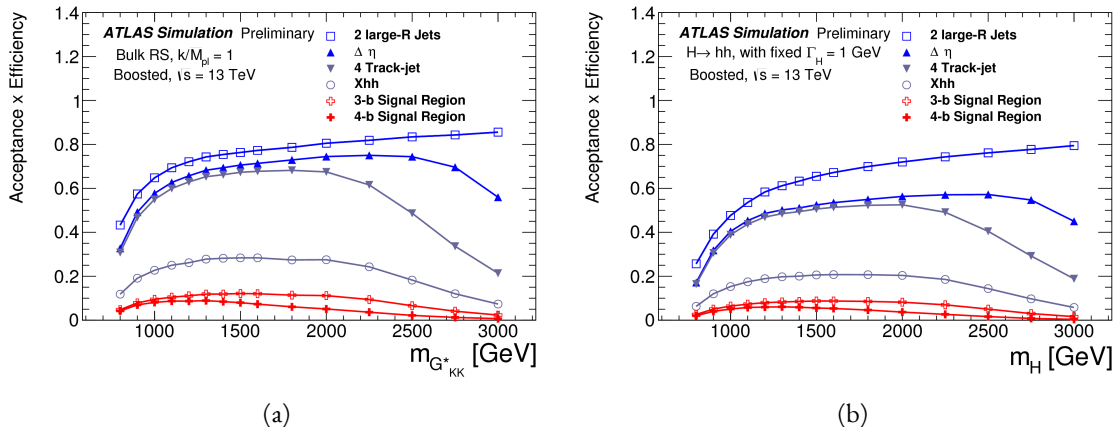


Figure 7.9: Acceptance × efficiency as a function of mass for (a) RSG and (b) narrow heavy scalar signal models [126].

2456 Figure 7.9 shows the product of acceptance and efficiency as a function of mass for both the RSG and  
 2457 narrow heavy scalar resonance signal models. After  $m_X > 1 \text{ TeV}$ , the efficiency of the  $4b$  requirement  
 2458 begins to decline. After  $m_X > 2 \text{ TeV}$ , the efficiency of requiring two track jets in each Higgs candidate  
 2459 begins to decline as well. Both of these behaviors illustrate the difficulty of resolving the merged decay

products at high mass. Figure 7.10 shows a more detailed comparison of the signal efficiency in the  $3b$  vs  $4b$  signal regions for the RSG model. The efficiencies shown here are relative to all prior selection requirements. It can be seen there that at high masses the  $3b$  signal region is more efficient for signal.

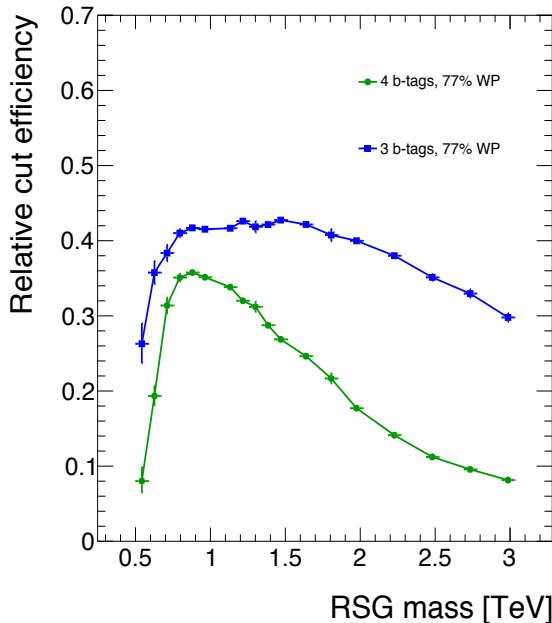


Figure 7.10: Efficiency of requiring 3 or 4  $b$ -tagged track jets vs. RSG mass. The efficiency quoted is relative to the previous selection requirements (rather than an absolute efficiency).

To investigate the degradation of  $b$ -tagging efficiency at high  $p_T$ , the individual jet tagging efficiencies can be compared as a function of signal mass. This is shown in figure 7.11. The figure shows that the leading jet tagging efficiency in both calorimeter jets degrades heavily, while the sub-lead jet tagging efficiency remains relatively constant. More details on the cause of this degradation are shown in appendix A.

The final discriminating variable used in the boosted analysis is  $M_{2J}$ , the invariant mass of the two Higgs candidates. In order to improve the mass resolution, the four-momenta of each Higgs candidate are scaled by  $m_h/M_J$ . The effect of this correction is small in the boosted analysis but is done for consistency with the resolved selection. Table 7.2 shows the effect of the selection requirements on signal and background simulations as well as data.

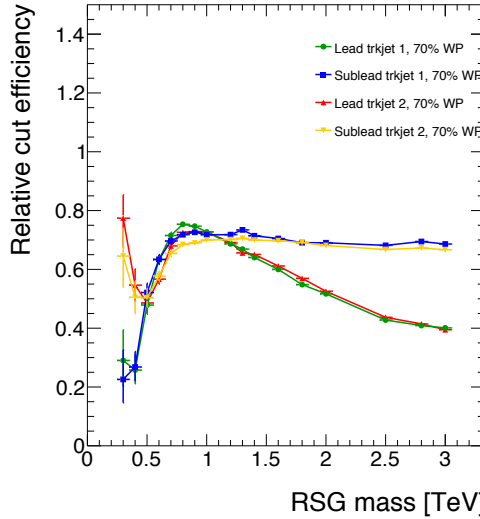


Figure 7.11: MV2c20  $b$ -tagging efficiency for each of the four track jets in the boosted  $4b$  selection as a function of RSG mass for  $c = 1$  models.

Selection	Data	$m_{G_{KK}^*} = 1\text{TeV}$	$m_{G_{KK}^*} = 2\text{TeV}$	$t\bar{t}$	$Z + \text{jets}$
$N(\text{fiducial large-R jets}) \geq 2$	2202396	23.3	0.48	32345.2	4255.7
leading large-R jet $p_T > 350\text{ GeV}$	1873741	22.9	0.48	26511.7	3649.9
Both large-R jet $m > 50\text{ GeV}$	1854625	21.2	0.47	24369.8	3575.8
Both large-R jet $p_T < 1500\text{ GeV}$	1853601	21.2	0.46	24346.5	3572.9
$ \Delta\eta(JJ)  < 1.7$	1435273	20.8	0.44	20751.0	3265.8
$\geq 2$ track-jets per large-R jet	1224727	19.8	0.40	18234.5	2692.6
$3$ $b$ -tags, $X_{hh} < 1.6$	316	3.4	0.067	46.7	2.0
$4$ $b$ -tags, $X_{hh} < 1.6$	20	2.9	0.030	1.4	0.0

Table 7.2: Effect of boosted selection on data, RSG signal models,  $t\bar{t}$ , and  $Z + \text{jets}$ . The numbers from simulation are normalized with the MC generator cross section and do not take into account the data driven estimates described in section 7.6 [127].

## 2472 7.6 DATA-DRIVEN BACKGROUND ESTIMATION

2473 The largest background to the  $X \rightarrow HH \rightarrow b\bar{b}b\bar{b}$  final state is QCD multijet production, constituting 2474 80-90% of the total background. Because of the difficulties in modeling higher order QCD processes, 2475 this background is estimated with a fully data-driven method. The only other non-negligible background 2476 is  $t\bar{t}$ , constituting the other 10-20%. Due to the presence of  $t\bar{t}$  in the sideband region where the QCD

<sup>4</sup>The  $Z + \text{jets}$  background is a sub-percent level contribution

<sup>2477</sup> background will be estimated, the normalization of the QCD and  $t\bar{t}$  backgrounds are simultaneously es-  
<sup>2478</sup> timated.

#### <sup>2479</sup> 7.6.1 MASS REGION DEFINITIONS

<sup>2480</sup> The first step in the data-driven background estimate is to define a sideband mass region where the back-  
<sup>2481</sup> ground normalization can be derived. Additionally, a control region is defined where the background  
<sup>2482</sup> estimate can be validated. The control (CR) and sideband (SB) regions are defined using a radial distance  
<sup>2483</sup> in the two-dimensional large-R jet mass plane,  $R_{hh}$ , which is defined in equation 7.4.

$$R_{hh} = \sqrt{(M_J^{\text{lead}} - 124 \text{ GeV})^2 + (M_J^{\text{sublead}} - 115 \text{ GeV})^2} \quad (7.4)$$

<sup>2484</sup> Events in the control region are required to fail the signal region  $X_{hh} < 1.6$  requirement and have  
<sup>2485</sup>  $R_{hh} < 35.8 \text{ GeV}$ . The sideband region consists of those events which are not in the signal or control  
regions. Figure 7.12 shows the definition of the signal, control, and sideband mass regions. Table 7.3 sum-

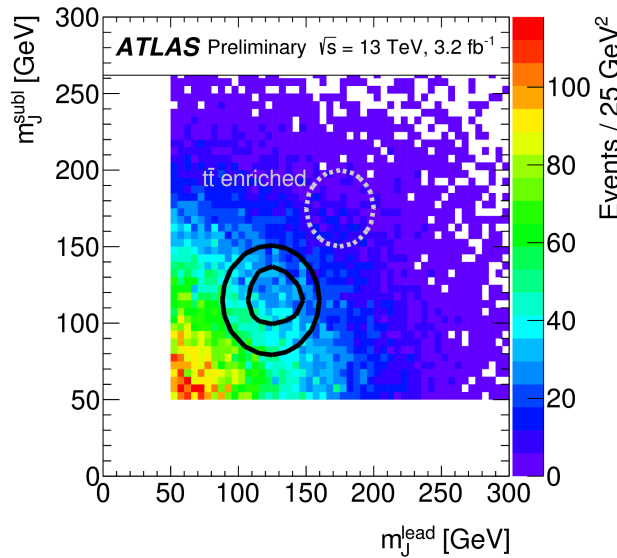


Figure 7.12:  $M_J^{\text{sublead}}$  vs.  $M_J^{\text{lead}}$  in a 2  $b$ -tag data sample. The signal region is defined by the inner black contour ( $X_{hh} < 1.6$ ) and the sideband region is defined by the outer contour ( $R_{hh} > 35.8 \text{ GeV}$ ). The region between the black contours is the control region. The mass region which is enriched in  $t\bar{t}$  background is also shown for illustration [[126](#)].

<sup>2486</sup> marizes the mass region selections for the three different regions used in the analysis.  
<sup>2487</sup>

Region	Requirement	Notes
Signal Region (SR)	$X_{hh} < 1.6$	-
Control Region (CR)	$R_{hh} < 35.8 \text{ GeV}$ and $X_{hh} > 1.6$	Used for validation of background estimates
Sideband Region (SB)	$R_{hh} > 35.8 \text{ GeV}$	Used to derive background normalization

Table 7.3: Mass region definitions used for background estimation.

2488    7.6.2 BACKGROUND ESTIMATION

2489    The method for estimating the background in this analysis is similar to the ABCD method presented in  
 2490    Chapter 5. In this case, the two handles used to define different regions for the estimate are the number  
 2491    of  $b$ -tagged track jets and the mass requirements. A region requiring exactly two  $b$ -tagged track jets in one  
 2492    large-R jet (referred to as the 2-tag or  $2b$  region) is defined for use in the background estimate. The number  
 2493    of expected background events in the  $3b$  and  $4b$  signal regions is then given by equation 7.5.

$$N_{\text{bkg}}^{3(4)-\text{tag},\text{SR}} = \mu_{\text{Multijet}} N_{\text{Multijet}}^{2-\text{tag},\text{SR}} + \beta_{t\bar{t}} N_{t\bar{t}}^{3(4)-\text{tag},\text{SR}} + N_{Z+\text{jets}}^{3(4)-\text{tag},\text{SR}} \quad (7.5)$$

2494    In this equation,  $N_{\text{bkg}}^{3(4)-\text{tag}}$  is the expected number of background events in the  $3b$  or  $4b$  signal regions.  
 2495     $N_{\text{Multijet}}^{2-\text{tag}}$  is the number of multijet events in the 2-tag region.  $N_{t\bar{t}}^{3(4)-\text{tag}}$  is the number of  $t\bar{t}$  events pre-  
 2496    dicted in the MC for the  $3b$  or  $4b$  signal region, and the variable is similarly defined for the  $Z+\text{jets}$  back-  
 2497    ground. The  $\beta_{t\bar{t}}$  parameter is a scale factor used to correct the normalization of the  $t\bar{t}$  estimate in the signal  
 2498    region.  $\mu_{\text{Multijet}}$  is an extrapolation factor that is derived in the sideband region and used to estimate the  
 2499    ratio of 2-tag events to 3(4)-tag events in the signal region. It is defined in equation 7.6.

$$\mu_{\text{Multijet}} = \frac{N_{\text{Multijet}}^{3(4)-\text{tag},\text{SB}}}{N_{\text{Multijet}}^{2-\text{tag},\text{SB}}} = \frac{N_{\text{data}}^{3(4)-\text{tag},\text{SB}} - \beta_{t\bar{t}} N_{t\bar{t}}^{3(4)-\text{tag},\text{SB}} - N_{Z+\text{jets}}^{3(4)-\text{tag},\text{SB}}}{N_{\text{data}}^{2-\text{tag},\text{SB}} - \beta_{t\bar{t}} N_{t\bar{t}}^{2-\text{tag},\text{SB}} - N_{Z+\text{jets}}^{2-\text{tag},\text{SB}}} \quad (7.6)$$

2500    The  $t\bar{t}$  scale factor ( $\beta_{t\bar{t}}$ ) and the QCD multijet extrapolation factor ( $\mu_{\text{Multijet}}$ ) are estimated together in  
 2501    a simultaneous fit in the sideband region. Then, the number of events in the 2-tag signal region is used,  
 2502    along with the  $t\bar{t}$  estimate in the  $3b$  and  $4b$  signal regions and  $\mu_{\text{Multijet}}$ , to estimate the total number  
 2503    of background events in the two final signal regions. The shape of the final discriminant  $M_{2J}$  is also

2504 taken from the 2-tag signal region where there are more events. This method is illustrated graphically in  
 figure 7.13. In the  $3b$  region, the fit yields values of  $\mu_{\text{Multijet}} = 0.160 \pm 0.03$  and  $\beta_{t\bar{t}} = 1.02 \pm 0.09$ .

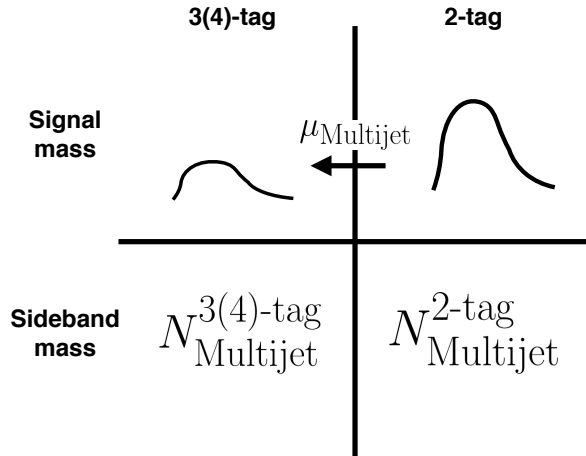


Figure 7.13: An illustration of the data-driven background estimation technique for the boosted analysis

2505  
 2506 In the  $4b$  region, the fit gives  $\mu_{\text{Multijet}} = 0.0091 \pm 0.0007$  and  $\beta_{t\bar{t}} = 0.82 \pm 0.39$ . The uncertainties  
 2507 quoted are statistical only. The larger uncertainties in the  $4b$  values indicate the lower statistics available in  
 2508 that region.

2509 Figure 7.14 shows the distributions of data and background estimates in the  $3b$  and  $4b$  sideband regions  
 2510 after the background fit has been done. The normalizations are constrained from the fit to match that of  
 2511 the data, but good modeling of the shape of the mass of the leading large-R jet is seen as well. The shapes  
 2512 of the kinematic distributions for the  $t\bar{t}$  background in the  $4b$  region are taken from the  $3b$  region due to  
 2513 the better MC statistics in that region.

### 2514 7.6.3 BACKGROUND SHAPE FIT

2515 As mentioned in the previous section, the background shape in the 3-tag and 4-tag signal regions is taken  
 2516 from the 2-tag signal mass region. Due to the limited statistics available, the background shapes are addi-  
 2517 tionally smoothed after being extrapolated to the 3-tag and 4-tag signal regions. Only the data in the range  
 2518  $900 < M_{2J} < 2000$  GeV is included in the shape fit due to the limited statistics available above 2 TeV.  
 2519 Both the  $t\bar{t}$  and QCD multijet background are independently fit with an exponential shape,  $y = e^{ax+b}$ .

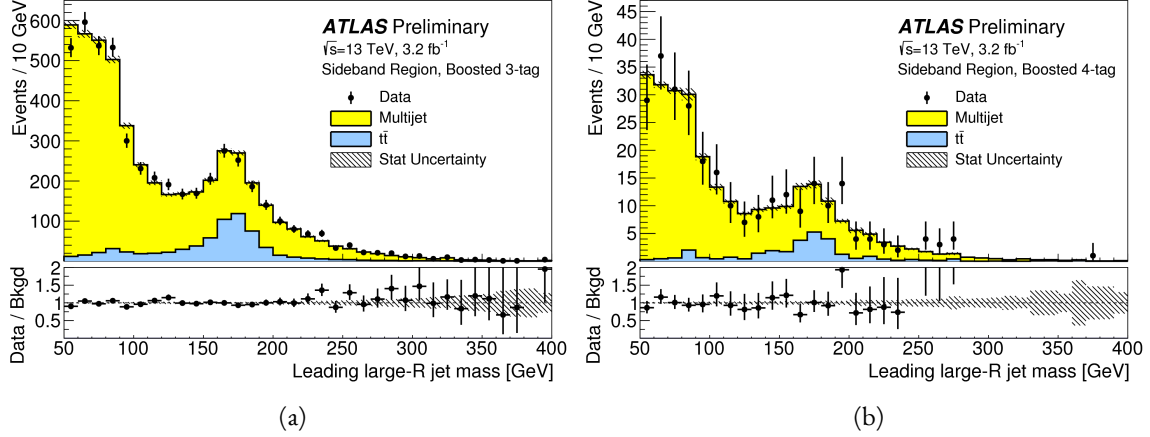


Figure 7.14: Leading large-R jet mass in the 3b (a) and 4b (b) sideband regions. The multijet and  $t\bar{t}$  backgrounds are estimated using the data-driven methods described above. Because their normalizations are derived in the sideband region, the total background normalization is constrained by default to match the normalization of the data [126].

2520 Other shapes are considered and used for the systematic uncertainties. Table 7.4 shows the fit values for  
 2521 the parameters. Because both the 3b and 4b QCD shapes come from the 2-tag region, the slopes derived  
 2522 are very similar.

	$a$	$b$
QCD (4b)	$0.00545 \pm 0.00021$	$5.44 \pm 0.24$
$t\bar{t}$ (4b)	$0.00746 \pm 0.00021$	$4.88 \pm 0.36$
QCD (3b)	$0.00545 \pm 0.00021$	$8.30 \pm 0.24$
$t\bar{t}$ (3b)	$0.00746 \pm 0.00021$	$8.58 \pm 0.36$

Table 7.4: Parameters derived for exponential fit to background  $M_{2J}$  shape in the 3b and 4b signal regions [127].

#### 2523 7.6.4 VALIDATION OF BACKGROUND ESTIMATE

2524 The background estimate can be validated by using the method to estimate the number of events in the  
 2525 control mass region rather than the signal mass region. Figure 7.15 shows the  $M_{2J}$  distribution in the 3b  
 2526 and 4b control regions, comparing data and background estimates. In both cases, both the background  
 2527 shape and normalization are consistent with the data, indicating good agreement. The ratio of data to the  
 2528 background estimates is also fit to a line in the figure to test for any shape difference. The slope of the  
 2529 line is within  $1\sigma$  (from the fit uncertainties) of flat, further indicating that the data is consistent with the  
 2530 background estimate in the control region.

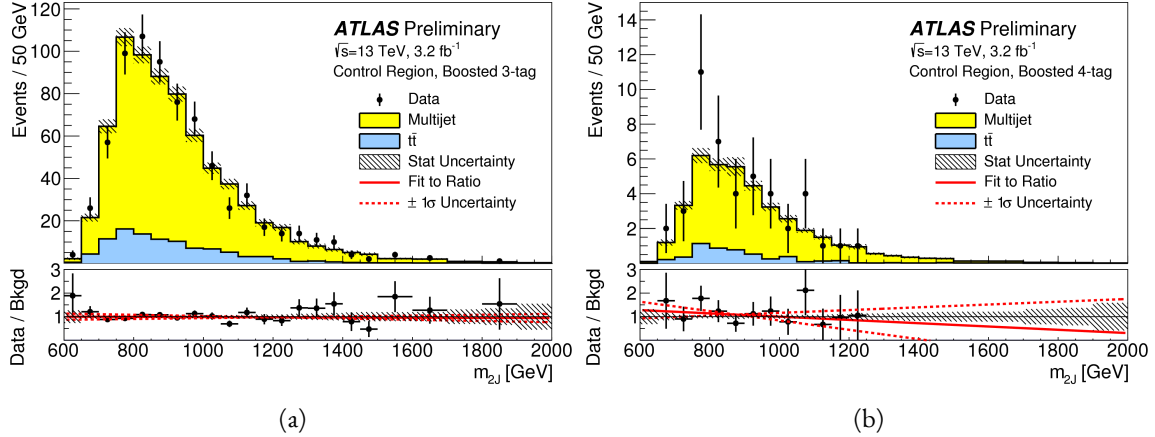


Figure 7.15: Di-jet invariant mass ( $M_{2J}$ ) in the 3b (a) and 4b (b) control regions. The multijet and  $t\bar{t}$  backgrounds are estimated using the data-driven methods described above [126].

Table 7.5 shows the yields in data and background estimates in the 3-tag and 4-tag sideband and control regions. Again, here, it can be seen that the total number of predicted background events from the data driven method is consistent with the number of data events in the region.

Sample (3-tag)	Sideband Region	Control Region
Multijet	$4328 \pm 27$	$607 \pm 10$
$t\bar{t}$	$683.5 \pm 8.1$	$99.6 \pm 3.1$
Z+jets	$31.8 \pm 3.7$	$7.7 \pm 1.8$
Total	$5043 \pm 28$	$715 \pm 11$
Data	5043	724
Sample (4-tag)	Sideband Region	Control Region
Multijet	$247.4 \pm 1.5$	$34.7 \pm 0.6$
$t\bar{t}$	$28.4 \pm 1.5$	$5.1 \pm 0.7$
Z+jets	$3.4 \pm 1.2$	$0.6 \pm 0.5$
Total	$279.2 \pm 2.5$	$40.3 \pm 1.0$
Data	279	45

Table 7.5: The number of events in data and predicted background events in the boosted 3-tag and 4-tag sideband and control regions [126]. The uncertainties shown are statistical only.

2534 7.7 SYSTEMATIC UNCERTAINTIES

2535 The systematic uncertainties in this analysis can be divided into two broad categories. The first type is  
2536 uncertainties associated with the modeling of the signal processes. The second type of uncertainty is asso-  
2537 ciated with both the shape and normalization of the background prediction.

2538 7.7.1 SIGNAL MODELING UNCERTAINTIES

2539 The signal modeling uncertainty has three main components: theoretical uncertainty on the acceptance,  
2540 experimental uncertainties on the large-R jets, and experimental uncertainties on the track jets related to  
2541  $b$ -tagging. In this analysis the experimental uncertainties are the most significant.

2542 The first uncertainty on signal modeling is the theoretical uncertainty on the acceptance. As explained  
2543 in section 5.6.1, there are four components to this uncertainty. The first is related to missing higher order  
2544 terms from the matrix element calculations which is estimated by varying the QCD renormalization and  
2545 factorization scales. The second is uncertainty due to the PDF set used. The third is a generator uncer-  
2546 tainty which is estimated by modifying the generator used to model the underlying event and hadroniza-  
2547 tion. Finally, there is an uncertainty associated with the modeling of the initial state and final state radia-  
2548 tion (ISR/FSR). The total theoretical uncertainty on the signal yield is 3%, and this is dominated by the  
2549 ISR/FSR modeling.

2550 There are uncertainties on the large-R jets in both the jet energy scale (JES) and jet energy resolution  
2551 (JER) as well as the jet mass scale (JMS) and jet mass resolution (JMR). These are evaluated using  $\sqrt{s} =$   
2552 8 TeV data from Run 1 of ATLAS and extrapolated to the Run 2 beam and detector conditions using  
2553 MC<sup>5</sup>. The details of these uncertainties can be found in reference [128].

2554 Uncertainties on the track jets are related to the  $b$ -tagging efficiency. The total uncertainty on the signal  
2555 yield due to  $b$ -tagging is evaluated by propagating variations of the  $b$ -tagging efficiency through the boosted  
2556 selection requirements. The uncertainties are calculated jet-by-jet and parameterized as a function of  $b$ -jet  
2557  $p_T$  and  $\eta$  [106]. For high  $p_T$   $b$ -jets (with  $p_T > 300$  GeV), the uncertainties are extrapolated using MC  
2558 simulation from the lower  $p_T$   $b$ -jets [129].

---

<sup>5</sup>The uncertainties are correspondingly larger due to the uncertainty of this extrapolation.

2559 Table 7.6 shows the systematic uncertainties on the signal normalization for models with  $m_{G_{\text{KK}}^*} =$   
 2560  $1.5 \text{ TeV}$  and both  $c = 1$  and  $c = 2$  as well as a narrow width heavy scalar. The dominant uncertainty  
 2561 comes from  $b$ -tagging and this uncertainty is larger in the 4-tag region than the 3-tag region.

Source	Background		$G_{\text{KK}}^*$	$H$
	$c = 1$	$c = 2$		
Luminosity	-	5.0	5.0	5.0
3-tag				
JER	< 1	< 1	< 1	< 1
JES	2	< 1	< 1	< 1
JMR	1	12	12	11
JMS	5	14	13	17
$b$ -tagging	1	23	22	23
Theoretical	-	3	3	3
Multijet Normalization	3	-	-	-
Statistical	2	1	1	1
Total	7	31	30	33
4-tag				
JER	< 1	< 1	< 1	< 1
JES	< 1	< 1	< 1	< 1
JMR	4	12	13	13
JMS	5	13	13	14
$b$ -tagging	2	36	36	36
Theoretical	-	3	3	3
Multijet Normalization	14	-	-	-
Statistical	3	1	1	1
Total	15	42	42	43

Table 7.6: Summary of systematic uncertainties in the total background and signal event yields (expressed in %) in the boosted 3-tag and 4-tag signal regions. Systematic uncertainties on the signal normalization are shown for models with  $m_{G_{\text{KK}}^*} = 1.5 \text{ TeV}$  and both  $c = 1$  and  $c = 2$  as well as a narrow width heavy scalar.

## 2562 7.7.2 BACKGROUND UNCERTAINTIES

2563 Uncertainties on the QCD multijet background normalization and shape are estimated using the con-  
 2564 trol mass region. As shown previously, the background predictions in the control region match with the

2565 data yields within the statistical uncertainty in both the 3-tag and 4-tag control regions. As an additional  
 2566 protection, the statistical uncertainty on the background prediction in the control region is assigned as a  
 2567 systematic uncertainty on the normalization of the QCD background.

2568 Additional robustness tests are done by varying the definition of the control mass region and the  $b$ -  
 2569 tagging requirements used to define the 2-tag sample. In all cases, the effect of the variations is found to be  
 2570 within the statistical uncertainties on the background normalization in the control region.

2571 Shape uncertainties on the background are evaluated using two techniques. First, as shown in fig-  
 2572 ure 7.15, the ratio between the data and background prediction is fit with a linear function. The uncer-  
 2573 tainties on the slope of this fit are assigned as shape uncertainties. An additional uncertainty is assigned by  
 2574 using alternate power law fit functions for the smoothing of the background shape. Table 7.7 shows the  
 2575 alternate shapes used. The largest difference between the nominal fit function and the alternates, taking  
 2576 into account the  $1\sigma$  uncertainty band on each fit as well, is taken as a shape uncertainty.

Functional Form
$f_1(x) = p_0(1 - x)^{p_1}x^{p_2}$
$f_2(x) = p_0(1 - x)^{p_1}e^{p_2 x^2}$
$f_3(x) = p_0(1 - x)^{p_1}x^{p_2}x$
$f_4(x) = p_0(1 - x)^{p_1}x^{p_2} \ln x$
$f_5(x) = p_0(1 - x)^{p_1}(1 + x)^{p_2}x$
$f_6(x) = p_0(1 - x)^{p_1}(1 + x)^{p_2} \ln x$
$f_7(x) = \frac{p_0}{x}(1 - x)^{p_1-p_2} \ln x$
$f_8(x) = \frac{p_0}{x^2}(1 - x)^{p_1-p_2} \ln x$

Table 7.7: Alternate fit functions used to model the  $M_{2J}$  distribution in the QCD multijet background. In the equations,  $x = M_{2J}/\sqrt{s}$ .

2577 The uncertainties on the  $t\bar{t}$  background are obtained by propagating the various experimental variations  
 2578 (JES, JER, JMS, JMR,  $b$ -tagging) through the analysis selection requirements. Table 7.6 summarizes the  
 2579 background uncertainties in the 3-tag and 4-tag regions.

2580 7.8 RESULTS

2581 Table 7.8 shows the observed yields in the 3-tag and 4-tag signal regions for the boosted analysis compared  
 2582 to the predicted number of background events. In the 3-tag region, 316 events are observed with a pre-  
 2583 dicted background of  $285 \pm 19$ . In the 4-tag region, 20 events are observed with a predicted background  
 2584 of  $14.6 \pm 2.4$ . Figure 7.16 shows the  $M_{2J}$  distribution in the 3-tag and 4-tag regions. There are some  
 2585 small excesses in the data, in particular in the 3-tag region around  $M_{2J} \approx 900$  GeV and in the region of  
 2586  $1.6 < M_{2J} < 2.0$  TeV. The significance of these excesses will be evaluated in the next chapter in the  
 2587 statistical combination with the resolved results.

Sample	Signal Region (3-tag)	Signal Region (4-tag)
Multijet	$235 \pm 14$	$13.5 \pm 2.4$
$t\bar{t}$	$48 \pm 22$	$1.2 \pm 1.0$
$Z + \text{jets}$	$2.0 \pm 2.2$	-
Total	$285 \pm 19$	$14.6 \pm 2.4$
Data	316	20
$G_{\text{KK}}^*$ (1000 GeV), $c = 1$	$3.4 \pm 0.9$	$2.9 \pm 1.1$

Table 7.8: Observed yields in the 3-tag and 4-tag signal regions for the boosted analysis compared to the predicted number of background events Errors correspond to the total uncertainties in the predicted event yields. The yields for a graviton with  $m_{G_{\text{KK}}^*} = 1$  TeV and  $c = 1$  are also shown [126].

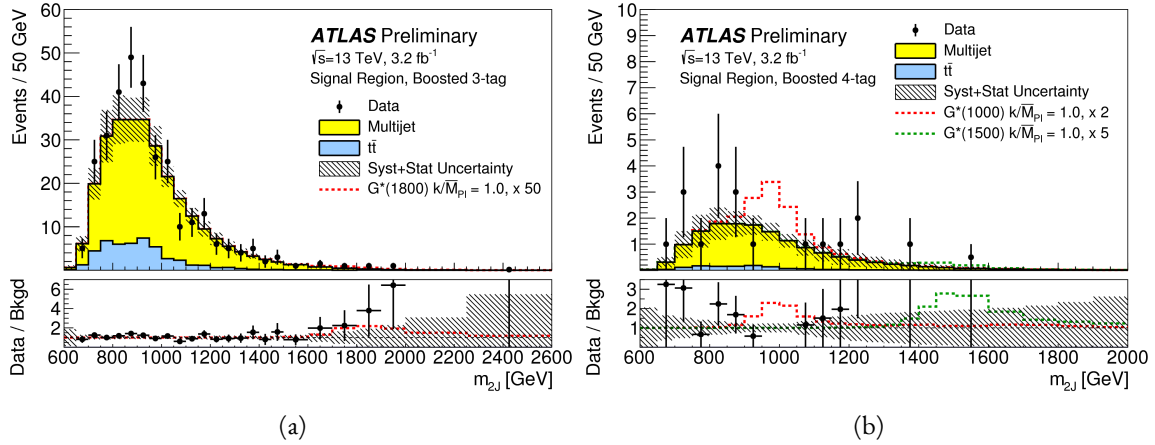


Figure 7.16: Di-jet invariant mass ( $M_{2J}$ ) in the 3b (a) and 4b (b) signal regions. The multijet and  $t\bar{t}$  backgrounds are estimated using the data-driven methods described above. In the 3b region, a graviton signal with  $m_{G_{KK}^*} = 1.8$  TeV and  $c = 1$  is overlaid, with the cross section multiplied by a factor of 50 so that the signal is visible. In the 4b region, signals with  $m_{G_{KK}^*} = 1.0$  TeV and  $m_{G_{KK}^*} = 1.5$  TeV are overlaid, both with  $c = 1$  and the yields multiplied by factors of 2 and 5 respectively [126].

*There is no real ending. It's just the place where you stop  
the story.*

Frank Herbert

# 8

2588

2589

## Combined limits from boosted and resolved searches

2590

2591

### 8.1 INTRODUCTION

2592 In order to cover the full mass range of possible resonances decaying to di-Higgs final states, two distinct  
2593 tailored selections were produced. The resolved selection is more sensitive in the mass range of  $400 < m_X < 1100$  GeV while the boosted selection is more sensitive to masses in the range  $1100 < m_X < 3000$  GeV. Chapter 7 presents the details of the boosted selection and results. In setting limits on spin-2  
2594 Randall-Sundrum graviton (RSG) and narrow width heavy scalar ( $H$ ) models, the results of the boosted  
2595 selection are combined with the results of the resolved selection to cover the full mass range.  
2596

2597 This chapter presents limits on signal models resulting from the  $X \rightarrow HH \rightarrow b\bar{b}b\bar{b}$  search in both  
2598 the resolved and boosted selections. It first presents a brief overview of the resolved results that go into

2600 the limit setting. Then, an overview of the statistical methods used for the search and limit setting is given.  
2601 Finally, limits on the RSG and heavy scalar models are presented.

2602 **8.2 RESOLVED RESULTS**

2603 The details of the resolved selection will not be presented here and can be found in reference [126]. In  
2604 basic terms, the selection searches for four  $R = 0.4$  b-tagged calorimeter jets (where each pair of jets is  
2605 one Higgs candidate). This is distinct from the boosted methodology which searches for merged decay  
2606 products. The backgrounds to the resolved selection are the same as those presented in Chapter 7 for the  
2607 boosted analysis.

2608 Table 8.1 shows the results for data yields and expected background in the resolved signal region. Fig-  
2609 ure 8.1 shows the  $M_{2J}$  distribution in the resolved signal region. The total number of events is consistent  
2610 with the prediction and no significant excess is seen. One event in the boosted 4-tag signal is shared with  
2611 the resolved signal region and has a mass of 852 GeV.

Sample	Signal Region Yield
Multijet	$43.3 \pm 2.3$
$t\bar{t}$	$4.3 \pm 3.0$
$Z + \text{jets}$	-
Total	$47.6 \pm 3.8$
Data	46
SM $hh$	$0.25 \pm 0.07$
$G_{\text{KK}}^*(800 \text{ GeV}), c = 1$	$5.7 \pm 1.5$

Table 8.1: Observed yields in the resolved selection 4-tag signal region compared to the predicted number of background events Errors correspond to the total uncertainties in the predicted event yields. The yields for a graviton with  $m_{G_{\text{KK}}^*} = 800$  GeV and  $c = 1$  are also shown [126].

2612 **8.3 SEARCH TECHNIQUE AND RESULTS**

2613 The statistical technique used for the search in this analysis is the same as that used in the  $H \rightarrow WW^*$   
2614 analysis presented in section 3.6.2. The test statistic  $q_0$  is used to define the  $p$ -values which measure the

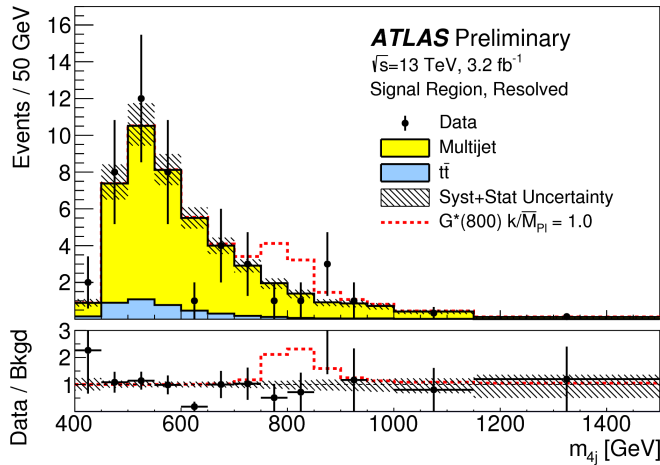


Figure 8.1: Di-jet invariant mass ( $M_{2J}$ ) in the resolved signal region. A graviton signal with  $m_{G_{KK}^*} = 800$  GeV and  $c = 1$  is overlaid. [126].

compatibility of the data with the background-only hypothesis corresponding to a signal strength  $\mu = 0$ .

Local  $p_0$  values are computed to quantify the probability that the background could produce a fluctuation greater than or equal to the one observed in the data. In the resolved analysis, no significant excesses are observed. The largest discrepancy with respect to the background only hypothesis occurs near a resonance mass of 900 GeV and is found to be less than  $2\sigma$  in significance.

In the boosted selection, the largest local excess is a broad excess in the  $3b$  signal region that begins near  $M_{2J} \approx 1.7$  GeV. Assuming a  $G_{KK}^*$  with this mass and  $c = 1.0$ , the local significance of this excess is  $2.0\sigma$ .

#### 8.4 LIMIT SETTING

In the absence of any significant excess observed in the data, limits on different signal models can be set. This section describes the limit setting procedure and presents combined results of the resolved and boosted analyses.

##### 8.4.1 LIMIT SETTING PROCEDURE

The procedure used for setting exclusion limits in this analysis is the  $CL_s$  method [130]. The first step in setting the limits is to define a test statistic which will be used. For limit setting, the test statistic is shown

2630 in equation 8.1.

$$\widetilde{q}_\mu = \begin{cases} -2 \ln \frac{L(\mu, \hat{\theta}(\mu))}{L(0, \hat{\theta}(0))} & \hat{\mu} < 0 \\ -2 \ln \frac{L(\mu, \hat{\theta}(\mu))}{L(\hat{\mu}, \hat{\theta})} & 0 \leq \hat{\mu} < \mu \\ 0 & \hat{\mu} > \mu \end{cases} \quad (8.1)$$

2631 In the above equation,  $\mu$  is the value of the signal strength under test,  $\hat{\mu}$  is the best fit  $\mu$ ,  $\hat{\theta}$  is the best fit  
2632 value of the nuisance parameters,  $\hat{\theta}$  is the best fit value of the nuisance parameters under the fixed  $\mu$  value,  
2633 and  $L$  is the Poisson likelihood of the data (as described in section 3.6.2).

2634 The test statistic  $\widetilde{q}_\mu$  is constructed to protect against two interesting corner cases when setting the upper  
2635 limit on the cross section. First, it protects against negative signal strengths  $\mu$  which are unphysical. Second,  
2636 it does not count excesses in the data larger than those expected by a signal strength  $\mu$  as evidence against  
2637 the  $\mu$  hypothesis.

2638 The  $CL_s$  statistic is constructed by taking a ratio of two probabilities.  $CL_{s+b}$  is the probability that the  
2639 signal+background hypothesis would produce a value of the test statistic that is less than or equal to the  
2640 observed value<sup>1</sup>.  $CL_b$  is the probability that the background only hypothesis will produce a value  
2641 of the test statistic less than or equal to the observed. The  $CL_s$  statistic is the ratio  $CL_{s+b}/CL_b$ . A 95%  
2642 upper limit on the cross section is set at the value of  $\mu$  that makes the  $CL_s$  statistic less than 5%. In practice,  
2643 the limits are computed numerically within an asymptotic approximation for the distribution of the test  
2644 statistic  $\widetilde{q}_\mu$ . The details of this approximation can be found in reference [76].

2645 The resolved and boosted analyses are combined using a very simple procedure rather than a full statis-  
2646 tical combination. For each mass point tested, the limit which gives the most stringent constraint is used.  
2647 This means that for mass points below 1.1 TeV the resolved signal region is used, while at and above this  
2648 point the combination of the orthogonal 3b and 4b boosted signal regions is used.

#### 2649 8.4.2 LIMIT SETTING RESULTS

2650 Figure 8.2 shows the combined 95% upper bounds as a function of mass for three different models:  $G_{KK}^*$   
2651 with  $c = 1$ ,  $G_{KK}^*$  with  $c = 2$ , and a narrow heavy scalar  $H$ .

---

<sup>1</sup>Lower values of  $\widetilde{q}_\mu$  mean better compatibility.

2652        The cross section of  $\sigma(pp \rightarrow G_{\text{KK}}^* \rightarrow hh \rightarrow b\bar{b}b\bar{b})$  with  $c = 1$  is constrained to be less than 70 fb  
2653        for masses in the range  $600 < m_{G_{\text{KK}}^*} < 3000$  GeV. For the RSG model with  $c = 2$ , cross sections limits  
2654        between 40 fb and 200 fb are set for the mass range of  $500 < m_{G_{\text{KK}}^*} < 3000$  GeV. Masses in the range  
2655        of  $475 < m_{G_{\text{KK}}^*} < 785$  GeV are excluded with  $c = 1$  (with an exclusion of the range 465 to 745 GeV  
2656        expected). Masses less than 980 GeV are excluded with  $c = 2$  (with an exclusion for masses less than  
2657        1 TeV expected).

2658        In the heavy Higgs model, the cross section upper limits for  $\sigma(pp \rightarrow H \rightarrow hh \rightarrow b\bar{b}b\bar{b})$  ranges from  
2659        30 to 300 fb in the mass range of  $500 < m_H < 3000$  GeV. The resolved analysis can also set an upper  
2660        limit on the Standard Model di-Higgs production cross section discussed in chapter 3. The upper limit on  
2661         $\sigma(pp \rightarrow hh \rightarrow b\bar{b}b\bar{b})$  in the Standard Model is constrained to be less than 1.22 pb.

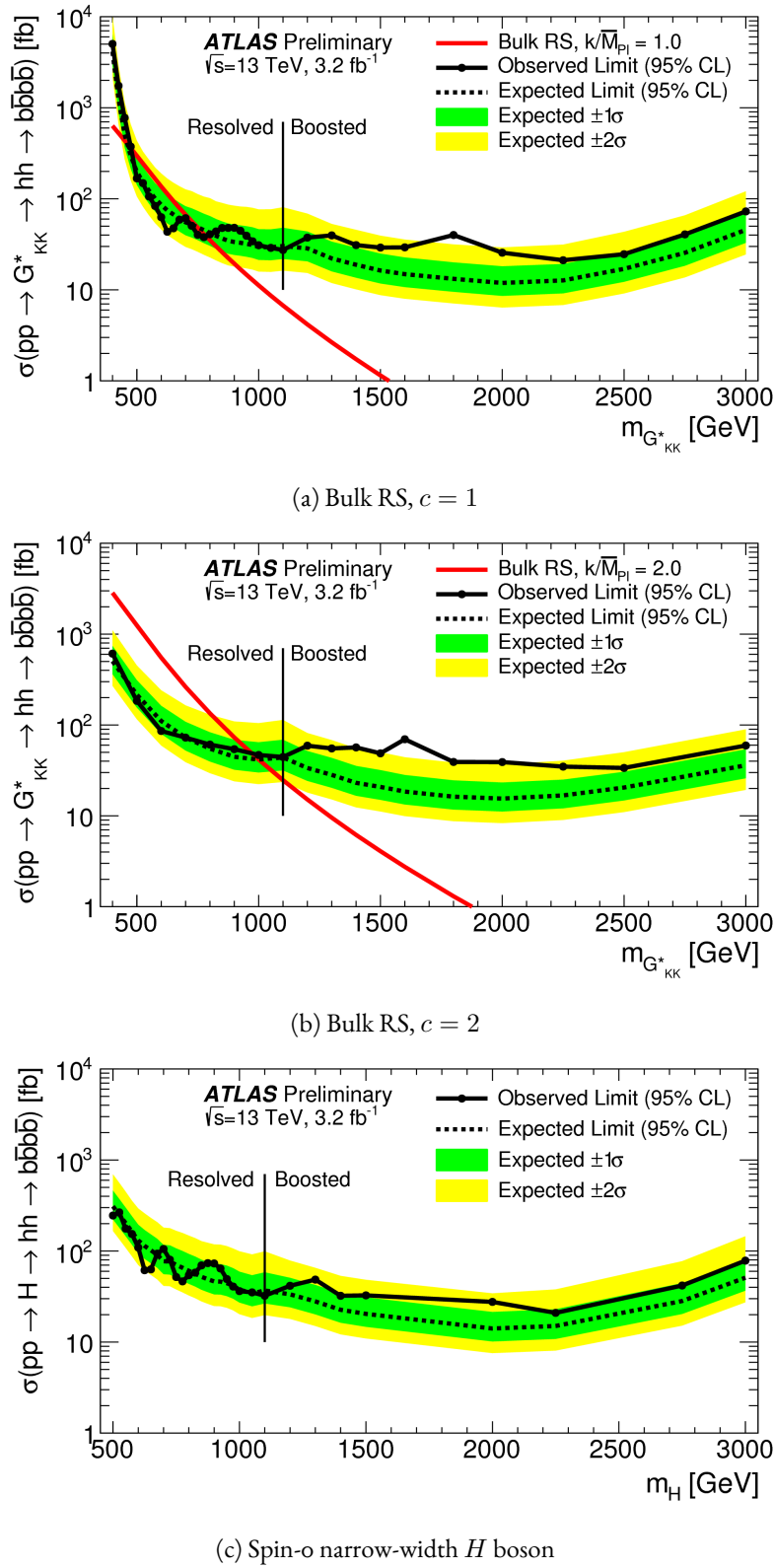


Figure 8.2: Expected and observed upper limit as a function of mass for  $G^*_{KK}$  in the RSG model with (a)  $c = 1$  and (b)  $c = 2$ , as well as (c)  $H$  with fixed  $\Gamma_H = 1$  GeV, at the 95% confidence level in the  $CL_s$  method [126].

2662

## Part IV

2663

## Looking ahead

# 9

2664

## Conclusion

2665

2666 After being sought for many years at different collider experiments, the Higgs boson was discovered by  
2667 the ATLAS and CMS experiments in 2012, confirming the leading theory for the source of electroweak  
2668 symmetry breaking and filling in the last missing piece of the Standard Model. After its discovery, mea-  
2669 surements of the particle's detailed properties and searches for new particles decaying to Higgs final states  
2670 were both extremely important in constraining physics beyond the Standard Model. This dissertation  
2671 presented this evolution through two results: the observation and measurement of the Higgs boson in the  
2672  $H \rightarrow WW^* \rightarrow \ell\nu\ell\nu$  channel at  $\sqrt{s} = 7$  TeV and  $\sqrt{s} = 8$  TeV and a search for Higgs pair production  
2673 in the  $HH \rightarrow b\bar{b}b\bar{b}$  channel at  $\sqrt{s} = 13$  TeV with the ATLAS detector in  $pp$  collisions at the Large  
2674 Hadron Collider.

2675 In the  $H \rightarrow WW^* \rightarrow \ell\nu\ell\nu$ , results from both the discovery of the Higgs boson and the full ATLAS  
2676 Run 1 dataset were presented. The Higgs boson was discovered with a  $5.9\sigma$  significance in a combination  
2677 of the  $H \rightarrow \gamma\gamma$ ,  $H \rightarrow ZZ \rightarrow 4\ell$ ,  $H \rightarrow WW^* \rightarrow \ell\nu\ell\nu$  with  $4.2 \text{ fb}^{-1}$  at  $\sqrt{s} = 7$  TeV and  $5.2 \text{ fb}^{-1}$  at

2678     $\sqrt{s} = 8$  TeV. With the full  $20.3 \text{ fb}^{-1}$  at  $\sqrt{s} = 8$  TeV and  $4.2 \text{ fb}^{-1}$  at  $\sqrt{s} = 7$  TeV, ATLAS achieved dis-  
2679    covery level significance in the  $H \rightarrow WW^*$  channel alone and obtained the first evidence of vector boson  
2680    fusion production in that channel. The combined signal strength was measured to be  $\mu = 1.09^{+0.23}_{-0.21}$ . The  
2681    total observed significance of the  $H \rightarrow WW^*$  process was observed to be  $6.1\sigma$  (with  $5.8\sigma$  expected). Ad-  
2682    vanced methods for background reduction and estimation, particularly in same-flavor lepton final states,  
2683    were shown. The VBF signal strength was measured to be  $\mu_{\text{VBF}} = 1.27^{+0.53}_{-0.45}$  with an observed signifi-  
2684    cance of  $3.2\sigma$  (with  $2.7\sigma$  expected).

2685    These results required many novel innovations. The increase of pileup interactions in the higher in-  
2686    stantaneous luminosity LHC conditions of 2012 led to a degradation of missing transverse momentum  
2687    resolution. As a result, the prominent  $Z/\gamma^* + \text{jets}$  background of the same flavor  $H \rightarrow WW^* \rightarrow \ell\nu\ell\nu$   
2688    final states increased greatly. New variables, including a track-based missing transverse momentum and a  
2689    measurement of the balance between the dilepton system and recoiling jets, allowed for significant reduc-  
2690    tion of this background. In the VBF channel, selections were optimized to exploit the unique VBF final  
2691    state topology. Incorporating these variables into a boosted decision tree technique allowed the analysis  
2692    to exceed the  $3\sigma$  statistical significance threshold.

2693    After the end of Run 1, the results of Higgs measurements from ATLAS were combined with those  
2694    from CMS to produce the most precise measurements of the Higgs boson so far [131]. Figure 9.1 shows the  
2695    combination of ATLAS and CMS data for the Higgs signal strength in and coupling measurements. In the  
2696    signal strength measurements of gluon fusion and vector boson fusion, the  $H \rightarrow WW^*$  channel provides  
2697    the tightest constraints. Additionally, the Higgs coupling to  $W$  bosons is the most precisely measured with  
2698    a relative uncertainty of 10%.

2699    With the discovery of the Higgs firmly established and its properties measured, a natural next step was  
2700    to search for new physics with Higgs final states. At  $\sqrt{s} = 13$  TeV, a search for Higgs pair production  
2701    in the  $b\bar{b}b\bar{b}$  final state with  $3.2 \text{ fb}^{-1}$  was conducted. A signal region optimized for the boosted final states  
2702    arising from high mass resonances was constructed. This signal region utilized large-radius calorimeter jets  
2703    and  $b$ -tagging with small radius track jets to maximize the signal acceptance. No significant excesses were  
2704    observed, and upper limits on cross sections are placed for spin-2 Randall Sundrum gravitons (RSG) and

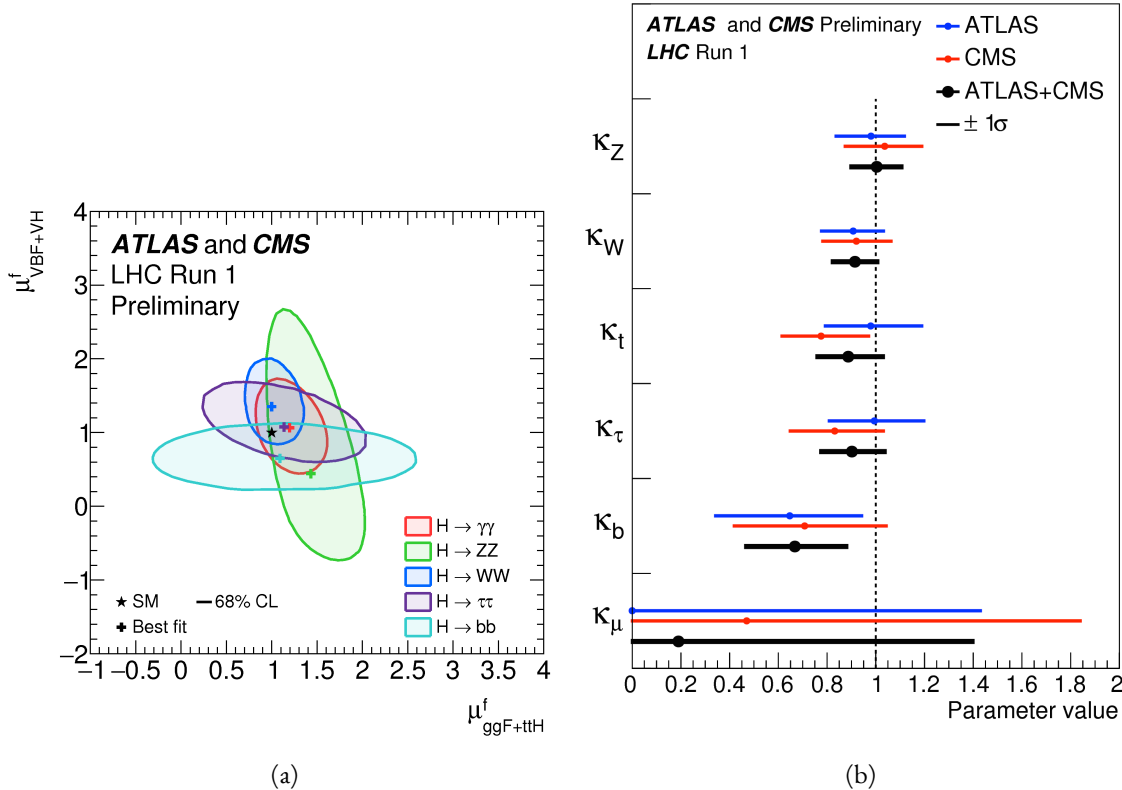


Figure 9.1: Combined ATLAS and CMS measurements in Run 1 for (a) Higgs signal strength in gluon fusion and VBF and (b) Higgs couplings normalized to their SM predictions

heavy narrow scalar resonances. The increase in center of mass energy in Run 2 allowed this analysis to quote upper cross section up to masses 3 TeV, while previous results from ATLAS in Run 1 only quote limits up to 2 TeV. The cross section of  $\sigma(pp \rightarrow G_{KK}^* \rightarrow hh \rightarrow b\bar{b}b\bar{b})$  with  $k/\bar{M}_{\text{Pl}} = 1$  was constrained to be less than 70 fb for masses in the range  $600 < m_{G_{KK}^*} < 3000$  GeV. For the RSG model with  $k/\bar{M}_{\text{Pl}} = 2$ , cross sections limits between 40 fb and 200 fb are set for the mass range of  $500 < m_{G_{KK}^*} < 3000$  GeV. The cross section upper limits for  $\sigma(pp \rightarrow H \rightarrow hh \rightarrow b\bar{b}b\bar{b})$  ranges from 30 to 300 fb in the mass range of  $500 < m_H < 3000$  GeV.

While there has been a rigorous program of measurements and searches involving the Higgs, there is still much room for improvement at the High Luminosity LHC (HL-LHC) and beyond. The measured signal strength for VBF production in  $H \rightarrow WW^*$  still has a relative error at the level of 40%, largely dominated by statistical uncertainty. Projections for the HL-LHC show that the uncertainty on the VBF signal strength can be reduced to approximately 15% with  $3000 \text{ fb}^{-1}$  [132, 133]. This projection also assumes

2717 that theoretical uncertainties on the signal, which would be the largest contribution in the future dataset,  
 2718 remain as they are now. Improvements in the theoretical understanding of the Higgs signal would also  
 2719 reduce the signal strength uncertainty dramatically. Such precision results allow for measurements of the  
 2720 Higgs coupling to vector bosons precise to the few percent level, therefore giving much power to constrain  
 2721 or discover new physics.

2722 The prospects for detection of beyond the Standard Model resonant di-Higgs production at the HL-  
 2723 LHC are also quite promising. Figure 9.2 shows projections for the discovery significance of RSG signals at  
 2724 the HL-LHC in the  $X \rightarrow HH \rightarrow b\bar{b}b\bar{b}$  search [133]. In all detector budget scenarios, a 1.5 TeV resonance  
 is above or near  $5\sigma$  significance, while a 2 TeV resonance is between  $4-5\sigma$  except for the lowest budget.

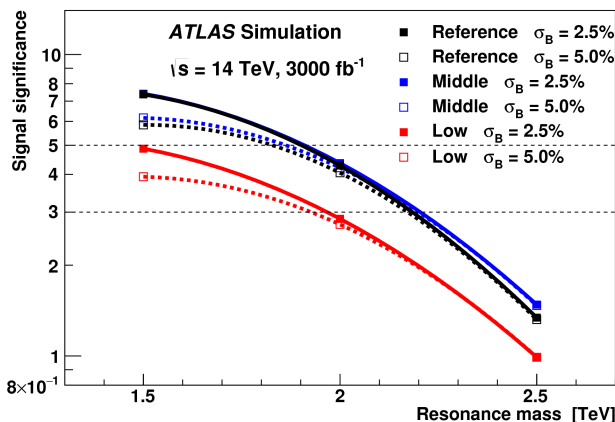


Figure 9.2: Discovery significance for RSG models at the HL-LHC in three different budget scenarios [133].  
 Systematic uncertainties on the background prediction ( $\sigma_B$ ) of 2.5% and 5.0% are both tested.

2725  
 2726 The Higgs will continue to be an incredibly powerful tool in the understanding of nature at the HL-  
 2727 LHC and beyond. Through both precision measurements and searches, the nature of electroweak symme-  
 2728 try breaking will be better understood and the potential for the discovery of physics beyond the Standard  
 2729 Model has never been greater.

# A

2730

2731

## *b*-tagging performance at high $p_T$

2732 One of the limiting factors of the signal acceptance in the  $X \rightarrow HH \rightarrow b\bar{b}b\bar{b}$  search at high resonance  
2733 masses is the degradation of the *b*-tagging efficiency for high  $p_T$  jets. This appendix presents a study of the  
2734 underlying causes of this degradation.

### 2735 A.I CHANGES IN MV<sub>2</sub> SCORE AT HIGH $p_T$

2736 The degradation of *b*-tagging at high  $p_T$  was studied in particular in the context of RSG models at high  
2737 mass. Figure A.i shows the  $p_T$  of the leading track jet inside of the leading calorimeter jet in RSG events.  
2738 At high  $m_{G_{KK}^*}$ , the  $p_T$  spectrum of track jets is much harder than at lower masses due to the increased  
2739 Higgs  $p_T$ .

2740 Figure A.2 shows the MV<sub>2c2o</sub> algorithm score for the leading and subleading track jets inside of the  
2741 leading calorimeter jet. In both cases, it can be seen that at higher RSG masses the MV<sub>2</sub> score shifts towards  
2742 more background like (negative) values. Additionally, this effect is more pronounced in the leading track

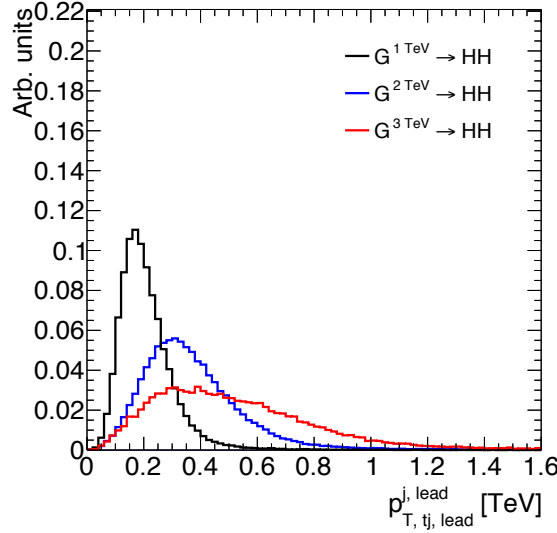


Figure A.1:  $p_T$  of the leading track jet in the leading calorimeter jet for different signal masses in RSG  $c = 1$  models

<sup>2743</sup> jet than the subleading.

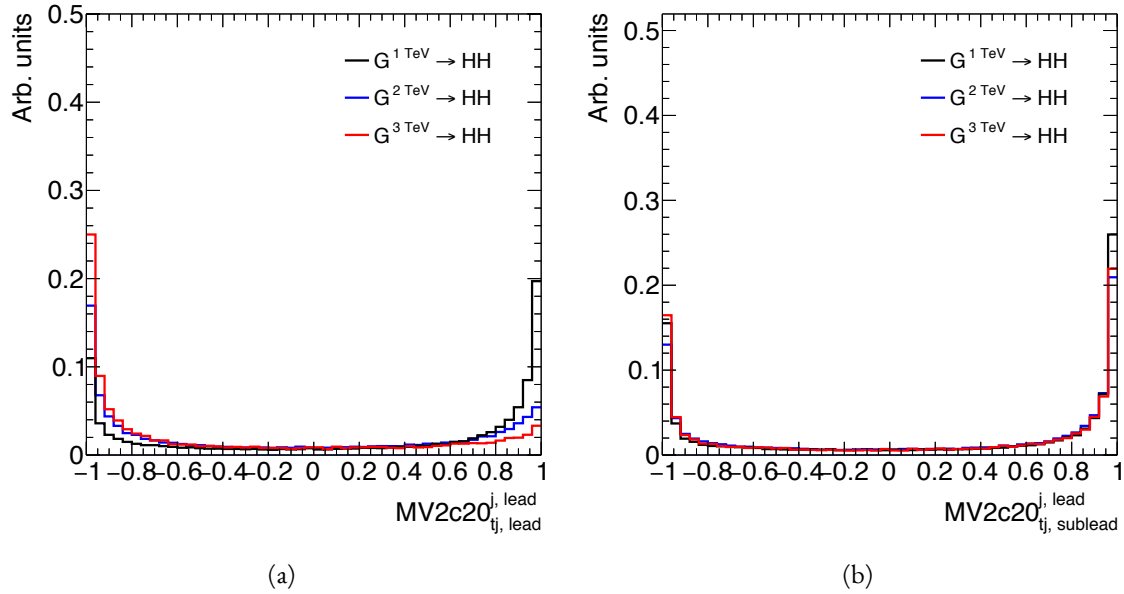


Figure A.2: MV2c20 score for the leading track jet (a) and subleading track jet (b) of the leading calorimeter jet for different signal masses in RSG  $c = 1$  models

<sup>2744</sup> To understand what is causing this change in the MV2c20 score, the same comparisons can be made for  
<sup>2745</sup> the input variables of MV2c20. The focus in these comparisons will be on the leading track jet as this is the  
<sup>2746</sup> one seen to have the largest difference in MV2 score. Figure A.3 shows the log likelihood ratio  $\log(p_b/p_u)$

2747 from the IP<sub>3</sub>D (three dimensional impact parameter) algorithm. At higher masses, the IP<sub>3</sub>D likelihood  
 2748 ratio distribution does become more background-like.

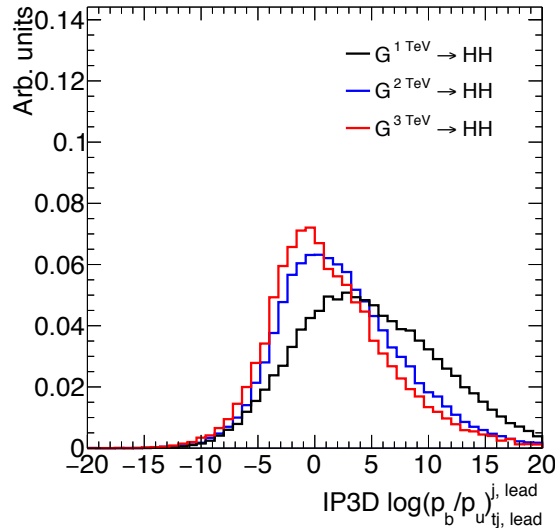


Figure A.3: IP<sub>3</sub>D log-likelihood ratio ( $\log(p_b/p_u)$ ) of the leading track jet in the leading calorimeter jet for different signal masses in RSG  $c = 1$  models

2749 Figure A.4 shows the mass and number of tracks at the secondary vertex computed by the SV1 algorithm.  
 2750 When there is no secondary vertex found, the algorithm assigns a default negative value for these quantities.  
 2751 Both of these distributions show that there is a significantly larger fraction of jets where no secondary vertex  
 2752 is found in the high mass samples compared to the  $m_{G_{KK}^*} = 1$  TeV sample. The SV1 algorithm's inability  
 2753 to find a secondary vertex could be an important factor in the overall MV<sub>2</sub> score shift, as this eliminates  
 2754 eight of the input variables that would normally contribute information to the algorithm.

2755 Figure A.5 shows the same quantities for the JetFitter algorithm. In this case, there is also a change in  
 2756 the fraction of jets which have their secondary vertices successfully reconstructed, but this change is not as  
 2757 drastic as that seen in SV1. There is also an increase in the number of jets which have high values of mass.

## 2758 A.2 EFFECT OF MULTIPLE $b$ -QUARKS INSIDE ONE JET

2759 One hypothesis for why the efficiency of  $b$ -tagging the leading track jet degrades is that at high masses, the  
 2760  $b$  quarks get close enough together that both of them are inside of the leading track jet. Because MV<sub>2</sub> is not

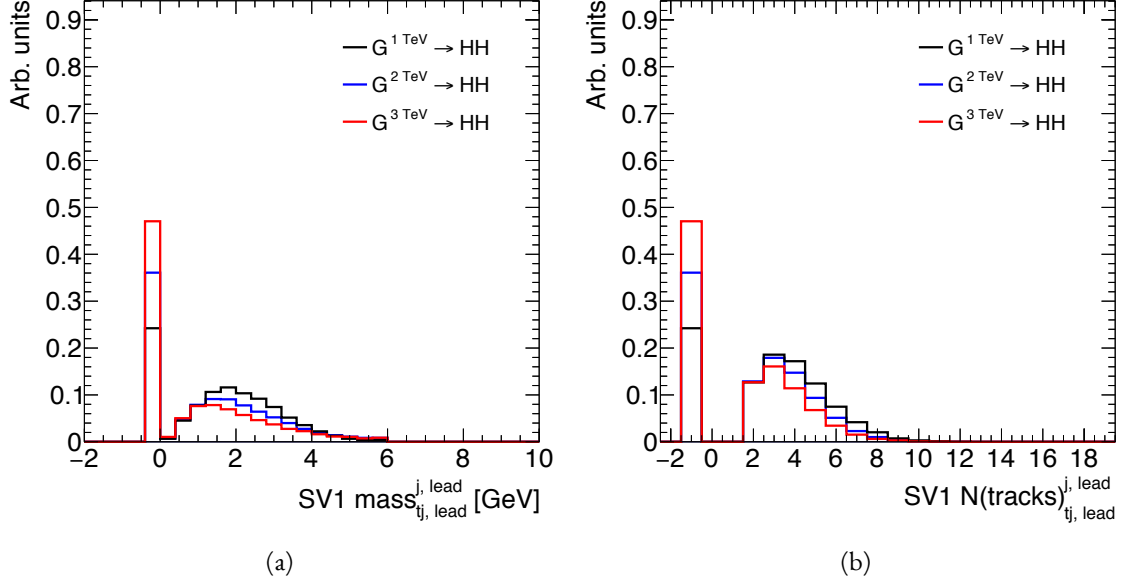


Figure A.4: Mass (a) and number of tracks (b) for the secondary vertices computed with the SV1 algorithm. When no secondary vertex is found, the quantities are assigned to default negative values.

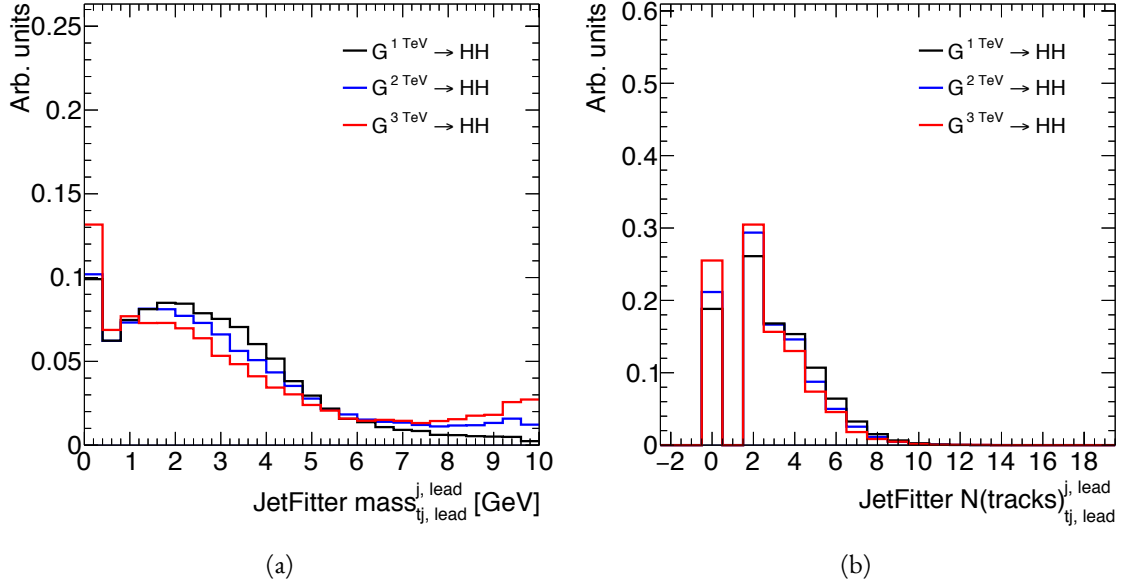


Figure A.5: Mass (a) and number of tracks (b) for vertices computed with the JetFitter algorithm. When no vertices are found, the quantities are assigned to default negative values.

<sup>2761</sup> tuned for tagging multiple  $b$  quarks inside one jet, the tagging efficiency could degrade. Figure A.6 shows  
<sup>2762</sup> MV2 scores and SV1 mass for cases where there are two  $b$  quarks at truth level within the radius of the

leading track jet compared to cases where there is only one true  $b$ <sup>1</sup>. This figure suggests that the presence

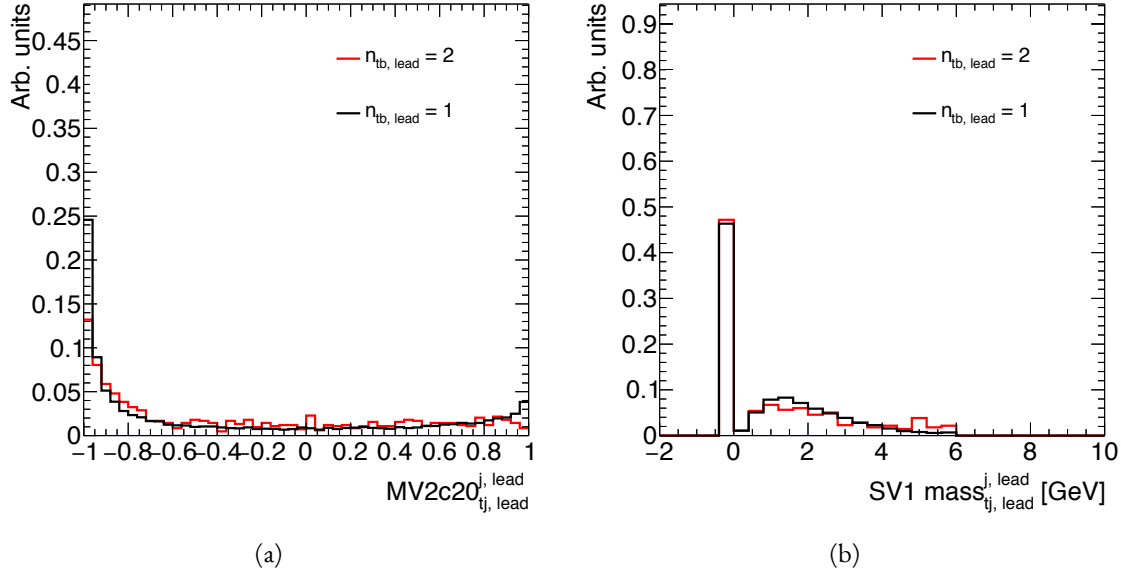


Figure A.6: MV<sub>2</sub>c20 score (a) and SV1 mass (b) for leading track jets with two truth  $b$  quarks ( $n_{tb, \text{lead}} = 2$ ) compared to those with only one truth  $b$  ( $n_{tb, \text{lead}} = 1$ ).

of two  $b$ -quarks inside the leading jet is not the cause of the degradation in efficiency. There is a change in the shape of the MV<sub>2</sub> score distribution, but it is not nearly as pronounced as that seen in A.2 at higher masses. Additionally, the fraction of jets with no secondary vertex found is nearly identical in the track jets with two truth  $b$ -quarks.

### A.3 CHANGES IN TRACK QUALITY AT HIGH $p_T$

Another hypothesis for the degradation of the  $b$ -tagging efficiency is a decrease in track quality for high  $p_T$   $b$  jets. One way to check the overall quality of the tracking inside the jet is to investigate quantities related to the leading track inside of the track jet. Figure A.7 shows the fit  $\chi^2/n_{\text{DOF}}$  and number of hits in the pixel detector for the leading track of the leading track jet. In both cases, the figure shows that in higher mass samples, the quality of the leading track inside of the track jet degrades substantially. The fit quality is lessened and the tracks have less hits in the pixel detector. This is likely due to the fact that at higher  $p_T$ ,

<sup>1</sup>When two truth  $b$  quarks are required in the leading jet, the subleading jet is required to have zero. When one is required for the leading, one is also required for the subleading.

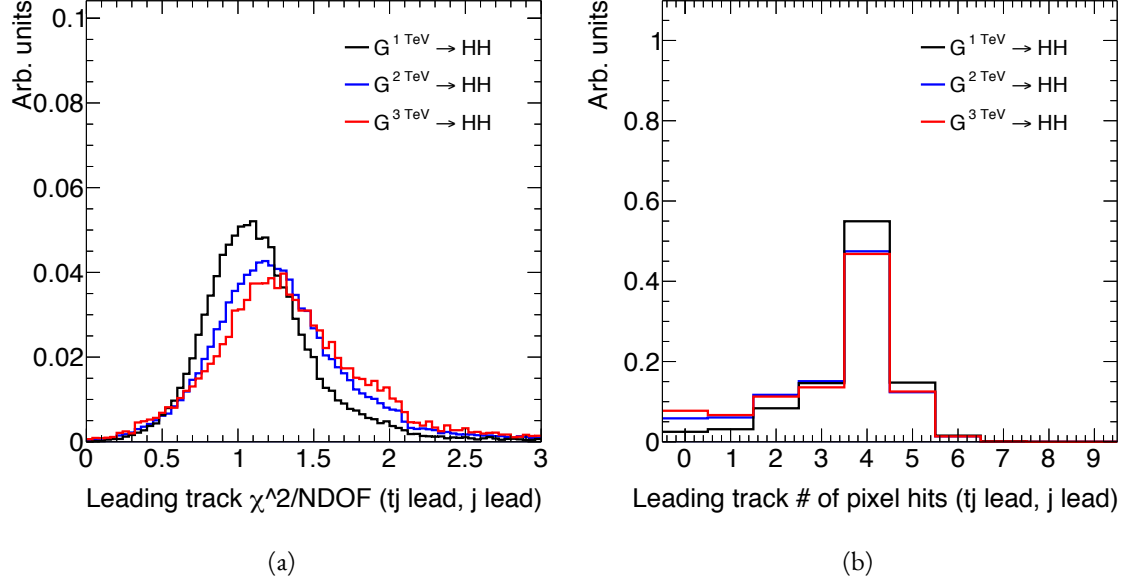


Figure A.7: Track fit  $\chi^2/\text{nDOF}$  (a) and number of pixel detector hits (b) for the leading track of the leading track jet in different mass RSG  $c = 1$  samples

the  $B$ -hadron will sometimes live long enough to miss the IBL and first pixel layer, thus decreasing the number of hits on the track.

To check whether this is the cause for the shift in the  $\text{MV}_2$  score and the higher difficulty in reconstructing secondary vertices, jets whose leading track have at least four pixel hits are compared with those whose tracks have less than four pixel hits. The results for the  $\text{MV}_2$  score and  $\text{SV}_1$  mass are shown in figure A.8. Track jets where the leading track does not have at least four pixel hits are more likely to not have a secondary vertex reconstructed. Additionally, their  $\text{MV}_{2c2o}$  score is shifted more significantly to background-like values. This seems to confirm the hypothesis that degrading track quality is responsible for the lowered  $b$ -tagging efficiency at high  $p_T$ .

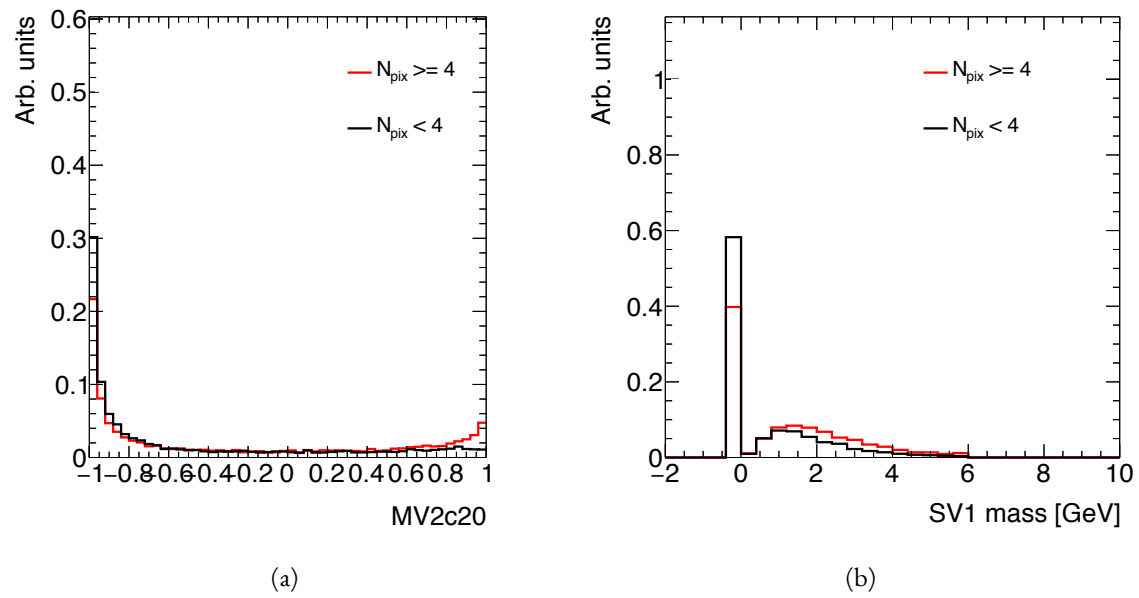


Figure A.8: MV<sub>2</sub>c<sub>20</sub> score (a) and SV<sub>1</sub> mass (b) for leading track jets whose leading track jet has at least four pixel hits ( $N_{\text{pix}} \geq 4$ ) compared to those which do not ( $N_{\text{pix}} < 4$ ).

# References

2784

- 2785 [1] Georges Aad et al. Observation of a new particle in the search for the Standard Model Higgs boson  
2786 with the ATLAS detector at the LHC. *Phys. Lett.*, B716:1–29, 2012. doi: 10.1016/j.physletb.2012.  
2787 08.020.
- 2788 [2] Serguei Chatrchyan et al. Observation of a new boson at a mass of 125 GeV with the CMS experi-  
2789 ment at the LHC. *Phys. Lett.*, B716:30–61, 2012. doi: 10.1016/j.physletb.2012.08.021.
- 2790 [3] David Griffiths. *Introduction to elementary particles*. 2008.
- 2791 [4] F. Halzen and Alan D. Martin. *QUARKS AND LEPTONS: AN INTRODUCTORY COURSE*  
2792 *IN MODERN PARTICLE PHYSICS*. 1984. ISBN 0471887412, 9780471887416.
- 2793 [5] Christopher G. Tully. *Elementary particle physics in a nutshell*. 2011.
- 2794 [6] K. A. Olive et al. Review of Particle Physics. *Chin. Phys.*, C38:090001, 2014. doi: 10.1088/1674-1137/  
2795 38/9/090001.
- 2796 [7] Matthew D. Schwartz. *Quantum Field Theory and the Standard Model*. Cambridge University  
2797 Press, 2014. ISBN 1107034736, 9781107034730. URL <http://www.cambridge.org/us/academic/subjects/physics/theoretical-physics-and-mathematical-physics/quantum-field-theory-and-standard-model>.
- 2800 [8] S. Dawson. Introduction to electroweak symmetry breaking. In *High energy physics and cosmology.*  
2801 *Proceedings, Summer School, Trieste, Italy, June 29-July 17, 1998*, pages 1–83, 1998. URL <http://alice.cern.ch/format/showfull?sysnb=0301862>.
- 2803 [9] S. L. Glashow. Partial Symmetries of Weak Interactions. *Nucl. Phys.*, 22:579–588, 1961. doi: 10.  
2804 1016/0029-5582(61)90469-2.
- 2805 [10] Steven Weinberg. A Model of Leptons. *Phys. Rev. Lett.*, 19:1264–1266, 1967. doi: 10.1103/  
2806 *PhysRevLett*.19.1264.
- 2807 [11] A. Salam. *Elementary Particle Theory*. Almqvist and Wiksell, Stockholm, 1968.
- 2808 [12] J. Iliopoulos S.L. Glashow and L. Maiani. *D2*:1285, 1970.
- 2809 [13] R. Keith Ellis, W. James Stirling, and B. R. Webber. *QCD and collider physics*. *Camb. Monogr.*  
2810 *Part. Phys. Nucl. Phys. Cosmol.*, 8:1–435, 1996.

- <sup>2811</sup> [14] P. W. Higgs. Broken symmetries and the masses of gauge bosons. *13*:508, 1964.
- <sup>2812</sup> [15] P. W. Higgs. Spontaneous symmetry breakdown without massless bosons. *145*:1156, 1966.
- <sup>2813</sup> [16] F. Englert and R. Brout. Broken symmetry and the mass of gauge vector mesons. *13*:321, 1964.
- <sup>2814</sup> [17] G. S. Guralnik, C. R. Hagen, and T. W. .B. Kibble. Global conservation laws and massless particles. *Phys. Rev. Lett.*, *13*:585, 1964. doi: [10.1103/PhysRevLett.13.585](https://doi.org/10.1103/PhysRevLett.13.585).
- <sup>2815</sup> [18] LHC Higgs Cross Section Working Group, S. Heinemeyer, C. Mariotti, G. Passarino, and R. Tanaka (Eds.). Handbook of LHC Higgs Cross Sections: 3. Higgs Properties. 2013.
- <sup>2816</sup> [19] Charalampos Anastasiou and Kirill Melnikov. Higgs boson production at hadron colliders in NNLO QCD. *Nucl. Phys.*, *B 646*:220, 2002. doi: [10.1016/S0550-3213\(02\)00837-4](https://doi.org/10.1016/S0550-3213(02)00837-4).
- <sup>2817</sup> [20] M. Spira, A. Djouadi, D. Graudenz, and P. M. Zerwas. Higgs boson production at the LHC. *Nucl. Phys.*, *B 453*:17, 1995. doi: [10.1016/0550-3213\(95\)00379-7](https://doi.org/10.1016/0550-3213(95)00379-7).
- <sup>2818</sup> [21] Giuseppe Degrassi and Fabio Maltoni. Two-loop electroweak corrections to Higgs production at hadron colliders. *Phys. Lett.*, *B 600*:255, 2004.
- <sup>2819</sup> [22] U. Aglietti, R. Bonciani, G. Degrassi, and A. Vicini. Master integrals for the two-loop light fermion contributions to  $gg \rightarrow H$  and  $H \rightarrow \gamma\gamma$ . *600*:57, 2004. doi: [10.1016/j.physletb.2004.09.001](https://doi.org/10.1016/j.physletb.2004.09.001).
- <sup>2820</sup> [23] D. de Florian and M. Grazzini. Higgs production at the LHC: updated cross sections at  $\sqrt{s} = 8$  TeV. *Phys. Lett.*, *B 718*:117, 2012.
- <sup>2821</sup> [24] P. Bolzoni, F. Maltoni, S.-O. Moch, and M. Zaro. Higgs production via vector-boson fusion at NNLO in QCD. *105*:011801, 2010. doi: [10.1103/PhysRevLett.105.011801](https://doi.org/10.1103/PhysRevLett.105.011801).
- <sup>2822</sup> [25] Tao Han, G. Valencia, and S. Willenbrock. Structure function approach to vector boson scattering in  $p p$  collisions. *Phys. Rev. Lett.*, *69*:3274–3277, 1992. doi: [10.1103/PhysRevLett.69.3274](https://doi.org/10.1103/PhysRevLett.69.3274).
- <sup>2823</sup> [26] Mariano Ciccolini, Ansgar Denner, and Stefan Dittmaier. Electroweak and QCD corrections to Higgs production via vector-boson fusion at the LHC. *Phys. Rev.*, *D 77*:013002, 2008. doi: [10.1103/PhysRevD.77.013002](https://doi.org/10.1103/PhysRevD.77.013002).
- <sup>2824</sup> [27] S. Catani, D. de Florian, M. Grazzini, and P. Nason. Soft-gluon re-summation for Higgs boson production at hadron colliders. *JHEP*, *0307*:028, 2003. doi: [10.1088/1126-6708/2003/07/028](https://doi.org/10.1088/1126-6708/2003/07/028).
- <sup>2825</sup> [28] Abdelhak Djouadi. The Anatomy of electro-weak symmetry breaking. I: The Higgs boson in the standard model. *Phys. Rept.*, *457*:1–216, 2008. doi: [10.1016/j.physrep.2007.10.004](https://doi.org/10.1016/j.physrep.2007.10.004).

- 2840 [29] J. Baglio, A. Djouadi, R. Gröber, M. M. Mühlleitner, J. Quevillon, and M. Spira. The mea-  
 2841 surement of the Higgs self-coupling at the LHC: theoretical status. *JHEP*, 04:151, 2013. doi:  
 2842 10.1007/JHEP04(2013)151.
- 2843 [30] Matthew J. Dolan, Christoph Englert, and Michael Spannowsky. New Physics in LHC Higgs boson  
 2844 pair production. *Phys. Rev.*, D87(5):055002, 2013. doi: 10.1103/PhysRevD.87.055002.
- 2845 [31] Roberto Contino, Margherita Ghezzi, Mauro Moretti, Giuliano Panico, Fulvio Piccinini, and An-  
 2846 drea Wulzer. Anomalous Couplings in Double Higgs Production. *JHEP*, 08:154, 2012. doi:  
 2847 10.1007/JHEP08(2012)154.
- 2848 [32] R. Grober and M. Mühlleitner. Composite Higgs Boson Pair Production at the LHC. *JHEP*, 06:  
 2849 020, 2011. doi: 10.1007/JHEP06(2011)020.
- 2850 [33] Lisa Randall and Raman Sundrum. A Large mass hierarchy from a small extra dimension. *Phys.*  
 2851 *Rev. Lett.*, 83:3370–3373, 1999. doi: 10.1103/PhysRevLett.83.3370.
- 2852 [34] Kaustubh Agashe, Hooman Davoudiasl, Gilad Perez, and Amarjit Soni. Warped Gravitons at the  
 2853 LHC and Beyond. *Phys. Rev.*, D76:036006, 2007. doi: 10.1103/PhysRevD.76.036006.
- 2854 [35] A. Liam Fitzpatrick, Jared Kaplan, Lisa Randall, and Lian-Tao Wang. Searching for the Kaluza-  
 2855 Klein Graviton in Bulk RS Models. *JHEP*, 09:013, 2007. doi: 10.1088/1126-6708/2007/09/013.
- 2856 [36] Julien Baglio, Otto Eberhardt, Ulrich Nierste, and Martin Wiebusch. Benchmarks for Higgs Pair  
 2857 Production and Heavy Higgs boson Searches in the Two-Higgs-Doublet Model of Type II. *Phys.*  
 2858 *Rev.*, D90(1):015008, 2014. doi: 10.1103/PhysRevD.90.015008.
- 2859 [37] G. C. Branco, P. M. Ferreira, L. Lavoura, M. N. Rebelo, Marc Sher, and Joao P. Silva. Theory and  
 2860 phenomenology of two-Higgs-doublet models. *Phys. Rept.*, 516:1–102, 2012. doi: 10.1016/j.physrep.  
 2861 2012.02.002.
- 2862 [38] Howard E. Haber and Oscar Stål. New LHC benchmarks for the  $\mathcal{CP}$ -conserving two-Higgs-  
 2863 doublet model. *Eur. Phys. J.*, C75(10):491, 2015. doi: 10.1140/epjc/s10052-015-3697-x.
- 2864 [39] Jose M. No and Michael Ramsey-Musolf. Probing the Higgs Portal at the LHC Through Resonant  
 2865 di-Higgs Production. *Phys. Rev.*, D89(9):095031, 2014. doi: 10.1103/PhysRevD.89.095031.
- 2866 [40] Johan Alwall, Michel Herquet, Fabio Maltoni, Olivier Mattelaer, and Tim Stelzer. MadGraph  
 2867 5:Going Beyond. *JHEP*, 1106:128, 2011. doi: 10.1007/JHEP06(2011)128.
- 2868 [41] Oleg Antipin, Tuomas Hapola. CP3 Origins implementation of Randall-Sundrum model. 2013,  
 2869 URL <http://cp3-origins.dk/research/units/ed-tools>.

- 2870 [42] Georges Aad et al. Constraints on new phenomena via Higgs boson couplings and invisible decays  
 2871 with the ATLAS detector. *JHEP*, 11:206, 2015. doi: 10.1007/JHEP11(2015)206.
- 2872 [43] Lyndon R Evans and Philip Bryant. LHC Machine. *J. Instrum.*, 3:S08001, 164 p, 2008. URL  
 2873 <https://cds.cern.ch/record/1129806>. This report is an abridged version of the LHC De-  
 2874 sign Report (CERN-2004-003).
- 2875 [44] ATLAS Collaboration. The ATLAS experiment at the CERN Large Hadron Collider. *JINST*, 3:  
 2876 S08003, 2008. doi: 10.1088/1748-0221/3/08/S08003.
- 2877 [45] CMS Collaboration. The cms experiment at the cern lhc. *Journal of Instrumentation*, 3(08):S08004,  
 2878 2008. URL <http://stacks.iop.org/1748-0221/3/i=08/a=S08004>.
- 2879 [46] LHCb Collaoration. The LHCb Detector at the LHC. *JINST*, 3:S08005, 2008. doi: 10.1088/  
 2880 1748-0221/3/08/S08005.
- 2881 [47] ALICE Collaboration. The alice experiment at the cern lhc. *Journal of Instrumentation*, 3(08):  
 2882 S08002, 2008. URL <http://stacks.iop.org/1748-0221/3/i=08/a=S08002>.
- 2883 [48] Lyndon Evans. The Large Hadron Collider. In Holstein, BR and Haxton, WC and Jawah-  
 2884 ery, A, editor, *ANNUAL REVIEW OF NUCLEAR AND PARTICLE SCIENCE, VOL*  
 2885 *61*, volume 61 of *Annual Review of Nuclear and Particle Science*, pages 435–466. 2011. doi:  
 2886 {10.1146/annurev-nucl-102010-130438}.
- 2887 [49] ATLAS Collaboration. Luminosity Determination in  $pp$  Collisions at  $\sqrt{s} = 7$  TeV Using the  
 2888 ATLAS Detector at the LHC. *Eur. Phys. J.*, C 71:1630, 2011. doi: 10.1140/epjc/s10052-011-1630-5.
- 2889 [50] Mike Lamont for the LHC team. The First Years of LHC Operation for Luminosity Production.  
 2890 International Particle Accelerator Conference, 2013. URL <https://accelconf.web.cern.ch/>  
 2891 [accelconf/IPAC2013/talks/moyab101\\_talk.pdf](https://accelconf/IPAC2013/talks/moyab101_talk.pdf).
- 2892 [51] Paul Collier for the LHC team. LHC Machine Status. CERN Resource Review Board, 2015. URL  
 2893 <https://cds.cern.ch/record/2063924/files/CERN-RRB-2015-119.PDF>.
- 2894 [52] Track Reconstruction Performance of the ATLAS Inner Detector at  $\sqrt{s} = 13$  TeV. Technical  
 2895 Report ATL-PHYS-PUB-2015-018, CERN, Geneva, Jul 2015. URL <http://cds.cern.ch/>  
 2896 [record/2037683](https://cds.cern.ch/record/2037683).
- 2897 [53] M Capeans, G Darbo, K Einsweiller, M Elsing, T Flick, M Garcia-Sciveres, C Gemme, H Perneg-  
 2898 ger, O Rohne, and R Vuillermet. ATLAS Insertable B-Layer Technical Design Report. Technical  
 2899 Report CERN-LHCC-2010-013, ATLAS-TDR-19, CERN, Geneva, Sep 2010. URL <https://cds.cern.ch/>  
 2900 [record/1291633](https://cds.cern.ch/record/1291633).

- 2901 [54] ATLAS Collaboration. ATLAS Trigger Operations Public Results. 2015. URL <https://twiki.cern.ch/twiki/bin/view/AtlasPublic/TriggerOperationPublicResults>.
- 2902
- 2903 [55] ATLAS Collaboration. ATLAS Luminosity Public Results, Run 1. 2012. URL <https://twiki.cern.ch/twiki/bin/view/AtlasPublic/LuminosityPublicResults>.
- 2904
- 2905 [56] ATLAS Collaboration. ATLAS Luminosity Public Results, Run 2. 2015. URL <https://twiki.cern.ch/twiki/bin/view/AtlasPublic/LuminosityPublicResultsRun2>.
- 2906
- 2907 [57] T Kawamoto, S Vlachos, L Pontecorvo, J Dubbert, G Mikenberg, P Iengo, C Dallapiccola, C Amelung, L Levinson, R Richter, and D Lellouch. New Small Wheel Technical Design Report. Technical Report CERN-LHCC-2013-006. ATLAS-TDR-020, CERN, Geneva, Jun 2013.
- 2908
- 2909 URL <https://cds.cern.ch/record/1552862>. ATLAS New Small Wheel Technical Design
- 2910 Report.
- 2911
- 2912 [58] Y. Giomataris, Ph. Rebours, J.P. Robert, and G. Charpak. Micromegas: a high-granularity position-sensitive gaseous detector for high particle-flux environments. *Nuclear Instruments and Methods in Physics Research Section A: Accelerators, Spectrometers, Detectors and Associated Equipment*, 376(1):29 – 35, 1996. ISSN 0168-9002. doi: [http://dx.doi.org/10.1016/0168-9002\(96\)00175-1](http://dx.doi.org/10.1016/0168-9002(96)00175-1). URL <http://www.sciencedirect.com/science/article/pii/0168900296001751>.
- 2913
- 2914
- 2915
- 2916
- 2917
- 2918 [59] T. Alexopoulos, J. Burnens, R. de Oliveira, G. Glonti, O. Pizzirussi, V. Polychronakos, G. Sekhniadze, G. Tsipolitis, and J. Wotschack. A spark-resistant bulk-micromegas chamber for high-rate applications. *Nuclear Instruments and Methods in Physics Research Section A: Accelerators, Spectrometers, Detectors and Associated Equipment*, 640(1):110 – 118, 2011. ISSN 0168-9002. doi: <http://dx.doi.org/10.1016/j.nima.2011.03.025>. URL <http://www.sciencedirect.com/science/article/pii/S0168900211005869>.
- 2919
- 2920
- 2921
- 2922
- 2923
- 2924 [60] Joao Pequenao and Paul Schaffner. An computer generated image representing how ATLAS detects particles. Jan 2013. URL <https://cds.cern.ch/record/1505342>.
- 2925
- 2926
- 2927
- 2928
- 2929 [61] Improved electron reconstruction in ATLAS using the Gaussian Sum Filter-based model for bremsstrahlung. Technical Report ATLAS-CONF-2012-047, CERN, Geneva, May 2012. URL <https://cds.cern.ch/record/1449796>.
- 2930
- 2931
- 2932 [62] Electron efficiency measurements with the ATLAS detector using the 2012 LHC proton-proton collision data. Technical Report ATLAS-CONF-2014-032, CERN, Geneva, Jun 2014. URL <https://cds.cern.ch/record/1706245>.
- 2933
- 2934 [63] Georges Aad et al. Electron and photon energy calibration with the ATLAS detector using LHC Run 1 data. *Eur. Phys. J.*, C74(10):3071, 2014. doi: 10.1140/epjc/s10052-014-3071-4.

- 2934 [64] Georges Aad et al. Measurement of the muon reconstruction performance of the ATLAS detector  
 2935 using 2011 and 2012 LHC proton–proton collision data. *Eur. Phys. J.*, C74(11):3130, 2014. doi:  
 2936 10.1140/epjc/s10052-014-3130-x.
- 2937 [65] Georges Aad et al. Muon reconstruction performance of the ATLAS detector in proton–proton  
 2938 collision data at  $\sqrt{s}=13$  TeV. 2016.
- 2939 [66] W Lampl, S Laplace, D Lelas, P Loch, H Ma, S Menke, S Rajagopalan, D Rousseau, S Snyder,  
 2940 and G Unal. Calorimeter Clustering Algorithms: Description and Performance. Technical Re-  
 2941 port ATL-LARG-PUB-2008-002. ATL-COM-LARG-2008-003, CERN, Geneva, Apr 2008. URL  
 2942 <https://cds.cern.ch/record/1099735>.
- 2943 [67] Georges Aad et al. Topological cell clustering in the ATLAS calorimeters and its performance in  
 2944 LHC Run 1. 2016.
- 2945 [68] Matteo Cacciari, Gavin P. Salam, and Gregory Soyez. The Anti- $k(t)$  jet clustering algorithm. *JHEP*,  
 2946 04:063, 2008. doi: 10.1088/1126-6708/2008/04/063.
- 2947 [69] Monte Carlo Calibration and Combination of In-situ Measurements of Jet Energy Scale, Jet Energy  
 2948 Resolution and Jet Mass in ATLAS. Technical Report ATLAS-CONF-2015-037, CERN, Geneva,  
 2949 Aug 2015. URL <http://cds.cern.ch/record/2044941>.
- 2950 [70] Georges Aad et al. Performance of  $b$ -Jet Identification in the ATLAS Experiment. 2015.
- 2951 [71] Expected performance of the ATLAS  $b$ -tagging algorithms in Run-2. Technical Report  
 2952 ATL-PHYS-PUB-2015-022, CERN, Geneva, Jul 2015. URL <http://cds.cern.ch/record/2037697>.
- 2953 [72] Georges Aad et al. Performance of Missing Transverse Momentum Reconstruction in Proton-  
 2954 Proton Collisions at 7 TeV with ATLAS. *Eur. Phys. J.*, C72:1844, 2012. doi: 10.1140/epjc/  
 2955 s10052-012-1844-6.
- 2956 [73] Performance of Missing Transverse Momentum Reconstruction in ATLAS studied in Proton-  
 2957 Proton Collisions recorded in 2012 at 8 TeV. Technical Report ATLAS-CONF-2013-082, CERN,  
 2958 Geneva, Aug 2013. URL <http://cds.cern.ch/record/1570993>.
- 2959 [74] ATLAS Collaboration. Observation and measurement of Higgs boson decays to  $WW^*$  with the  
 2960 ATLAS detector. *Phys. Rev. D*, 92(012006), 2015.
- 2961 [75] Aaron James Armbruster. Discovery of a Higgs Boson with the ATLAS detector. 2013. CERN-  
 2962 THESIS-2013-047.
- 2963 [76] G. Cowan, K. Cranmer, E. Gross, and O. Vitells. Asymptotic formulae for likelihood-based tests  
 2964 of new physics. *Eur. Phys. J.*, C71:1554, 2011. doi: 10.1140/epjc/s10052-011-1554-0.

- 2966 [77] R.K. Ellis, I. Hinchliffe, M. Soldate, and J.J. Van Der Bij. Higgs decay to  $\tau+\tau$ –a possible signature  
 2967 of intermediate mass higgs bosons at high energy hadron colliders. *Nuclear Physics B*, 297(2):221  
 2968 – 243, 1988. ISSN 0550-3213. doi: [http://dx.doi.org/10.1016/0550-3213\(88\)90019-3](http://dx.doi.org/10.1016/0550-3213(88)90019-3). URL <http://www.sciencedirect.com/science/article/pii/0550321388900193>.
- 2970 [78] ATLAS Collaboration. Limits on the production of the Standard Model Higgs Boson in  $pp$   
 2971 collisions at  $\sqrt{s} = 7$  TeV with the ATLAS detector. *Eur. Phys. J.*, C 71:1728, 2011. doi:  
 2972 [10.1140/epjc/s10052-011-1728-9](https://doi.org/10.1140/epjc/s10052-011-1728-9).
- 2973 [79] Leo Breiman, Jerome Friedman, Charles J Stone, and Richard A Olshen. *Classification and regres-*  
 2974 *sion trees*. CRC press, 1984.
- 2975 [80] Yoav Freund and Robert E Schapire. A decision-theoretic generalization of on-line learning and an  
 2976 application to boosting. *Journal of Computer and System Sciences*, 55(1):119 – 139, 1997. ISSN 0022-  
 2977 0000. doi: <http://dx.doi.org/10.1006/jcss.1997.1504>. URL <http://www.sciencedirect.com/science/article/pii/S002200009791504X>.
- 2979 [81] Jerome H. Friedman. Stochastic gradient boosting. *Computational Statistics and Data Analysis*, 38  
 2980 (4):367 – 378, 2002. ISSN 0167-9473. doi: [http://dx.doi.org/10.1016/S0167-9473\(01\)00065-2](http://dx.doi.org/10.1016/S0167-9473(01)00065-2). URL <http://www.sciencedirect.com/science/article/pii/S0167947301000652>. Non-  
 2981 linear Methods and Data Mining.
- 2983 [82] ATLAS Collaboration. Performance of the ATLAS muon trigger in  $pp$  collisions at  $\sqrt{s} = 8$  TeV.  
 2984 *Eur. Phys. J. C*, (arXiv:1408.3179. CERN-PH-EP-2014-154):75, 19 p, Aug 2014. URL <https://cds.cern.ch/record/1749694>.
- 2986 [83] ATLAS collaboration. Electron trigger performance in 2012 ATLAS data, 2015. ATLAS-COM-  
 2987 DAQ-2015-091.
- 2988 [84] Paolo Nason. A new method for combining NLO QCD with shower Monte Carlo algorithms.  
 2989 *JHEP*, 11:040, 2004.
- 2990 [85] B. P. Kersevan and E. Richter-Was. The Monte Carlo event generator AcerMC version 2.0 with  
 2991 interfaces to PYTHIA 6.2 and HERWIG 6.5. 2004.
- 2992 [86] Nikolas Kauer and Giampiero Passarino. Inadequacy of zero-width approximation for a light Higgs  
 2993 boson signal. 2012.
- 2994 [87] T. Gleisberg, Stefan Hoeche, F. Krauss, M. Schonherr, S. Schumann, et al. Event generation with  
 2995 SHERPA 1.1. *JHEP*, 0902:007, 2009. doi: <10.1088/1126-6708/2009/02/007>.
- 2996 [88] Michelangelo L. Mangano et al. ALPGEN, a generator for hard multiparton processes in hadronic  
 2997 collisions. *JHEP*, 0307:001, 2003. doi: <10.1088/1126-6708/2003/07/001>.

- 2998 [89] Torbjorn Sjostrand, Stephen Mrenna, and Peter Z. Skands. PYTHIA 6.4 Physics and Manual.  
 2999 *JHEP*, 0605:026, 2006. doi: [10.1088/1126-6708/2006/05/026](https://doi.org/10.1088/1126-6708/2006/05/026).
- 3000 [90] Torbjorn Sjostrand, Stephen Mrenna, and Peter Z. Skands. A Brief Introduction to PYTHIA 8.1.  
 3001 *Comput.Phys.Commun.*, 178:852–867, 2008. doi: [10.1016/j.cpc.2008.01.036](https://doi.org/10.1016/j.cpc.2008.01.036).
- 3002 [91] G. Corcella et al. HERWIG 6: An event generator for hadron emission reactions with interfering  
 3003 gluons (including super-symmetric processes). *JHEP*, 01:010, 2001. doi: [10.1088/1126-6708/2001/01/010](https://doi.org/10.1088/1126-6708/2001/01/010).
- 3005 [92] J. M. Butterworth, Jeffrey R. Forshaw, and M. H. Seymour. Multiparton interactions in photo-  
 3006 production at HERA. *Z. Phys.*, C 72:637, 1996. doi: [10.1007/s002880050286](https://doi.org/10.1007/s002880050286).
- 3007 [93] Jun Gao, Marco Guzzi, Joey Huston, Hung-Liang Lai, Zhao Li, et al. The CT10 NNLO Global  
 3008 Analysis of QCD. *Phys.Rev.*, D89:033009, 2014. doi: [10.1103/PhysRevD.89.033009](https://doi.org/10.1103/PhysRevD.89.033009).
- 3009 [94] P. M. Nadolsky. Implications of CTEQ global analysis for collider observables. *Phys. Rev.*, D 78:  
 3010 013004, 2008. doi: [10.1103/PhysRevD.78.013004](https://doi.org/10.1103/PhysRevD.78.013004).
- 3011 [95] A. Sherstnev and R. S. Thorne. Parton distributions for the LHC. *Eur. Phys. J.*, C 55:553, 2009. doi:  
 3012 [10.1140/epjc/s10052-008-0610-x](https://doi.org/10.1140/epjc/s10052-008-0610-x).
- 3013 [96] A. Bredenstein, Ansgar Denner, S. Dittmaier, and M. M. Weber. Precise predictions for the Higgs-  
 3014 boson decay  $H \rightarrow WW/ZZ \rightarrow 4$  leptons. *Phys. Rev.*, D74:013004, 2006.
- 3015 [97] A. Djouadi, J. Kalinowski, and M. Spira. HDECAY: A program for Higgs boson decays in the  
 3016 standard model and its supersymmetric extension. *Comput. Phys. Commun.*, 108:56, 1998. doi:  
 3017 [10.1016/S0010-4655\(97\)00123-9](https://doi.org/10.1016/S0010-4655(97)00123-9).
- 3018 [98] S. Agostinelli et al. GEANT4, a simulation toolkit. *Nucl. Instrum. Meth.*, A 506:250, 2003. doi:  
 3019 [10.1016/S0168-9002\(03\)01368-8](https://doi.org/10.1016/S0168-9002(03)01368-8).
- 3020 [99] Eilam Gross and Ofer Vitells. Transverse mass observables for charged Higgs boson searches at  
 3021 hadron colliders. *Phys. Rev.*, D81:055010, 2010. doi: [10.1103/PhysRevD.81.055010](https://doi.org/10.1103/PhysRevD.81.055010).
- 3022 [100] J. R. Andersen et al. Les Houches 2013: Physics at TeV Colliders: Standard Model Working Group  
 3023 Report. 2014.
- 3024 [101] I. Stewart and F. Tackmann. Theory uncertainties for Higgs mass and other searches using jet bins.  
 3025 *Phys. Rev.*, D 85:034011, 2012. doi: [10.1103/PhysRevD.85.034011](https://doi.org/10.1103/PhysRevD.85.034011).
- 3026 [102] ATLAS Collaboration. Luminosity Determination in  $pp$  Collisions at  $\sqrt{s} = 7$  TeV Using the  
 3027 ATLAS Detector at the LHC. *Eur. Phys. J.*, C 71:1630, 2011. doi: [10.1140/epjc/s10052-011-1630-5](https://doi.org/10.1140/epjc/s10052-011-1630-5).

- 3028 [103] Jet energy scale and its systematic uncertainty in proton-proton collisions at  $\sqrt{s} = 7$  tev with atlas  
 3029       2011 data. *ATLAS-CONF-2013-004*, 2013.
- 3030 [104] Calibrating the  $b$ -tag efficiency and mistag rate in  $35 \text{ pb}^{-1}$  of data with the atlas detector. *ATLAS-*  
 3031       *CONF-2011-089*, 2011.
- 3032 [105] ATLAS Collaboration. Measurement of the  $b$ -tag Efficiency in a Sample of Jets Containing Muons  
 3033       with  $5 \text{ fb}^{-1}$  of Data from the ATLAS Detector. *ATLAS-CONF-2012-043*, 2012. URL <http://cdsweb.cern.ch/record/1435197>.
- 3034 [106] ATLAS Collaboration. Calibration of  $b$ -tagging using dileptonic top pair events in a combinatorial  
 3035       likelihood approach with the ATLAS experiment. (ATLAS-CONF-2014-004), 2014. URL <http://cds.cern.ch/record/1664335>.
- 3038 [107] Georges Aad et al. Measurement of the Higgs boson mass from the  $H \rightarrow \gamma\gamma$  and  $H \rightarrow ZZ^* \rightarrow$   
 3039        $4\ell$  channels with the ATLAS detector using  $25 \text{ fb}^{-1}$  of  $pp$  collision data. *Phys. Rev.*, D90(5):052004,  
 3040       2014. doi: 10.1103/PhysRevD.90.052004.
- 3041 [108] Georges Aad et al. Measurements of the Higgs boson production and decay rates and coupling  
 3042       strengths using  $pp$  collision data at  $\sqrt{s} = 7$  and  $8$  TeV in the ATLAS experiment. *Eur. Phys. J.*,  
 3043       C76(1):6, 2016. doi: 10.1140/epjc/s10052-015-3769-y.
- 3044 [109] W.J. Stirling.  $7/8$  and  $13/8$  TeV LHC luminosity ratios. 2013. URL [http://www.hep.ph.ic.ac.uk/~wstirlin/plots/lhclumi7813\\_2013\\_v0.pdf](http://www.hep.ph.ic.ac.uk/~wstirlin/plots/lhclumi7813_2013_v0.pdf).
- 3046 [110] J Alison. Experimental Studies of hh. Oct 2014. URL <http://cds.cern.ch/record/1952581>.
- 3047 [111] J. Alwall et al. The automated computation of tree-level and next-to-leading order differential cross  
 3048       sections, and their matching to parton shower simulations. *JHEP*, 07:079, 2014.
- 3049 [112] Richard D. Ball et al. Parton distributions with LHC data. *Nucl. Phys. B*, 867:244, 2013.
- 3050 [113] ATLAS Collaboration. ATLAS Run 1 Pythia8 tunes. (ATL-PHYS-PUB-2014-021), Nov 2014.  
 3051       URL <https://cds.cern.ch/record/1966419>.
- 3052 [114] M. Bahr et al. Herwig++ Physics and Manual. *Eur. Phys. J. C*, 58:639–707, 2008. doi: 10.1140/  
 3053       epjc/s10052-008-0798-9.
- 3054 [115] Stefan Gieseke, Christian Rohr, and Andrzej Siódmiok. Colour reconnections in Herwig++. *Eur.*  
 3055       *Phys. J. C*, 72:2225, 2012. doi: 10.1140/epjc/s10052-012-2225-5.
- 3056 [116] Simone Alioli, Paolo Nason, Carlo Oleari, and Emanuele Re. A general framework for implement-  
 3057       ing NLO calculations in shower Monte Carlo programs: the POWHEG BOX. *JHEP*, 06:043,  
 3058       2010.

- 3059 [117] Peter Zeiler Skands. Tuning Monte Carlo Generators: The Perugia Tunes. *Phys. Rev. D*, 82:074018,  
 3060 2010. doi: 10.1103/PhysRevD.82.074018.
- 3061 [118] Michal Czakon and Alexander Mitov. Top++: A Program for the Calculation of the Top-Pair  
 3062 Cross-Section at Hadron Colliders. 2011.
- 3063 [119] Baojia (Tony) Tong. Private communication.
- 3064 [120] D. Krohn, J. Thaler, and L.-T. Wang. Jet Trimming. *JHEP*, 02:084, 2010. doi: 10.1007/  
 3065 JHEP02(2010)084.
- 3066 [121] ATLAS Collaboration. Identification of Boosted, Hadronically Decaying W Bosons and Compar-  
 3067 isons with ATLAS Data Taken at  $\sqrt{s} = 8$  TeV. 2015.
- 3068 [122] Expected Performance of Boosted Higgs ( $\rightarrow b\bar{b}$ ) Boson Identification with the ATLAS Detector  
 3069 at  $\sqrt{s} = 13$  TeV. Technical Report ATL-PHYS-PUB-2015-035, CERN, Geneva, Aug 2015. URL  
 3070 <https://cds.cern.ch/record/2042155>.
- 3071 [123] Flavor Tagging with Track Jets in Boosted Topologies with the ATLAS Detector. Technical Report  
 3072 ATL-PHYS-PUB-2014-013, CERN, Geneva, Aug 2014. URL <https://cds.cern.ch/record/1750681>.
- 3073 [124] Matteo Cacciari and Gavin P. Salam. Pileup subtraction using jet areas. *Phys. Lett. B*, 659:119, 2008.  
 3075 doi: 10.1016/j.physletb.2007.09.077.
- 3076 [125] Glen Cowan, Eilam Gross. Discovery significance with statistical uncertainty in the background  
 3077 estimate. 2008. URL <http://www.pp.rhul.ac.uk/~cowan/stat/notes/SigCalcNote.pdf>.
- 3078 [126] Search for pair production of Higgs bosons in the  $b\bar{b}b\bar{b}$  final state using proton-proton collisions  
 3079 at  $\sqrt{s} = 13$  TeV with the ATLAS detector. Technical Report ATLAS-CONF-2016-017, CERN,  
 3080 Geneva, Mar 2016. URL <https://cds.cern.ch/record/2141006>.
- 3082 [127] Qi Zeng. Private communication.
- 3083 [128] ATLAS Collaboration. Identification of boosted, hadronically-decaying  $W$  and  $Z$  bosons in  
 3084  $\sqrt{s} = 13$  TeV Monte Carlo Simulations for ATLAS. (ATL-PHYS-PUB-2015-033), Aug 2015. URL  
 3085 <https://cds.cern.ch/record/2041461>.
- 3086 [129] ATLAS Collaboration. Performance of  $b$ -Jet Identification in the ATLAS Experiment. 2015.
- 3087 [130] Alexander L. Read. Presentation of search results: The CL(s) technique. *J. Phys. G*, 28:2693, 2002.  
 3088 doi: 10.1088/0954-3899/28/10/313.

- 3089 [131] Measurements of the Higgs boson production and decay rates and constraints on its couplings  
3090 from a combined ATLAS and CMS analysis of the LHC pp collision data at  $\sqrt{s} = 7$  and 8 TeV.  
3091 Technical Report ATLAS-CONF-2015-044, CERN, Geneva, Sep 2015. URL <http://cds.cern.ch/record/2052552>.  
3092
- 3093 [132] Projections for measurements of Higgs boson signal strengths and coupling parameters with the  
3094 ATLAS detector at a HL-LHC. Technical Report ATL-PHYS-PUB-2014-016, CERN, Geneva,  
3095 Oct 2014. URL <http://cds.cern.ch/record/1956710>.
- 3096 [133] ATLAS Phase-II Upgrade Scoping Document. Technical Report CERN-LHCC-2015-020. LHCC-  
3097 G-166, CERN, Geneva, Sep 2015. URL <http://cds.cern.ch/record/2055248>.